MICROWAVE ABSORBERS USING M-TYPE BARIUM HEXAFERRITE-NOVOLAC PHENOLIC RESIN NANOCOMPOSITE IN X-BAND – DESIGN, DEVELOPMENT AND ANALYSIS

A thesis submitted in partial fulfillment of the requirements for the degree of Doctor of Philosophy

By

Sikhajyoti Ozah

Registration No: 002 of 2011

Department of Physics

School of Sciences

Tezpur University

Napaam, Tezpur - 784028

Assam, India

July, 2014

I dedicate this work to my 'PAPA' and 'MAA'

Sri. Kanbap Ozah

&

Smti. Suroma Ozah

Preface

There are unwanted external electromagnetic (em) waves from various wireless sources, which not only interfere with other communication devices, but have detrimental effects on device performance. Effectively minimizing the electromagnetic radiations has become mandatory for reliable communication of information. The challenges lie in achieving sufficiently good absorption over a broad range of frequencies. In this dissertation, shields are developed to effectively suppress leakages in X-band i.e. 8.2-12.4 GHz. For effective absorption of incident electromagnetic wave- firstly, the em wave should enter the absorber matrix and then effectively attenuate within the matrix. An impedance matching at air-absorber interface will minimize the reflections and lossy material will effectively reduce the amplitude within the shield. For metal back absorbers, a thickness of $\lambda/4$ will give a destructive interference condition at the interface thus further reducing the reflected em wave. Considering applications in airborne and handheld devices light weight and thin absorbers are desired.

In this work magnetic absorbers are developed, considering the fact that permeability of magnetic material gives better impedance matching condition and reduces thickness. M type nanosized barium ferrites ($BaFe_{12}O_{19}$) with high saturation magnetization and high crystalline anisotropy are synthesized as the magnetic inclusions and incorporated in different weight ratios in novalac polymer resin (NPR). The size of inclusions are verified from XRD and TEM and uniformity of distribution in matrix by SEM. $BaFe_{12}O_{19}$ is substituted with aluminium and strontium to enhance anisotropy and hence absorption. The crystallite size of barium ferrite and substituted barium ferrite at 900^{0}C annealing temperatures are found to be in nanometer range. The use of nanosized ferrite material reduces the weight of absorber and increases the interacting surface for em wave within the absorbing material. The ferrite-NPR nanocomposite is characterize for other relevant properties

for absorbers viz. thermal stability, density, water absorbance and saturation magnetization.

The two critical material properties for design of absorbers are complex permittivity and permeability. Nicolson Ross method is used to determine complex permittivity value and permeability value over the X-band, the results are verified using cavity perturbation technique.

Using the complex permittivity and permeability values, design optimization is carried out for a conductor backed single layer microwave absorber, over the X-band, using transmission line model (TLM). Thickness optimization is further carried. Absorber with optimized thickness is fabricated and reflection loss is measured using free space technique. Single layer $BaFe_{12}O_{19}$-NPR nanocomposite with 50 wt. % shows a maximum reflection loss of -37.06 dB at 9.5 GHz with -10 dB bandwidth of 2.05 GHz and -20 dB bandwidth of 0.60 GHz.

A three layer design using the best performance single layer of $BaFe_{12}O_{19}$-NPR nanocomposite and Al^{3+} and Sr^{2+} ions substituted $BaFe_{12}O_{19}$-NPR nanocomposite is designed using TLM, where optimization of the total and individual thickness of the layers and possible compositions of the layers are carried out to achieve broad band absorption.

Field distribution in the single layer $BaFe_{12}O_{19}$-NPR absorber is analyzed using a full wave FDTD modeling algorithm.

DECLARATION

I hereby declare that the thesis *"Microwave Absorbers using M-type Barium Hexaferrite-Novolac Phenolic Resin Nanocomposite in X-Band - Design, Development and Analysis"*, being submitted to Department of Physics, Tezpur University, Tezpur, Assam in partial fulfillment for the award of the degree of Doctor of Philosophy in Physics, has previously not formed the basis for the award of any degree, diploma, associateship, fellowship or any other similar title or recognition.

Date: July 31st, 2014

Place: Tezpur

Sikhajyoti Ozah

(Sikhajyoti Ozah)

Department of Physics

School of Sciences

Tezpur University

TEZPUR UNIVERSITY

(A Central University by an Act of Parliament)

Napaam, Tezpur-784028

DISTRICT: SONITPUR::ASSAM::INDIA

Ph. 03712-267008(O) 5551,5555 (EPABX) 9435084076 (M)

Fax: 03712-267006

Email: *nidhi@tezu.ernet.in*

CERTIFICATE OF THE PRINCIPAL SUPERVISOR

This is to certify that the thesis entitled "***Microwave Absorbers using M-type Barium Hexaferrite-Novolac Phenolic Resin Nanocomposite in X-Band – Design, Development and Analysis***", being submitted to Tezpur University in requirement of partial fulfillment for the award of the degree of Doctor of Philosophy in Physics is a record of research work carried out by Ms. Sikhajyoti Ozah under my supervision and guidance.

All helps received from various sources have been duly acknowledged. No part of this thesis has been submitted elsewhere for award of any degree.

Date: July 31, 2014

Place: Tezpur

(Nidhi S. Bhattacharyya)

Professor

Department of Physics

Tezpur University

TEZPUR UNIVERSITY

(A Central University by an Act of Parliament)

Napaam, Tezpur-784028

DISTRICT: SONITPUR::ASSAM::INDIA

Ph. 03712-267004 (O) 9957198489 (M) Fax: 03712-267006 Email: *adm@tezu.ernet.in*

Certificate of the External Examiner and ODEC

This is to certify that the thesis entitled "***Microwave Absorbers using M-type Barium Hexaferrite-Novolac Phenolic Resin Nanocomposite in X-Band – Design, Development and Analysis***" being submitted by Ms. Sikhajyoti Ozah to Tezpur University in the **Department of Physics** under the **School of Sciences** in requirement of partial fulfillment for the award of the degree of Doctor of Philosophy in **Physics** has been examined by us on _____ and found to be satisfactory. The committee recommends for the award of the degree of Doctor of Philosophy.

Supervisor

(N. S. Bhattacharyya)

Date: _____

External Examiner

(**)**

Date: _____

Acknowledgements

"I can no other answer make, but, thanks, and thanks."

William Shakespeare

I would like to express my deep gratitude to Prof. Nidhi S. Bhattacharyya, my research supervisor, for her patient guidance, enthusiastic encouragement and useful critiques of this research work.

I would like to thank Prof. Satyajib Bhattacharyya, Dr. Pritam Deb and Dr Bhupen deka for their useful and constructive recommendations on this project.

I would like to thank Hon'ble Vice Chancellor of Tezpur University, Prof. Mihir Kanti Chaudhuri for giving inspiration and encouraging advice throughout my research work.

I am highly grateful to Prof. A. Choudhury, Prof. J. K. Sarma, Prof. A. Kumar, Prof. N. Das, Dr. G.A. Ahmed, Dr. D. Mahanta, Dr. P. Deb, Dr. K. Barua, Dr. P.K. Karmakar, Dr. M.K. Das, Dr. P. Nath and Mr. R. Biswas of Department of Physics for their personal involvement, timely help, stimulating discussion to carry out research. I acknowledge the help received from the technical staff of Department of Physics.

I am thankful to Shri R. S. Shinde, RRCAT, Indore, for his valuable suggestions.

I would like to thank SAIF, Shillong, IIT Guwahati, Department of Chemical Sciences, Tezpur University for allowing me to avail the analytical facilities required in my research work.

I am extremely indebted to Department of Information Technology, Govt. of India, for their financial assistance through the project to carry out the research work

I would like to thank the office staff of Dept. of Physics, Mr. U. Patir and Mr. N. Sarma, technical staff of Central Workshop, Tezpur University, Mr. M. Handique, Mr. K. Rangpi, Mr. D. Gogoi, Mr. P. Rabha, Mr. S.K. Nath and Mr. M. Mali for their help and support. Thanks to the Library staff and administrative staff of Tezpur University for their help.

A special thanks to all the research scholars of Department of Physics, Tezpur University for their company and wonderful time I enjoyed with them during my research work. Bondita, Anup, Deepak, Angshumanda, Swatiba, Ankurda, Mansiba, Sovanda, Mayuriba, Manjit, Anil, Madhulekha, Biswajit, Namita, Chandrani, Priyanka, Samiran, Kaushik, Saurav, Pawan, Ananya, thank you all for your support and encouragement.

Thank you Priyanka Agarwal, Sayan, Banasri and Nibedita for your constant care and support throughout my journey, you all need special mention.

Also I am grateful to all the research scholars of Tezpur University, specially Prarthana and Anisha for sharing a wonderful time during my research work. Nilima, Momina, Shyamalima, Monalisha and Dipannita , thank you for your love and care.

I thank my friends, Partha P Borah, Partha P Bharali, Manash P. Gogoi, Plabita Gogoi, Dipika Rabidas and Arunav Kalita for their encouragement and good wishes.

My lab-mates Debashisda, Tanuj, Pulin, Subasitda, Kunalda, Lutu and Dipankar, a big thank you for all the wonderful times, academic and otherwise, that we shared together.

No one walks alone on the journey of life. And I do not know where to start to thank all those people who walked with me and helped me along the way continuously urging me in my work and shared my insights. Arunav and Jyotida, thank you for your constant inspiration and help throughout my research life. Pragyan and Rocktotpal, thank you for your support and care.

No words can repay for the continuous encouragement, moral support, blessings and everything else that I received from my parents, Kanbap Ozah and Suroma Ozah. Thank you Pa, Maa for keeping faith on me. I am thankful to my brother Nabajyoti, Dhrubajyoti, Sauravjyoti for their love and support. You were always there whenever needed. Thanks to my sister Debajyoti, Bhindeu, Pankaj Tamuly, Bou, Ivy and my Khura, Prabin Ozah for your love. Kuu and Nee, thank you for your concern.

Sikhajyoti Ozah

CONTENTS Page no.

CONTENTS Page no.

CONTENTS Page no.

CONTENTS Page no.

CONTENTS

List of Tables

List of Figures

List of symbols and abbreviations

EMI	Electromagnetic interference
MAM	microwave absorbing material
RAM	Radar absorbing material
FNP	Ferrite nanoparticle
NPR	Novolac Phenolic Resin
CNT	Carbon Nano Tube
XRD	X-ray Difraction
SEM	Scanning Electron Microscopy
TEM	Transmission Electron Microscope
TLM	Transmission line model
TGA	Thermo Gravimetric Analysis
TRL	Through-Reflect-Line
VNA	Vector Network Analyzer
BW	Bandwidth
RF	Radio Frequency
RL	Reflection loss
ω	Angular frequency
γ	Propagation constant
ε_{eff}	Effective permittivity
ε_o	Free space permittivity
ε_r	Relative permittivity
ε_r''	Imaginary part of the complex permittivity

ε_r'	Real part of complex permittivity
μ_o	Free space permeability
μ_{eff}	Effective permeability
μ_r	Relative permeability
μ_r''	Imaginary part of complex permeability
μ_r'	Real part of complex permeability
$\tan\delta_\varepsilon$	Dielectric loss tangent
$\tan\delta_\mu$	Magnetic loss tangent
A	Ampere
dB	decibel
E	Electric field vector
EM	Electromagnetic
f_r	Resonant frequency
GHz	Giga Hertz
σ_s	Static conductivity
σ_e	Effective conductivity
σ_a	Conductivity due to alternating field
κ	Filling factor
K	Co- efficient of thermal conductivity
Q	Quality Factor
Z_0	Characteristic impedance
λ_0	Free space wavelength
λ_g	Guide wavelength

F	Farad
G	Gauss
$4\pi M_s$	Saturation magnetization in CGS unit
Oe	Oersted
S11	Scattering parameter
Z_0	Characteristic impedance
λ_0	Free space wavelength
λ_g	Guide wavelength

CHAPTER I

INTRODUCTION TO THE RESEARCH PROBLEM

1.1 INTRODUCTION

There are unwanted external electromagnetic (em) waves from various wireless sources, which not only interfere with other communication devices, but have detrimental effects on device performance [1]. For reliable communication and detection of information, minimizing the electromagnetic radiations is mandatory.

Electromagnetic interference can be minimized by either shielding the device by placing it inside a reflecting enclosure or absorbing the incident em radiations. The former way of shielding can cause secondary interfering reflections affecting other devices in vicinity and hence studies on EMI shields of absorber type are chosen (throughout the thesis EMI shields will refer to only absorption type) [2]. Absorption mechanism works on the principle of conversion of the interfering wave energy into thermal energy [3].

Essentially two important conditions in an absorber are to be satisfied to suppress electromagnetic radiations - firstly, minimum reflection at the air-absorber interface and secondly, sufficient attenuation of the incident wave energy within the absorber, refer to figure 1.1 [4].

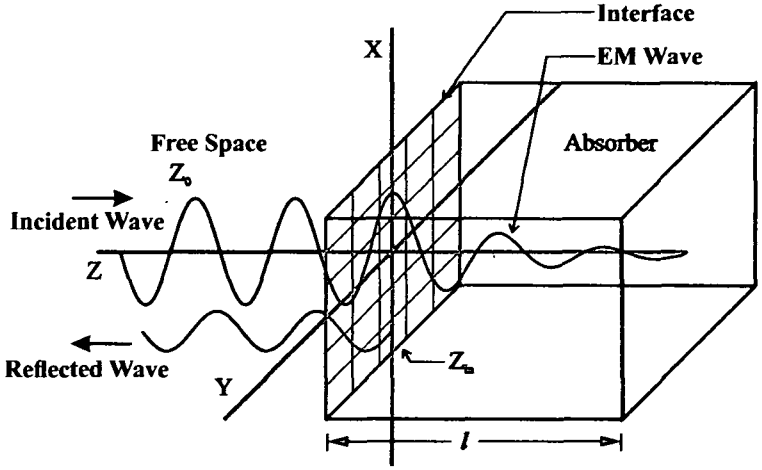

Figure 1.1 Absorption mechanism in single layer absorber

Reduction of reflection at the interface can be obtained by taking the conditions of impedance matching at the air-absorber interface i.e. $Z_{air} = Z_{in}$ and thereafter,

attenuation within the absorber matrix using lossy material. The two conditions can be tailored by complex permittivity, $\varepsilon_r=\varepsilon_r'-j\varepsilon_r''$ and complex permeability, $\mu_r=\mu_r'-j\mu_r''$ of the absorbing material at the desired frequency. Absorption shields are generally fabricated as composites, using dielectric or magnetic lossy materials as inclusions in an insulating polymer matrix [5, 6]. The two main loss mechanisms for dielectric materials are conduction and dielectric losses. High conductivity leads to conduction losses and dipolar losses are due to polarization effects. On the other hand, magnetic composite absorption depends on magnetic hysteresis effect of the magnetic inclusions incorporated into the matrix [7-9]. Permeability and permittivity of magnetic inclusions gives the matching condition and ε'' and μ'' accounts for the microwave energy loss in the materials. Absorber research took a major lunge with World War II, where stealth mechanism was used to avoid radar detection of airborne vehicles and missiles. First reported absorption EMI shields dates back to 1936, when a quarter-wave resonant absorber based on carbon black and titanium dioxide was developed and patented in Netherlands [10]. During World War II, America developed "Halpern Anti Radiation Paint (HARP)" used on airborne and seaborne vehicles for stealthing from radar detection with 15–20 dB absorption in the X-band. Absorbing paint was made using rubber filled with carbon black, disc shaped aluminum flakes and barium titanate [11, 12]. During the same time Germans developed "Wesch" material and also produced Jaumann absorbers, a multilayer structure of alternating resistive sheets and rigid plastics [13]. In 1952, another narrow band resonant absorber Salisbury screen was patented, consisting of resistive sheet placed at odd multiple of ¼ wavelengths from a metal plate.

Most of the absorbers developed were dielectric absorbers. In year 1952, first Dallenbach layer magnetic absorber, using ferrite materials was patented [14]. G. Rado and his group from Naval Research Laboratoy, USA [15] investigated extensively mechanisms of absorption in magnetic ferrites and alloys based absorbers. Thin absorbers developed by this group were extensively used as

prototype stealth treatments for missile-like drones, aircraft, and ships, by the Joint Cruise Missile Program Office and the other services.

Kunihiro Suetake, in 1969, patented thin microwave absorbing wall using magnetic materials [16]. A pyramidal structure using nickel-zinc ferrite [17] was developed which showed a broadband absorption. A group from Tokyo Institute of Technology extensively studied ferrite absorbers with matching thickness and frequency [18].

Subsequently a lot of work was carried out on absorbers with magnetic inclusions [19-29]. Iron fillings were used as magnetic inclusions for EMI shields by many research groups [30, 31]. In spite of being an efficient absorbing material, iron metal was prone to corrosion and was heavy in weight. References [32-35] report use of the metallic magnetic powders, Fe-Si-Al alloy, Fe, Co or Ni and their permalloys as magnetic inclusions in absorbing materials. Alternately, magnetic inclusions like iron oxide and carbonyl iron have been widely used by G. Viau, et al. and S. Sugimoto et al. [35, 36]. The electric conductivity of these materials are generally high and at high frequencies the permeability decreases rapidly and becomes less as compared to permittivity [36, 37], thus the resonance frequency is low.

Ferrites because of its high corrosion resistance, high value of complex permeability, good resistivity and good chemical stability are good candidate for magnetic absorbers [38]. Ni- Zn, cobalt ferrite and other substituted spinel ferrite have been used as magnetic inclusions in references [39-41]. However, use of spinel ferrites get limited to lower frequencies, as the complex permeability drops at higher frequency, given by Snoek's limit [42].

Hexagonal ferrites has high crystalline anisotropy, high natural resonance frequency (not limited by Snoek's limit) and high saturation magnetization and has been extensively studied in past few decades as inclusions for development of magnetic absorbers for frequency applications >1GHz [43-47]. M-type barium hexaferrites have been extensively used as microwave absorber material [48, 49].

It is well known that the dielectric and magnetic properties can be modulated by substituting Fe^{3+} and Ba^{2+} with other ions [50, 51]. Fe^{3+} ions substituted with Al^{3+} ions in barium and strontium ferrites have been reported [52] with enhanced absorption. Absorption properties of M-type barium ferrite have been further tuned at higher frequencies by varying particle size, shape and sintering temperature [53].

The density of the magnetic materials is too high to use them in large quantity as filler in polymer matrix, as it increases the weight of absorber. Absorbers are increasingly being used in airborne and handheld devices and reducing the weight of the absorbing material is an important concern for applications in defense and commercial purpose [54].

Nanosized materials are reported to have low density and high surface to volume ratio [55-57]. Hence, nanosized inclusions in polymer matrix reduce the weight of absorber and also increase the interacting surface for em wave within the material. Carbon nanotubes (CNT) [58, 59] and expanded graphite nano flakes was used by different groups [60] as nano inclusions for developing light weight em shields.

Nanosized ferrites as inclusions have also shown promise for development of light weight and thin magnetic shields. During 2000 to 2014, lots of work on absorbing material using nanosized ferrites and iron oxides were reported. Fe_3O_4 nanoparticles and ferrite nanoparticles were used for development of magnetic absorbers in references [61, 62]. In 2000, Shengping Ruan and his group studied microwave absorption of ZnCo-substituted W-type barium nano hexaferrite. An enhancement of absorption from -17 dB to - 28.5 dB was observed with a -10 dB bandwidth of 5 GHz, with reduction of particles size from 5 μm to 65 nm [63]. Vladimir B. Bregar conducted a comparative study on iron nanocomposite and ferrite nanocomposites and ~-29 dB absorption peak was observed for nanosized ferrite inclusions while nano iron inclusions showed ~-11 dB absorption peak [64]. Study of absorption with Co, Mg and Cu doping in NiZn spinel ferrite nanocrystals in thermalplastic polyurethane (TPU) elastomer was carried out in

the reference [65] and reported an enhancement of absorption with doping and reduction in size of inclusions. Investigation on absorption properties of nano sized barium ferrite prepared by ball milling process was carried out by Jianxun Qiu and his group in 2005 [66]. The absorption was studied with different ball milling time and found that nanoscale milled barium ferrite improves microwave loss by 8 dB in comparison to the bulk and broadens the frequency bandwidth with loss above 10 dB, by 5.3 GHz. Microwave absorbing properties on doped Z-type barium hexaferrites ($Ba_3Co_{1.3}Zn_{0.3}Cu_{0.4}Fe_{24}O_{41}$)/poly-chloroprene (CR) nanocomposites was reported by Caffarena et al. [67]. The nanocomposite showed use as potential absorbers in X/Ku bands, with absorption band of ≤ -10 dB at 10.0-12.5 GHz for absorber thickness of 2.5 mm and bandwidth of 13.0-16.0 GHz for 2.0 mm thick absorber. In 2008, Anil Ohan et al. studied barium ferrite nano inclusions in conducting polymer from 12.4 GHz to 18 GHz, a high shielding effectiveness of 28.9 dB was reported [68]. Dhawan et al. reported improvement of the magnetic and dielectric properties of polymer matrix by incorporating nanosized barium ferrite or Fe_2O_3 particles in the polymer matrix [69, 70]. Esmail Kiani et al. reported a study on effect of doping on microwave properties of $SrFe_{12-2x}La_x(Mn_{0.5}Zr_{0.5})_xO_{19}$ nanoparticles [71]. Seyed H. Hosseini and M. Moloudi's study on strontium substituted barium ferrite nanocomposite ($Ba_xSr_{1-x}Fe_{12}O_{19}/Fe_3O_4$/PAA nanocomposites), showed a reflection loss <-9 dB [72].

Achieving sufficiently good absorption over a broad range of frequencies is desired for many applications. Bandwidth of absorption can be enhanced by multilayering the shield structure. In 1984, a two layer absorber design with a ferrite layer at the air/absorber interface and a layer containing ferrite and short metal fibres as the absorber/metal interface was developed by K. Hatakeyama and T. Inui [73] with absorption of -20 dB over 8-12 GHz for a thickness of 4.6 mm. A double layer absorber using nanosized strontium ferrite and iron microfiber was developed and its thickness optimization was carried out by Wei Chun-Yu, Shen Xiang-Qian, and Song Fu-Zhan from China [74], with a

maximum absorption of -63 dB for thickness of 2 mm. Several works on multilayer microwave absorber for bandwidth enhancement had been reported by M. R. Mesharam and his group [25, 75]. A three layer absorber with samples of M-type hexagonal ferrite powders, namely $Ba(MnTi)_xFe_{12-x}O_{19}$, with x=1.6,1.7,1.8 was developed and maximum absorption of 10 dB is observed from 12.5 to 18 GHz.

Another aspect to be considered while fabricating microwave absorbing material is the polymer base matrix Several reports on choice and influence of polymer matrix is reported in literature. Use of epoxy resin and conducting polymer as matrix was reported for development of EMI shields in [68, 70]. Reference [76] reports, that the use of phenolic resin matrix in carbon black composite instead of epoxy resin matrix enhances the electrical properties of the composite. NPR being good heat resistance has dimensional stability, flame and chemical resistance as well as low cost [77] can be used as base matrix while developing microwave absorbing materials.

The challenge lies in developing light weight, thin, corrosion resistant shields having sufficiently good absorption over a broad range of frequencies.

1.2 ELECTROMAGNETIC THEORY FOR MAGNETIC ABSORBER

Before designing absorbers, it is important to understand the mechanism of absorption. The absorption of microwaves in magnetic medium depends on the material's complex permittivity and permeability. The mathematical formulation of this loss mechanism can be obtained using Maxwell's wave equations [78].

The modified curl equations in phasor form are

$$\nabla \times \bar{H} = \bar{J} + j\omega\bar{D} \quad (1.1)$$

$$\nabla \times \bar{E} = -j\omega\bar{B} \quad (1.2)$$

where, $\bar{D} = \varepsilon\bar{E}$, (1.3)

$$\bar{B} = \mu\bar{H} \quad (1.4)$$

$$\bar{J} = \sigma_s\bar{E} \quad (1.5)$$

$\bar{D}$ is the electric flux density and $\varepsilon = \varepsilon_0\varepsilon_r$ is the permittivity and $\bar{B}$ is the magnetic flux density and $\mu = \mu_0\mu_r$ is the permeability. $\bar{J}$ is the conduction current density, caused by application of an external field and σ_s, the conductivity. Since in this work ferrite-polymer composites have been used i.e. $\sigma_s \sim 0$, conductivity term can be neglected in equation 1.1.

Thus equation 1.1 becomes,

$$\nabla \times \bar{H} = j\omega\varepsilon_0\varepsilon_r\bar{E} \qquad (1.6)$$

where, ε_0 , is the permittivity of free space (ε_0= 8.86 x 10^{-12} F/m) and ε_r , the relative permittivity of the medium is a complex quantity expressed as

$$\varepsilon_r = \varepsilon_r' - j\varepsilon_r'' \qquad (1.7)$$

where, ε_r' is the real part of complex permittivity and ε_r'' is the effective relative dielectric loss factor [79].

Similarly, equation 1.2 gives,

$$\nabla \times \bar{E} = -j\omega\mu_0\mu_r\bar{H} \qquad (1.8)$$

where, μ_0, is the permeability of free space ($\mu_0 = 4\pi \times 10^{-7}$H/m) and μ_r , the relative permittivity of the medium is expressed as

$$\mu_r = \mu_r' - j\mu_r''$$

where, μ_r' is the real part of complex permeability and μ_r'' is the effective relative magnetic loss factor [79].

When an oscillating electric field interacts with the dipole, the dipole rotates to align itself according to the polarity. During the alignment the energy is lost through the generation of heat (friction) and the acceleration and deceleration of the rotational motion. The degree to which the dipole is out of phase with the incident electric field is a characteristic to the material and depends on frequency of the oscillating electric field, which determines the magnitude of the imaginary part of the permittivity. The larger the imaginary part, more the energy is being dissipated through the alignment motion and hence, less energy is available to propagate past the dipole. Thus, the imaginary part of the relative permittivity directly relates to loss in the system.

Similarly, in case of magnetic materials, the field interacts with the magnetic dipoles. There are three main loss mechanisms for magnetic materials, viz. hysteresis, eddy current and residual loss. Residual losses include the resonance losses which dominate at high frequencies.

The equation, (1.5) is given as

$$\nabla \times \bar{H} = j\omega(\varepsilon' - j\varepsilon'')\bar{E} \tag{1.9}$$

$$\nabla \times \bar{H} = j\omega\varepsilon'\left(1 - j\frac{\varepsilon''}{\varepsilon'}\right)\bar{E} \tag{1.10}$$

The term $tan\delta_e = \varepsilon'' / \varepsilon'$ describes the amount of energy supplied by an external electric field that gets dissipated in alignment motion of dipole and heat which is more evident in dielectrics.

The phasor form (frequency domain) of wave equations are

$$\nabla^2\bar{E} = \mu\varepsilon(j\omega)^2\bar{E} \tag{1.11}$$

$$\nabla^2\bar{H} = \mu\varepsilon(j\omega)^2\bar{H}$$

$$= -\omega^2\varepsilon\mu\bar{H} \tag{1.12}$$

Let, $-\omega^2\varepsilon\mu = \gamma^2$ (1.13)

The equations (1.11) and (1.12) reduce to

$$\nabla^2\bar{E} - \gamma^2\bar{E} = 0 \tag{1.14}$$

$$\nabla^2\bar{H} - \gamma^2\bar{H} = 0 \tag{1.15}$$

where, $\gamma = \sqrt{-\omega^2\varepsilon\mu} = j\omega\sqrt{\varepsilon_0\mu_0}\sqrt{\varepsilon_r\mu_r} = j\frac{2\pi f}{c}\sqrt{\varepsilon_r\mu_r} = \alpha + j\beta$ (1.16)

γ, is the propagation constant, α, is the attenuation constant which defines the rate at which the fields of the electromagnetic wave attenuates as the wave propagates and β, is the phase constant defining the rate at which the phase changes as the wave propagates.

If the electromagnetic wave propagates through the absorber in y-direction (figure 1.2), the uniform plane wave has only z-component of the electric field and x-component of the magnetic field which are both functions of y only.

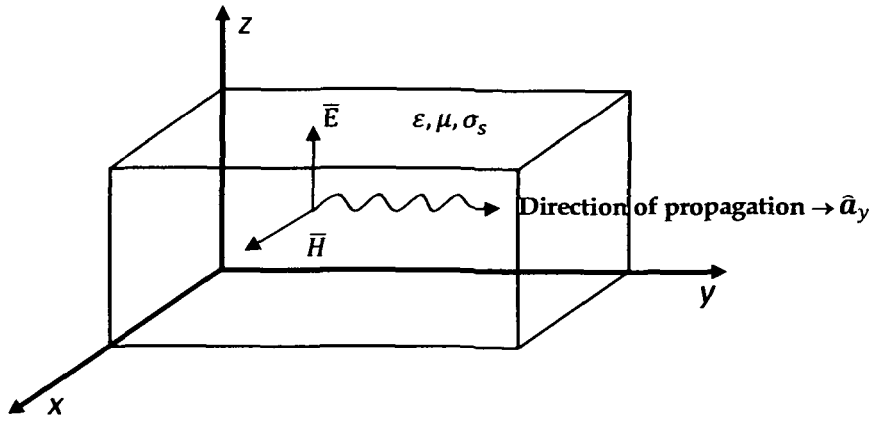

Figure 1.2 Uniform plane wave propagating in y-direction within an absorber block

The wave equations for the two field components ($\bar{E}_z$,$\bar{H}_x$) are

$$\frac{d^2\bar{E}_z}{dy^2} - \gamma^2\bar{E}_z = 0 \tag{1.17}$$

$$\frac{d^2\bar{H}_x}{dy^2} - \gamma^2\bar{H}_x = 0 \tag{1.18}$$

The general solution to the wave equations (1.17) and (1.18) are

$$\begin{aligned}\bar{E}_z(y) &= E_1e^{\gamma y} + E_2e^{-\gamma y}\\ &= E_1e^{(\alpha+j\beta)y} + E_2e^{-(\alpha+j\beta)y}\\ &= E_1e^{\alpha y}e^{j\beta y} + E_2e^{-\alpha y}e^{-j\beta y}\end{aligned} \tag{1.19}$$

and $$\begin{aligned}\bar{H}_x(y) &= H_1e^{\gamma y} + H_2e^{-\gamma y}\\ &= H_1e^{(\alpha+j\beta)y} + H_2e^{-(\alpha+j\beta)y}\\ &= H_1e^{\alpha y}e^{j\beta y} + H_2e^{-\alpha y}e^{-j\beta y}\end{aligned} \tag{1.20}$$

Assuming the uniform plane wave as travelling in $+y$ direction, the electric field

$$\bar{\mathrm{E}} = \bar{E}_z\hat{a}_z = E_0e^{-\gamma y}\hat{a}_z \tag{1.21}$$

The corresponding magnetic field, found from the source free Maxwell's equations

$$\nabla \times \bar{E} = -j\omega\mu\bar{H} \tag{1.22}$$

$$\begin{aligned}\bar{H} = -\frac{1}{j\omega\mu}\nabla\times\bar{E} &= -\frac{1}{j\omega\mu}\left[\frac{\partial\bar{E}_z}{\partial y}\hat{a}_x - \frac{\partial\bar{E}_z}{\partial x}\hat{a}_y\right]\\ &= -\frac{1}{j\omega\mu}\left[\frac{\partial}{\partial y}(E_0e^{-\gamma y})\hat{a}_x\right]\\ &= -\frac{1}{j\omega\mu}(-\gamma E_0e^{-\gamma y})\hat{a}_x\end{aligned}$$

$$= \frac{\gamma}{j\omega\mu} E_0 e^{-\gamma y} \hat{a}_x = \bar{H}_x \hat{a}_x \qquad (1.23)$$

The intrinsic impedance (η) of the wave is defined as the ratio of the electric field and magnetic field phasors (complex amplitudes)

$$\eta = \frac{\bar{E}_z}{\bar{H}_x} = \frac{E_0 e^{-\gamma y}}{\frac{\gamma}{j\omega\mu} E_0 e^{-\gamma y}} = \frac{j\omega\mu}{\gamma} = \frac{j\omega\mu_0\mu_r}{j\omega\sqrt{\varepsilon_0\mu_0}\sqrt{\varepsilon_r\mu_r}} \qquad (1.24)$$

$$\eta = \sqrt{\frac{\mu_0}{\varepsilon_0}}\sqrt{\frac{\mu_r}{\varepsilon_r}} = \eta_0\sqrt{\frac{\mu_r}{\varepsilon_r}} \qquad (1.25)$$

where, η_0 is the characteristic impedance of free space.

Intrinsic impedance of the medium determines the amount of electromagnetic wave which will get reflected at the air-absorber interface and the amount which will propagate through the medium. Once the incident wave enters the absorbing material, the wave should exponentially decay with distance, y, by the factor, $e^{-\alpha y}$ where α is the attenuation constant as shown in figure 1.3. Expanding equation (1.15), α can be expressed [80] as

$$\alpha = \frac{\sqrt{2}\pi f}{c} \times \sqrt{(\mu_r''\varepsilon_r'' - \mu_r'\varepsilon_r') + \sqrt{(\mu_r''\varepsilon_r'' - \mu_r'\varepsilon_r')^2 + (\varepsilon_r'\mu_r'' + \varepsilon_r''\mu_r')^2}} \qquad (1.26)$$

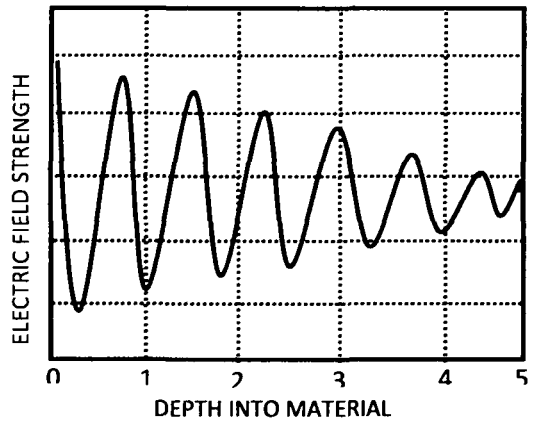

Figure 1.3 Progressive attenuation of electric field strength into the depth of the absorber

It is seen from the above equation that larger the values of complex permittivity and permeability, larger will be the attenuation of the microwave energy. However, larger value of complex permittivity and permeability results in more reflection due to impedance mismatch at the absorber interface thus restricting

the electromagnetic wave from entering the media [81]. Thus, a compromise has to be worked out while choosing the material for the absorber.

Design of absorbers is critical in development of shields which can effectively soak the em wave incident on it. Transmission line model (TLM) is used for designing of absorbers [82]. The theory of TLM is discussed in the following section.

1.3 TRANSMISSION LINE ANALOGY FOR MICROWAVE ABSORBER

Plane electromagnetic waves propagating in bulk slabs can be modeled by transmission line equations [82]. TLM is a numerical technique based on temporal and spatial sampling of electromagnetic fields. The transmission lines are simulated as propagation domain, where the electric and magnetic vectors of propagating electromagnetic wave are made equivalent to voltages and currents on the network, respectively.

1.3.1 Transmission line modeling for single layer absorber

A transmission line carrying TEM wave is represented as distributed elements in a network having series impedance $Z = R + j\omega L$ and shunt admittance

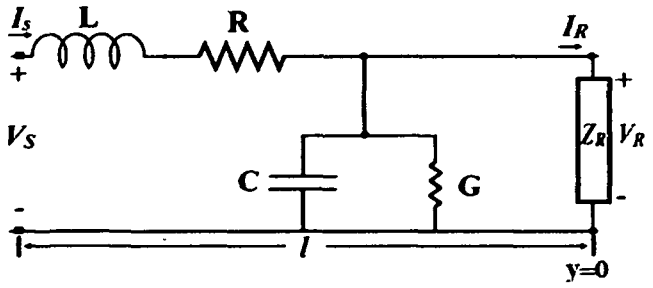

Figure 1.4 A circuit representation of a transmission line

$Y = G + j\omega C$ per unit length [7] as shown in figure 1.4.

The voltage and current distribution along the transmission line are functions of both time and position and are mainly determined from the shape, dimension and the properties of the conductors and dielectrics [83]. For a uniform

transmission line having the constants R, L, C and G per unit length, the voltage and current equations can be written in the differential form as

$$\frac{\partial \tilde{V}}{\partial y} + L\frac{\partial \tilde{I}}{\partial t} + R\tilde{I} = 0 \quad (1.27)$$

$$\frac{\partial \tilde{I}}{\partial y} + C\frac{\partial \tilde{V}}{\partial t} + G\tilde{V} = 0 \quad (1.28)$$

If the voltages and currents vary sinusoidally with time, the phasor notation of equations (1.27) and (1.28) become

$$\frac{\partial V}{\partial y} + (R + j\omega L)I = 0 \quad (1.29)$$

$$\frac{\partial I}{\partial y} + (G + j\omega C)V = 0 \quad (1.30)$$

The analogous relation between electric and magnetic field components of plane wave to the transmission line parameters are given as $\frac{\partial E_z}{\partial y} + j\omega\mu H_x = 0$ and $\frac{\partial H_x}{\partial y} + (\sigma_s + j\omega\varepsilon)E_z = 0$.

Differentiating equations (1.29) and (1.30) with respect to x and combining gives

$$\frac{\partial^2 V}{\partial y^2} - (R + j\omega L)(G + j\omega C)V = 0 \quad (1.31)$$

$$\frac{\partial^2 I}{\partial y^2} - (R + j\omega L)(G + j\omega C)I = 0 \quad (1.32)$$

A possible solution for these equations is of the form

$$V \text{ or } I = Ae^{-\gamma y} + Be^{\gamma y} \quad (1.33)$$

where, $\gamma^2 = (R + j\omega L)(G + j\omega C)$ (1.34)

When the variation with time is expressed explicitly, the first term of the expression (1.33) represents a wave travelling in forward direction and the second term represents a wave travelling in reverse direction.

In hyperbolic function form, the solutions to equations (1.31) and (1.32) are

$$V = A_1 cosh\, \gamma y + B_1 sinh\, \gamma y \quad (1.35)$$

$$I = A_2 cosh\, \gamma y + B_2 sinh\, \gamma y \quad (1.36)$$

Considering the location of the terminating impedance Z_R the reference point (y = 0), the other end is left of this reference point, i.e. in the -y direction as

shown in figure 1.4. Solving the constants, A_1, B_1, A_2 and B_2 and writing $l = -y_1$, equations (1.35) and (1.36) becomes

$$V_S = V_R cosh\,\gamma l + Z_0 I_R\, sinh\,\gamma l \quad (1.37)$$

$$I_S = I_R cosh\,\gamma l + \frac{V_R}{Z_0} sinh\,\gamma l \quad (1.38)$$

The general expression for the input impedance of the transmission line is obtained by dividing equation (1.37) by equation (1.38) i.e.

$$Z_{in} = \frac{V_S}{I_S} = \frac{V_R cosh\,\gamma l + Z_0 I_R\, sinh\,\gamma l}{I_R cosh\,\gamma l + \frac{V_R}{Z_0} sinh\,\gamma l} \quad (1.39)$$

or

$$Z_{in} = Z_0 \frac{Z_R + Z_0 tanh\,\gamma l}{Z_0 + Z_R tanh\,\gamma l} \quad (1.40)$$

The expression (1.40) gives the input impedance of the transmission line terminated by a load, Z_R. The input impedance of a single layer absorber can be expressed as,

$$Z_{in} = Z_0 tanh\left[j\left(2\pi f l/c\right)\sqrt{\mu_r \varepsilon_r}\right] \quad (1.41)$$

where, ε_r $(=\varepsilon_r' - j\varepsilon_r'')$, *is the* complex permittivity, μ_r $(=\mu_r' - j\mu_r'')$, is the complex permeability, and, l, is the thickness of the absorber and, f, is the incident microwave frequency [84].The reflection coefficient and the reflection loss in dB is expressed as,

$$\Gamma = \frac{Z_{in} - Z_0}{Z_{in} + Z_0} \quad (1.42a)$$

$$RL = 20log|\Gamma| = 20log\left|\frac{Z_{in} - Z_0}{Z_{in} + Z_0}\right| \quad (1.42b)$$

1.3.2 Transmission line modeling for multilayer absorber

The transmission line section in figure 1.4 is extended to multi section as shown in figure 1.5 then the input impedance at the i^{th} layer is given as

$$Z_{in} = Z_{oi} \frac{Z_{i-1} + Z_{oi} tanh\,\gamma_i l_i}{Z_{oi} + Z_{i-1} tanh\,\gamma_i l_i} \quad (1.43)$$

Where Z_{oi} is the characteristic impedance of the i^{th} layer.

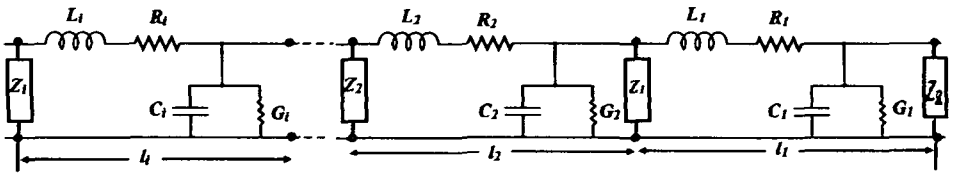

Figure 1.5 A circuit representation of a multisection transmission line

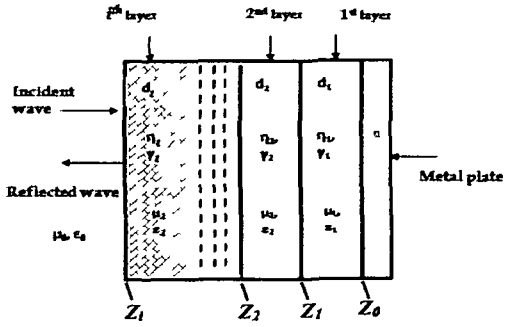

Figure 1.6 Distributed parameters of a multilayer absorber structure

Similar to equation (1.43), the input impedance of a plane wave incident normal to the surface of a absorber or composite substrate backed by a metal as shown in figure 1.6, can be expressed as

$$Z_{in} = \eta_i \frac{Z_{i-1}+\eta_i tanh\,\gamma_i d_i}{\eta_i+Z_{i-1}tanh\,\gamma_i d_i} \tag{1.44}$$

where, η_i is the intrinsic impedance of the i^{th} layer and is calculated from $\eta = \sqrt{\frac{\mu}{\varepsilon}}$, (Equation (1.24)).

For free space medium, $\mu = \mu_0 = 4\pi \times 10^{-7}(N/A^2)$ and $\varepsilon = \varepsilon_0 = 8.8541 \times 10^{-12}F/m$, so the value of $\eta = \eta_0 \approx 377\ \Omega$.

For a three layer absorber, i=3,

$$Z_3 = \eta_3 \frac{Z_2+\eta_3 tanh\,\gamma_3 d_3}{\eta_3+Z_2 tanh\,\gamma_3 d_3} \tag{1.45}$$

The reflection coefficient and reflection loss in dB, of the normal incidence plane wave is expressed [81, 85] as

$$\Gamma = \frac{Z_3-377}{Z_3+377} \tag{1.46a}$$

$$RL = 20log|\Gamma| = 20log\left|\frac{Z_{in}-Z_0}{Z_{in}+Z_0}\right| \tag{1.46b}$$

1.4 PROBLEM DEFINITION

Considering the fact that EMI shields are finding numerous applications in military and commercial devices, and the background analysis of absorbers has brought in some important aspects:

1. Minimum reflection of the incident em wave is required at the air absorber interface.
2. Maximum attenuation of the em wave within the absorber.
3. Absorber should be thin
4. Reduction in weight of the absorber
5. Corrosion resistive with low water absorbance and thermally stabile absorbers
6. Absorption over a broad frequency range and
7. Lastly, ease of processing and overall cost of development of the absorber.

The leakages in X- band can be generated from widely used sources like precision approach radar (PAR) (9.0-9.2 GHz), military communication satellites (7.9 to 8.4 GHz for uplink & 7.25 to 7.75 GHz for downlink), terrestrial communication and networking (10.15 to 10.7 GHz), motion detectors (10.525 GHz), traffic light crossing detectors (10.4 GHz), weather radars (9.3-9.5 GHz) [86-91] and many other local area networking or wireless devices. The thesis problem focuses on developing em shields that can effectively reduce leakages in the X-band i.e. 8.2-12.4 GHz.

Based on the requisites discussed above the research work is focussed on developing- microwave absorbers using nanosized M-type barium hexaferrite and substituted barium ferrite in NPR matrix. Design considerations will be carried out to reduce the thickness enhanced bandwidth of absorption for X-band applications.

Thus, the research is essentially directed towards:

- Synthesis and development of the nanosized ferrite and composite materials.
- Investigation of other necessary factor requirements of microwave absorber applications like homogeneity of filler in the base matrix, light weight, thermal, electrical, magnetic and environmental inertness.
- EMI shielding/microwave absorber having the desirable microwave permittivity, permeability, dielectric and magnetic loss properties for application over the X-band frequency.
- Design, thickness optimization and fabrication of single layer microwave absorber using developed magnetic composites in X-band.
- Design optimization and development of multilayer microwave structure for enhancing the absorption bandwidth.
- Analysis of field distribution within the absorber using finite difference time domain (FDTD) Technique.

1.5 THESIS STRUCTURE AND OUTLINE

The thesis structurally consists of seven chapters and four appendixes. A thorough understanding of electromagnetic wave propagation through the absorber and its equivalent Transmission line model is discussed in *chapter I.*

M-type nanosized barium hexaferrite as reinforcers in novolac phenolic resin matrix is developed as magnetic absorber material and is dealt in *chapter II.* The synthesis of substituted barium ferrite compositions with Al^{3+} replacing Fe^{3+} and Sr^{2+} ions substituting Ba^{2+} ions, is also discussed. The chapter also includes microstructural studies conducted for structural, size of the synthesized ferrite particles and ascertaining the homogeneous composite formation. Other essential properties required for absorbers like thermal stability, density, water absorbance, in - plane dc conductivity and saturation magnetization are included in *chapter II.*

Chapter III includes studies on complex permittivity and permeability of the ferrite composites at microwave frequencies for different weight percentages of unsubstituted and substituted ferrite-NPR compositions. Nicolson-Ross technique is used for determining the complex permittivity and permeability values. The values are substantiated by cavity perturbation technique.

Single layer Dallenbach absorber using ferrite-NPR composite with conductor backing is designed and fabricated and the thickness is optimized to achieve minimum reflection loss is discussed in *chapter IV*. Free space technique is used to measure the reflection loss.

Chapter V describes enhancement of bandwidth by using multilayer structure where the thickness of individual layer as well as the total thickness and the layer combinations is optimized to achieve a broad absorption bandwidth.

Theoretical background of the 3D FDTD technique is discussed in *chapter VII*. The technique has been adopted for single layer absorber. MATLAB code has been developed using the FDTD formulation to determine the field distribution throughout the absorber and S_{11} parameters are computed.

Chapter VII summarizes the suitability of the developed ferrite-NPR nanocomposites as broadband absorber in X-band. The limitations and future direction of work that can be incorporated are also highlighted.

Appendix A gives the detail of mathematical formulation for theoretical thickness limitation for broadband microwave absorption. MATLAB programs developed for optimizing multilayer microwave absorber parameters are also discussed in **Appendix B**. **Appendix C** gives the detail equations for PML boundary conditions as applied in the modeling. 3D FDTD code developed in MATLAB in which *E* and *H* updating code modules are given in **Appendix D**.

References

1. Tong, X. C. *Advance Materials and Design for Electromagnetic Interference Shielding*, Taylor and Francis, London,' 2009.
2. Hong, S. K., et al. Electromagnetic interference shielding effectiveness of monolayer graphene, *Nanotechnology* **23**, 455704 (1-5), 2012.
3. Han, M. & Deng, L. Doping effect of multiwall carbon nanotubes on the microwave electromagnetic properties of NiCoZn spinel ferrites, *Appl. Phys. Lett.* **90**, 011108(1-3), 2007.
4. Saville, P. Optimisation of Dallenbach Layers using Real Materials, Technical Memorandum, DRDC Atlantic TM 2007-012, 2007. http://www.dtic.mil/cgi-bin/GetTRDoc?AD=ADA475367
5. Chung, D. D. L. Electromagnetic interference shielding effectiveness of carbon materials, *Carbon* **39**, 279–285, 2001.
6. Elimat, Z. M. AC electrical conductivity of poly (methyl methacrylate) /carbon black composite, *J. Phys. D: Appl. Phys.* **39**, 2824-2828, 2006.
7. Du, J. H., et al. Microwave electromagnetic characteristics of a microcoiled carbon fibers/paraffin wax composite in Ku band, *J Mater. Res. Soc.* **17**, 1232-1236, 2002.
8. Luo, X. & Chung, D. D. L. Electromagnetic interference shielding using continuous carbon-fiber carbon-matrix and polymer-matrix composite, *Composites: Part B* **30**, 227-231, 1999.
9. Das, N. C., et al. Electromagnetic interference shielding effectiveness of carbon black and carbon fibre filled EVA and NR based composite, *Composites: Part A* **31** (10), 1069-1081, 2000.
10. Machinerieen, N. V. *Dispositif et procÃ©dÃ© pour l'amÃ©lioration de dispositifs de production et de rÃ©ception d'ondes Ã©lectriques ultra-courtes*, **French Patent 802 728**, 1936.
11. Stonier, R. A. Stealth aircraft & technology from world war II to the gulf [J], *SAMPE Journal* **27**, 9-18, 1991.

12. Halpern, O. *Method and means for minimizing reflection of high frequency radio waves,* **U.S. Pat. No. 2923934,** February 2, 1960.
13. Saville, P. *Review of Radar Absorbing Materials,* Technical Memorandum DRDC Atlantic TM 2005-003, http://www.dtic.mil/dtic/tr/fulltext/u2/a436262.pdf, 2005.
14. Salisbury, W. W. *Absorbent body for electromagnetic waves,* **U.S. Patent No, 2599944,** June 10, 1952.
15. Rath, B. B. & DeYoung D. J. The Naval Research Laboratory: 75 Years of Materials Innovation, http://www.tms.org/pubs/journals/jom/9807/rath-9807.html, 1998.
16. Suetake, K. *Microwave absorbing wall,* **U.S. Patent No. 3460142,** August 5, 1969.
17. Wright, R. W. *Magnetic ceramic absorber,* **U.S. Patent No. 4023174,** May 10, 1977.
18. Suetake, K. & Naito, Y. Application of ferrite to electromagnetic wave absorber, *IEEE Trans. Microw. Theory Techn.* **19** (1), 65-72, 1971.
19. Surig, C. Formation and microwave absorption of barium and strontium ferrite prepared by solgel technique, *Appl. Phys. Lett.* **63**, 2836-2838, 1993.
20. Gau, J. J. & Burnside, W. D. Transmission line approximation for periodic structures of dielectric bodies and its application to absorber design, Antennas and Propagation Society International Symposium, 1994, 2148-2158.
21. Kim, S. S. & Choi, I. K. Design and fabrication of wide band ferrite absorber used in anechoic chamber, *J Magn.* **2** (1), 25-27, 1977.
22. Sugimoto, S., et al. M-type ferrite composite as a microwave absorber with wide bandwidth in the GHz range, *IEEE Trans. Magn.* **35** (5), 3154-3156, 1999.
23. Yusoff, A. N., et al. Electromagnetic and absorption properties of some microwave absorbers, *J Appl. Phy.* **92** (2), 876-882, 2002.
24. Meshram, M. R. *Transmission line modeling (TLM) for evaluation of absorption in ferrite based multi-layer microwave absorber,* Conference on Convergent Technologies for the Asia-Pacific Region (TENCON 2003), 626-630.

25. Yongbao, F., et al. Complex Permeability and Permittivity and Microwave Absorption Property of Barium Ferrite/EPDM Rubber Radar Absorbing Materials in 2-18GHz (APMC' 05).
26. Li, B. W., et al. Enhanced microwave absorption in nickel/hexagonal-ferrite/polymer composites, *Appl. Phy. Lett.* **89**, 132504-1-3, 2006.
27. Ghasemi, A., et al. Investigation of the microwave absorptive behaviour of doped barium ferrites, *Mater. Design* **29**, 112-117, 2008.
28. Li, Z. W., et al. High-frequency magnetic properties at K and Ka bands for barium-ferrite/ silicon composites, *J. Magn. Magn. Mater.* **325**, 82-86, 2013.
29. Chua, M. J., et al. Structural and microwave attenuation characteristics of ZnCuY barium ferrites synthesized by asol-gel auto combustion method, *J. Magn. Magn. Mater.* **368**, 21-24, 2014.
30. Che, R., et al. Microwave absorption enhancement and complex permittivity and permeability of Fe encapsulated within carbon nanotubes, *Adv. Mater.* **16** (5), 401-405, 2004.
31. Lu, B., et al. Microwave absorption properties of the core/shell-type iron and nickel nanoparticles, *J. Magn. Magn. Mater.* **320** (6), 1106–1111, 2008.
32. Sato, M., Yoshida, S., Sugawara, E. and Shimada, Y. *J. Magn. Soc. Jpn.* **20**, 4214, 1996.
33. Matsumoto M., and Y. Miyata, Two-Layer Wave Absorber Composed of Soft-Magnetic, *IEEE Trans. Magn.* **33**, 3427, 1997.
34. Olmedo, L., et al. Microwave characterization and modelization of magnetic granular materials. *J. Appl. Phys.* **73** (10), 6992-6994, 1993.
35. Viau, G., et al. Reparation and microwave characterization of spherical and monodisperse $Co_{20}Ni_{80}$ particles. *J. Appl. Phys.* **76** (10), 6570-6572, 1994.
36. Sugimoto, S., et al. GHz microwave absorption of a fine α-Fe structure produced by the disproportionation of Sm_2Fe_{17} in hydrogen. *J. Alloy. & Compd.* **330**, 301-306, 2002.
37. Rousselle, D., et al. Effective medium at finite frequency: Theory and experiment. *J. Appl. Phys.* **74** (1), 475-479, 1993.

38. Goldman, A. *Modern Ferrite Technology,* Van Nostrand Reinhold, New York, 1990.
39. Liu, Y., et al. Effect of heat treatment on microwave absorption properties of Ni-Zn-Mg-La ferrite nanoparticles, *J. Magn. Magn. Mater.* **349**, 57-62, 2014.
40. Alcantara, G. B., et al. Morphology of cobalt ferrite nanoparticle-polyelectrolyte multilayered nanocomposites, *J. Magn. Magn. Mater.* **323**, 1372-1377, 2011.
41. Hosseini, S. H. & Asadnia, A. Synthesis, characterization, and microwave-absorbing properties of polypyrrole/$MnFe_2O_4$nanocomposite, *J. Nano Mat.* **2012**, 198973-1-6, 2012.
42. Nakamura, T. Snoek's limit in high-frequency permeability of polycrystalline Ni - Zn, Mg - Zn, and Ni - Zn - Cu spinel ferrites, *J Appl. Phy.* **88** (1), 348-353, 2000.
43. Li, Z. W., et al. Studies of static and high-frequency magnetic properties for M-type ferrite $BaFe_{12-2x}Co_xZr_xO_{19}$, *J Appl. Phys.* **92** (7), 3902-3907, 2002.
44. Kim, Y. J. & Kim, S. S. Microwave Absorbing Properties of Co- substituted Ni_2W hexaferrites in Ka-band frequencies (26.5-40GHz), *IEEE Trans. Magn.* **38** (5), 3108-3110, 2002.
45. Kwon, H. J., et al. The microwave absorbing and resonance phenomena of Y type hexagonal ferrite microwave absorbers, *J Appl. Phys.***75** (10), 6109-6111, 1994.
46. Cullity, B. D., & Graham C. D., *Introduction to Magnetic Materials,* Addison-Wesley, Reading, MA, 1972.
47. Pardavi-Horvath, M. Microwave applications of soft ferrites, *J. Magn. Magn. Mater.* **215-216**, 171-183, 2000.
48. Sugimoto, S. M-type ferrite composite as a microwave absorber with wide bandwidth in the GHz range, *IEEE Trans. Magn.* **35**, 3154-3156, 1999.
49. Cho, H. S. & Kim, S. S. M-hexaferrites with planar magnetic anisotropy and their application to high-frequency microwave absorbers, *IEEE Trans. Magn.* **35** (5), 3151-3153, 1999.

50. Gairola, S. P., et al. Modified composition of barium ferrite to act as a microwave absorber in X-band frequencies, *Solid State Commun.* **150**, 147–151, 2010.
51. Liu, Y., et al. Efficiency and purity control in the preparation of pure and/or aluminum-doped barium ferrites by hydro- thermal methods using ferrous ions as reactants, *J. Magn. Magn. Mater.* **322**, 366–374, 2010.
52. Qiu, J., et al. Microwave absorption properties of Al- and Cr-substituted M-type barium hexaferrite, *J. Magn. Magn. Mater.* **295**, 263–268, 2005.
53. Kumar, A., et al. Effect of particle size of $BaFe_{12}O_{19}$ on the microwave absorption characteristics in X-band, *Prog. Electromagn. Res. M* **29**, 223-236, 2013.
54. Feng, Y. B., et al. Absorbing properties and structural design of microwave absorbers based on carbonyl iron and barium ferrite, *J. Magn. Magn. Mater.* **318**, 8-13, 2007.
55. Peng, C. H., et al. Microwave absorbing materials using Ag–NiZn ferrite core–shell nanopowders as fillers, *J. Magn. Magn. Mater.***284**, 113-119, 2004.
56. Kodama, R.H. Magnetic nanoparticles, *J. Magn. Magn. Mater.***200**, 359–372, 1999.
57. Chen, X., et al. Microwave absorption properties of barium titanate/epoxide resin composites, *J. Phys. D.* **40**, 1827–1830, 2007.
58. Saito, R. Dresselhaus G., and Dresselhaus M. S., *Physical Properties of Carbon Nanotubes*, Imperial College Press, London, 1988.
59. Baughman, R. H. Carbon nanotubes--the route toward applications, *Science* **297**, 787-792, 2002.
60. Gogoi, J. P. Expanded graphite-novolac phenolic resin based electromagnetic interference (EMI) shielding material over the x-band: synthesis, characterization, analysis and design optimization, Ph. D. Thesis, Tezpur University, India, 2012.
61. H. Zheng, et al., Hyperne Interact, 189, 131 (2009).

62. Roy, P. K. & Bera, J. Effect of Mg substitution on electromagnetic properties of (Ni0.25Cu0.20Zn0.55) Fe2O4 ferrite prepared by auto combustion method, *J Magn. Magn. Mater.* **298**, 38-42, 2006.
63. Ruan, S., et al. Microwave absorptive behavior of ZnCo-substituted W-type Ba hexaferrite nanocrystalline composite material, *J Magn. Magn. Mater.* **212**, 175-177, 2000.
64. Vladimir, B. B. Advantages of Ferromagnetic Nanoparticle Composites in Microwave Absorbers, *IEEE Trans. Magn.* **40** (3), 1679-1684, 2004.
65. Peng, C.-H., et al. Microwave-absorbing characteristics for the composites of thermal-plastic polyurethane (TPU)-bonded NiZn-ferrites prepared by combustion synthesis method, *Mater. Sci. Eng. B* **117**, 27–36, 2005.
66. Qiu, J., et al. Microwave absorption of nanosized barium ferrite particles prepared using high-energy ball milling, *Powder Technol.* **154**, 116 - 119, 2005.
67. Caffarena, V. R., et al. Microwave absorption properties of Co, Cu, Zn - substituted hexaferrite polychloroprene nanocomposites, *Mater. Res.* **11** (3), 335-339, 2008.
68. Ohlan, A., et al. Microwave absorption properties of conducting polymer composite with barium ferrite nanoparticles in 12.4–18 GHz, *Appl. Phys. Lett.* **93**, 053114-1-3, 2008.
69. Singh, K., et al. Synthesis of conducting ferromagnetic nanocomposite with improved microwave absorption properties. *Mater. Chem. Phys.* **119**, 201-207, 2010.
70. Ohlan A., et al. Microwave absorption behaviour of core–shell structured poly (3,4-ethylenedioxy thiophene)–barium ferrite nanocomposites. *ACS Appl. Mater. Interfaces* **2** (3), 927-933, 2010.
71. Kiani, E., et al. The Effects of doping on crystal structure, magnetic and microwave properties of $SrFe_{12-2x}La_x(Mn_{0.5}Zr_{0.5})_xO_{19}$ Nanoparticles, *J Supercond. Nov. Magn.* **26**, 733–738, 2013.
72. Hosseini, S. H. and Moloudi, M. Synthesis, magnetic, and microwave absorption properties of multi core-shell structured Ba_xSr_{1-}

$_xFe_{12}O_{19}/Fe_3O_4$/polyacrylic acid nanocomposites, *Synthesis and Reactivity in Inorganic, Metal-Organic, and Nano-Metal Chemistry***43**, 671-676, 2013.

73. Hatkeyama, K. & Inui, T. Electromagnetic wave absorber using ferrite absorbing material dispersed with short metal fibers, *IEEE Trans. Magn.* **20** (5), 1261-1263, 1984.
74. Chun-Yu, W. Double-layer microwave absorber of nanocrystalline strontium ferrite and iron microfibers, *Chin. Phys. B* **21** (2), 028101-1-2, 2012.
75. Meshram, M.R., et al. Characterization of M-type barium hexagonal ferrite-based wide band microwave absorber, *J Magn. Magn. Mater.* **271**, 207–214, 2004.
76. Kakati, B. K. & Deka, D. Effect of resin matrix precursor on the properties of graphite composite bipolar plate for PEM fuel cell, *Energ. Fuel* **21**, 1681-1687, 2007.
77. Knop, A. & Pilato, L. A. *Phenolic Resins/Chemistry, Applications and Performance. Future Directions,* Springer Verlag, Berlin, 1985.
78. Balanis, A. C. *Advanced Engineering Electromagnetics,* John Wiley & Sons, USA, 1989.
79. Michielssen, E., et al. Design of Lightweight, Broad-Band Microwave Absorbers Using Genetic Algorithms, *IEEE. Trans. Microw. Theory* **41**, 1024-1030, 1993.
80. Zhang, B., et al. Microwave absorbing properties of de-aggregated flake shaped carbonyl iron particle composites at 2-18 GHz, *IEEE. Trans. Magn.***42**, 1778-1781, 2006.
81. Saville, P. Review of Radar Absorbing Materials, *Technical Memorandum DRDC Atlantic TM 2005-003,* 2005.
82. Sjöberg, D. Analysis of wave propagation in stratified structures using circuit analogues, with application to electromagnetic absorbers, *Eur. J. Phys.* **29**, 721–734, 2008.
83. Chen, F. L., et al. *Microwave Electronics Measurement and Materials Characterization,* John Wiley & Sons, Ltd., England, 2004.

84. Jarvis, J. B. Transmission/reflection and short-circuit line permittivity measurements, NIST Project, Boulder, CO, Tech. Note 1341, 1990.
85. Cho, S. H. & Kim, S. S. Two layered microwave absorber of ferrite and carbon fiber composite substrate, *J Magn.* **3** (2), 64-67, 1998.
86. Vuong, X. T. Military X-band very small aperture terminals (VSATs) - to spread or not to spread, in Proceedings, IEEE , Military Communications Conference (MILCOM '96), McLean, VA, 6-10, 1996.
87. Huang, Y., et al. The influence of single-walled carbon nanotube structure on the electromagnetic interference shielding efficiency of its epoxy composites, *Carbon* **45**, 1614-1621, 2007.
88. Damini, A., et al. G.E. X-band wideband experimental airborne radar for SAR, GMTI and maritime surveillance, *IEE Proc.-Radar Sonar Navig.* **150**, 305-312, 2003.
89. Jung, E., et al. SIW-based array antennas with sequential feeding for X-band satellite communication, *IEEE Trans. Antennas Propag.* **60**, 3632-3639, 2012.
90. Chu, C. K., et al. An X-band high-power and high-PAE PHEMT MMIC power amplifier for pulse and CW operation, *IEEE Microw. Wirel. Compon. Lett.* **18**, 707–709, 2008.
91. Pande, S., et al. Improved electromagnetic interference shielding properties of MWCNT–PMMA composites using layered structures, *Nanoscale Res. Lett.* **4**, 327–334, 2009.

CHAPTER II

MATERIAL SELECTION, SYNTHESIS AND CHARACTERIZATIONS

2.1 INTRODUCTION

As evident from chapter 1, selection of materials for electromagnetic interference (EMI) shields are critical for effective absorption, keeping in mind that contradictory material parameters are required for achieving both impedance matching at the interface and subsequent attenuation in the shields [1]. In addition, light weight and thickness consideration also plays an important role in applications of shield in various handheld and combat devices [2, 3].

Material selection, synthesis and preparation of shields are discussed initially in the chapter, followed by microstructural studies viz. X-Ray diffraction (XRD) and transmission electron micrograph (TEM); to find the formation, size and shape of the reinforcers. Homogeneous distribution of inclusions in the shield is found from scanning electron micrograph (SEM) images. Other properties like thermal stability, density, behavior of material in humid conditions are deciding factors for choice of the materials for EMI shields and are studied thereafter.

In-plane dc electrical conductivity [4] and saturation magnetization studies are also carried out on the developed magnetic material to check the applicability of the magnetic properties for microwave absorption.

2.2 MATERIAL SELECTION AND SYNTHESIS

Particulate composites give an ease to combine constituent fillers with the host polymer matrix to achieve desired absorption. Introduction of magnetic materials reduce the thickness of the absorber [5-7]. Magnetic metal inclusions like Fe, $Fe(CO)_5$ though increases dissipation of electromagnetic (em) wave, are corrosive in humid environment and heavy. Magnetic ferrites inclusions are more resistive to environmental variations, but bulk ferrites are mostly dense leading to increase in weight of the absorber. As reported in [8-13], nano-sized particles have high interfacial area, which creates a large interaction zone, leading to enhanced dielectric and magnetic properties and hence increases microwave absorption. Moreover, low densities of nano-ferrites reduce the weight, without compromising on the absorption properties.

In the following subsections, choice and synthesis of fillers and polymer matrix and development of the absorber composite is discussed.

2.2.1 Selection and synthesis of inclusions

At microwave frequencies spinel and hexagonal ferrites are used [14-18]. However, complex permeability of spinel ferrites follows Snoek's limit [19], restricting its use in the gigahertz range. M-type hexagonal ($MFe_{12}O_{19}$) ferrite with high crystalline anisotropy, high saturation magnetization and chemical stability finds use as constituent material for development of electromagnetic wave absorbers [20-22].

Variation in the magnetic properties, viz. saturation magnetization, coercivity, anisotropy and ferromagnetic resonant frequency, of barium ferrite ($BaFe_{12}O_{19}$) can be varied by substituting either the Ba^{2+} by Sr^{2+}, La^{3+} and Na^{+} and Fe^{3+} by Al^{3+}, Mn^{2+} and Ti^{4+} etc [23-25]. Al-substituted and Sr-substituted M-type hexagonal ferrite is reported to have larger anisotropy field [26] than $BaFe_{12}O_{19}$, indicating high attenuation of the electromagnetic wave.

M-type nano barium based hexagonal ferrite ($BaFe_{12}O_{19}$) with substitutions is used for development of X-band absorbers. The molecular structure of M-type barium ferrite is shown in figure 2.1.

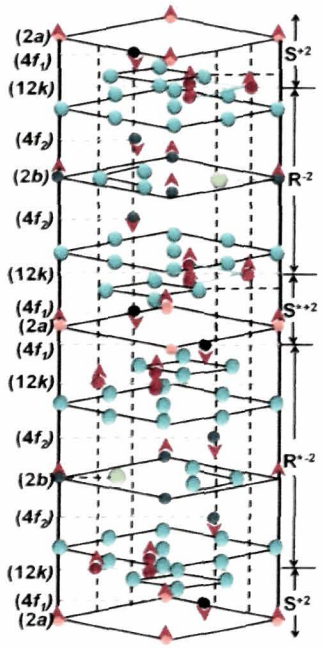

Figure 2.1 Molecular structure of M-type barium ferrite

In the present work, following M-type magnetic fillers are synthesized

- $BaFe_{12}O_{19}$, where the size and shape of ferrite particles are studied with three different annealing temperatures viz. 700 °C, 800 °C and 900 °C.
- $BaAl_xFe_{12-x}O_{19}$ with stoichiometric substitution of Fe^{3+} ions by Al^{3+}, with x=1.0, 1.2, 1.4 and 1.6 at 900 °C.
- $Ba_{1-x}Sr_xFe_{12}O_{19}$ with stoicheometric substitution of Ba^{2+} ions by Sr^{2+}, with x=0.2, 0.4, 0.6 and 1.0 at 900 °C.

M-type barium ferrite ($BaFe_{12}O_{19}$) particles are prepared from nitrate precursors using co-precipitation technique. Barium nitrate (≥98%) and iron (III) nitrate nonahydrate (≥98%) precursors are used as the base materials to which sodium hydroxide is added dropwise to control the size of the particles. Aqueous solutions of barium and iron salts are prepared separately by dissolving the salts in reverse osmosis (RO) deionized water maintaining the molar ratio of barium to ferric nitrate as 1:12 with constant magnetic stirring condition. Figure 2.2 shows the flow chart of synthesis of M-type ferrite particles.

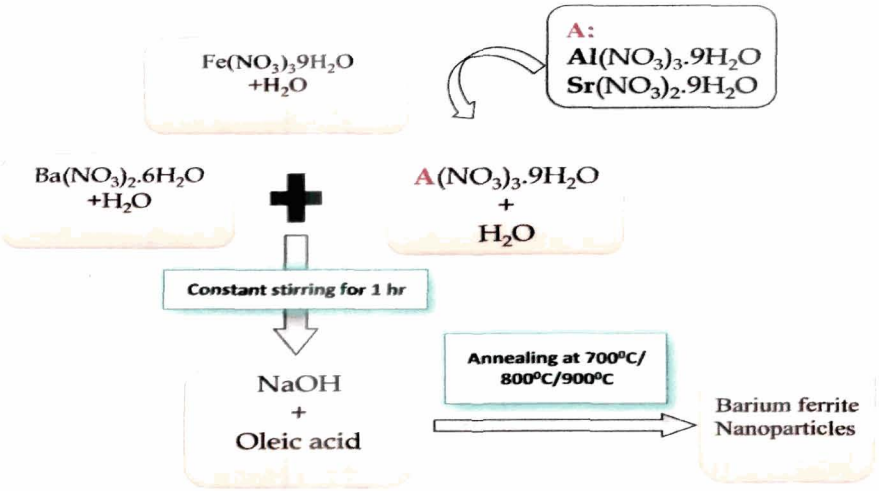

Figure 2.2 Flow chart of synthesis technique of ferrite particles

The iron and barium salt solutions are mixed together and heated at 70 °C with continuous magnetic stirring for one hour. 4M (25 ml) solution of sodium hydroxide is prepared separately and slowly added to the salt solution drop wise. The pH of the solution is maintained to a level of 11-12. A few drops (~ 0.1 ml) of oleic acid ($C_{17}H_{33}COOH$) is added to the solution as a surfactant and coating material [27]. The system is cooled to room temperature. Subsequently, the precipitate is washed with distilled water and ethanol to get the precipitate free from sodium and nitrate compounds. Finally, the precipitate is dried at 100 °C. The dried powder is crumbled and annealed at three different temperatures, 700 °C, 800 °C and 900 °C for two hours to get barium ferrite particles and then microstructurally analyzed.

$BaAl_xFe_{12-x}O_{19}$ (x = 1.0, 1.2, 1.4 and 1.6), is synthesized by adding stoichiometrical solution of aluminium nitrate (≥98%) dissolved in RO deionized water at the mixing stage. Similarly, strontium substituted barium ferrite is synthesized by adding solution of strontium (II) nitrate (≥97%) in stoicheometric ratio at the mixing stage. The substituted precursor powders are annealed at 900 °C with a temperature stability of ±1 °C for two hours to form substituted barium ferrite. Annealing temperature of 900 °C is chosen for synthesis of substituted ferrite, as

all the further studies conducted on $BaFe_{12}O_{19}$ ferrite showed that 900 °C is the optimum temperature for synthesis.

2.2.2 Selection of host matrix and fabrication of magnetic composite material

Novolac phenolic resins (NPR) are condensed polymerization product of phenol and formaldehyde with water as byproduct. The polymerization takes place when the molar ratio of formaldehyde to phenol is less than one and it is brought to completion using acid-catalysis such as oxalic acid, hydrochloric acid or sulfonate acids. In the initial stage (A-stage), the polymer is of low molecular mass, soluble and fusible. As the condensation continues more molecules are involved and resin becomes rubbery, thermoplastic phase, which is only partially soluble (B-stage). The resin is then cured to fully cross-linked intractable material(C- Stage). Figure 2.3 shows the structure of NPR. NPR is amorphous thermoplastics which is solid at room temperature and softens and flows at temperatures 65 °C - 105 °C. They have good heat resistance, electrical insulation, dimensional stability and are flame and chemical resistant [28]. The hydroxyl and methylene linkages present in NPR chemical structure facilitates bonding for composite formation [29], and hence is selected as the base matrix.

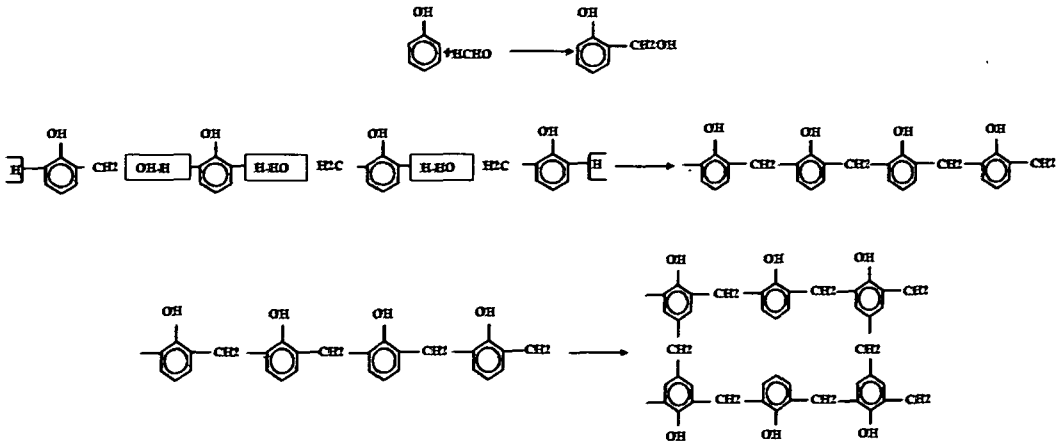

Figure 2.3 Polymerization of novolac phenolic resin (NPR)

Novolac type phenolic resin is mixed with 10% hexamethylene tetramine as harderner (supplier Pheno Organic Limited, New Delhi). The synthesized ferrite and NPR powder are mechanically blended at ~ 15000 rpm for different weight percentages of filler in the base matrix. Mathematically, if total weight of the composite is Z grams, X and Y are the weights of filler and polymer matrix, respectively, i.e. Z = X + Y, then, for *N* wt.% of filler-NPR composite, amount of filler present in the composite is given by

$$\text{Filler} = X = (N/100) \times Z \text{ grams} \quad (2.1)$$

and amount of NPR present in the composite is given by

$$\text{Polymer matrix} = Y = (Z-X) \text{ grams} \quad (2.2)$$

Using the relation (2.1) and (2.2), a uniform mixture of ferrite and NPR powder is obtained with different wt.% of ferrite nanoparticles. The mixture is placed in a specially designed three-piece die-mould consisting of a cavity, upper and lower plunger with spacer and initially heated up to 95–100 °C. A pressure up to 1.5-2 tons is slowly applied and the fixture with the sample is isothermally heated at 150 °C for 2 hours and then allowed to cool at room temperature. The processing chart is given in figure 2.4.

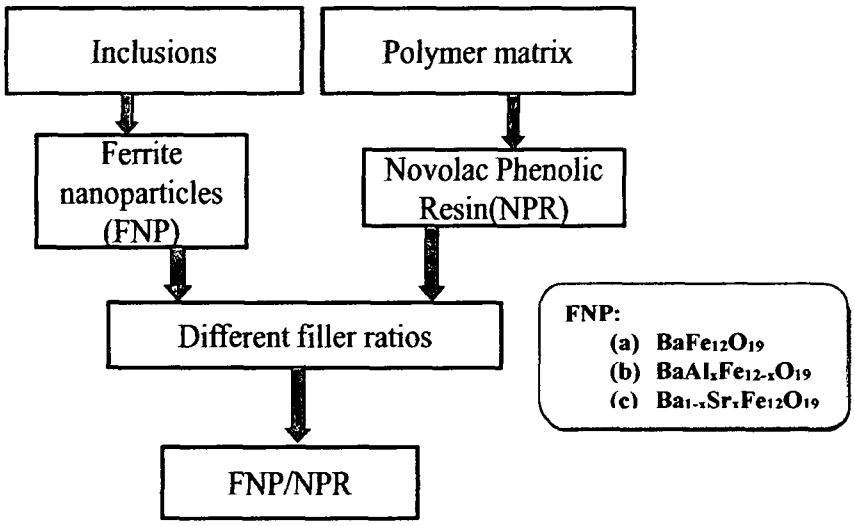

Figure 2.4 Block diagram of composite preparation

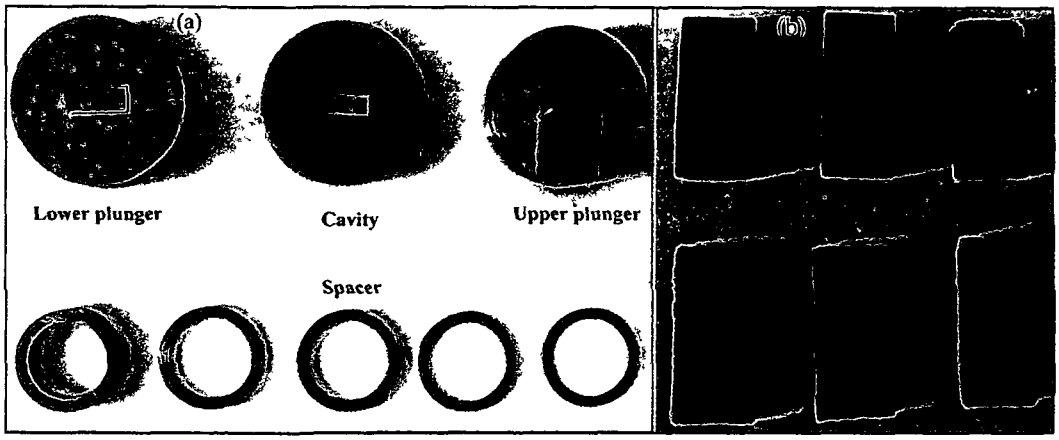

Figure 2.5 (a) Three piece die mold and (b) prepared ferrite -NPR nanocomposites for X-band characterization

Pellets of different dimensions are molded for different characterization. A three piece die mould with spacer, with the provision of varying the thickness, d, of the sample is designed and fabricated for microwave characterization in the X-band with the sample dimension of 10.16 mm × 22.86 mm × *d* mm (figure 2.5).

Three wt.% of $BaFe_{12}O_{19}$-NPR composite viz. 30 wt.%, 40 wt.% and 50 wt.% is prepared. Beyond 50 wt.%, sinkage in filler is observed leading to cracks and brittleness in the composite.

2.3 MICROSTRUCTURAL STUDIES

The morphology of the synthesized ferrite samples are studied using XRD and TEM. SEM studies are conducted on developed ferrite-polymer composite to find homogeneity of filler distribution in the host matrix.

Propagation of electromagnetic wave, passing through the composite material depends not only on the intrinsic properties of the constituents, but also on the size of the inclusions and the change in structural configuration of the inclusion particles in the composite matrix. Microstructural studies gives the complete picture of the composite deciding its utility as substrate in the microwave technology. Micro-structural studies of the synthesized nanocomposites conducted are described in following sub sections.

Again in all the further studies conducted on $BaFe_{12}O_{19}$-NPR composite system, it is seen that 50 wt.% gives the best result. Hence, Al^{3+} and Sr^{2+} substituted barium ferrite-NPR composites are only fabricated for the further studies.

2.3.1 X-ray diffraction

X-ray diffraction (XRD) patterns of the ferrite particles are carried using Rigaku, Miniflex 200 X-ray diffractometer with Cu Kα line of wavelength λ= 1.541841 Å, are recorded at 2θ values from 10° to 70°. Crystallinity and size of the particles are calculated from the XRD patterns using Debye-Scherrer's formula [30]. The lattice parameters for the hexagonal magnetoplumbite phases are computed using the d-spacings value and the respective (*h k l*) parameters. Interplanar distance, d is given by

$$\frac{1}{d^2} = \frac{4}{3}\left(\frac{h^2 + k^2 + l^2}{a^2}\right) + \frac{l^2}{c^2} \qquad (2.3)$$

X-ray diffraction of $BaFe_{12}O_{19}$ particles

Diffraction patterns of $BaFe_{12}O_{19}$ particles annealed at different annealing temperatures, are shown in figures 2.6a, 2.6b and 2.6c. The reflection planes: (1 0 2), (1 1 0), (1 0 7), (1 1 4), (2 0 0), (2 0 3), (0 0 10), (2 0 5), (10 12), (3 0 0), (2 1 7), (2 0 11), (2 2 0), (2 0 14), (3 1 6) and (4 0 4) indicate presence of a hexagonal structure. It is found that all diffraction peaks can be perfectly indexed to the M-type hexagonal structure, and no characteristic peaks of impurities are detected in the XRD pattern. The lattice constants, a=5.88 Å and c=23.22 Å matches with those reported in JCPDS card number 43-0002 for barium ferrite particles. The average crystalline size is in nanometre range and is found to increase with annealing temperatures (table 2.1). The size variation can be achieved by the annealing conditions.

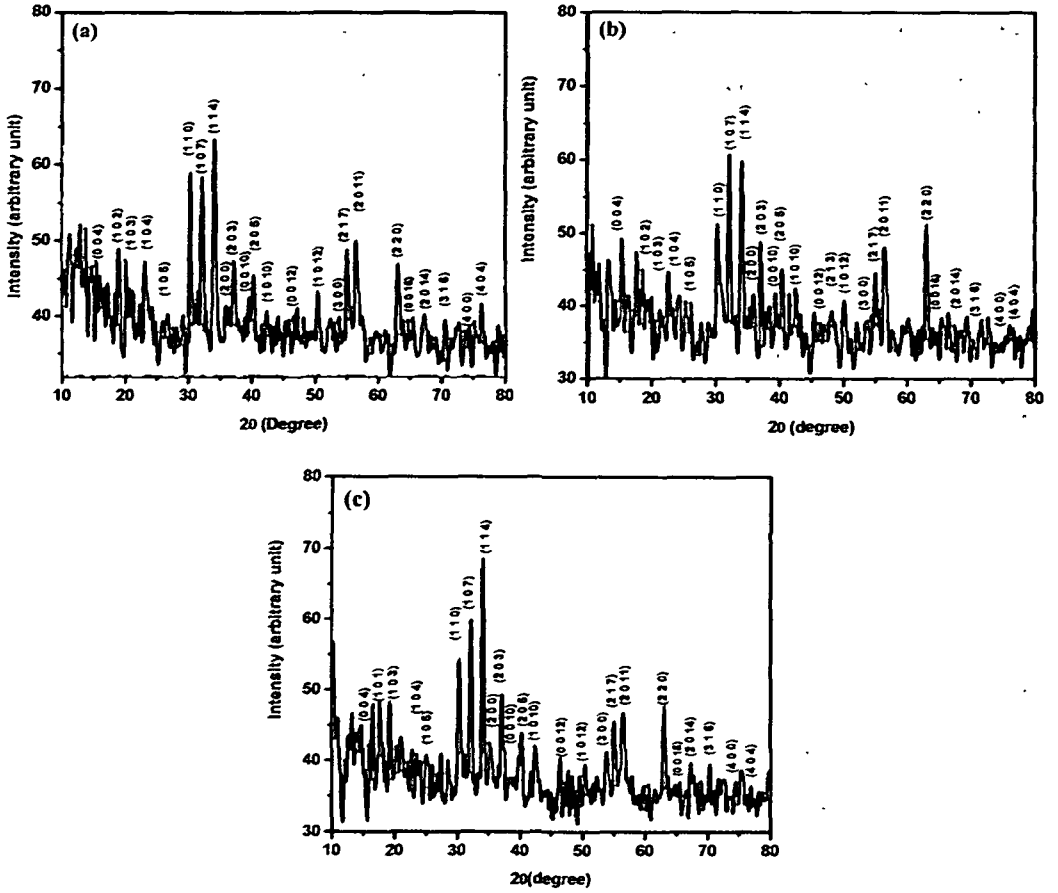

Figure 2.6 XRD patterns of $BaFe_{12}O_{19}$ particles annealed at (a) 700 °C, (b) 800 °C and (c) 900 °C

Table 2.1 Calculated crystallite size and lattice parameter of $BaF_{12}O_{19}$ particles

$BaF_{12}O_{19}$	Average crystallite size (nm)	Lattice parameter (Å)	
		a	*c*
Annealed at 700 °C	18.46	5.87	23.17
Annealed at 800 °C	23.80	5.90	23.26
Annealed at 900 °C	26.64	5.87	23.23

X-ray diffraction of $BaAl_xFe_{12-x}O_{19}$ particles

XRD pattern of $BaAl_xFe_{12-x}O_{19}$ particles with x=1.0, 1.2, 1.4 and 1.6 are shown in figures 2.7a, 2.7b, 2.7c and 2.7d, respectively. Like $BaFe_{12}O_{19}$, $BaAl_xFe_{12-x}O_{19}$ also shows single phase M- type hexagonal structure. No characteristic plane of Al^{3+} ions is observed confirming that the Al^{3+} ions enter the lattice of barium ferrite

[31]. The lattice constants, a=5.65 Å and c=22.89 Å corresponds to the JCPDS card number 43-0002. Table 2.2 shows the lattice parameters and crystalline size.

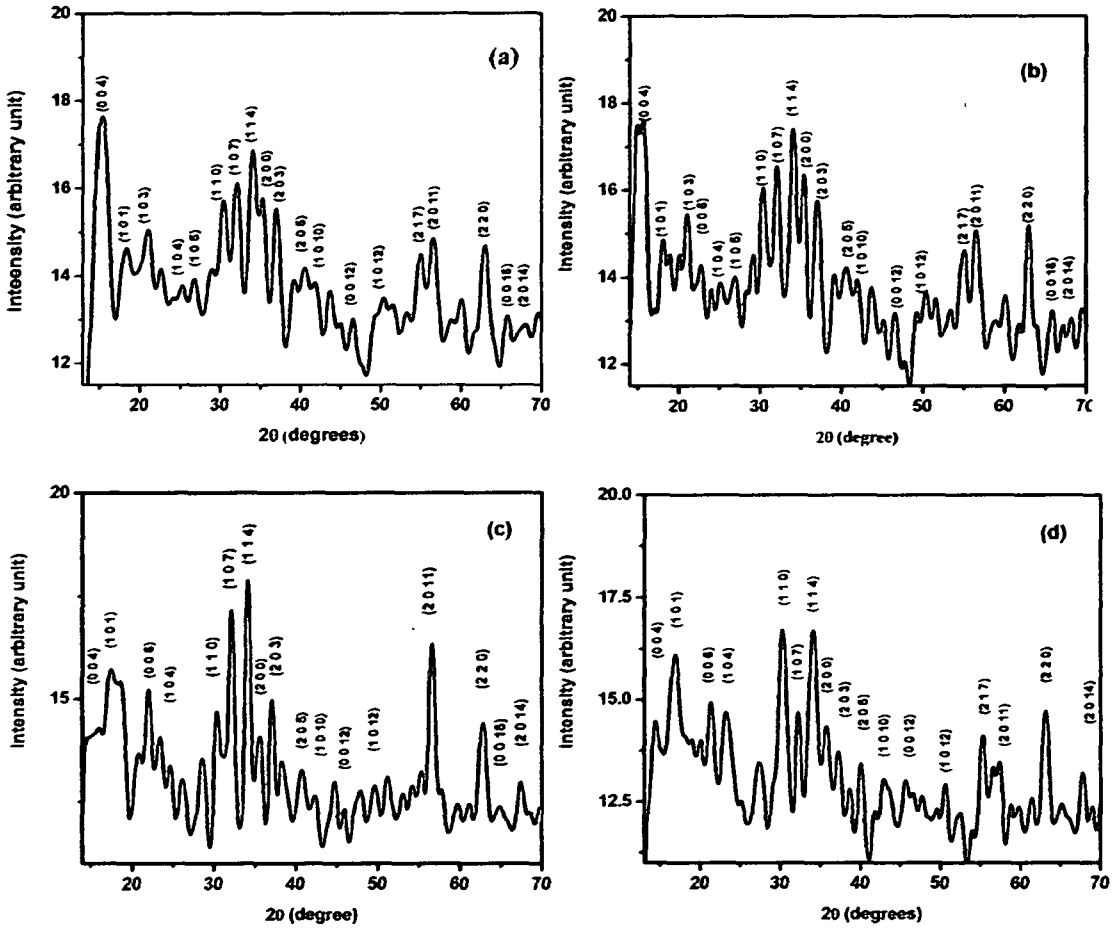

Figure 2.7 XRD patterns of $BaAl_xFe_{12-x}O_{19}$ (with x =1, 1.2, 1.4 and 1.6) particles annealed at 900 °C

Table 2.2 Average crystallite size and lattice parameters of $BaAl_xFe_{12-x}O_{19}$ ferrite

Ferrites composition	Aluminium content	Average crystallite size (nm)	Lattice parameter (Å)	
			a	*c*
$BaAl_1Fe_{11}O_{19}$	1.0	5.92	5.90	23.23
$BaAl_{1.2}Fe_{10.8}O_{19}$	1.2	5.78	5.89	23.17
$BaAl_{1.4}Fe_{10.6}O_{19}$	1.4	4.15	5.87	23.08
$BaAl_{1.6}Fe_{10.4}O_{19}$	1.6	3.87	5.83	23.02

The crystallite size of the $BaAl_xFe_{12-x}O_{19}$ particles is in nanorange. It is observed that with increase in the Al^{3+} substitution, the lattice constants *a* and *c* decreases.

X-ray diffraction of $Ba_{1-x}Sr_xFe_{12}O_{19}$ particles

XRD patterns of $Ba_{1-x}Sr_xFe_{12}O_{19}$ particles with x=0.2, 0.4, 0.6 and 1.0 are shown in figures 2.8a, 2.8b, 2.8c and 2.8, respectively.

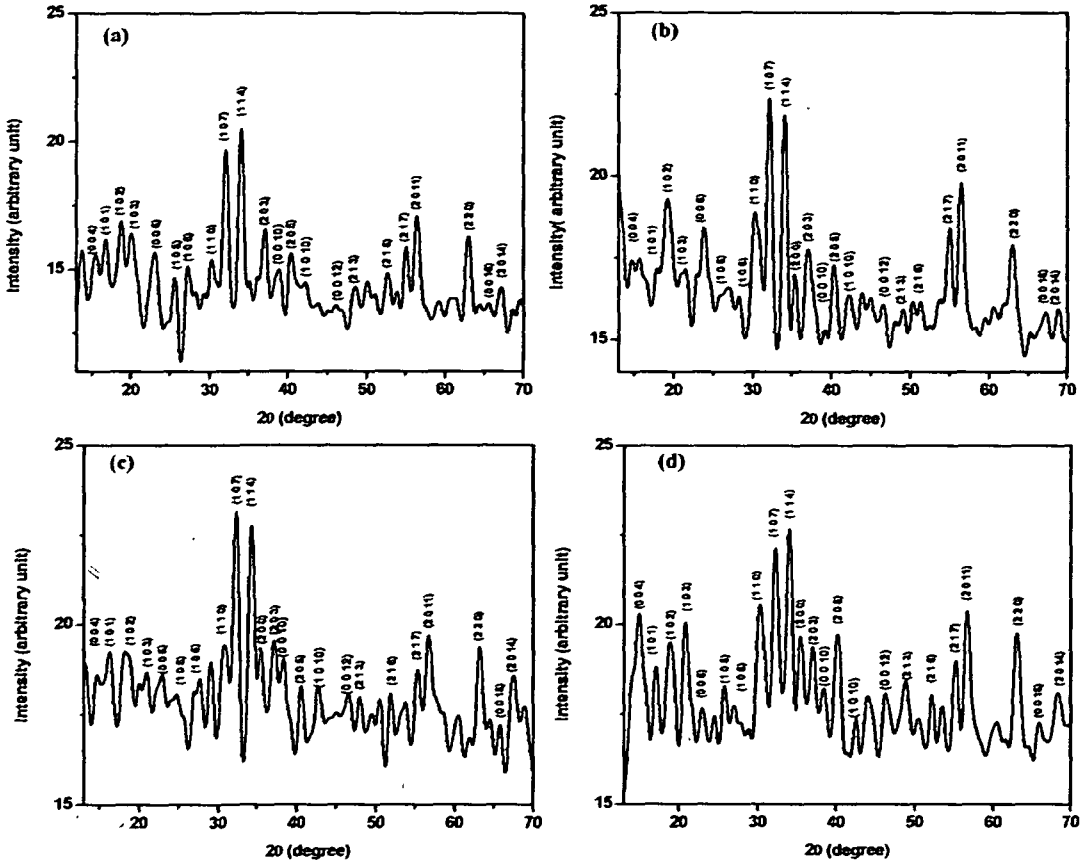

Figure 2.8 XRD patterns of $Ba_{1-x}Sr_xFe_{12}O_{19}$ (with x =0.2, 0.4, 0.6 and 1.0) annealed at 900 ^{0}C

The lattice parameters for $Ba_{1-x}Sr_xFe_{12}O_{19}$ are, a = 5.72 Å and c = 22.61 Å and matches with those reported in JCPDS card number 84-1531. The crystallite size variation is observed as the Sr^{2+} ion substitutes Ba^{2+} (Table 2.3).

Table 2.3: Average crystallite diameter and lattice parameters of strontium substituted barium ferrite

Sample	Strontium content	Average crystallite sizes (nm)	Lattice parameter (Å)	
			a	*c*
$Ba_{0.8}Sr_{0.2}Fe_{12}O_{19}$	0.2	10.4	5.76	22.46
$Ba_{0.6}Sr_{0.4}Fe_{12}O_{19}$	0.4	9.55	5.74	22.58
$Ba_{0.4}Sr_{0.6}Fe_{12}O_{19}$	0.6	7.85	5.71	22.61
$SrFe_{12}O_{19}$	1.0	7.90	5.71	22.80

2.3.2 Transmission electron micrographs of the ferrite particles

Transmission electron microscopy (TEM) is the premier tool for understanding the internal microstructure of materials at the nanometer level. Electrons have an important advantage over X-rays in that they can be focused using electromagnetic lenses. One can obtain real-space images of materials with resolutions of the order of a few tenths to a few nanometers, depending on the imaging conditions, and simultaneously obtain diffraction information from specific regions [32].

Transmission electron micrograph is taken to see the microstructural properties like shape and size using JEOL JEM-2100 transmission electron microscope (TEM;Akishima, Tokyo, Japan) operating at an accelerating voltage of 200 kV (Collidion Coated Copper Grids).

TEM of $BaFe_{12}O_{19}$ particles

Most of the particles appear hexagonal in shape for all the three annealing temperatures as seen in TEM images, figures 2.9a, 2.9b and 2.9c. The particle shape is hexagonal and its size is ~50 nm and ~60 nm for the samples annealed at temperature, T=700 °C and 800 °C. Extended rod like shape in one direction is observed for the particles annealed at 900 °C with crystal lattice plane anisotropy with particle size of ~70 nm and explained in terms of surface energy. The surface energy of barium ferrite is different along different directions of the unit cell. The growth of the nanoparticles along [0001] direction is preferential i.e. the c-axis, as it is energetically favorable due to minimum surface energy at higher temperature and hence, the elongated rod shaped nanostructure formation is observed [33].

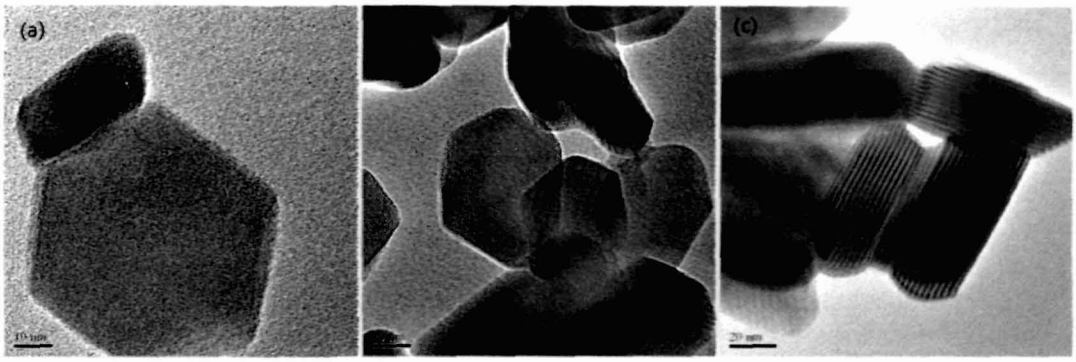

Figure 2.9 TEM micrographs of $BaFe_{12}O_{19}$ particles annealed at (a) 700°C, (b) 800 °C, and (c) 900 °C

TEM of $BaAl_xFe_{12-x}O_{19}$ particles

The TEM images of aluminium substituted barium ferrites particles are shown in show the particle shapes are hexagonal and the average particle size is ~90 nm (figure 2.10a, 2.10b, 2.10c and 2.10d).

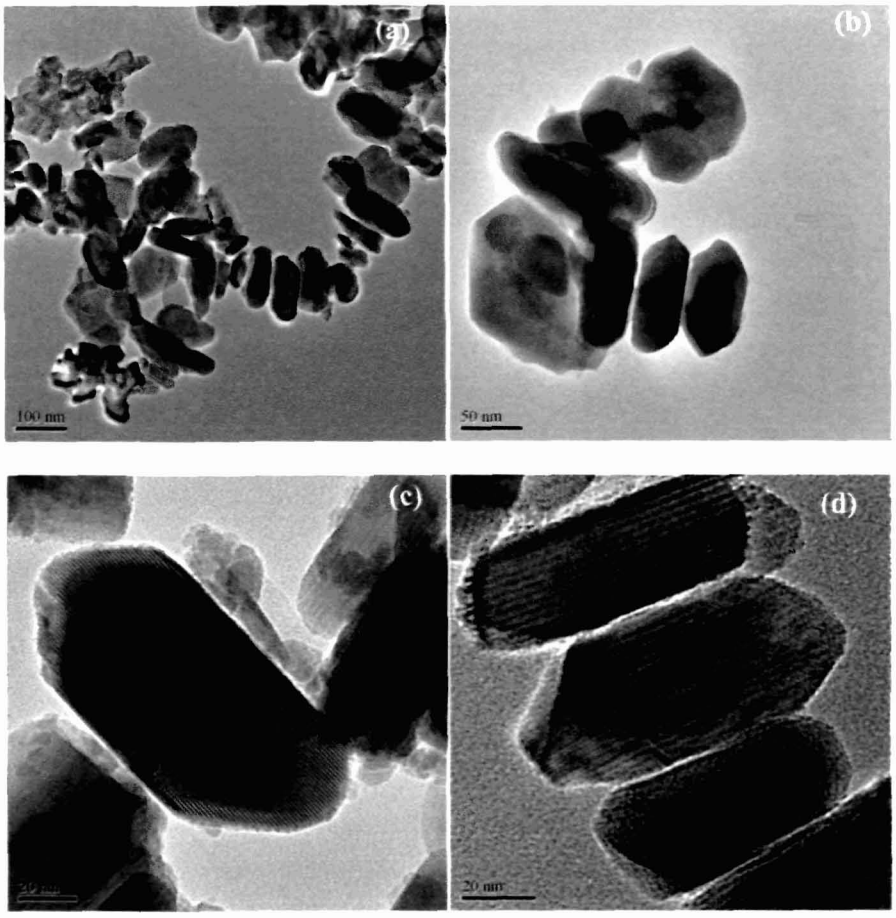

Figure 2.10 TEM micrographs of $BaAl_xFe_{12-x}O_{19}$ particles with x=1.0 (a), 1.2 (b), 1.4 (c) and 1.6 (d).

The shape tends to extend like rod in one direction along c-axis. The lattice plane anisotropy can be observed from the images.

TEM of $Ba_{1-x}Sr_xFe_{12}O_{19}$ particles

The TEM images of strontium substituted barium ferrites particles annealed at T=900°C are shown in figure 2.11(a-d). Hexagonal rod shaped structure with length ~90 nm is observed.

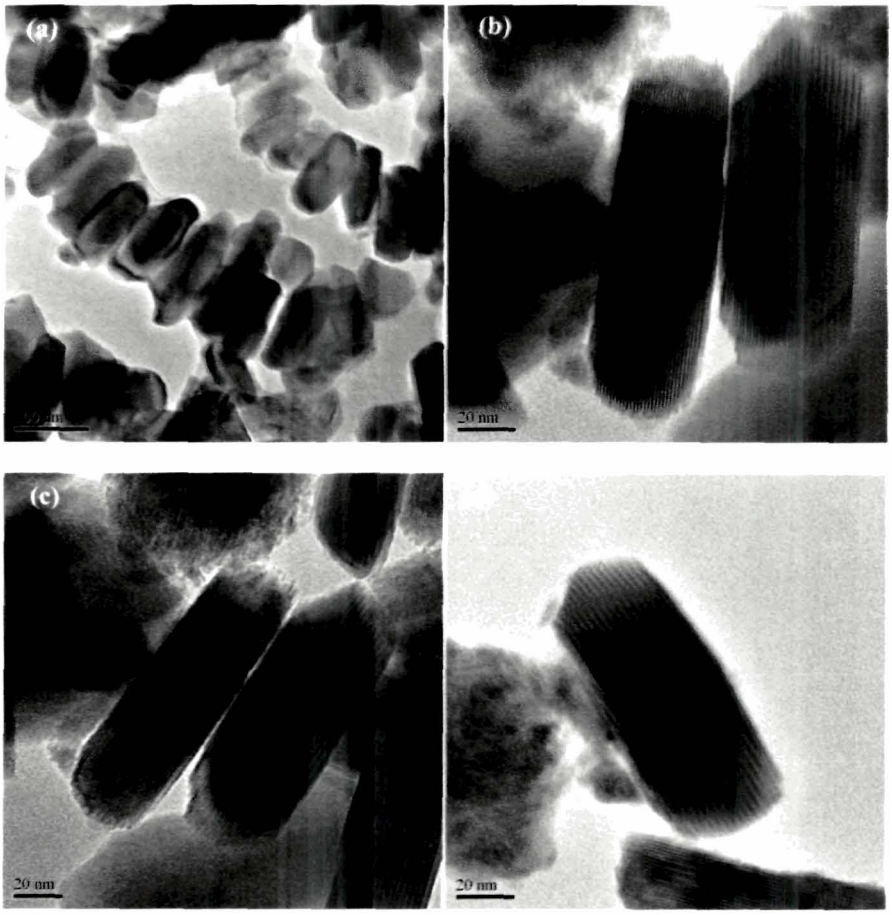

Figure 2.11 TEM micrographs of $Ba_{1-x}Sr_xFe_{12}O_{19}$ particles with x=0.2, 0.4, 0.6 and 1.0

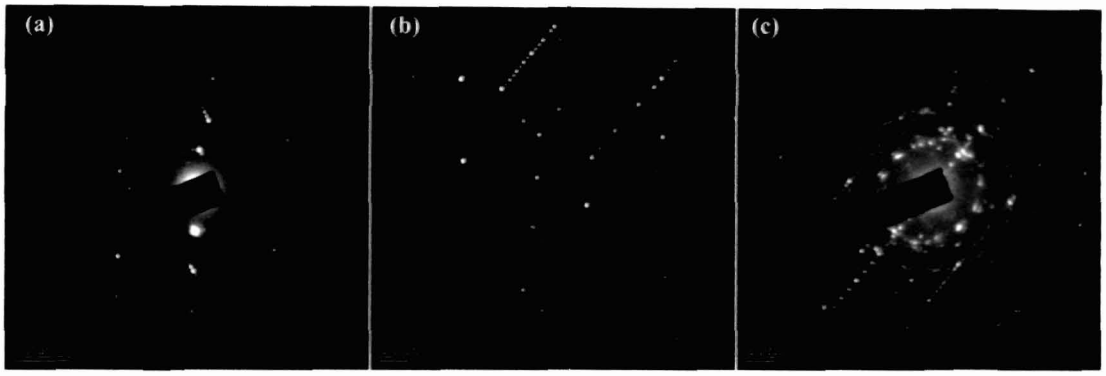

Figure 2.12 SAED pattern of (a) barium ferrite, (b) aluminum substituted barium ferrite and (c) strontium substituted barium ferrite particles annealed at 900°C

All the barium ferrite particles along with substitution shows crystalline nature with double diffraction pattern which can be observed from the selected area electron diffraction (SAED) patterns in figure 2.12 (a-c).

2.3.3. Scanning electron micrographs of the ferrite composite

Scanning electron microscopy (SEM) of particulate magnetic nanocomposite is taken by JEOL-JSM-6390. The surface of each samples are platinum coated before taking the micrographs. The micrographs are taken at 10^{-11} Å probe current and 20 KV accelerating voltage at different resolutions. Figure 2.13 (a–c) shows the SEM micrographs of 50wt.% $BaFe_{12}O_{19}$-NPR, $BaAl_{1.4}Fe_{10.6}O_{19}$-NPR and $Ba_{0.6}Sr_{0.4}Fe_{12}O_{19}$-NPR nanocomposite, respectively.

Most of the particles are homogeneously distributed over the matrix as seen from the SEM images.

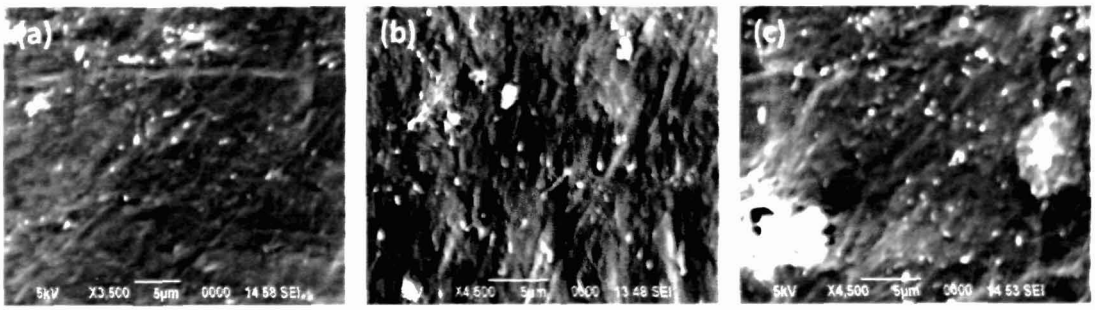

Figure 2.13 SEM micrographs of (a) $BaFe_{12}O_{19}$-NPR, (b) $BaAl_{1.4}Fe_{10.6}O_{19}$-NPR and (c) $Ba_{0.6}Sr_{0.4}Fe_{12}O_{19}$-NPR nanocomposites

2.4 DENSITY AND WATER ABSORBANCE

Light weight microwave absorbers are easy to install and this in turn makes them suitable for free space applications. Density of a composite gives an idea of the compactness of the material and its weight. Measurement of density of the ferrite-NPR nanocomposites is carried out by using Archimedes's principle [34]. The samples of dimension 10.16 mm × 22.86 mm × 2.0 mm are prepared and weight is measured in air, W_{air}. The composite is suspended in water and apparent immersed weight of the sample is measured, referred as W_{app}. Then the experimental bulk density (d_s) of the composite is measured by the Archimede's principle and is given by

$$d_s = \frac{W_{air}}{W_{air}-W_{app}} \times D_{water} \quad (2.4)$$

$$\text{or } d_s = \frac{W_{air}}{W} \times D_{water} \quad (2.5)$$

where

W_{air} = Weight of the sample in air (gm)

W_{app} = Weight of the sample in air - weight of the displaced water (gm)

D_{water} = Density of water at room temperature (=0.997 g/cc at 25 °C)

Water absorbance studies of the material help in determining the porosity of the material in humid and wet environmental conditions in which the system can work without affecting its microwave performance. The sample is inserted in water for 72 hours at room temperature. Thereafter pat dried at room temperature. The percentages of water absorption of the composites are determined according to the expression

$$Water\ absorbance\ (\%) = \frac{W_t-W_0}{W_0} \times 100 \quad (2.6)$$

where, W_t and W_0 are the weights of the wet and dry composites respectively.

2.4.1 Results and analysis of $BaFe_{12}O_{19}$-NPR nanocomposites

The bulk density of the magnetic nanocomposite increases with increase in the ferrite content in the NPR matrix (table 2.4). Composites with higher wt.% of barium ferrite contain less amount of NPR than composites with low wt.% of barium ferrite. Decrease of density for composites with higher NPR content is due to the increase in ultimate weight loss during curing process. Percentages of water absorbance of the $BaFe_{12}O_{19}$-NPR nanocomposites are tabulated in table 2.4. It is found that there is a slight increase of weight gain with increasing concentration in the composites due to presence of porosity in the samples. The maximum weight gain is only ~0.03%.

Table 2.4 Density and percentage of water absorbance of $BaFe_{12}O_{19}$-NPR nanocomposites

Sample composition	Density (g/cc)	(%)Water absorbance
$BaFe_{12}O_{19}$-NPR		
T=700°C	1.18	0.01
T=800°C	1.14	0.03
T=900°C	1.12	0.02
30wt.% (T=900°C)	1.18	0.01
40wt% (T=900°C)	1.23	0.02
50wt.% (T=900°C)	1.36	0.03

2.4.2 Results and analysis of $BaAl_xFe_{12-x}O_{19}$-NPR and $Ba_{1-x}Sr_xFe_{12}O_{19}$-NPR nanocomposites

The bulk density and water absorbance of the 50 wt.% $BaAl_xFe_{12-x}O_{19}$-NPR and $Ba_{1-x}Sr_xFe_{12}O_{19}$-NPR nanocomposites are tabulated in table 2.5. The bulk density of the magneto dielectric composite for both Al^{3+} and Sr^{2+} substitution is ~1.22. Maximum water absorbance of 0.03 % is observed and indicates its use in high humidity environment, without affecting the performance. The inclusions taken are annealed at 900 °C.

Table 2.5 Density and percentage of water absorbance of 50 wt.% $BaAl_xFe_{12-x}O_{19}$-NPR and $Ba_{1-x}Sr_xFe_{12}O_{19}$-NPR nanocomposites

Sample composition	**Density (g/cc)**	**(%)Water absorbance**
$BaAl_xFe_{12-x}O_{19}$-NPR T=900 °C and 50 wt.%		
x=1.0	1.14	0.01
x=1.2	1.24	0.02
x=1.4	1.36	0.02
x=1.6	1.15	0.01
$Ba_{1-x}Sr_xFe_{12}O_{19}$-NPR T=900 °C and 50 wt.%		
x=0.2	1.27	0.01
x=0.4	1.23	0.02
x=0.6	1.19	0.03
x=1.0	1.18	0.01

2.5 THERMO GRAVIMETRIC ANALYSIS (TGA)

The thermo gravimetric analysis (TGA) is performed to predict the thermal stability of a material. The TGA analysis gives the weight loss of the samples in the temperature range of 50°C to 900°C. The TGA for pure NPR, $BaFe_{12}O_{19}$ and (30, 40 and 50 wt.%) $BaFe_{12}O_{19}$-NPR composites, 50 wt.% $BaAl_xFe_{12-x}O_{19}$-NPR composites with x=1.0, 1.2, 1.4 and 1.6 and $Ba_{1-x}Sr_xFe_{12}O_{19}$-NPR composites with x=0.2, 0.4, 0.6 and 1.0 are carried out on Thermal Analyzer, Model STA 6000, Perkin Elmer.

2.5.1 Result and analysis of $BaFe_{12}O_{19}$-NPR composites

The thermal stability of the prepared samples of $BaFe_{12}O_{19}$-NPR nanocomposite is measured in the air atmosphere as shown in figures 2.14a and 2.14b. TGA curve of NPR shows that there is small weight loss up to 160 °C. The major weight loss occurs due to growth of volatiles in between the temperature 390-685 °C [35]. The $BaFe_{12}O_{19}$ particles show thermal stability throughout the temperature range with a very small weight loss after 550 °C. The TGA graph of

all the three samples with varying weight percentage of ferrite inclusions (30 wt.%, 40 wt.% and 50 wt.%) shows thermal stability up to 400 °C. 30 wt.% and 40 wt.% show continuous weight loss of 28% and 31%, respectively up to 685 °C. With increase in the $BaFe_{12}O_{19}$ contents in the NPR matrix, thermal stability of the absorber samples increases. The thermal stability of the $BaFe_{12}O_{19}$-NPR nanocomposite does not change with the annealing temperature of the ferrite particles as can be seen from figure 2.14a.

2.5.2 Result and analysis of $BaAl_xFe_{12-x}O_{19}$-NPR and $Ba_{1-x}Sr_xFe_{12}O_{19}$-NPR nanocomposites

All the compositions of $BaAl_xFe_{12-x}O_{19}$-NPR and $Ba_{1-x}Sr_xFe_{12}O_{19}$-NPR nanocomposites show thermal stability upto ~ 400 °C, figures 2.15a and 2.15b. With increase in the aluminium substitution, thermal stability increases and the major weight loss occur after 744 °C. The thermal stability of $Ba_{1-x}Sr_xFe_{12}O_{19}$-NPR nanocomposites decreases with increase in the Sr^{2+} substitution in the $Ba_{1-x}Sr_xFe_{12}O_{19}$ particles. The major weight loss occurs at 800 °C and continues upto 896 °C.

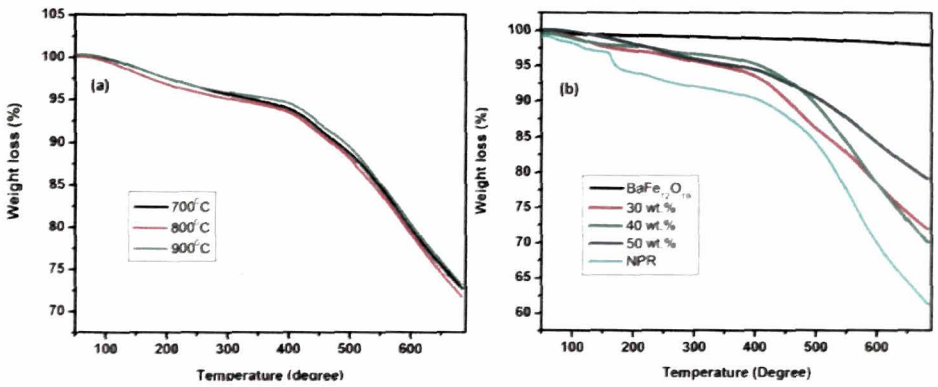

Figure 2.14 Thermo gravimetric analysis (TGA) curves of (a) $BaFe_{12}O_{19}$-NPR nanocomposite with ferrite particles annealed at T=700 °C, 800 °C and 900 °C, (b) $BaFe_{12}O_{19}$-NPR nanocomposite with 30 wt.%, 40 wt.% and 50 wt.% and $BaFe_{12}O_{19}$ particles annealed at 900 °C and NPR

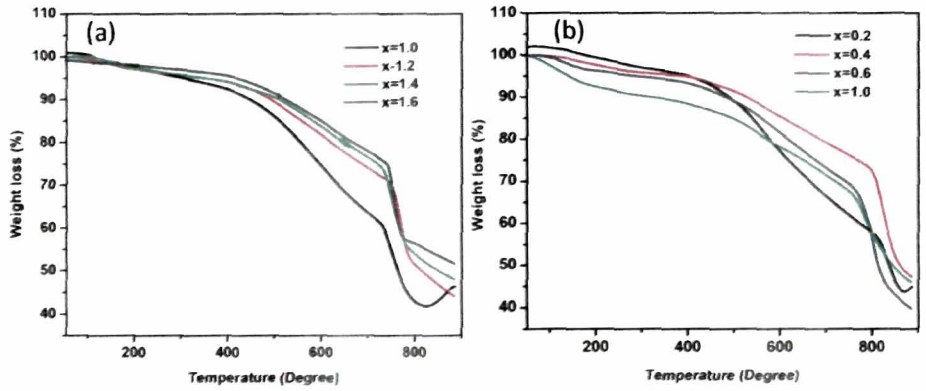

Figure 2.15 Thermo gravimetric analysis (TGA) curves of (a) $BaAl_xFe_{12-x}O_{19}$-NPR composite with x=1.0, 1.2, 1.4 and 1.6 and (b) $Ba_{1-x}Sr_xFe_{12}O_{19}$-NPR with x=0.2, 0.4, 0.6 and 1.0

2.6 IN-PLANE DC ELECTRICAL CONDUCTIVITY

In-plane dc electrical conductivity of the ferrite-NPR nanocomposite is measured by two probe method using Keithley 2400-C source meter interfaced with PC using GPIB port. Initially, resistance of the samples is calculated from current-voltages (I-V) characteristics at room temperature. The resistivity of a bulk samples is based on accurate measurement of resistance and the sample dimensions. For a homogenous bar of length, L and uniform cross section *A*, the resistance, *R*, is related to the resistivity, ρ by

$$R = \rho L/A \tag{2.7}$$

The reciprocal of ρ gives the conductivity (σ) of the samples given as

$$\sigma = 1/\rho \tag{2.8}$$

The schematic diagram of in- plane dc conductivity measurement is shown in figure 2.16.

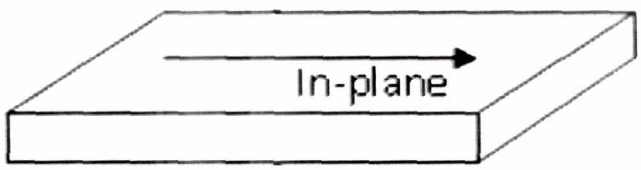

Figure 2.16 Schematic diagram of plane of dc conductivity measurement

2.6.1 Results and analysis of $BaFe_{12}O_{19}$-NPR nanocomposites

The in-plane I-V characteristics of $BaFe_{12}O_{19}$-NPR composites with barium ferrite particles annealed at 700 °C, 800 °C and 900 °C and with varying weight% (30 wt.%, 40 wt.% and 50 wt.%) of barium particle in the NPR matrix are shown in figure 2.17a and figure 2.17b respectively. From equation (2.7) and (2.8), the in-plane conductivity of the composites is calculated and tabulated in table 2.6. Pure NPR shows insulating behaviour. Figures 2.17a and 2.17b show the variation of in-plane electrical conductivity of the $BaFe_{12}O_{19}$-NPR nanocomposite with increasing annealing temperature of the $BaFe_{12}O_{19}$ particles and with increasing $BaFe_{12}O_{19}$ particles in the NPR matrix, respectively. The dc conductivity of the composite samples increases with increase in the annealing temperature and increase in the ferrite contents. The electrical conductivity in ferrites is due to the electron hoping mechanism that takes place between Fe^{2+} and Fe^{3+} ions in the octahedral sites [36]. The increase in the annealing temperature and concentration increases the number of free Fe^{2+} ions which lead to an increase in the dc conductivity.

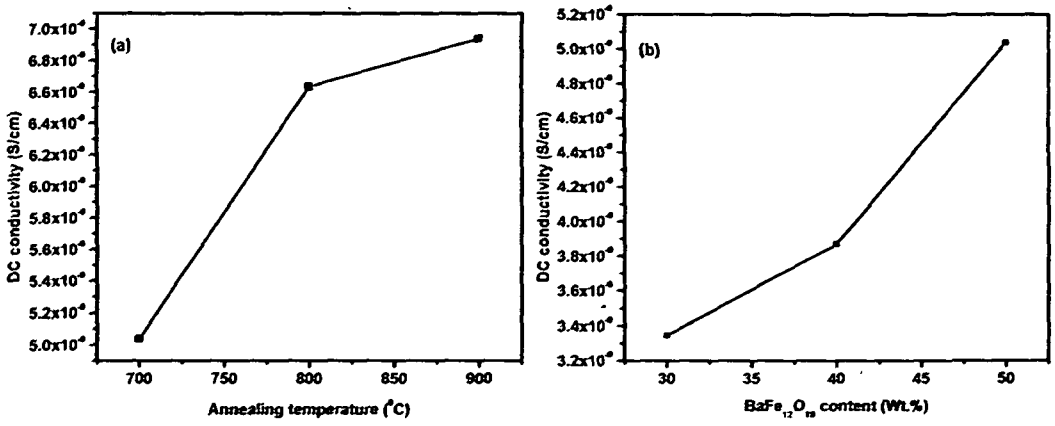

Figure 2.17 Measured in–plane dc conductivity of $BaFe_{12}O_{19}$-NPR composite (a) with annealing temperature of the ferrite inclusions, (b) with percentage of $BaFe_{12}O_{19}$ ferrite content

2.6.2 Results and analysis of $BaAl_xFe_{12-x}O_{19}$-NPR and $Ba_{1-x}Sr_xFe_{12}O_{19}$-NPR nanocomposites

The in-plane I-V characteristics of $BaAl_xFe_{12-x}O_{19}$-NPR nanocomposites with x=1.0, 1.2, 1.4 and 1.6 and $Ba_{1-x}Sr_xFe_{12}O_{19}$-NPR nanocomposites with x=0.2, 0.4, 0.6 and 1.0 are shown in figure 2.18a and figure 2.18b, respectively. Al^{3+} substitution decreases the conductivity as the number of Fe^{3+} ions decreases in the octahedral sites. Moderate increase in conductivity is observed in case of Sr^{2+} substitution.

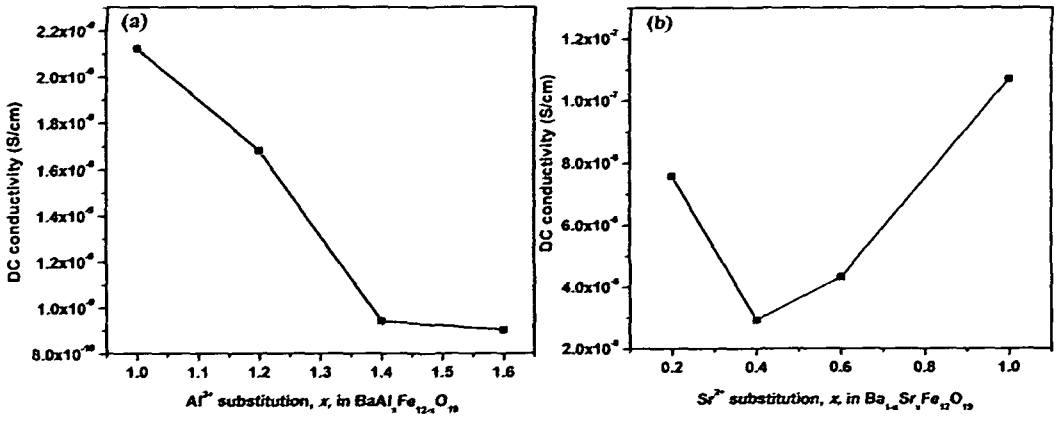

Figure 2.18 Measured in – plane dc conductivity of (a) $BaAl_xFe_{12-x}O_{19}$-NPR nanocomposite with x=1.0, 1.2, 1.4 and 1.6, (b) $Ba_{1-x}Sr_xFe_{12}O_{19}$-NPR nanocomposite with x=0.2, 0.4, 0.6 and 1.0

Table 2.7 shows that the maximum dc electrical conductivity of $BaAl_xFe_{12-x}O_{19}$-NPR nanocomposite and $Ba_{1-x}Sr_xFe_{12}O_{19}$-NPR nanocomposite are 2.12 x 10^{-9} S/cm and 1.06 x 10^{-7} S/cm, respectively.

Table 2.6 In plane dc electrical conductivity of $BaFe_{12}O_{19}$-NPR nanocomposites

Sample composition	Annealing temperature of $BaFe_{12}O_{19}$ ferrite particles	In plane dc conductivity σ_{in} (S/cm)	Sample composition	Wt.% of $BaFe_{12}O_{19}$	In plane conductivity σ_{in} (S/cm)
Pure NPR		2.4E-11			
30 wt.% $BaFe_{12}O_{19}$-NPR	700 °C	5.04E-09	$BaFe_{12}O_{19}$-NPR	30 wt.%	3.34E-09
	800 °C	6.62E-09		40 wt.%	3.86E-09
	900 °C	6.93E-09		50 wt.%	5.03E-09

Table 2.7 In plane dc electrical conductivity of $BaAl_xFe_{12-x}O_{19}$-NPR and $Ba_{1-x}Sr_xFe_{12}O_{19}$-NPR composites with 50 wt.%

Sample composition	Al^{3+} content	In plane conductivity σ_{in} (S/cm)	Sample composition	Sr^{2+} Content	In plane conductivity σ_{in} (S/cm)
$BaAl_xFe_{12-x}O_{19}$-NPR	x=1.0	2.12E-9	$Ba_{1-x}Sr_xFe_{12}O_{19}$-NPR	x=0.2	7.56E-8
	x=1.2	1.68E-9		x=0.4	2.89E-8
	x=1.4	9.4E-10		x=0.6	4.27E-8
	x=1.6	9.01E-10		x=1.0	1.06E-7

2.7 SATURATION MAGNETIZATION STUDY OF THE COMPOSITE MATERIAL

Magnetization properties of the magnetic nanocomposites have been studied using Pulsed Field Magnetometer indigenously developed in RRCAT, Indore.

2.7.1 Theory of operation of pulsed field magnetometer for magnetization study

The system consists of a solenoid and a pick up coil assembly. A furnace made with platinum wire wound on a quartz tube is placed in the pickup coil. A magnetic sample can be inserted in the furnace and a resistance thermometer is placed in contact with the sample to read its temperature. The schematic of the measurement set up is shown in figure 2.19.

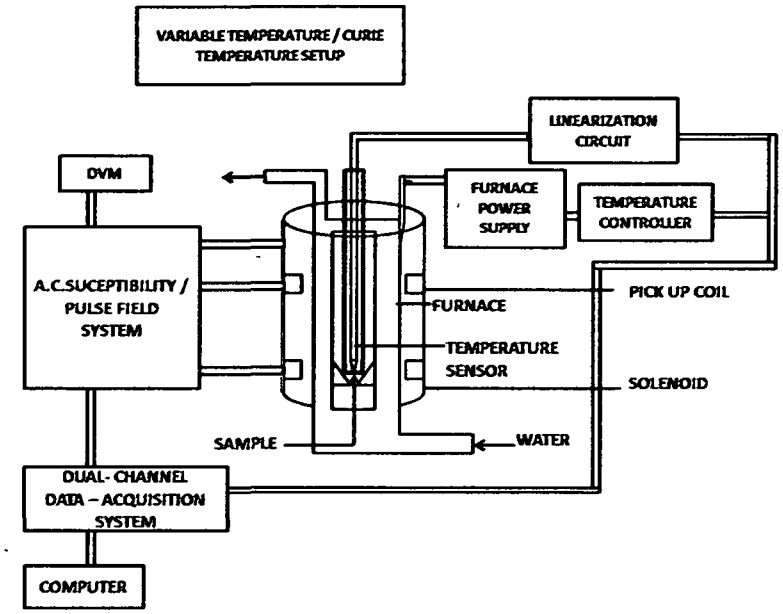

Figure 2.19 Pulsed –field magnetometer measurement set up

A pulsed magnetic field of sinusoidal shape is generated in the solenoid of the order of 2.5 kilo oersted (KOe) using a solid state relay circuit. The pickup coil detects the magnetization signal of the sample. The signal is processed to produce a steady output to be read on a digital meter. The temperature of the sample is controlled by a programmable temperature-controller. The magnetization signal and the temperature signal are digitized by a micro-controller at regular intervals and the data is sent to a computer. A special software is designed to plot the graph of magnetization at different temperatures.

2.7.2 Results and analysis

The saturation magnetization ($4\pi M_s$) measurements are carried out for different (30-50) wt.% of the barium ferrite nanoparticles, annealed at 900 °C, reinforced in NPR matrix and Al^{3+} and Sr^{2+} substituted barium ferrite nanocomposites with 50 wt.% at room temperature. The applied field is 2.5 KOe. The $4\pi M_s$ values of barium ferrite and substituted barium ferrite nanocomposites are given in table 2.8 and 2.9.

Table 2.8 Results of saturation magnetization of $BaFe_{12}O_{19}$-NPR nanocomposites with 30 wt.%, 40 wt.% and 50 wt.%

Sample composition	wt.%	$4\pi M_S$ (G)
$BaFe_{12}O_{19}$-NPR	30 wt.%	96.85
	40 wt.%	99.92
	50 wt.%	114.29

Table 2.9 Results of saturation magnetization of $BaAl_xFe_{12-x}O_{19}$-NPR and $Ba_{1-x}Sr_xFe_{12}O_{19}$-NPR nanocomposites with 50 wt.%

Sample	Al^{3+} content	$4\pi M_S$ (G)	Sample	Sr^{2+} content	$4\pi M_S$ (G)
$BaAl_xFe_{12-x}O_{19}$	x=1.0	113.39	$Ba_{1-x}Sr_xFe_{12}O_{19}$	x=0.2	104.20
	x=1.2	110.34		x=0.4	103.08
	x=1.4	102.31		x=0.6	102.92
	x=1.6	96.14		x=1.0	85.20

The saturation magnetization of M- type hexaferrite depends on the electronic configuration and the distribution of the substituted ions at different sites in the crystal structure. For 30 wt.% $BaFe_{12}O_{19}$-NPR nanocomposite, the $4\pi M_S$ is found to be 96.85 G and with increase in the barium ferrite inclusions, $4\pi M_S$ increases upto 114.29 G. The lower value of saturation magnetization is observed for lower wt.% of the barium-NPR nanocomposites. Ferrite nanoparticles dispersed in the NPR matrix in lower wt.% have large surface-to-volume ratio and less magnetic moment. This led to reduction of net magnetic moment and hence the smaller saturation magnetization.

The $BaAlFe_{11}O_{19}$-NPR nanocomposite shows a $4\pi M_S$ value of 113.39 G and the saturation magnetization reduces with increase in the Al^{3+} substitution. The lowest value of $4\pi M_S$ for this series is 96.14 G with x=1.6. For substitution of Al^{3+}<1.9, the contributions to the anisotropy constant of Fe^{3+} ions on $4f_2$, $2a$, and $4f_1$ are relatively small as the Fe^{3+} ions on a $12k$ site have a negative effect on

anisotropy constant, thus reducing the overall anisotropy effect [38]. The substitution of Fe^{3+} ions by Al^{3+} ions leads to a slight increase in the magneto crystalline anisotropic field and subsequently, reduction in saturation magnetization. $BaFe_{12}O_{19}$ induced low anisotropy in the composite before Sr^{2+} ion substitution in $Ba_{1-x}Sr_xFe_{12}O_{19}$. However, in the series of $Ba_{1-x}Sr_xFe_{12}O_{19}$-NPR nanocomposites, with increase in the Sr^{2+} substitution from 0.2 to 1, saturation magnetization decreases due to relatively high induced anisotropy. The $4\pi M_s$ values vary from 104.20 G to 85.20 G for the $Ba_{1-x}Sr_xFe_{12}O_{19}$-NPR nanocomposites.

2.8. CONCLUSIONS

Barium ferrite nanoparticles with aluminium and strontium substitution are synthesized from nitrate precursor by co-precipitation technique. Formation of single phase M-type barium ferrite is confirmed from XRD pattern. The average crystalline size of barium ferrite particles is in nanometre range and is found to increase with annealing temperatures. The size variation and control can be achieved by the annealing conditions. Barium ferrite particles with aluminium and strontium substitution also form single phase M-type hexagonal ferrite. TEM analysis of barium ferrite shows that the ferrite nanoparticles appear hexagonal in shape for all the three annealing temperatures. The size is ~50 nm and ~60 nm for the samples annealed at temperature, T=700 °C and 800 °C, is observed. Extended rod like shape in one direction is observed for the particles annealed at 900 °C with crystal lattice plane anisotropy with particle size of ~70 nm. The density measurement shows that compactness of both composite system increases with percentage increase in weight. The TGA curve shows that the developed composite is thermally stable up to 400 °C. DC conductivity increases with annealing temperature and wt. % of the ferrite nanoparticles. Aluminium substitution decreases the conductivity due to decrease in the Fe^{3+} ions but an increase in the conductivity results are observed for strontium substitution. The magnetic measurements confirm the magnetic nature of the composites at room temperature. The comparatively high values of saturation magnetization confirm its applicability as magnetic absorbers at microwave frequencies.

References

1. Srivastava, R. K., et al. Ni filled flexible multi-walled carbon nanotube-polystyrene composite films as efficient microwave absorbers, *J. Appl. Phys. Lett.* **99**, 113-116, 2011.

2. Min, E. H., et al. Microwave absorption properties in absorbers for mobile phones, *J Korean Phys. Soc.* **52** (6), 1850-1853, 2008.

3. Feng, Y. B., et al. Absorbing properties and structural design of microwave absorbers based on carbonyl iron and barium ferrite, *J. Magn. Magn. Mater.* **318**, 8-13, 2007.

4. Feng, X., et al. Electrical conductivity and microwave absorbing properties of nickel-coated multiwalled carbon nanotubes/poly(phthalazinone ether sulfone ketone)s composites, *Polym. Eng. Sci.* **48** (5), 1007-1014, 2008.

5. Zhang, B., et al. Microwave-Absorbing Properties of De-Aggregated Flake-Shaped Carbonyl-Iron Particle Composites at 2- 18 GHz, *IEEE Trans. Magn.* **42** (7), 1178-1781, 2006.

6. Xiao, H. M., et al. Synthesis, magnetic and microwave absorbing properties of core-shell structured $MnFe_2O_4/TiO_2$ nanocomposites, *Compos. Sci. Technol.* **66** (13), 2003-2008, 2006.

7. Verma, A., et al. Microwave permittivity and permeability of ferrite–polymer thick films, *J. Magn. Magn. Mater.* **263** (1-2), 228–234, 2003.

8. Peng, C. H., et al. Microwave absorbing materials using Ag–NiZn ferrite core–shell nanopowders as fillers, *J. Magn. Magn. Mater.* **284**, 113-119, 2004.

9. Kodama, R. H., Magnetic nanoparticles, *J. Magn. Magn. Mater.* **200** (1-3), 359–372, 1999.

10. Chen, X., et al. Microwave absorption properties of barium titanate/epoxide resin composites, *J. Phys. D Appl. Phys.* **40** (6), 1827–1830, 2007.

11. Wadhawan, A., et.al Nanoparticle-assisted microwave absorption by single-wall carbon nanotubes, *J. Appl. Phys. Lett.* **83** (13), 2683- 2685, 2003.

12. Kwon, H. J., et al. The microwave absorbing and resonance phenomena of Y type hexagonal ferrite microwave absorbers, *J. Appl. Phys.* **75** (10), 6109-6111, 1994.

13. Cullity, B. D & Graham, C. D. *Introduction to Magnetic Materials*, 2nd ed., Wiley, IEEE Press, USA, 2008.

14. Petrov, V. M., & Gagulin, V. V. Microwave absorbing materials, *J. Inorg. Mater.* **37** (2), 93-98, 2001.

15. Pinho, M. S., et al. Aging effect on the reflectivity measurements of polychloroprene matrices containing carbon black and carbonyl- iron powder, *J Polym. Degrad. Stab.* **73**, 1-5, 2001.

16. Knott, E. F., Shaeffer, J. F & Tuley M.T. *Radar cross section*, 2nd ed., Artech House, Norwood, 1993.

17. Carvalho, S. A., et al. Determination of microwave intrinsic properties of hexaferrite samples, *Micro. Opt. Tech. Lett.* **16** (6), 393–397, 1997.

18. Chung, D. D. L., Electromagnetic interference shielding effectiveness of carbon materials, *Carbon* **39**, 279–285, 2001.

19. Nakamura, T., Snoek's limit in high-frequency permeability of polycrystalline Ni - Zn, Mg - Zn, and Ni - Zn - Cu spinel ferrites, *J. Appl. Phys.* **88** (1), 348-353, 2000.

20. Li, Z. W., et al. Studies of static and high-frequency magnetic properties for M-type ferrite $BaFe_{12-2x}Co_xZr_xO_{19}$, *J. Appl. Phys.* **92** (7), 3902-3907, 2002.

21. Kim, Y. J., & Kim, S.S. Microwave Absorbing Properties of Co- substituted Ni_2W hexaferrites in Ka-band frequencies (26.5-40GHz), *IEEE Trans. Magn.* **38** (5), 3108-3110, 2002.

22. Kwon, H. J., et al. The microwave absorbing and resonance phenomena of Y-type hexagonal ferrite microwave absorbers, *J. Appl. Phys.* **75** (10) 6109-6111, 1994.

23. Ghasemi, A., et al. Investigation of the microwave absorptive behavior of doped barium ferrites, *Mater. Design* **29** (1), 112–117, 2008.

24. Kubo, O., & Ogawa, E. Barium ferrite particles for high density magnetic recording, *J. Magn. Magn. Mater.* **134**, 376-381, 1994.

25. Agresti, D. G., et al. A Mossbauer study of CoMo-substituted barium ferrite, *IEEE Trans. Magn.* **25** (5), 4069- 4071, 1989.

26. Wang, S., et al. High coercivity in mechanically alloyed $BaFe_{10}Al_2O_{19}$, *J. Magn. Magn. Mater.* **219** (2), 206-212, 2000.

27. Hyeon, T., et al. Synthesis of Highly Crystalline and Monodisperse Cobalt Ferrite Nanocrystals, *J. Phys. Chem. B* **106** (27), 6831-6833, 2002.

28. Bishop, G. R., & Sheard P.A. Fire-resistant composites for structural sections, *Compos. Struct.* **21** (2) 85–89, 1992.

29. Kumar, H., et al. Synthesis, characterization and application of coatings based on epoxy novolac and liquid rubber blend, *E-J Chem.* **6** (4), 1253–1259, 2009.

30. Klug, H. P. & Alexander, L. E., *X-ray Diffraction Procedures for Poly Crystalline and Amorphous Materials*, 2nd ed., Wiley Interscience, New York, 1974.

31. Qiu, J., et al. Microwave absorption properties of Al- and Cr-substituted M-type barium hexaferrite, *J. Magn. Magn. Mater.* **295** (3), 263–268, 2005.

32. Ruska, E., The Development of the Electron microscope and of Electron Microscopy, Nobel Lecture, December 8, 1986, http://nobelprize.org/nobel_prize/physics/laureates/1986/ruska-lecture.pdf

33. Ge, M. Y., et al. Nanostructured ZnO: From monodisperse nanoparticles to nanorods, *J. Cryst. Growth* **305** (1), 162-166, 2007.

34. Pratten, N. A. The precise measurement of the density of small samples, *J Mater. Sci.* **16**, 1737-1747, 1981.

35. Gogoi, J. P., et al. Synthesis and microwave characterization of expanded graphite/novolac phenolic resin composite for microwave absorber applications, *J Compos. B: Engineering* **42** (5), 1291–1297, 2011.

36. Verwey, E. J. W., Electronic Conduction of Magnetite (Fe_3O_4) and its Transition Point at Low Temperatures, *Nature* **144**, 327-328, 1939.

37. Qiu, J., et al. Effect of aluminum substitution on microwave absorption properties of barium hexaferrite, *J. Appl. Phys.* **98** (10), 103905-103905-5, 2005.

CHAPTER III

MICROWAVE CHARACTERIZATION OF M-TYPE FERRITE -NOVOLAC PHENOLIC RESIN COMPOSITES OVER THE X-BAND

3.1 INTRODUCTION

Extent of absorption within an absorber depends on electromagnetic wave interactions with the material properties, viz. complex permittivity ($\varepsilon_r = \varepsilon_r' - j\varepsilon_r''$) and complex permeability ($\mu_r = \mu_r' - j\mu_r''$). Accurate measurement of complex permittivity and permeability can help in accurate designing of absorber and hence its performance over a range of frequency band.

There are several methods reported on study of the material parameters at microwave frequencies based on transmission lines and resonant structures developed from transmission lines [1-7]. Nonresonant methods can be employed for broadband characterization of the dielectric and magnetic properties of material [8]. Resonant techniques generally determine complex permittivity and permeability at one spot frequency [9-11].

Complex permittivity and permeability of the barium hexaferrite-novolac phenolic resin composites over the X-band frequency are determined using Nicolson-Ross transmission/reflection (TRL) technique [1-5, 12]. Dielectric and magnetic loss tangent are calculated from the measured values of complex permittivity and permeability. Complex permittivity and permeability measurements are further verified using cavity perturbation technique [2, 9, 13] and is discussed later in the chapter.

3.2 NICHOLSON-ROSS TECHNIQUE FOR COMPLEX PERMITTIVITY AND PERMEABILITY DETERMINATION IN X-BAND

Nicolson-Ross technique is a non-resonant, broad band technique based on transmission/reflection line structure [1-8, 12]. Figure 3.1 shows a typical measurement configuration for a transmission/reflection method. Let the segment (shaded region in figure) has characteristic impedance Z_0 A rectangular shaped sample of thickness, d, permittivity, $\varepsilon = \varepsilon_0\varepsilon_r$ and permeability, $\mu = \mu_0\mu_r$ is inserted into a segment of transmission line. The new characteristic impedance of the segment with the sample be Z.

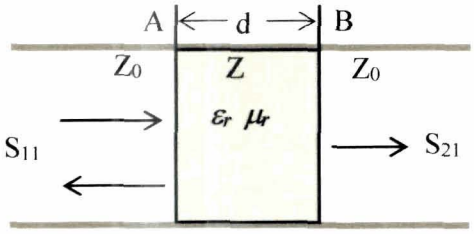

Figure 3.1 A schematic diagram of transmission/reflection method with rectangular shape material inserted

Then,

$$Z=\sqrt{\mu_r/\varepsilon_r}\,Z_0 \tag{3.1}$$

where, relative permeability and permittivity, μ_r and ε_r, are complex quantities, if the material is lossy in nature. For $d\rightarrow\infty$, the reflection coefficient, Γ, at the air-sample interface A is given as,

$$\Gamma = \frac{Z-Z_0}{Z+Z_0} = \frac{\sqrt{\frac{\mu_r}{\varepsilon_r}}-1}{\sqrt{\frac{\mu_r}{\varepsilon_r}}+1} \tag{3.2}$$

If d is finite, the transmission coefficient, T, through the segment AB is given as

$$\mathrm{T} = exp\left[-j\left(\frac{\omega}{c}\right)\sqrt{\mu_r\varepsilon_r}d\right] \tag{3.3}$$

where, ω and c is the frequency of operation and speed of light in free space.

The scattering coefficient S_{21} and S_{11} are given by following relations

$$S_{21}(\omega) = \frac{(1-\Gamma^2)T}{1-\Gamma^2T^2} \tag{3.4}$$

$$S_{11}(\omega) = \frac{(1-\mathrm{T}^2)\Gamma}{1-\Gamma^2T^2} \tag{3.5}$$

Let

$$\mathrm{X} = \frac{1-V_1V_2}{V_1-V_2} \tag{3.6}$$

where,

$$V_1 = S_{21} + S_{11} \tag{3.7}$$

$$V_2 = S_{21} - S_{11} \tag{3.8}$$

Using equations (3.4)-(3.8),

$$\Gamma = X \pm \sqrt{X^2-1} \tag{3.9}$$

For equation (3.9), the appropriate sign is chosen so that $|\Gamma| \leq 1$.

Similarly, using equations (3.4)-(3.8),

$$T = \frac{V_1 - \Gamma}{1 - V_1\Gamma} \tag{3.10}$$

Rearranging equation (3.2), gives

$$\frac{\mu_r}{\varepsilon_r} = \left(\frac{1+\Gamma}{1-\Gamma}\right)^2 = c_1(say) \tag{3.11}$$

Rearranging equation (3.3), let

$$c_2 = \mu_r\varepsilon_r = -\left[\frac{c}{\omega d}\ln\left(\frac{1}{T}\right)\right]^2 \tag{3.12}$$

From equations (3.11) and (3.12),

$$\varepsilon_r = \sqrt{\frac{c_2}{c_1}} \tag{3.13}$$

$$\mu_r = \sqrt{c_1 c_2} \tag{3.14}$$

Right-hand side of equations (3.13) and (3.14) are complex terms. Separating real and imaginary parts, the complex permittivity and permeability values can be obtained.

3.2.1 Measurements of complex permittivity and permeability

The schematic diagram of the measurement set up for X-band permittivity and permeability characterization is shown in figure 3.2a. The setup broadly consists of an Agilent E8362C vector network analyzer, Agilent WR-90 X11644A and an interfacing computer to collect the data. Figure 3.2b shows the photograph of the measurement set-up.

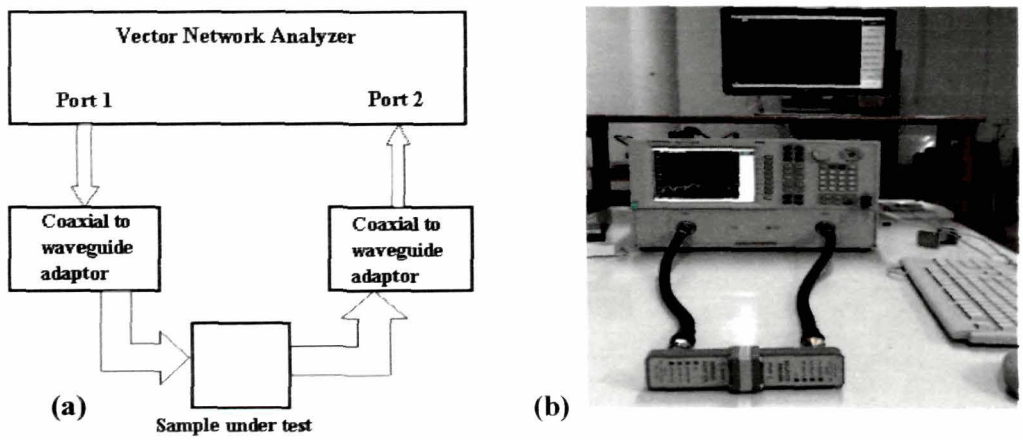

Figure 3.2 (a) Block diagram and (b) measurement set up of X-band microwave characterization set up using transmission/reflection technique

Prior to measurements, the system is calibrated, using thru-reflect-line (TRL) method [14, 15]. Schematic representation is shown in figure 3.3.

In the thru calibration, the two ports are connected directly at the desired reference plane, whereas, for reflect calibration, the ports are terminated with a load such that high reflection occurs (figures 3.3a and 3.3b). The two ports are connected by a quarter wavelength segment in line calibration (figure 3.3c). After TRL calibration, the ferrite-NPR nanocomposites of dimension 10.38 mm x 22.94 mm x 2.0 mm (chapter II, Section 2.2.2) are inserted inside the sample holder of length 9.78 mm (shown in figure 3.3d) and mounted on the zero reference plane, i.e., at the adapter of port 1.

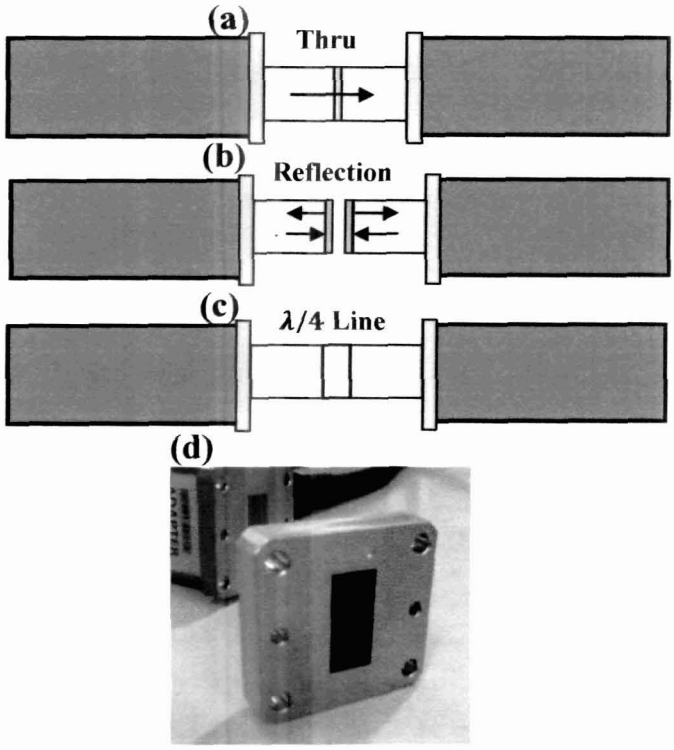

Figure 3.3 TRL calibration using Agilent WR90-X11644A calibration kit (a) Thru-calibration, (b) reflect-calibration and (c) Line-calibration and (d) X-band flange filled with sample of ferrite-NPR composite for X-band characterization

Scattering parameters (S_{11} and S_{21}) measured, are transformed to the sample edges, as described in reference [12].

The transformed S_{11} and S_{21} parameters are substituted in the equations (3.6 to 3.14) to determine the complex permittivity and permeability of the composites using Agilent 85071E material measurement software employing Nicolson-Ross method. The complex permittivity and permeability values of the composites with $BaFe_{12}O_{19}$, $BaAl_xFe_{12-x}O_{19}$ and $Ba_{1-x}Sr_xFe_{12}O_{19}$ nanoparticles as the ferrite inclusions in NPR matrix are measured in the frequency range 8.2 GHz-12.4 GHz.

3.3 RESULTS AND ANALYSIS OF COMPLEX PERMITTIVITY AND PERMEABILITY OF $BaFe_{12}O_{19}$-NPR NANOCOMPOSITE

Complex permittivity and permeability of $BaFe_{12}O_{19}$-NPR nanocomposite is first studied for $BaFe_{12}O_{19}$ particles annealed at 700 °C, 800 °C and 900 °C. The parameters are initially studied for 30 wt.% composition. Higher wt.% compositions, viz. 40% and 50% are further studied for the best complex permittivity and permeability readings obtained.

3.3.1 $BaFe_{12}O_{19}$ annealed at 700 °C, 800 °C and 900 °C

The complex permittivity and dielectric loss tangent spectra for 30 wt.% composite of $BaFe_{12}O_{19}$ fillers, annealed at T=700 °C, 800 °C and 900 °C, are plotted in figure 3.4a, 3.4b and 3.4c.

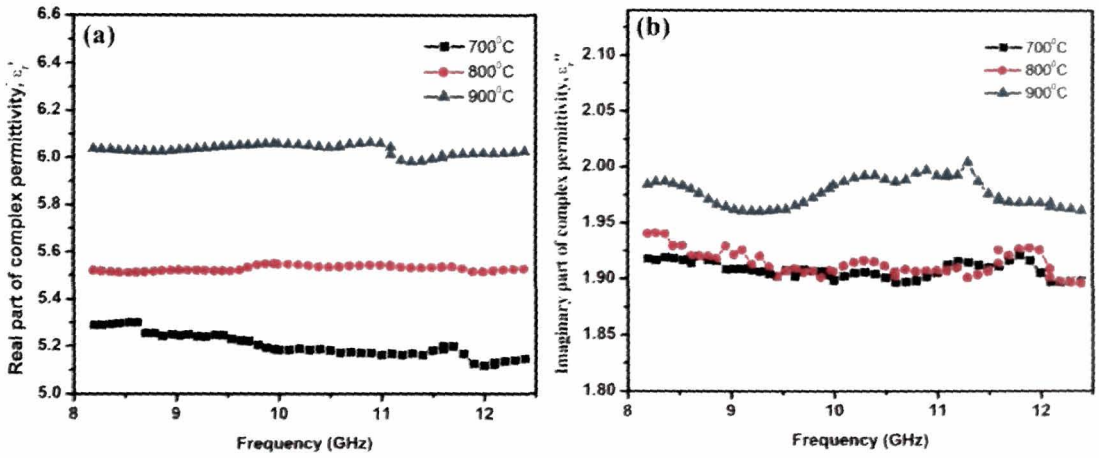

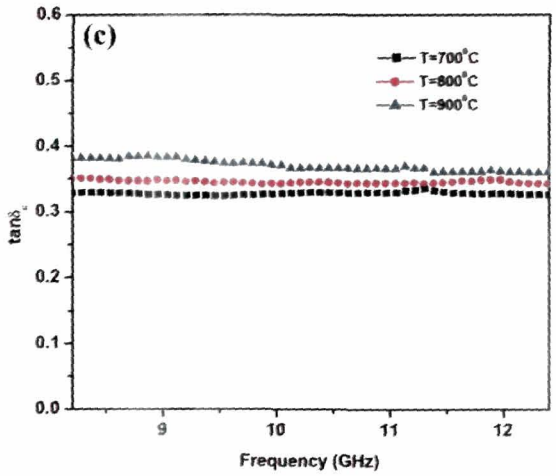

Figure 3.4 Complex permittivity of 30 wt.% $BaFe_{12}O_{19}$-NPR nanocomposite with $BaFe_{12}O_{19}$ annealed at, T=700 °C, 800 °C and 900 °C, (a) real part (b) imaginary part and (c) dielectric loss tangent

The plots show that the composite reinforced with barium ferrite at 900 °C has higher values for both real (ε_r') and imaginary (ε_r'') part of complex permittivity. The grain size of 900 °C barium ferrite, as seen from the TEM images [chapter II, section 2.3.2] are larger than others annealed at lower temperature. Larger grain size leads to high polarizability, as the developed opposing effect to electric field component in the material decreases. Also, at higher annealing temperatures, the number of Fe^{2+} ions increases by conversion of Fe^{3+} into Fe^{2+} leading to high polarization [16]. The $tan\delta_\varepsilon$ spectra of the $BaFe_{12}O_{19}$-NPR nanocomposites with varying annealing temperature show increase in the values with annealing temperature. $tan\delta_\varepsilon$ varies from 0.32 to 0.39 with annealing temperature, from 700 °C-900 °C.

The complex permeability spectra, as depicted in figures 3.5a and 3.5b, show higher value of permeability, μ' and magnetic loss, μ'' for higher annealing temperature. As the size of the $BaFe_{12}O_{19}$ particles increase, the domain wall length increases which lead to greater domain wall vibration and hence greater value of μ' and μ'' is obtained [17].

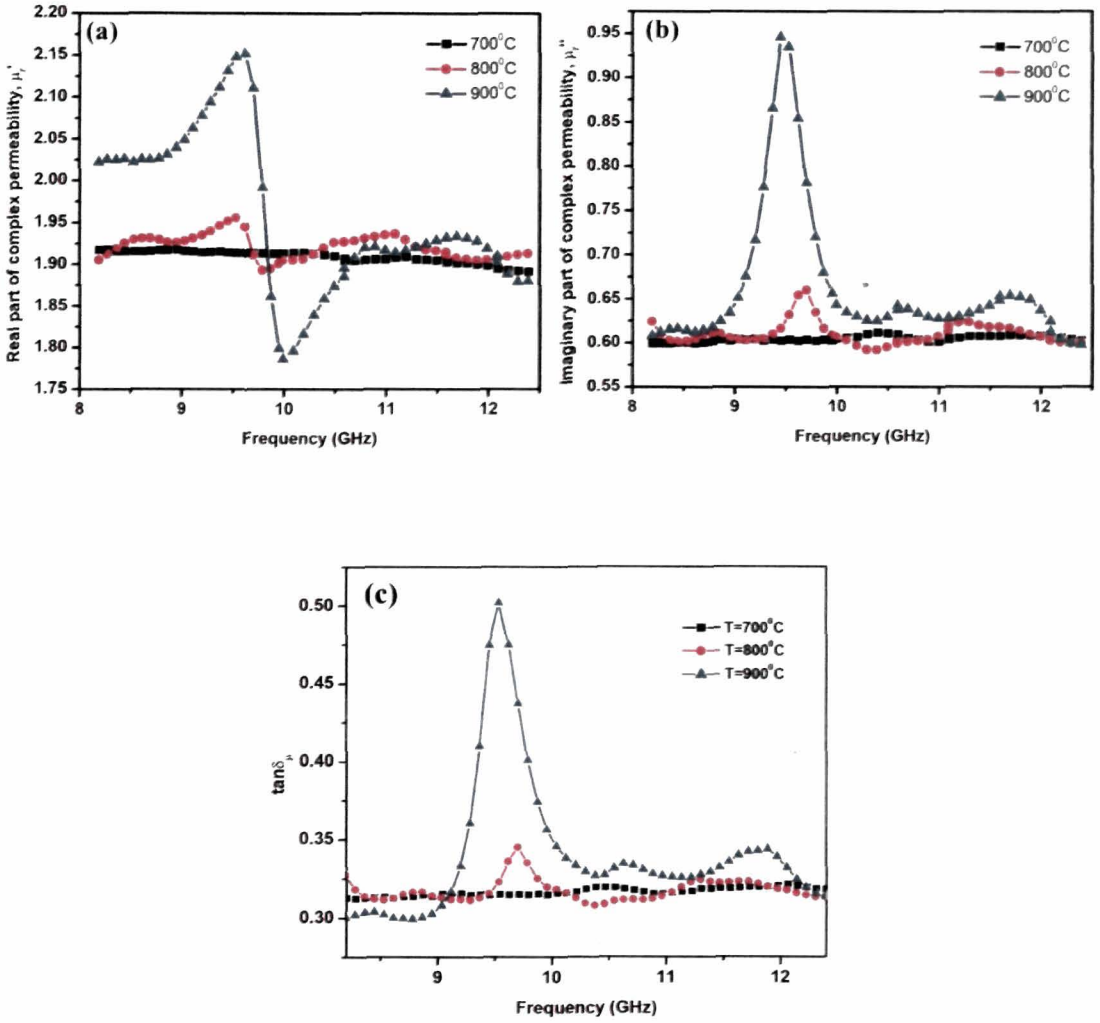

Figure 3.5 Complex permeability of 30 wt. % $BaFe_{12}O_{19}$-NPR nanocomposite with $BaFe_{12}O_{19}$ annealed at, T=700 °C, 800 °C and 900 °C, (a) real part (b) imaginary part and (c) dielectric loss tangent

The magnetic loss tangent spectra of the $BaFe_{12}O_{19}$-NPR nanocomposite show resonance, figure 3.5c. The maximum $tan\delta_{\mu}$ of 0.5 at 9.54 GHz is obtained for annealing temperature, 900 °C. A shift in the resonance frequency towards the lower frequency side is observed with annealing temperature.

High value of dielectric loss and magnetic loss, as seen from equation 1.26, chapter I, leads to higher absorption [18]. Henceforth, NPR filled with $BaFe_{12}O_{19}$ annealed at 900 °C is used for higher wt% compositions.

3.3.2 $BaFe_{12}O_{19}$ annealed at 900 °C with different weight %

$BaFe_{12}O_{19}$ particles annealed at 900 °C, henceforth mentioned as $BaFe_{12}O_{19}$ particles, are incorporated in NPR matrix to prepare the magnetic composite with 30 wt.%, 40 wt.% and 50 wt.%. The maximum wt.% is kept as 50% due to practical limitations in preparation of composite, as mentioned in chapter II. The real (ε_r') and imaginary part (ε_r'') of the relative complex permittivity ($\varepsilon_r = \varepsilon_r' - j\varepsilon_r''$) of the $BaFe_{12}O_{19}$-NPR nanocomposites in the frequency range 8.2 GHz to 12.4 GHz are shown in figure 3.6a and 3.6b. Both the dielectric constant (ε_r') and loss (ε_r'') are almost constant over the X-band for all the three weight ratios. The dielectric constant increases with increase in ferrite contents.

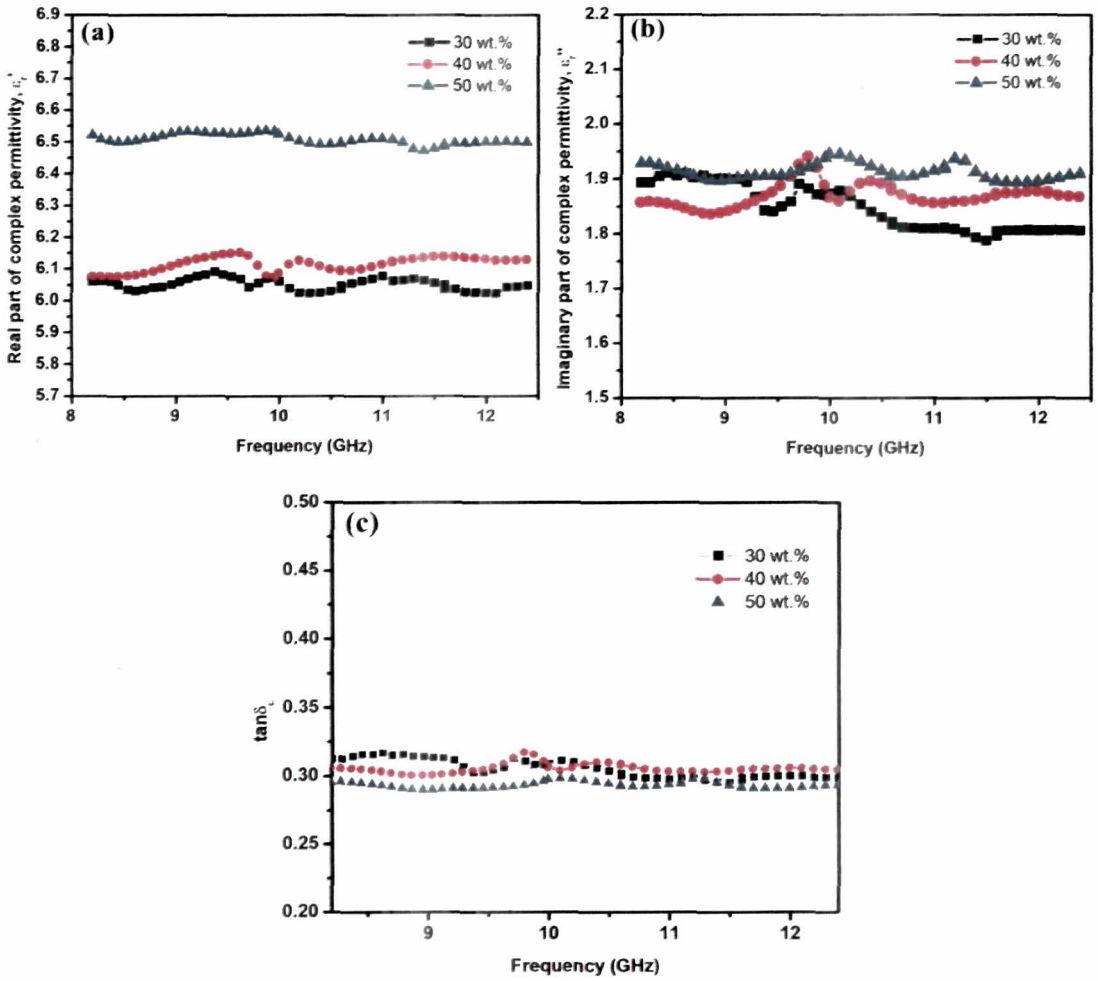

Figure 3.6 Complex permittivity of $BaFe_{12}O_{19}$-NPR nanocomposite with 30 wt.%, 40 wt.% and 50 wt.%, (a) real part (b) imaginary part and (c) dielectric loss tangent

The maximum complex permittivity is observed for the $BaFe_{12}O_{19}$-NPR nanocomposite for 50 wt.%. ε_r' increases from ~6 to ~6.52 and ε_r'' from ~ 1.88 to ~1.95 as weight % increases from 30 wt.% to 50 wt.%. The dielectric properties increase due to the interfacial polarization and intrinsic electric dipole polarization [19, 20]. The polarization in ferrites is mainly due to the presence of Fe^{2+} ions. Since, Fe^{2+} ions are easily polarizable, with increase in the number of Fe^{2+} ions, the dielectric constant increases with increase in ferrite inclusions [19].

The frequency dependent $tan\delta_\varepsilon$ variation of $BaFe_{12}O_{19}$-NPR composites with varying wt.% is shown in figure 3.6c. The dielectric loss tangent shows slight variation over the frequency range. 50 wt.% shows the least value of ~ 0.3.

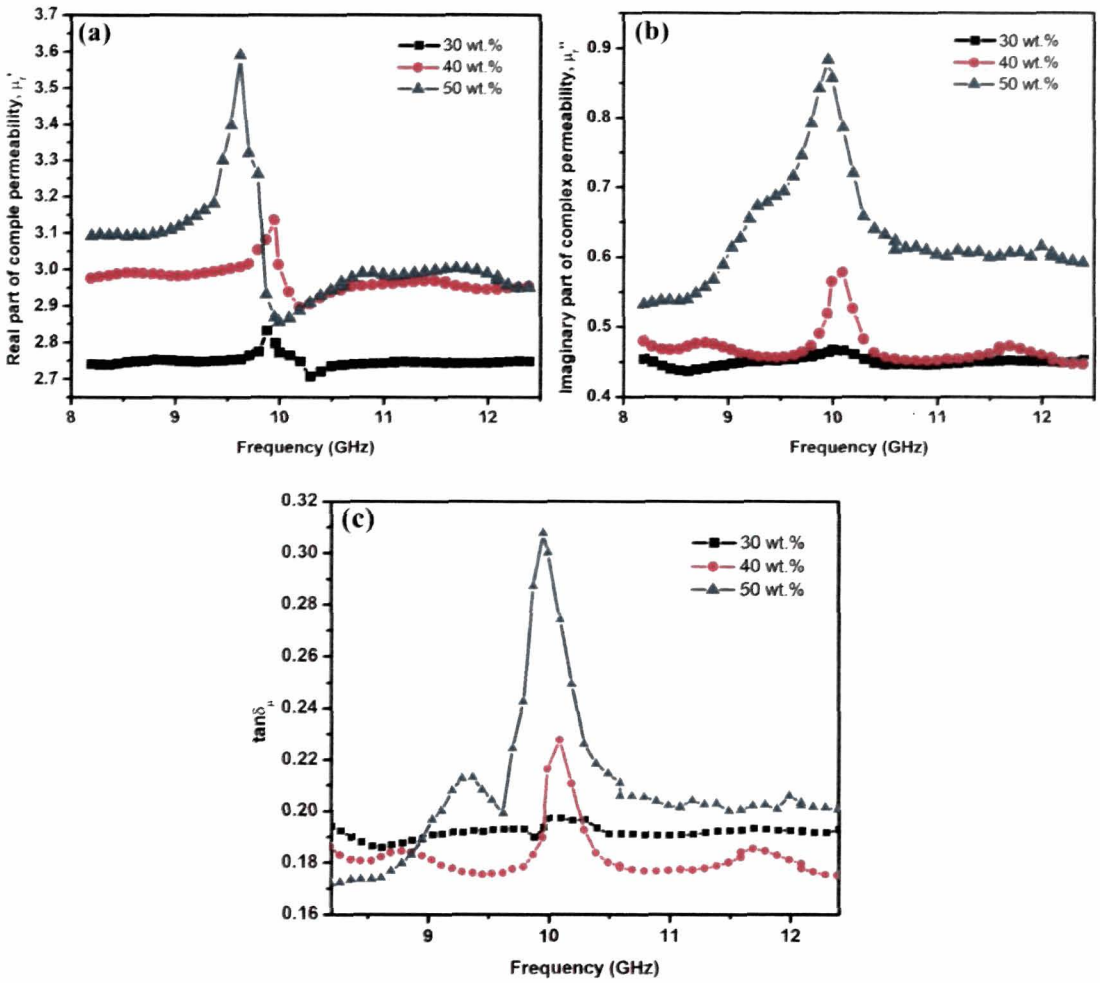

Figure 3.7 Complex permeability of $BaFe_{12}O_{19}$–NPR nanocomposite with 30 wt.%, 40 wt.% and 50 wt.%, (a) real part (b) imaginary part and (c) dielectric loss tangent

The complex permeability spectra for 30 wt.%, 40 wt.% and 50 wt.% composite are shown in figure 3.7a and 3.7b. The dispersion of complex permeability in the magnetic polymer composite is primarily due to the resonance of oscillating domain walls and the resonance of precessing magnetic moments in the domains, which is known as natural ferromagnetic resonance [17]. The peak in μ_r' and μ_r'' corresponds to natural resonance frequency (f_r) and shifts to lower frequencies with higher weight percentage. The maximum complex permeability is observed for 50 wt.% $BaFe_{12}O_{19}$-NPR nanocomposite.

All the three wt% $BaFe_{12}O_{19}$-NPR nanocomposites show magnetic loss tangent, $tan\delta_\mu$ resonance peak (figure 3.7c). $tan\delta_\mu$ values increase with increase in the barium ferrite inclusions in the polymer matrix.

3.4 COMPLEX PERMITTIVITY AND COMPLEX PERMEABILITY OF Al^{3+} AND Sr^{2+} SUBSTITUTED $BaFe_{12}O_{19}$-NPR NANOCOMPOSITE

The studies conducted on $BaFe_{12}O_{19}$-NPR nanocomposite shows that 50 wt.% composite with $BaFe_{12}O_{19}$ annealed at 900 °C, shows the best permittivity and permeability results. So the Al^{3+} and Sr^{2+} substituted $BaFe_{12}O_{19}$-NPR nanocomposite are prepared with 50 wt.% using the filler annealed at 900 °C. The complex permittivity and permeability are studied with stoichiometric variation of substitutions.

3.4.1 Results and analysis of complex permittivity and complex permeability of the $BaAl_xFe_{12-x}O_{19}$-NPR nanocomposite

The real and imaginary part of the relative complex permittivity ($\varepsilon_r=\varepsilon_r'-j\varepsilon_r''$), for 50 wt.% $BaAl_xFe_{12-x}O_{19}$-NPR nanocomposite is studied in the frequency range 8.2 GHz to 12.4 GHz. The aluminium content is varied as, x=1, 1.2, 1.4 and 1.6. The spectra are shown in figures 3.8a and 3.8b. Both ε_r' and ε_r'' increases with increase in Al^{3+} ion substitution. The maximum ε_r' is observed for the $BaAl_xFe_{12-x}O_{19}$-NPR composite with x=1.6. In $BaAl_xFe_{12-x}O_{19}$, Al^{3+} replaces the Fe^{3+} mostly in the octahedral sites (12k, $4f_2$, 2a), for x less than 1.9 [21]. With increase in the Al^{3+}

ions, Fe^{3+} reduces and hence the dielectric properties increase. The number of free Fe^{2+} ions increases in comparison to Fe^{3+} ions, thus leading to increase in complex permittivity values. [19].

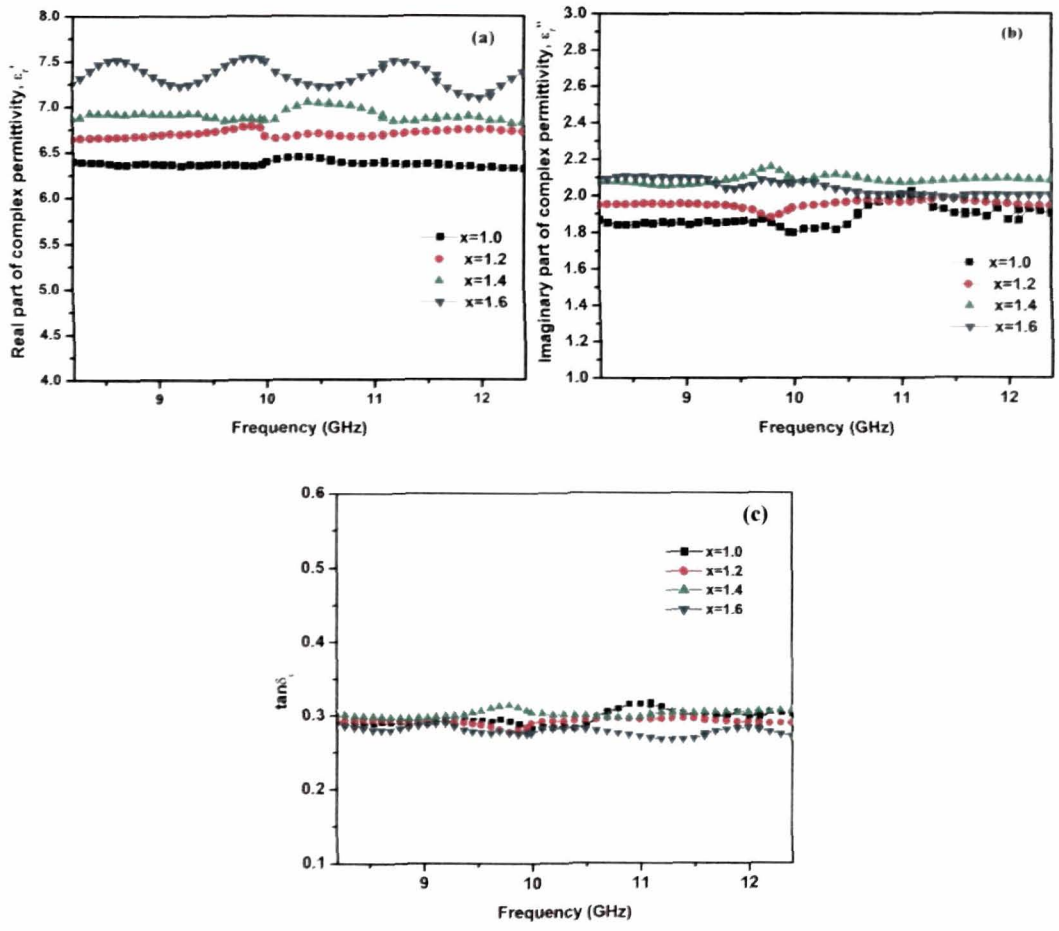

Figure 3.8 Complex permittivity of $BaAl_xFe_{12-x}O_{19}$–NPR (x = 1, 1.2, 1.4 and 1.6) composite, (a) real part (b) imaginary part and (c) magnetic loss tangent

Some fluctuations are observed in ε_r' over the X-band frequency range for all the samples. Electrons in a dielectric molecule, considered to be situated at different locations, experience different natural angular frequencies and damping.

If f_i is the bounded electrons, with frequency ω_i, mass m and damping γ_i in each molecule, interact with the electromagnetic wave of angular frequency ω, then the polarization P for a system with N molecules per unit volume, is given by [22]

$$\mathbf{P}=\mathrm{Re}(\mathbf{P}^*)=\mathrm{Re}\left[\frac{Nq^2}{m}\left(\sum_i \frac{f_i}{\omega_i^2-\omega^2-j\gamma_i\omega}\right)\boldsymbol{E}^*\right] \tag{3.15}$$

When pumped with microwave power with varying ω, the dipole moment and hence, the polarization of the molecules fluctuates in accordance with equation 3.15. Now, the relative complex permittivity is determined by relation

$$\varepsilon_r^* = 1+\frac{Nq^2}{m\varepsilon_0}\sum_i \frac{f_i}{\omega_i^2-\omega^2-j\gamma_i\omega} \tag{3.16}$$

where, complex permittivity, $\varepsilon^*=\varepsilon_0(1+\chi_e^*)$ and complex polarization, $\boldsymbol{P}^*=\varepsilon_0\chi_e^*\boldsymbol{E}^*$, and χ_e^* and $\boldsymbol{E}^*$ is the complex susceptibility and field, respectively. From equation 3.15, both real and imaginary part of relative complex permittivity of the system will vary with the frequency of pumped electromagnetic wave.

$BaAl_xFe_{12-x}O_{19}$ in composites will also have electrons having different locational natural frequencies and damping, hence, different interacting frequency with pumped microwave, leading to variation in ε' values of the composites.

The resonant behavior in the relative complex permeability ($\mu_r=\mu_r'-j\mu_r''$) is observed due to natural resonance phenomenon that takes place in the magneto-dielectric composite in the GHz range and plotted in figures 3.9a and 3.9b.

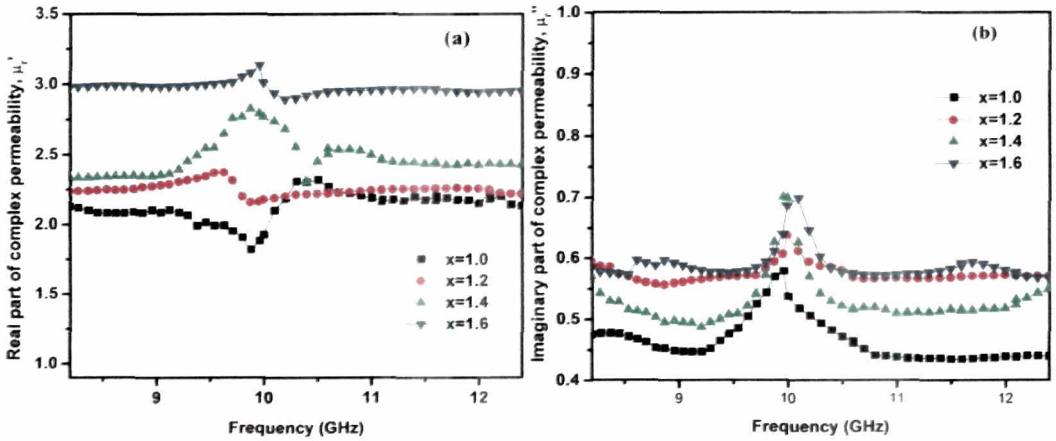

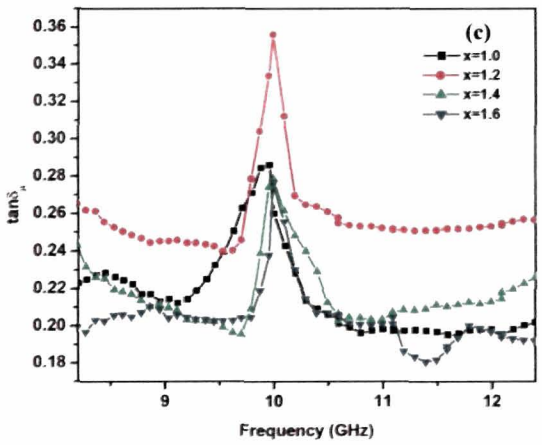

Figure 3.9 Complex permeability of $BaAl_xFe_{12-x}O_{19}$–NPR (x = 1, 1.2, 1.4 and 1.6) composite, (a) real part (b) imaginary part and (c) magnetic loss tangent.

As reported by Jianxun Qiu et. al. [21], for substitution of Al^{3+}<1.9, the contributions to the anisotropy constant of Fe^{3+} ions on $4f_2$, $2a$, and $4f_1$ are relatively small as the Fe^{3+} ions on a $12k$ site have a negative effect on anisotropy constant, thus reducing the overall anisotropy effect. Thus, substitution of Fe^{3+} ions by Al^{3+} ions leads to increase in the magneto crystalline anisotropic field. The ferromagnetic resonance frequency, f_r of the composites follows the relation [23],

$$f_r = \frac{\gamma}{2\pi} H_a \qquad (3.17)$$

Where, γ is the gyromagnetic ratio, H_a is the crystal anisotropy field.

Thus, the natural resonance frequency (f_r), corresponding to peak in μ_r' and μ_r'', shifts towards higher frequency side. The value of μ_r' and μ_r'' increases with increase in the Al^{3+} in the $BaAl_xFe_{12-x}O_{19}$-NPR nanocomposite.

Dielectric and magnetic loss tangent of the $BaAl_xFe_{12-x}O_{19}$–NPR nanocomposites are shown in figure 3.8c and 3.9c. $BaAl_xFe_{12-x}O_{19}$–NPR nanocomposite with x=1.4 shows maximum value of dielectric loss tangent of ~0.30 while, x=1.6 shows minimum $tan\delta_\varepsilon$ of ~0.28. $tan\delta_\mu$ shows resonance and the resonance frequency shifts towards higher frequency side. The $tan\delta_\mu$ intially increases with the Al^{3+}

substitution from x=1.0 to 1.2 and then decreases and the composite with x=1.6 gives the minimum value of resonant $tan\delta_{\mu}$.

3.4.2 Results and analysis of complex permittivity and complex permeability of the $Ba_{1-x}Sr_xFe_{12}O_{19}$–NPR nanocomposite

The real (ε_r') and imaginary part (ε_r'') of the relative complex permittivity of 50 wt.% $Ba_{1-x}Sr_xFe_{12}O_{19}$-NPR (x= 0.2, 0.4, 0.6 and 1.0) composite in the frequency range 8.2 GHz to 12.4 GHz, is shown in figures 3.10a and 3.10b. Both ε_r' and ε_r'' are almost independent of frequency for all the samples. A marginal increase in ε_r' and ε_r'' is observed with increase in Sr^{2+} ions. The maximum complex permittivity with ε_r'~8 and ε_r''~3, is observed when Sr^{2+} completely replaces Ba^{2+} ions in $Ba_{1-x}Sr_xFe_{12}O_{19}$-NPR composite i.e. for x=1.0.

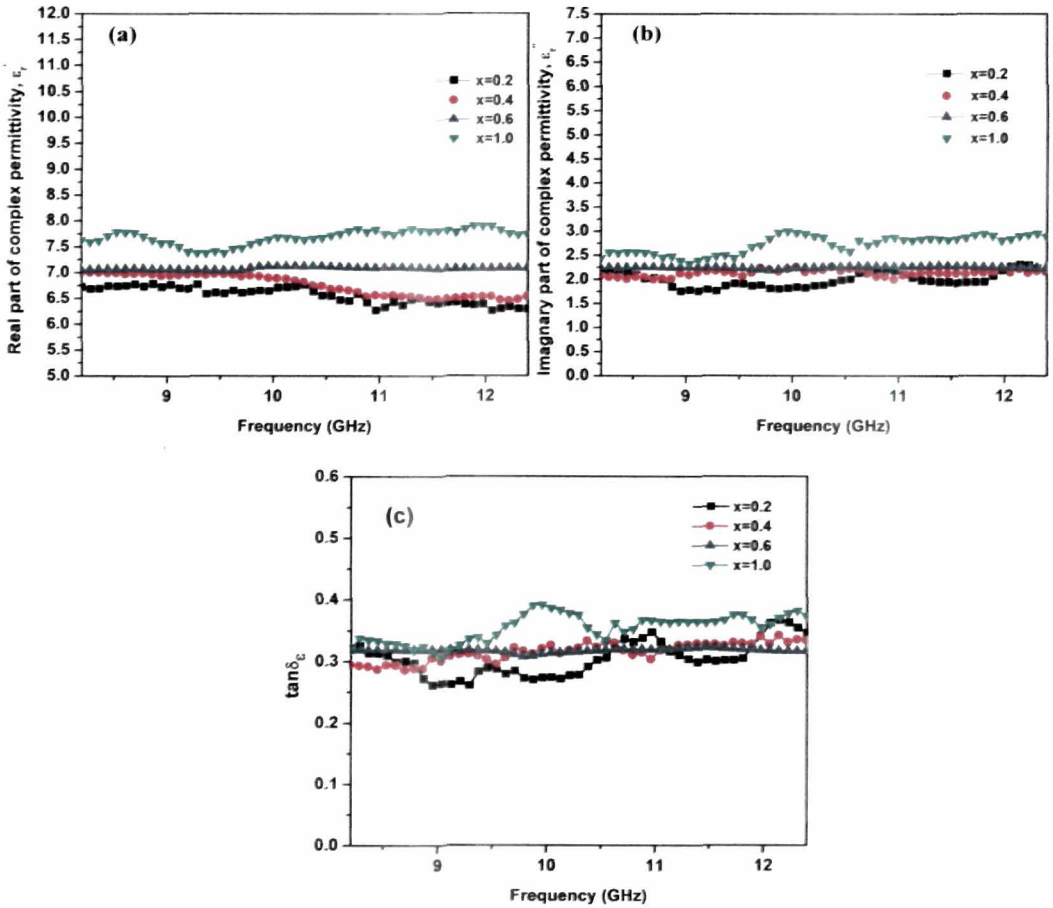

Figure 3.10 Complex permittivity of $Ba_{1-x}Sr_xFe_{12}O_{19}$–NPR (x = 0.2, 0.4, 0.6 and 1.0) composite, (a) real part (b) imaginary part and (c) dielectric loss tangent

Dielectric loss tangent, $tan\delta_e$, increases from ~0.30 to ~0.40 as Sr^{2+} ions increases from x= 0.2 to 1.0 in $Ba_{1-x}Sr_xFe_{12}O_{19}$–NPR composites. Figure 3.10c shows the loss plot with frequency.

Natural ferromagnetic resonance phenomenon is observed in ferrites at frequencies in gigahertz range. The resonance frequency (f_r) corresponds to the peak value of real (μ_r') and imaginary part (μ_r'') of permeability. The variation of real and imaginary part of complex permeability with frequency is shown in figures 3.11a and 3.11b.

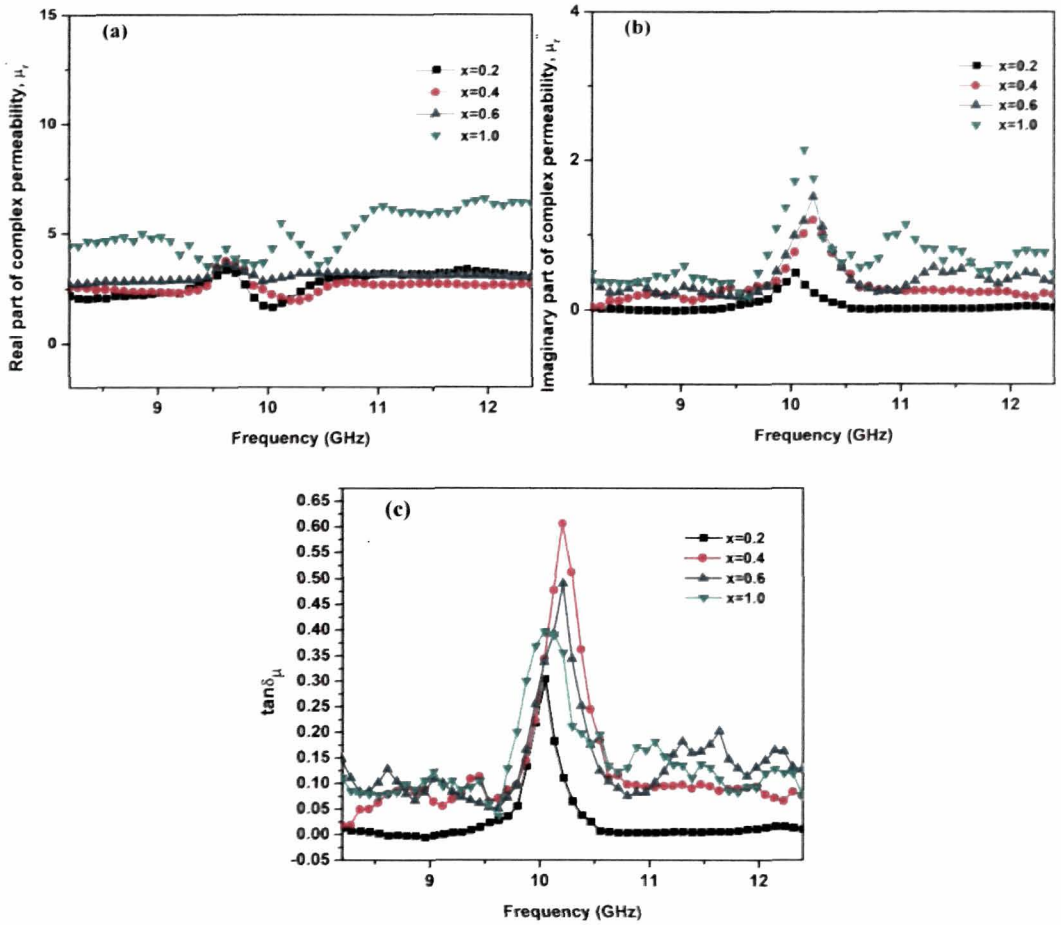

Figure 3.11 Complex permeability of $Ba_{1-x}Sr_xFe_{12}O_{19}$–NPR (x = 0.2, 0.4, 0.6 and 1.0) composite, (a) real part (b) imaginary part and (c) magnetic loss tangent

A shift of f_r towards higher frequency side is observed with increase in the Sr^{2+} in the $Ba_{1-x}Sr_xFe_{12}O_{19}$-NPR composite [24, 25]. Substitution of Ba^{2+} ions by Sr^{2+} ions lead to an increase of magneto crystalline anisotropic field from 17.6 kOe to

19 kOe [25], hence from equation 3.17 the ferromagnetic resonance frequency of the composites increases.

Magnetic loss tangent, $tan\delta_{\mu}$, spectra peaks between 10 -10.5 GHz and composite with x=0.4 shows maximum value of 0.62, figure 3.11c.

3.5 CAVITY PERTURBATION TECHNIQUE FOR DETERMINATION OF COMPLEX PERMITTIVITY AND PERMEABILITY

Cavity perturbation method is an accurate resonant method for evaluation of complex permittivity and permeability but is generally limited to single operational frequency [9, 13].

A TE_{103} cavity resonator designed at 9.9 GHz and TE_{102} resonator at 9.86 GHz, are employed for complex permittivity and permeability measurements, respectively, shown in figures 3.12a and 3.12b. The iris hole diameter for critical coupling in both the cavities is found to be 8.42mm. A tuning screw is incorporated into the cavity to handle frequency shift (both +ve and -ve) from the design frequency due to mismatch when the cavity is perturbed. It is placed subsequent to the iris coupling so as to adjust the Q of the incoming electromagnetic wave. The tuning screw has the ability to adjust the frequency shift by ± 5%, which is generally observed during the investigation. The loaded Q of the cavity is calculated using the formula given by

$$Q = \frac{Resonant\ frequency}{3dB\ band\ width} = \frac{f_r}{(f_2 - f_1)} \tag{3.18}$$

where, f_r is the resonant frequency, f_2 and f_1 are the frequencies corresponding to 3 dB point and f_2 being the higher frequency.

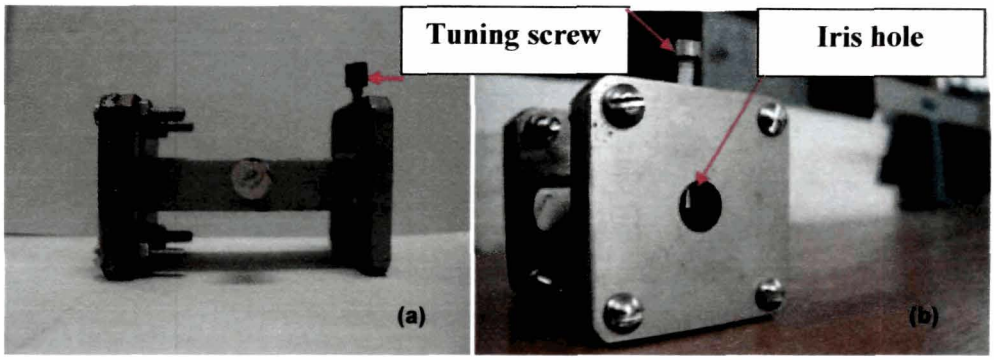

Figure 3.12 (a) TE_{103} and (b) TE_{102} rectangular resonant cavities with tuning screw and iris hole

The sample is mounted using Teflon sample holder at the point of maximum electric field and minimum magnetic field, i.e. at the centre of a TE_{103} rectangular cavity, for permittivity measurements. The test samples, used for the permittivity measurement, are of 1mm x 1mm x 1mm. Complex permittivity is determined from the following equations referred in [26],

$$\varepsilon' = 1 + \frac{f_0^2 - f_1^2}{f_1^2}\frac{V_c}{4V_s} \tag{3.19}$$

$$\varepsilon'' = \frac{V_c}{4V_s}\left[\frac{f_0^2}{f_1^2}\left(\frac{1}{Q_1} - \frac{1}{Q_0}\right)\right] \tag{3.20}$$

where,

f_1 and f_0 are the resonant frequencies with and without the samples,

V_s and V_c are the volume of the sample and the cavity,

Q_0 and Q_1 are the Q-factor of the cavity without and with the sample.

For complex permeability, TE_{102} cavity resonator designed at 9.86 GHz is used. The sample is placed at the centre of the TE_{102} cavity having maximum magnetic field and minimum electric field. The samples are spheres of 1-2 mm diameter. Complex permeability is calculated from the relations [2],

$$\mu' = 1 + \frac{1}{K}\frac{V_c}{V_s}\left(\frac{f_0 - f_1}{f_1}\right) \tag{3.21}$$

$$\mu'' = \frac{V_c}{KV_s}\left(\frac{1}{2Q_1} - \frac{1}{2Q_0}\right) \tag{3.22}$$

where, $K = \frac{2a^2}{a^2+l^2}$, and a and l are the broad dimension and length of the rectangular waveguide, respectively.

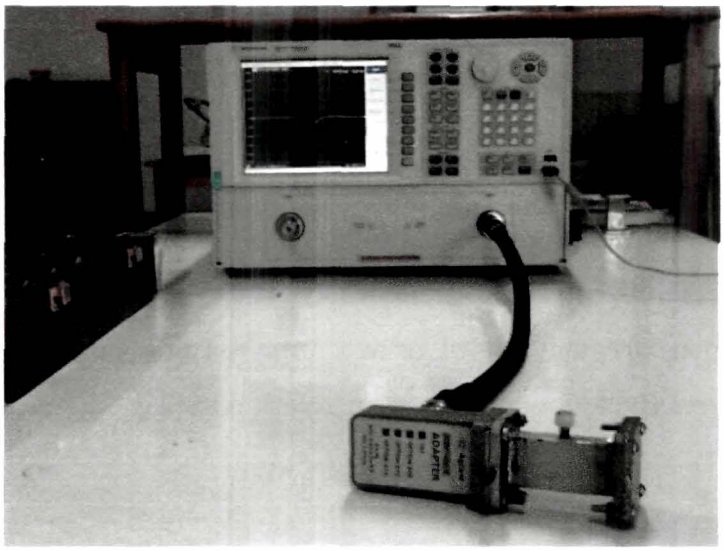

Figure 3.13 Complex permittivity and permeability measurement setup using cavity perturbation technique

3.5.1 Results and analysis of the complex permittivity and permeability values from cavity resonator technique

The frequency response of the two cavities is shown in figures 3.14a and 3.14b. Using equation 3.18, the Q for the TE_{103} reflection cavity is found to be 1833 and for TE_{102} reflection cavity is found to be 1401.

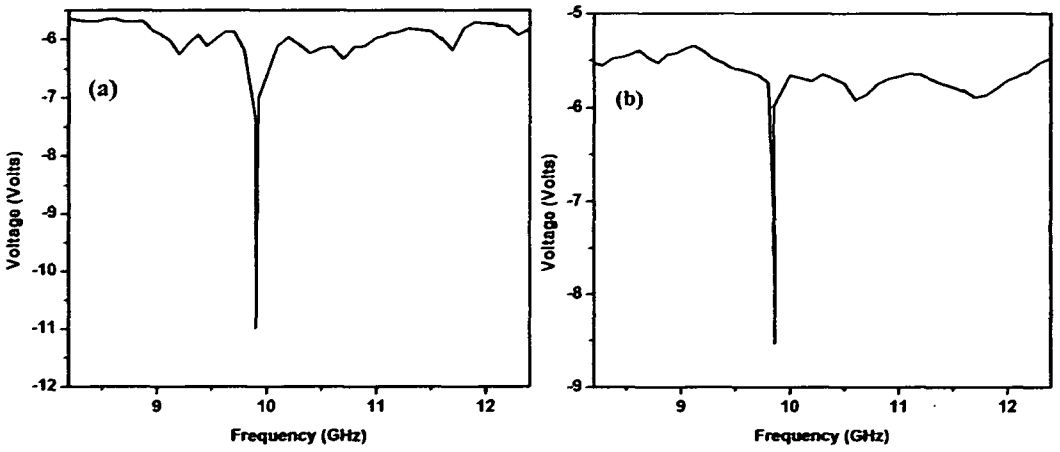

Figure 3.14 Resonant cavity plots for empty cavity (a) TE_{103} and (b) TE_{102}

The ε_r' and ε_r'' and μ_r' and μ_r'' of different ferrite nanocomposites are determined using equations 3.19-3.22. The results for $BaFe_{12}O_{19}$-NPR are tabulated in table 3.1 and table 3.2, $BaAl_xFe_{12-x}O_{19}$–NPR and $Ba_{1-x}Sr_xFe_{12}O_{19}$-NPR nanocomposite are tabulated in table 3.3 and table 3.4, respectively.

Table 3.1 Complex permittivity of developed $BaFe_{12}O_{19}$-NPR composite at 9.9GHz

Sample	At 9.9 GHz						%discrepancy		
	Cavity perturbation technique			Nicolson Ross technique					
	ε_r'	ε_r''	$\tan\delta_e$	ε_r'	ε_r''	$\tan\delta_e$	ε_r'	ε_r''	$\tan\delta_e$
$BaFe_{12}O_{19}$-NPR composite (T=900°C)									
30wt.%	5.83	1.73	0.297	6.07	1.87	0.311	3.9	7.4	4.5
40wt.%	5.92	1.75	0.295	6.08	1.90	0.312	2.6	7.8	5.4
50wt.%	7.01	1.81	0.258	6.53	1.93	0.296	7.3	6.2	12.8

Table 3.2 Complex permeability of developed $BaFe_{12}O_{19}$-NPR composite at 9.86 GHz

Sample	At 9.86GHz						%discrepancy		
	Cavity perturbation technique			Nicolson Ross technique					
	μ_r'	μ_r''	$\tan\delta_m$	μ_r'	μ_r''	$\tan\delta_m$	μ_r'	μ_r''	$\tan\delta_m$
$BaFe_{12}O_{19}$-NPR composite (T=900°C)									
30wt.%	2.73	0.51	0.187	2.84	0.47	0.165	3.8	8.51	13.2
40wt.%	2.95	0.43	0.146	3.09	0.49	0.159	4.5	12.2	8.1
50wt.%	3.01	0.78	0.259	3.24	0.85	0.262	7.0	8.2	1.1

Table 3.3 Complex permittivity of developed $BaAl_xFe_{12-x}O_{19}$-NPR and $Ba_{1-x}Sr_xFe_{12}O_{19}$-NPR composite at 9 9GHz

Sample	At 9.86 GHz						%discrepancy		
	Cavity perturbation technique			Nicolson Ross technique					
	ε_r'	ε_r''	$\tan\delta_e$	ε_r'	ε_r''	$\tan\delta_e$	ε_r'	ε_r''	$\tan\delta_e$
$BaAl_xFe_{12-x}O_{19}$-NPR									
x=1.0	6.14	1.54	0.251	6.37	1.83	0.287	3.6	15.8	12.5
x=1.2	6.82	1.69	0.247	6.79	1.92	0.283	0.5	11.9	12.7
x=1.4	6.41	1.95	0.304	6.88	2.14	0.311	6.8	8.8	2.25
x=1.6	6.99	1.78	0.255	7.55	2.08	0.275	7.4	14.4	7.27
$Ba_{1-x}Sr_xFe_{12}O_{19}$-NPR									
x=0.2	6.45	1.93	0.299	6.64	1.80	0.271	2.86	7.22	10.33
x=0.4	6.27	2.04	0.325	6.96	2.15	0.309	9.91	5.11	5.17
x=0.6	7.31	2.10	0.287	7.11	2.18	0.307	2.81	3.66	6.51
x=1.0	7.38	2.54	0.344	7.64	2.98	0.390	3.4	14.7	11.7

Table 3.4 Complex permeability of developed $BaAl_xFe_{12-x}O_{19}$-NPR and $Ba_{1-x}Sr_xFe_{12}O_{19}$-NPR nanocomposite at 9.86 GHz

Sample	At 9.86 GHz						%discrepancy		
	Cavity perturbation technique			Nicolson Ross technique					
	μ_r'	μ_r''	$\tan\delta_m$	μ_r'	μ_r''	$\tan\delta_m$	μ_r'	μ_r''	$\tan\delta_m$
$BaAl_xFe_{12-x}O_{19}$-NPR									
x=1.0	1.67	0.59	0.353	1.82	0.57	0.313	8.2	3.5	12.7
x=1.2	1.99	0.64	0.322	2.18	0.59	0.271	8.7	8.4	18.8
x=1.4	2.48	0.60	0.242	2.83	0.63	0.223	12.3	4.8	8.5
x=1.6	3.14	0.58	0.185	3.09	0.62	0.201	1.6	6.4	7.9
$Ba_{1-x}Sr_xFe_{12}O_{19}$-NPR									
x=0.2	2.32	0.31	0.134	2.15	0.28	0.130	7.9	10.7	3.07
x=0.4	2.45	0.40	0.162	2.71	0.41	0.151	9.5	2.44	7.3
x=0.6	3.16	0.53	0.167	3.21	0.55	0.171	1.6	3.6	2.34
x=1.0	3.59	0.98	0.272	3.75	1.11	0.296	4.2	11.7	8.1

The results are compared with the values obtained from Nicolson Ross method at the same frequency. The values from both the techniques agree well with % discrepancy and therefore, corroborate each other's accuracy.

3.6 CONCLUSIONS

Microwave characterization of ferrite-NPR nanocomposites are performed over the X-band. The complex permittivity and permeability are computed from measured values of S_{21} and S_{11} using Nicolson Ross method. The results obtained from this method are substantiated by cavity resonator method and found to be in close proximity.

The $BaFe_{12}O_{19}$-NPR nanocomposite with ferrite particles annealed at 900 °C gives the best microwave properties in comparison to the other annealing temperature. Weight variation is carried out using $BaFe_{12}O_{19}$ particles annealed at 900 °C and 50 wt.% shows a high permittivity of ~6.55 and permeability of ~3.59 and dielectric and magnetic loss tangent ~0.3 and ~0.26, respectively among the three compositions studied. 50 wt.% aluminum substituted barium ferrite-NPR nanocomposites show enhancement of complex permittivity and permeability values. As Sr^{2+}substitutes Ba^{2+} in the ferrite composite, both the complex permittivity and permeability increases. Out of the three ferrite compositions in NPR matrix, studied, strontium substituted shows maximum loss tangent with $SrFe_{12}O_{19}$-NPR nanocomposite, showing the maximum value of ~0.4 and ~0.35.

From the dielectric and magnetic loss spectra for the composites it is seen that the developed ferrite-NPR nanocomposites have the potential characteristics for microwave absorption.

References

1. Hajian, M., et al. Measurement of complex permittivity with waveguide resonator using perturbation technique, *Micro. Opt. Technol. Lett.* **21** (4), 269-272, 1999.
2. Murthy, V. R. K., Sunderam, S., & Viswanathan, B. *Microwave Materials,* Narosa Publishing House, New Delhi, 1990.
3. Chen, L. F., et al. *Microwave Electronics Measurement and Material Characterization,* John Willey and Sons, West Sussex, England, 2004.
4. Yamashita, E., et al. Microstrip dispersion in a wide frequency range, *IEEE Trans. Microw. Theory Tech.* **29** (6), 610-611, 1981.
5. Yamashita, E., et al. An approximate dispersion formula of microstrip lines for computer aided design of microwave integrated circuits, *IEEE Trans. Microw. Theory Tech.* **27** (12), 1036-1038, 1979.
6. Al-Moayed, N. N., et al. Nano ferrites microwave complex permeability and permittivity measurements by T/R technique in waveguide, *IEEE Trans. Magn.* **44** (7), 1768-1772, 2008.
7. Jarvis, J. B., et al. Improved technique for determining complex permittivity with the transmission/reflection method, *IEEE Trans. Microw. Theory Tech.* **38** (8), 1096-1103, 1990.
8. Krupka, J. Frequency domain complex permittivity measurements at microwave frequencies, *Meas. Sci. Technol.* **17**, 55-70, 2006.
9. Carter, R. G., Accuracy of microwave cavity perturbation measurements, *IEEE Trans. Microw. Theory Tech.* **49**, 918-923, 2001.
10. Sunny, V., et al. A flexible microwave absorber based on nickel ferrite nanocomposite, *J. Alloy Compd.* **489**, 297-303, 2010.
11. Borah, S. *Study of microstrip transmission line and adaptable radial stub resonator on nickel substituted cobalt ferrite/ LDPE nanocomposite as magneto – dielectric substrate at X- band,* Ph. D. Thesis, Tezpur University, India, 2011.

12. Nicolson, A. M. & Ross, G. F, Measurement of the intrinsic properties of materials by time-domain techniques, *IEEE. T. Instrum. Meas.* **19** (4), 377-382, 1970.
13. Chao, S. H. Measurements of microwave conductivity and dielectric constant by the cavity perturbation method and their errors, *IEEE Trans. Microw. Theory Tech.* **33** (6), 519-526, 1985.
14. TRL/LRM Calibration, Agilent E5070B/E5071B ENA Series RF Network Analyzers,1st Edition, Agilent Technologies, No. 16000-95026, Japan, 2004.
15. Engen, G. F. & Hoer C. A., Thru-reflect-line: An improved technique for calibrating the dual six-port automatic network analyzer, *IEEE Trans. Microw. Theory Tech.* **27** (12), 987–993, 1979.
16. Gupta, N., et al. Processing and properties of cobalt-substituted lithium ferrite in the GHz frequency range, *Ceram. Int.* **31** (1), 171-176, 2005.
17. Rado, G.T. Theory of the microwave permeability tensor and Faraday Effect in nonsaturated ferromagnetic materials, *Phys. Rev.* **89**, 529, 1953.
18. Zhang, B., et al. Microwave-Absorbing Properties of De-Aggregated Flake-Shaped Carbonyl-Iron Particle Composites at 2- 18 GHz, *IEEE Trans. Magn.* **42** (7), 1778-1781, 2006.
19. Abdullah, M.H., & Yusoff, A.N. Frequency dependence of the complex impedances and dielectric behaviour of some Mg-Zn ferrites, *J. Mater. Sci.* **32** 5817-5823, 1997.
20. Haijun, Z., et al. Complex permittivity, permeability, and microwave absorption of Zn- and Ti-substituted barium ferrite by citrate sol-gel process, Mater. Sci. Eng. **B 96,** 289-295, 2002.
21. Qiu, J., et al. Effect of aluminum substitution on microwave absorption properties of barium hexaferrite, *J. Appl. Phy.* **98,** 103905-1-5, 2005.
22. Griffiths, D. J. *Introduction to Electrodynamics*, third ed., PHI Learning Private Limited, New Delhi, 2011.
23. Ghasemi, A., et al. Investigation of the microwave absorptive behavior of doped barium ferrites, *Mater. Design* **29,** 112–117, 2008.

24. Hosseini, S. H. & Moloudi M. Synthesis, Magnetic, and Microwave Absorption Properties of Multi Core-Shell Structured $Ba_xSr_{1-x}Fe_{12}O_{19}/Fe_3O_4$/Polyacrylic Acid Nanocomposites, *Synthesis and Reactivity in Inorganic, Metal-Organic, and Nano-Metal Chemistry* **43**, 671–676, 2013

25. Saha, B. & Yetter W. On magnetic properties and domain structure of strontium ferrite particles, *J. Appl. Phys.* **73** (10), 6260-6262, 1993.

26. Ku, H. S., et al., Microwave processing and permittivity measurement of thermoplastic composites at elevated temperature, *J Mater. Process Tech.* **89-90**, 419-424, 1999.

CHAPTER IV

DESIGN, FABRICATION AND ABSORPTION STUDIES OF SINGLE LAYER MAGNETIC MICROWAVE ABSORBER WITH THICKNESS OPTIMIZATION OVER THE X-BAND

4.1 INTRODUCTION

Absorption shields for electromagnetic (em) waves essentially require two conditions- firstly, low reflection at the air-absorber interface for maximum entry of the incident em wave and secondly, sufficient attenuation of the incident signal within the absorber matrix [1].

Practical absorber should have impedance matching with air at the interface, to fulfill the first requirement. Hence, from the transmission line theory, discussed in chapter I, section 1.3, for a single layer absorber backed by a perfect electric conductor (PEC) (figure 4.1), input impedance, Z_{in} is given [2-5] as

$$Z_{in} = \eta_0\sqrt{\mu_r / \varepsilon_r}\, tanh\,(j2\pi f/c)\sqrt{\mu_r\varepsilon_r}d \tag{4.1}$$

where, $\eta_0 = 377\ \Omega$ (4.2)

$$\gamma = j(2\pi f / c)\sqrt{\mu_r\varepsilon_r} \tag{4.3}$$

$$\mu_r = \mu'_r - j\mu''_r \tag{4.4}$$

$$\varepsilon_r = \varepsilon'_r - j\,\varepsilon''_r \tag{4.5}$$

Realization of impedance matching condition between the absorbing material and the free space interface can be achieved, if the ratio of μ_r'/ε_r' should approach to unity [1].

The reflection loss (dB) of the single layer absorber is found from the expression

$$RL_c = 20\log\left|\frac{Z_{in}-\eta_0}{Z_{in}+\eta_0}\right| \tag{4.6}$$

or

$$RL_c = 20\log\left|\frac{\sqrt{\mu_r/\varepsilon_r}\, tanh\,(j2\pi f/c)\sqrt{\mu_r\varepsilon_r}d-1}{\sqrt{\mu_r/\varepsilon_r}\, tanh\,(j2\pi f/c)\sqrt{\mu_r\varepsilon_r}d+1}\right| \tag{4.7}$$

Equation (4.7) shows that calculated reflection loss value, RL_c can be determined from the complex permittivity, permeability, frequency of operation and thickness of the composite material.

The second condition can be realized by using lossy material to achieve high attenuation [6-8] of em wave. Within the absorber, microwave energy decays

exponentially with distance x, as $e^{-\alpha x}$, and the attenuation factor, α, is given by the analytical equation,

$$\alpha = \frac{\sqrt{2}\pi f}{c}\sqrt{(\mu_r''\varepsilon_r'' - \mu_r'\varepsilon_r') + \sqrt{(\mu_r''\varepsilon_r'' - \mu_r'\varepsilon_r')^2 + (\varepsilon_r'\mu_r'' + \varepsilon_r''\mu_r')^2}} \quad (4.8)$$

where, f is the frequency of operation and c is the velocity of light.

Large attenuation in a smaller thickness can be obtained with large α, which implies that ε_r'' and μ_r'' must be large. Paradoxically, a large impedance mismatch at the air-absorber interface is observed for high lossy material [9].

Further, reduction in power of incident wave can be carried out by applying condition of destructive interference i.e. the path traversed by the wave is integral multiple of $\lambda/2$. Hence, minimum thickness of the absorber for destructive interference is $d=\lambda/4$ (refer to the figure 4.1).

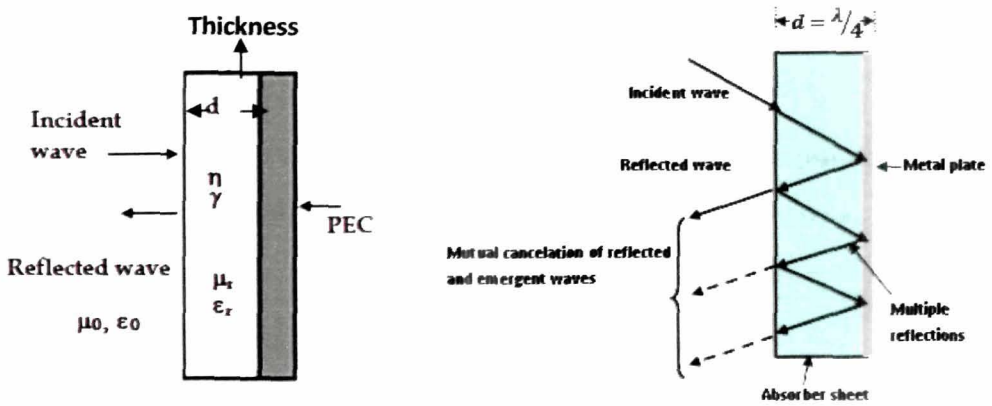

Figure 4.1 Design structure of conductor backed single layer absorber

In this chapter single layer Dallenbech structure is designed using transmission line model for all the ferrite-NPR nanocomposite systems. Reflection loss, complex input impedance and attenuation is calculated using the measured values of complex permittivity and permeability, studied in chapter III. Prior to fabrications the absorbers are optimized with thickness and absorption performance. Reflection loss measurements are carried out using free space measurement technique developed in-house, which is discussed in the section which follows.

4.2 FREE SPACE REFLECTION LOSS MEASUREMENT USING FOCUSING LENSES

The microwave power incident on the absorber sample is partly reflected from the interface surface and partly absorbed [10, 11] as shown in figure 4.2. Thus

$$P_{in} = P_R + P_A \tag{4.9}$$

where, P_{in} is the incident power density on the sample, P_R is the reflected power density and P_A is the absorbed power by the test sample.

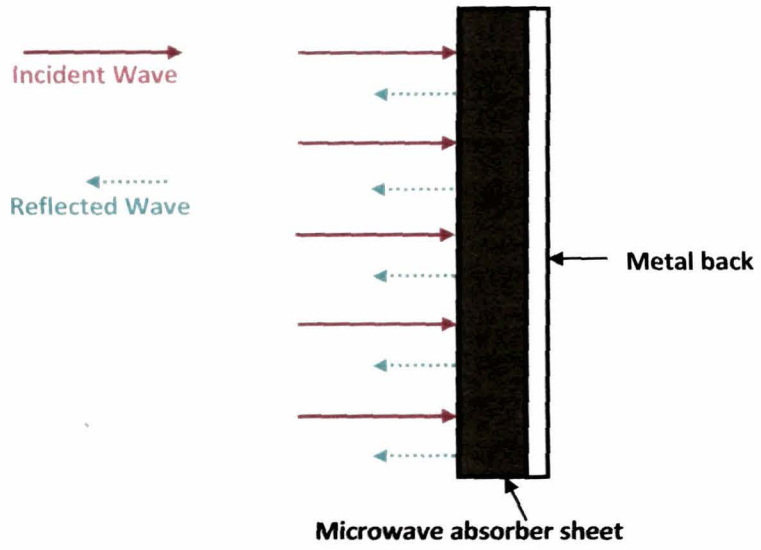

Figure 4.2 Schematic representation of microwave absorption measurement

If RL_m and A, are the measured reflection loss and the absorption loss in decibels (dB), respectively, then

$$RL_m = 10 \log P_R/P_{in} \tag{4.10}$$

$$A = 10 \log P_A/P_{in} \tag{4.11}$$

Thus, larger the absolute value of RL_m, higher the microwave absorption efficiency.

Free space technique is generally applied for broadband transmission/reflection absorption measurements [12]. The set-up requires large open space with no objects in vicinity to reflect em wave and also samples of fairly large dimensions. In laboratory, absorption measurements can be carried out using anechoic chambers [13]. Alternately, free space measurement system can be developed using horn antennas with spot focusing lens as described in schematic, as shown in figure 4.3. The arrangement can be confined to smaller space in laboratory with smaller sample dimensions.

A pair of spot focusing horn lens antenna focuses the microwave radiation to a single spot at the focal point of the lens, so a sample situated at the focal point of the spot focusing lens is sufficient to carry out the microwave absorption testing. In addition, the use of lens also reduces the edge effect from the samples during the measurement. A plano-convex lens is designed based on the application of phase equivalence to a generally curved aperture connected to a planar surface. Polyethylene with refractive index ($n = 1.5$ or $\varepsilon' = 2.25$) is used to make the lens with a focal length and diameter (f_L), kept at 30.5 cm. The schematic diagram of free space absorption measurement using spot focusing horn lens is shown in figure 4.3. The photograph of free space microwave measurement set up is shown in figure 4.4. The required dimension of the absorber sheet for this measurement set up for free space studies is, 152 mm x 152 mm x 2 mm. The set up consist of two spot focusing horn lens antennas connected to Agilent E8362C vector network analyzer using extendable cables and a sample holder between the lens to hold the absorber.

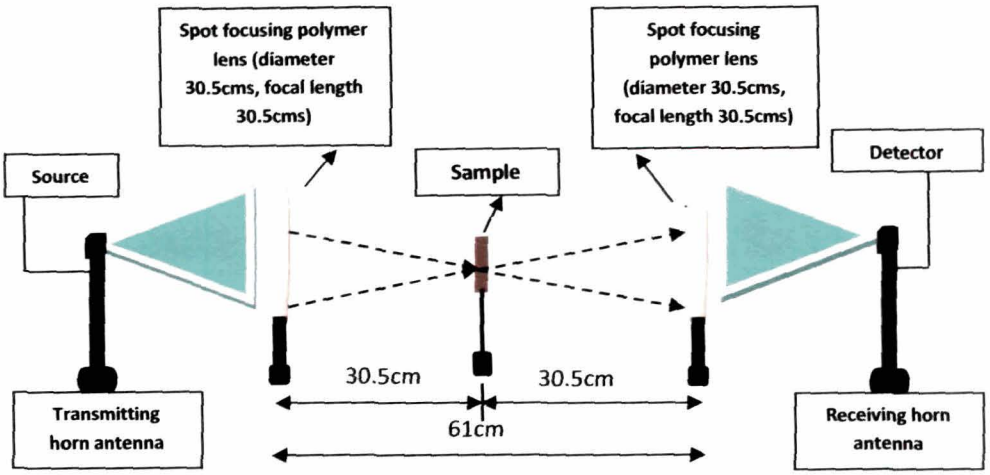

Figure 4.3 Schematic diagram of free space microwave absorption measurement using spot focusing horn lens antenna

Figure 4.4 Free space microwave absorption measurement setup of single layer ferrite-NPR composites over the X-band

The conductor backed ferrite-NPR sample is placed at the focal point of the lens system at a height of 15.25 cm from the base. The system is calibrated using thru-reflect-line (TRL) method [14, 15]. The reflection loss of the designed absorbers is measured using the expression (4.10).

4.3 DESIGN AND FABRICATION OF THE ABSORBER

The single layer Dallenbach absorber is designed based on transmission line theory [2-5]. A MATLAB program is developed using equations 4.1 - 4.7, to estimate the RL_c value of all the ferrite-NPR composites over the X-band. Design

optimization is carried out with minimum RL_C, least thickness and maximum -20 dB bandwidth of absorption. Algorithm of the program is given below,

Step 1: Read data from file.

Step 2: For each frequency from 8.2 GHz to 12.4 GHz at the step size of 0.02 GHz, calculate RL_c for each frequency for a fixed thickness. Store data and calculate RL_c for the other frequencies of the same thickness.

Step 3: Repeat step 2 for other thickness and store the data.

The flowchart of the program is given in figure 4.5.

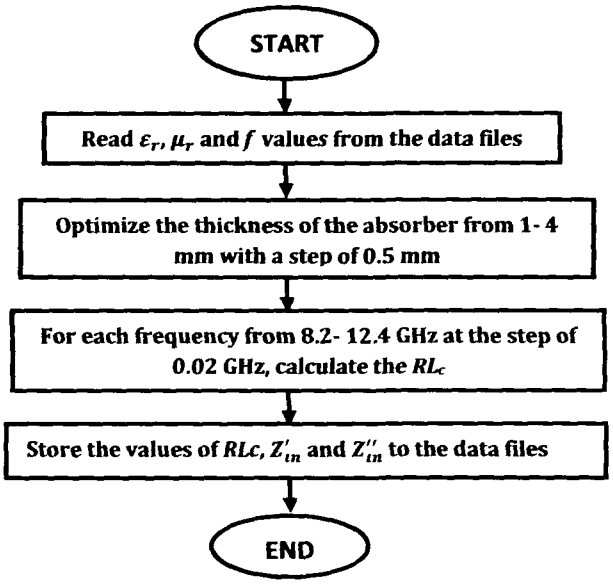

Figure 4.5 Flow chart of single layer absorber program

Based on the theoretical results, a practical conductor backed single layer microwave absorber with dimension of 152 mm x 152 mm and thickness d mm is fabricated using the ferrite nanoparticles in NPR matrix. The ferrite-polymer mixture is placed in a three-piece die-mould consisting of a cavity, upper and lower plunger with spacer (figure 4.6a). The fixture with the sample is initially heated up to 95–100 °C. A pressure up to 1.5-2 tons is slowly applied and then

after the system is isothermally heated at 150 °C for 2 hours and allowed to cool at room temperature. Prepared samples are shown in figure 4.6b.

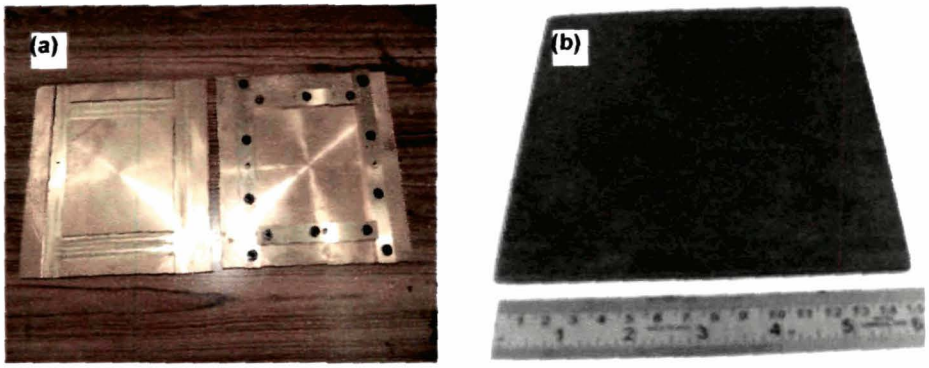

Figure 4.6 (a) Three-piece die-mould and (b) prepared samples, for free space measurement

The thickness of the nanocomposite is varied within 1 mm to 4 mm in steps of 0.5 mm using spacers. The step limit of 0.5 mm is kept taking into account that while fabrication, samples less than this breaks and become brittle.

The theoretical limit of total thickness for a broadband response for multilayer magnetic absorber structure [16] is given by inequality

$$\left|\int_0^\infty \ln|R(\lambda)|d\lambda\right| \leq 2\pi^2 \sum_i \mu_{si} d_i \qquad (4.12)$$

where, R is the reflection coefficient, λ is the wavelength and the μ_{si} is the static permeability and d_i is the thickness of the i^{th} layer. Equation 4.12 can be modified for single layer, i.e. $i=1$, as

$$\left|\int_0^\infty \ln|R(\lambda)|d\lambda\right| \leq 2\pi^2 \mu d \qquad (4.13)$$

As reflection, $RL_c=20log(R)$, the above equation reduces to

$$\int 2.303\, RL_c(\lambda)\, d\lambda \,/\, 40\pi^2 \leq \mu d \qquad (4.14)$$

For frequency range 8.2-12.4 GHz, the wavelength difference $d\lambda$=12.39 mm. For absorption level of -30 dB in the X-band, the minimum thickness of the absorber from equation (4.14) ranges from 0.5 mm, for μ=4.4 to 1.03 mm, for μ=2.1. The μ values are the practical maximum and minimum values observed for the ferrite – NPR nanocomposite system (refer to Chapter III, section 3.3.2). The minimum thickness of the ferrite composite is kept as 1 mm, taking into account the limit

that the sample breaks easily and difficult to handle. Strategic defense, applications require thickness of absorber not to exceed 4 mm [17], hence the maximum thickness is limited to 4 mm. The detail derivation is given in Appendix-A.

4.4 ABSORPTION STUDIES

Absorption studies are carried out over the X-band for all barium ferrite-NPR nanocomposite system and aluminium and strontium substituted barium ferrite-NPR nanocomposites. In absorption studies - calculated and measured reflection loss, real and imaginary input impedance and attenuation constant, are determined for all the samples.

4.4.1 Absorption studies of $BaFe_{12}O_{19}$-NPR nanocomposites

Absorption studies is carried out for $BaFe_{12}O_{19}$-NPR nanocomposites with 30 wt.%, 40 wt.% and 50 wt.% of $BaFe_{12}O_{19}$ in NPR matrix.

Calculated reflection loss and complex input impedance

The calculated reflection loss (RL_c) spectra, real and imaginary input impedance, determined using equation 4.1 to 4.7, for 30 wt. %, 40 wt. % and 50 wt. % $BaFe_{12}O_{19}$-NPR nanocomposites are shown in figures 4.7(a-c), 4.8(a-c) and 4.9(a-c), respectively.

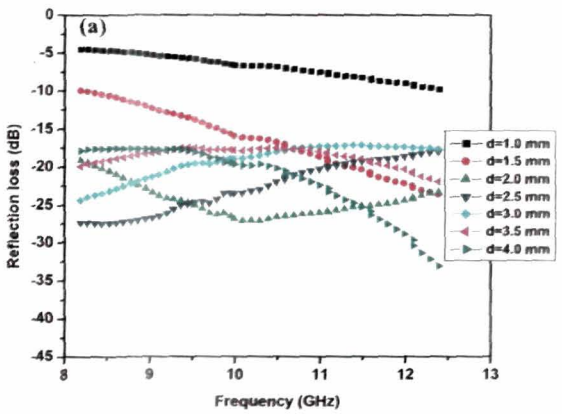

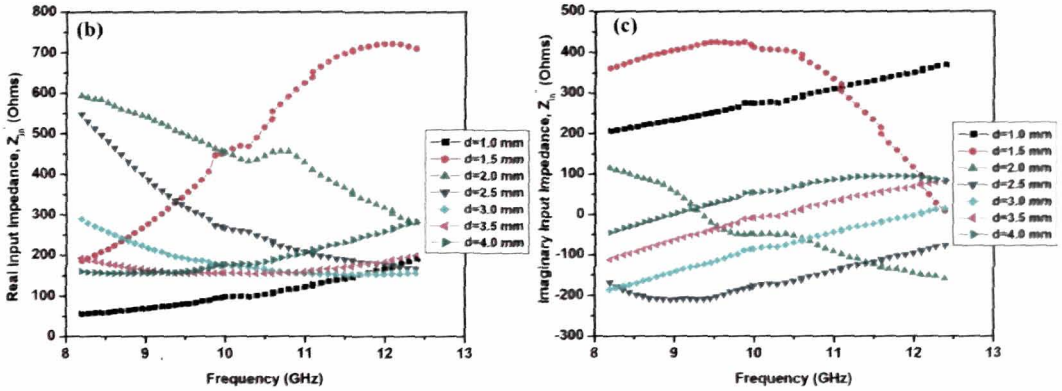

Figure 4.7 Calculated (a) reflection loss (b) real input impedance and (c) imaginary input impedance of 30 wt.% $BaFe_{12}O_{19}$-NPR nanocomposite with thickness from 1 mm to 4 mm

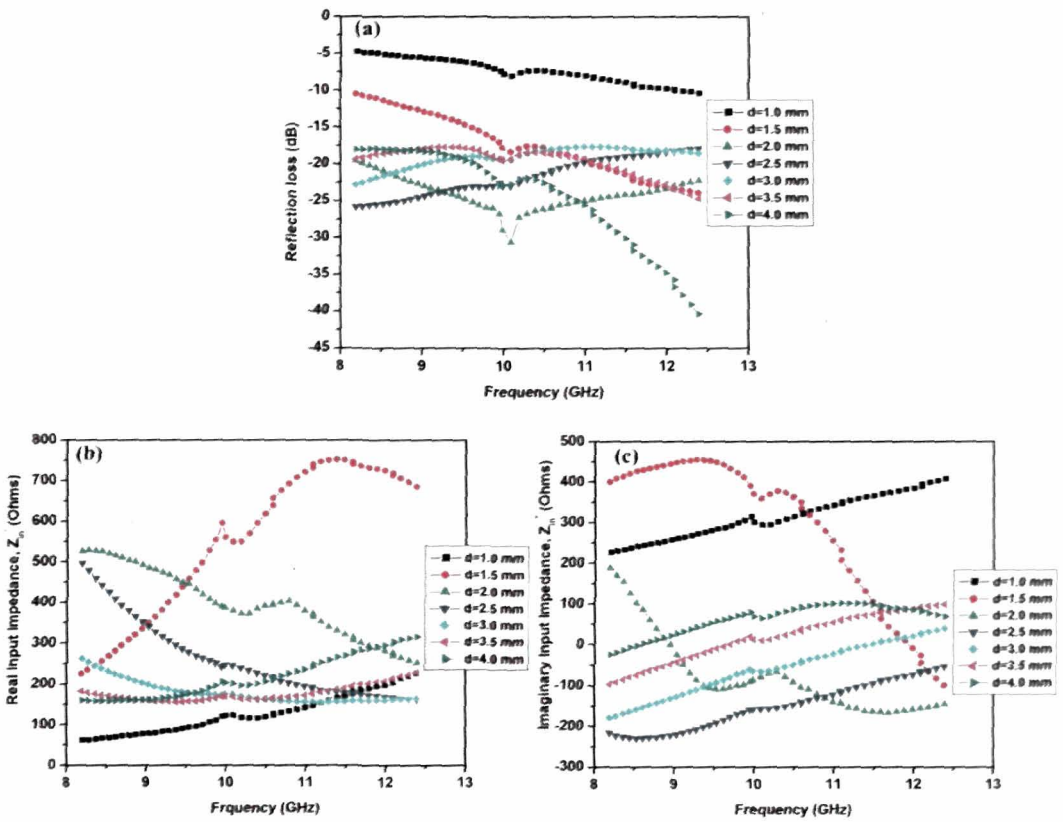

Figure 4.8 Calculated (a) reflection loss (b) real input impedance and (c) imaginary input impedance of 40 wt.% $BaFe_{12}O_{19}$-NPR nanocomposite with thickness from 1 mm to 4 mm

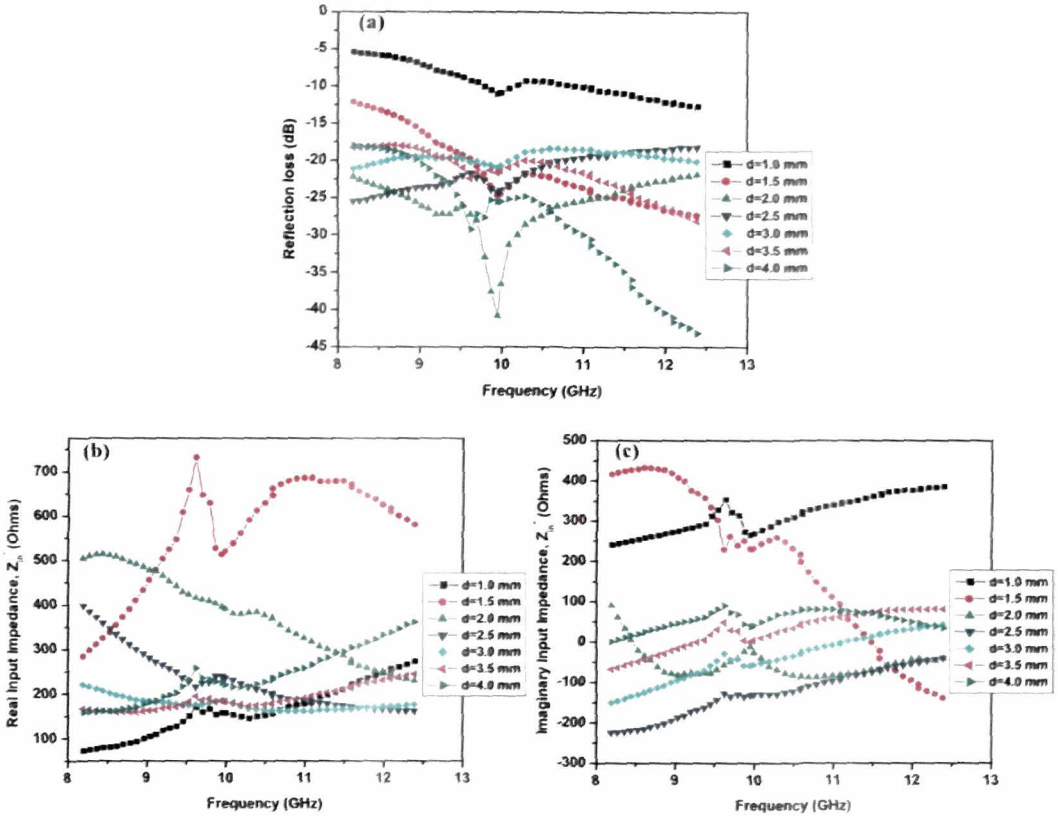

Figure 4.9 Calculated (a) reflection loss (b) real input impedance and (c) imaginary input impedance of 50 wt.% $BaFe_{12}O_{19}$-NPR nanocomposite with thickness from 1 mm to 4 mm

It is seen from the RL_c spectra, that all the compositions with thickness 1 mm has an absorption peak <-15 dB. The real (Z_{in}') and imaginary (Z_{in}'') input impedance for 1 mm thickness composites, at the absorption peak frequency, as seen from figures 4.7(b-c), 4.8(b-c) and 4.9(b-c), do not match with the free space real and imaginary impedance of 377 Ω and 0 Ω, respectively. Thicknesses greater than 1 mm upto 3 mm show a shift of the absorption peak towards the lower frequency side, while 3.5 to 4 mm thickness, the shift is towards higher frequency side and Z_{in}' and Z_{in}'' approaches the desired values of 377 Ω and 0 Ω at these frequencies.

The calculated reflection loss, -20 dB bandwidth and real and imaginary input impedance values with varying thickness of the composite is tabulated in table 4.1.

Table 4.1 Reflection loss of 30 wt. %, 40 wt. % and 50 wt. % $BaFe_{12}O_{19}$-NPR nanocomposite with varying thickness

$BaFe_{12}O_{19}$-NPR	*d* (mm)	RL_c (dB)	f_r (GHz)	-20dB BW	Z_{in}' (Ω)	Zin'' (Ω)
30 wt.%	1.0	-9.72	12.40	-	189.85	369.17
	1.5	-23.73	12.40	1.00	714.16	9.60
	2.0	-27.15	10.18	4.04	431.71	-49.82
	2.5	-27.36	8.20	2.80	549.93	166.38
	3.0	-24.38	8.20	1.16	290.09	-187.31
	3.5	-21.87	12.40	0.60	198.30	81.98
	4.0	-33.03	12.40	1.91	284.01	84.38
40 wt.%	1.0	-10.37	12.40	-	227.98	409.36
	1.5	-23.85	12.40	1.30	686.86	-97.76
	2.0	-30.73	10.06	4.00	372.15	-81.81
	2.5	-25.71	8.20	2.70	501.22	-217.00
	3.0	-22.85	8.20	0.82	263.26	-177.04
	3.5	-24.73	12.40	1.30	229.54	101.41
	4.0	-40.39	12.40	2.75	316.31	69.96
50 wt.%	1.0	-12.56	12.40	-	273.79	385.77
	1.5	-27.25	12.40	2.80	582.02	-138.82
	2.0	-41.05	9.95	4.20	389.70	-11.93
	2.5	-25.71	8.20	2.50	399.73	-222.90
	3.0	-21.06	8.20	0.34	222.32	-151.05
	3.5	-28.24	12.40	3.00	244.95	83.95
	4.0	-43.4	12.40	3.30	360.74	29.12

RLc=Maximum calculated reflection loss, *d*=thickness of the absorber,
f_r=frequency of maximum absorption, BW=bandwidth,
Z_{in}'=real input impedance and Zin''=imaginary input impedance

The $BaFe_{12}O_{19}$-NPR composites with 2 mm and 4 mm thickness show RL_c > -27 dB, for all the compositions. For these thicknesses, the Z_{in}' and Z_{in}'' show the closest value to the free space value, as seen from table 4.1. Samples with d=2 mm, shows a -20 dB reflection loss bandwidth > 4 GHz, almost covering the whole of X-band. Therefore, 2 mm thickness is selected as the optimized thickness for fabrication of the $BaFe_{12}O_{19}$-NPR nanocomposites and free space reflection loss study is carried out.

Measured reflection loss

Figure 4.10a shows the measured reflection loss (dB) spectra for 2 mm thickness 30 wt.%, 40 wt.% and 50 wt.% $BaFe_{12}O_{19}$-NPR nanocomposite. Measured reflection loss (RL_m) of -24.61 dB is observed at 10.26 GHz for 30 wt. % composite. 40 wt. % and 50 wt. % shows RL_m of -28.39 dB at 9.98 GHz and -37.06 dB at 9.5 GHz, respectively.

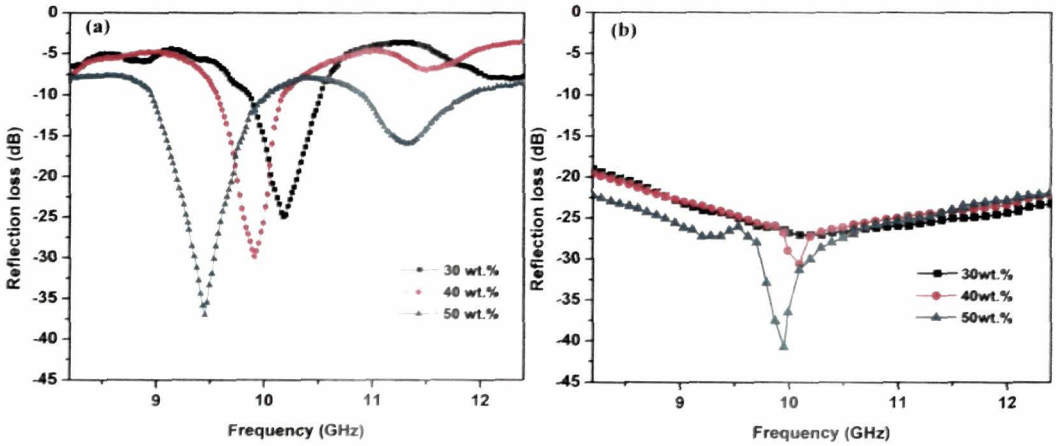

Figure 4.10 Reflection loss parameter of $BaFe_{12}O_{19}$-NPR composite with 30 wt. %, 40 wt. % and 50 wt. % of $BaFe_{12}O_{19}$ in NPR, (a) measured and (b) calculated

Increase in ferrite concentration increases the scattering centres, subsequently reducing the em wave reflected from the composite system, hence increase in absorption (figure 4.11a and 4.11b) is observed for 50 wt.% of $BaFe_{12}O_{19}$-NPR nanocomposite.

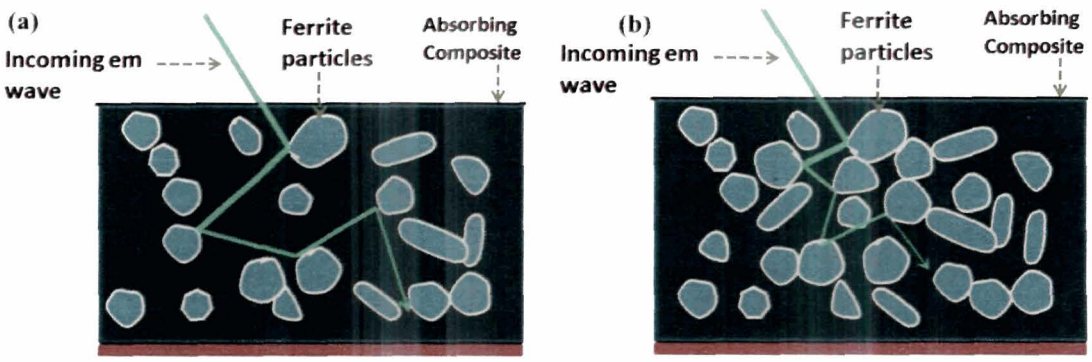

Figure 4.11 Scattering mechanism of em wave within a composite material with (a) lower wt.% and (b)higher wt.% of inclusions

The measured -20 dB bandwidth for 30 wt. % is 0.36 GHz, for 40 wt. % is 0.48 GHz and for 50 wt. % is 0.60 GHz. 50 wt % $BaFe_{12}O_{19}$-NPR composite shows a dual -10 dB bandwidth (i.e., over 90% microwave absorption) of 1.04 GHz and 1.01 GHz. RL_c spectra for d=2 mm for all the three compositions is given in figure 4.10b. The measured and calculated reflection loss shows close proximity in absorption peak and frequency, but -20 dB bandwidth in measured spectra is less than the calculated.

Attenuation constant

The attenuation constant (α) of the developed $BaFe_{12}O_{19}$-NPR nanocomposites is calculated in the frequency range 8.2-12.4 GHz from ε_r and μ_r values of the composites using equation 4.8.

The variation of attenuation constant with frequency of $BaFe_{12}O_{19}$-NPR nanocomposites with 30 wt.%, 40 wt.% and 50 wt.% of $BaFe_{12}O_{19}$ in the NPR matrix is shown in figure 4.12. Increase in the number of ferrite particles in the composite increases the dielectric and magnetic losses resulting in increase of attenuation constant. 50 wt. % of $BaFe_{12}O_{19}$-NPR nanocomposite shows maximum attenuation ranging from 15.5dB/cm to 24.5dB/cm over the frequency range 8.2 to 12.4 GHz. The attenuation spectra follow the resonant behaviour of complex permeability of the ferrite.

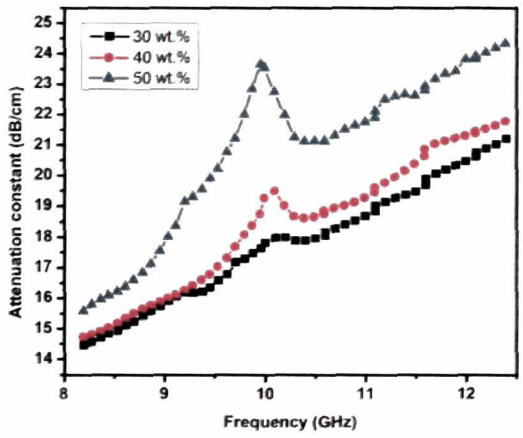

Figure 4.12 Attenuation constant spectra of $BaFe_{12}O_{19}$-NPR nanocomposites with 30 wt.%, 40 wt.% and 50 wt.%

Analysis

The $BaFe_{12}O_{19}$-NPR nanocomposites with 50 wt.% shows maximum reflection loss for 2 mm thickness. Attenuation constant increases with increase in the barium inclusions in the composite and it is maximum for 50 wt.% of the $BaFe_{12}O_{19}$-NPR nanocomposites. Therefore, for all the substituted barium ferrite compositions, investigated hereafter, 50 wt.% composition is selected.

4.4.2 Absorption studies of $BaAl_xFe_{12-x}O_{19}$-NPR nanocomposites

Transmission line theory is used to design 50 wt.% of $BaAl_xFe_{12-x}O_{19}$-NPR composites as single layer absorber with x=1.0, 1.2, 1.4 and 1.6. Thickness optimization is carried out using the MATLAB program discussed in section 4.3. Composite with best performance and least thicknesses are fabricated into sheets for reflection loss measurement (section 4.3).

Calculated reflection loss and complex input impedance

The input impedance and reflection loss of the designed single layer absorber is optimized with thickness for all the stoichiometric composition of 50wt.% $BaAl_xFe_{12-x}O_{19}$-NPR nanocomposites. The thickness of the absorber sample is varied from 1 mm-4 mm in step of 0.5 mm. All the four $BaAl_xFe_{12-x}O_{19}$-NPR composites for d >1 mm, show -10 dB reflection loss bandwidth over the X-band, as seen from the RL_c spectra figures 4.13a, 4.14a, 4.15a and 4.16a. Sample with thickness 2 mm shows absorption > -20 dB, over the X-band for all the compositions.

The real part of input impedance, Z_{in}', is plotted in figures 4.13b, 4.14b, 4.15b, 4.16b and imaginary part, Z_{in}', in figures 4.13c, 4.14c, 4.15c, 4.16c. The calculated reflection loss (RL_c) with -20 dB bandwidth, real and imaginary input impedance for all the compositions with varying thickness is given in table 4.2.

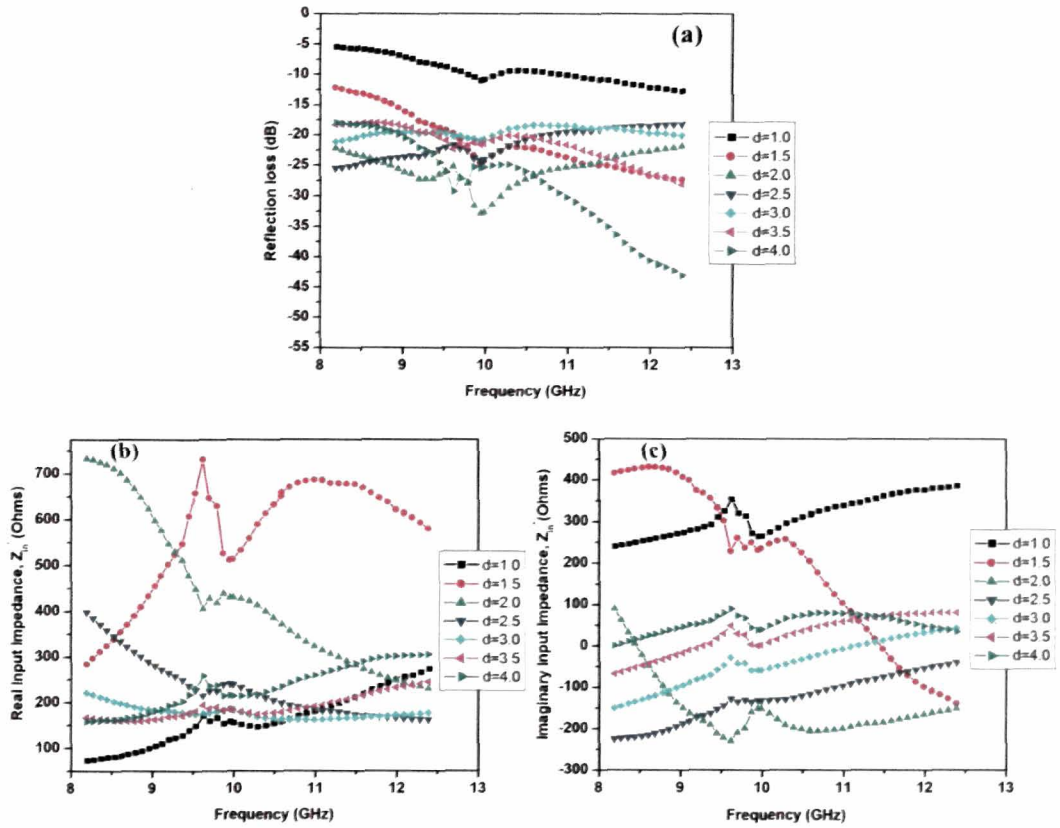

Figure 4.13 Calculated (a) reflection loss, (b) real input impedance and (c) imaginary input impedance of $BaAl_xFe_{12-x}O_{19}$ – NPR nanocomposite for x = 1.0 with thickness from 1 mm to 4 mm

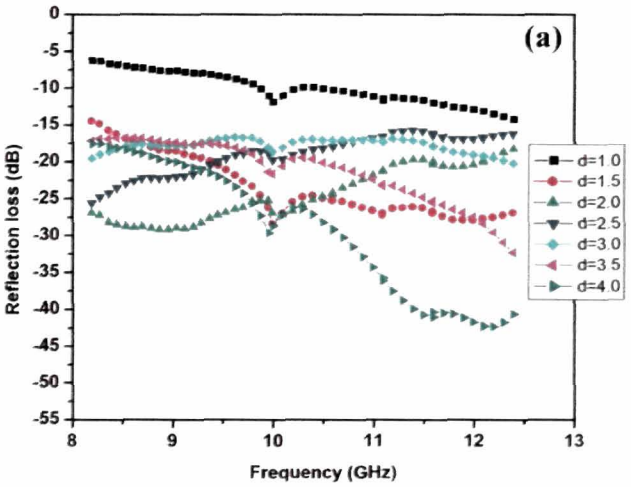

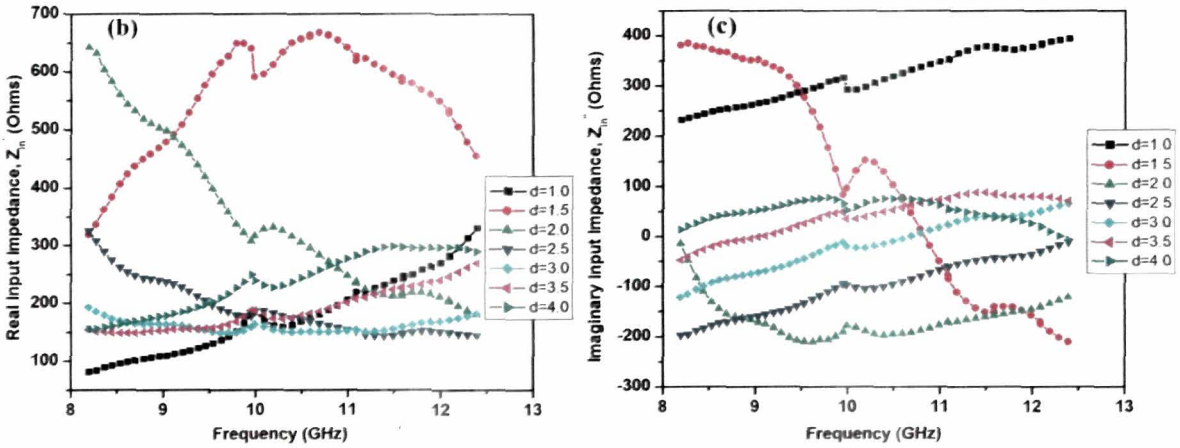

Figure 4.14 Calculated (a) reflection loss, (b) real input impedance and (c) imaginary input impedance of $BaAl_xFe_{12-x}O_{19}$–NPR nanocomposite for x = 1.2 with thickness from 1 mm to 4 mm

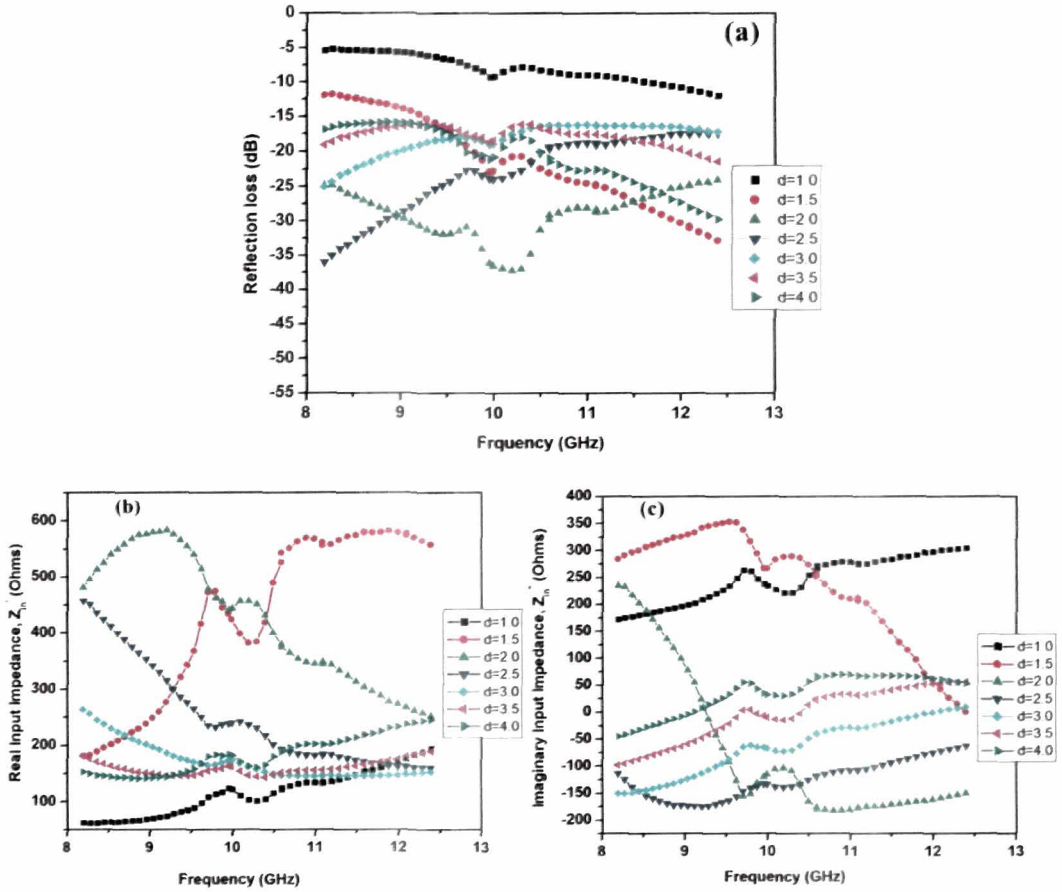

Figure 4.15 Calculated (a) reflection loss, (b) real input impedance and (c) imaginary input impedance of $BaAl_xFe_{12-x}O_{19}$–NPR nanocomposite for x = 1.4 with thickness from 1 mm to 4 mm

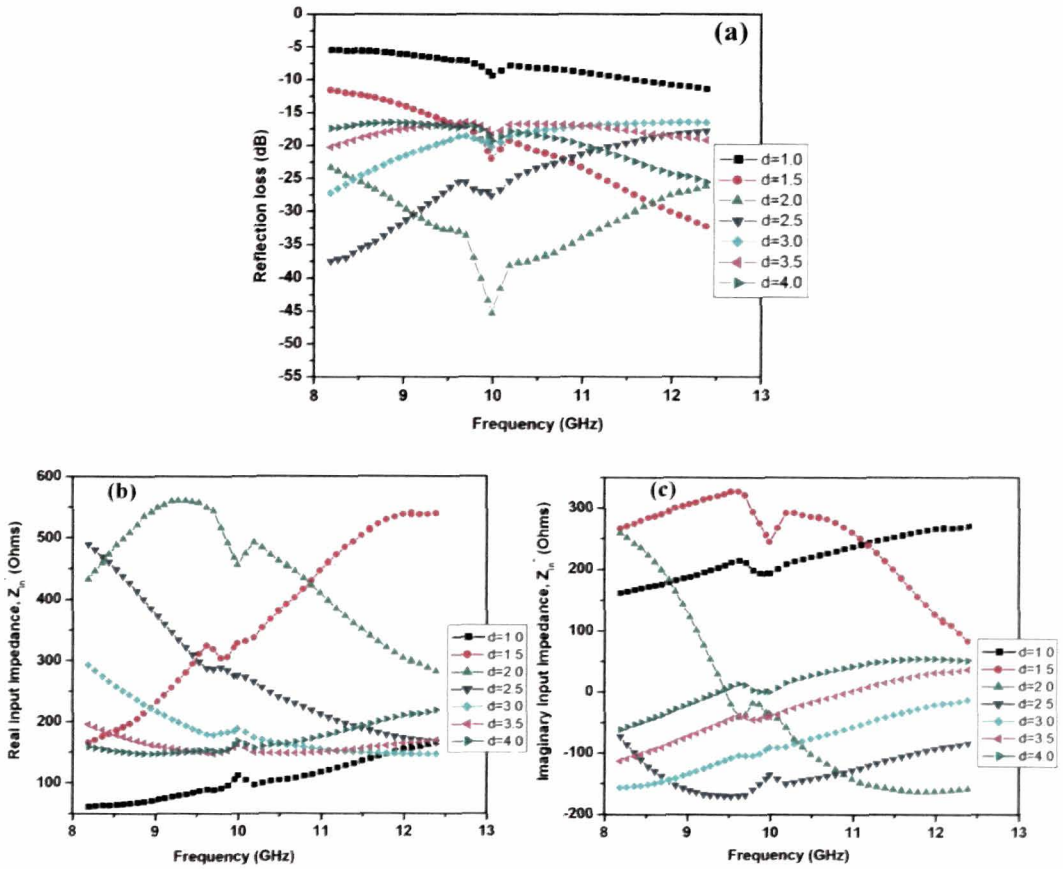

Figure 4.16 Calculated (a) reflection loss, (b) real input impedance and (c) imaginary input impedance of $BaAl_xFe_{12-x}O_{19}$–NPR nanocomposite for x = 1.6 with thickness from 1 mm to 4 mm

Table 4.2 Reflection loss and input impedance of $BaAl_xFe_{12-x}O_{19}$-NPR nanocomposite (x=1.0, 1.2, 1.4 and 1.6) with varying thickness

$BaAl_xFe_{12-x}O_{19}$-NPR	*d* (mm)	$RL_{c\,max}$ (dB)	f_r (GHz)	-20dB band width	Z_{in}' (Ω)	Zin'' (Ω)
x=1.0	1.0	-10.94	9.95	-	160.64	266.09
	1.5	-27.66	12.40	2.8	582.02	-138.82
	2.0	-32.85	9.96	4.0	416.48	-137.00
	2.5	-25.13	9.99	1.4	241.78	-128.33
	3.0	-21.35	9.95	1,1	187.16	-57.57
	3.5	-28.51	12.4	2.9	245.55	83.94
	4.0	-43.53	12.4	3.4	307.30	35.84
x=1.2	1.0	-14.1	12.4	-	333.06	396.96
	1.5	-28.25	10.00	3.0	592.95	97.01
	2.0	-28.25	10.04	3.9	295.49	-144.18
	2.5	-27.67	10.04	1.2	189.79	-96.06
	3.0	-19.9	12.40	0.2	182.58	65.47
	3.5	-32.64	12.40	2.2	267.76	73.46
	4.0	-42.85	12.12	3.3	298.99	21.46
x=1.4	1.0	-11.8	12.4	-	194.30	303.93
	1.5	-32.64	12.4	2.6	560.72	0.25
	2.0	-37.07	10.21	4.0	390.84	-112.60
	2.5	-35.99	10.00	2.33	241.15	-132.00
	3.0	-24.98	9.95	0.7	171.54	-65.46
	3.5	-21.62	12.40	0.4	189.89	58.06
	4.0	-29.95	12.40	1.9	247.38	53.63
x=1.6	1.0	-11.56	12.4	-	167.42	270.87
	1.5	-32.24	12.4	2.5	539.63	85.43
	2.0	-45.41	10.0	4.0	451.43	-19.70
	2.5	-37.88	8.2	3.0	489.93	-73.12
	3.0	-26.86	8.2	-	293.69	-155.10
	3.5	-18.66	10.0	1.1	167.41	-39.48
	4.0	-25.39	9.99	1.5	169.37	-0.45

RLc=Maximum calculated reflection loss, *d*=thickness of the absorber,
f_r=frequency of maximum absorption, BW=bandwidth,
Z_{in}'=real input impedance and impedance Zin''=imaginary input

As seen from table, Z_{in}' and Z_{in}'', of the $BaAl_xFe_{12-x}O_{19}$ -NPR nanocomposites with 2 mm thicknesses is closer to the complex impedance of free space, thus reducing reflection at the air absorber interface. Hence, a broad -20 dB absorption bandwidth of ~ 4 GHz with absorption of ~- 30 dB is seen for 2 mm thickness for all the compositions. An increase in the absorption with increasing Al^{3+} ions in the $BaAl_xFe_{12-x}O_{19}$ compositions is observed. Maximum absorption of -41.42 dB with -20 dB bandwidth of 4 GHz is obtained for $BaAl_xFe_{12-x}O_{19}$–NPR composite with x=1.6 for 2 mm thickness among all the other combinations of thickness as well as compositions.

Measured reflection loss

Measured reflection loss, RL_m (dB) versus frequency for 2 mm thick $BaAl_xFe_{12-x}O_{19}$-NPR nanocomposites with x=1.0, 1.2, 1.4 and 1.6 in the range 8.2-12.4 GHz is shown in figure 4.17a. The spectra show that the composite with x=1.0 shows RL_m of -27.56 dB at 9.99 GHz. With increasing Al^{3+} ions in the ferrite composition, the absorption increases. Rl_m for x=1.2, 1.4 and 1.6 of $BaAl_xFe_{12-x}O_{19}$ - NPR nanocomposite are, -29.99 dB at 11.65 GHz, -32.28 dB at 9.54 GHz and -40.06 dB at 9.56 GHz, respectively. The maximum absorption is obtained for the reported samples with x=1.6 with -10 dB bandwidth of 4.0 GHz i.e. more than 90% of absorption of the incident wave, over the entire X-band and -20 dB bandwidth of 0.84 GHz. All the four samples show dual absorption band nature. $BaAl_xFe_{12-x}O_{19}$-NPR nanocomposite with x=1.2 shows the maximum absorption of - 29.99 dB at 11.65 GHz i.e. in the higher frequency side. Figure 4.17b shows the RL_c spectra for d=2 mm for the $BaAl_xFe_{12-x}O_{19}$-NPR nanocomposites with x=1.0, 1.2, 1.4 and 1.6.

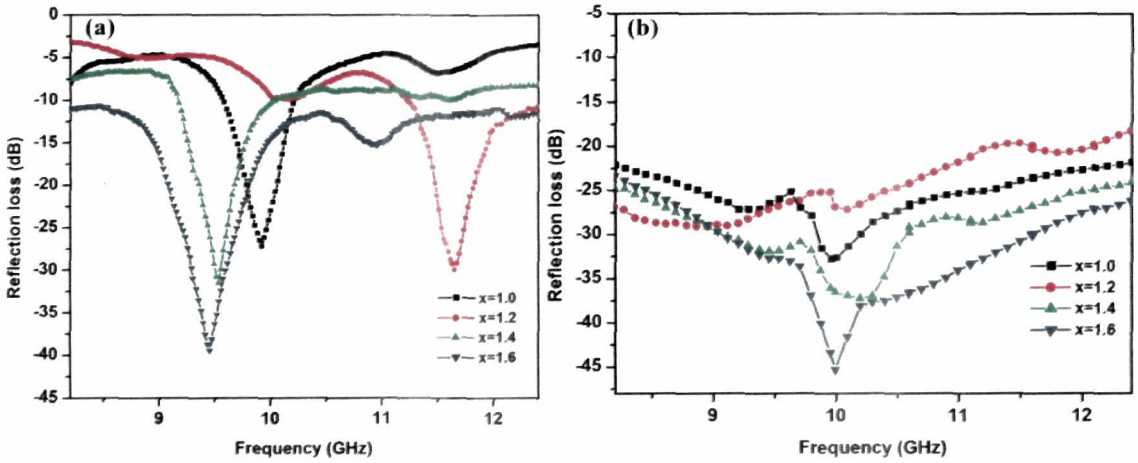

Figure 4.17 Reflection loss parameter of $BaAl_xFe_{12-x}O_{19}$–NPR (x = 1, 1.2, 1.4 and 1.6) nanocomposite with 2 mm thickness, (a) measured and (b) calculated

Attenuation constant

The variation of attenuation constant with frequency of $BaAl_xFe_{12-x}O_{19}$–NPR composites with x=1.0, 1.2, 1.4 and 1.6 is calculated using equation 4.8 and shown in figure 4.18. Increase in the Al^{3+} ions in the ferrite composition, $BaAl_xFe_{12-x}O_{19}$, shows an enhancement in dielectric and magnetic losses, (Chapter III, Section 3.4.1) which results in increase in the attenuation. Increase in attenuation constant with frequency in the X-band is observed for all the composites. The attenuation peak is obtained for the $BaAl_xFe_{12-x}O_{19}$-NPR composite with x=1.6 is 23.89 dB/cm at 10.99 GHz, 22.46 dB/cm at 10.99 GHz and 21.51 dB/cm at 9.47 GHz. $BaAl_xFe_{12-x}O_{19}$-NPR composite with x=1.2 shows attenuation peaks of 21.82 dB/cm and 24.69 dB/cm at 10.03 GHz and 11.65 GHz, respectively. For x=1.0 and 1.4, the maximum attenuation constant is 20.33 dB/cm at 11.05 GHz and 22.32 dB/cm at 11.60 GHz, respectively.

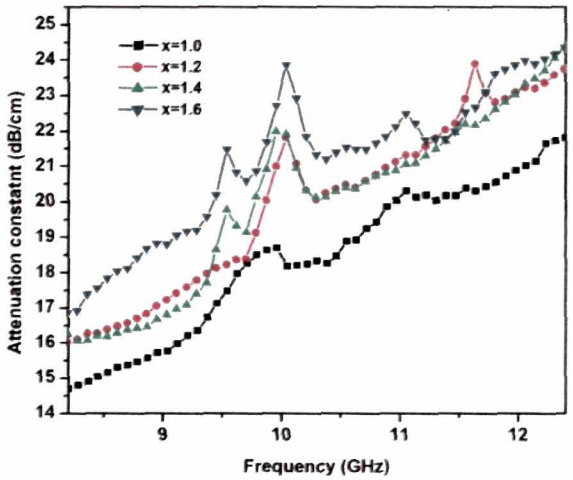

Figure 4.18 Attenuation constant spectra of $BaAl_xFe_{12-x}O_{19}$–NPR (x = 1, 1.2, 1.4 and 1.6)

Analysis

A slight frequency shift is observed in all the compositions for calculated and measured results. Attenuation constant and impedances justify the maximum absorption of the $BaAl_xFe_{12-x}O_{19}$–NPR composites. The lower absorption peak of $BaAl_{1.6}Fe_{10.4}O_{19}$–NPR composite could be due to mismatch in the matching thickness, d_m, of the absorber. For x=1.2 composition an absorption peak of -29.96 dB is observed at 11.65 GHz (Figure 4.17a), this can be due to large attenuation peak of 24.69 dB/cm at the same frequency and corresponding calculated reflection loss notch of -20.58 dB at the same frequency. While the lower absorption peak for x=1.2, of -10.24 dB (~90% absorption) is observed at 10.01 GHz corresponding to the calculated absorption peak of -27.25 dB and attenuation of 21.82 dB/cm at 10.00 GHz.

4.4.3 Absorption Studies of $Ba_{1-x}Sr_xFe_{12}O_{19}$-NPR nanocomposites

Theoretical and measured absorption studies are carried out on single layer 50 wt.% $Ba_{1-x}Sr_xFe_{12}O_{19}$-NPR nanocomposites with x=0.2, 0.4, 0.6 and 1.0.

Calculated reflection loss and complex input impedance

The RL_c spectra for 50wt.% $Ba_{1-x}Sr_xFe_{12}O_{19}$-NPR nanocomposites with x=0.2, 0.4, 0.6 and 1.0 is shown in figure 4.19a, 4.20a, 4.21a and 4.22a, respectively. All the four strontium substituted $Ba_{1-x}Sr_xFe_{12}O_{19}$-NPR nanocomposites show -10 dB reflection loss bandwidth over the X-band with thickness, d >1.5 mm. The

complex input impedance of the composite for all the four compositions are calculated and shown in figure 4.19(b-c), 4.20(b-c), 4.21(b-c) and 4.22(b-c).

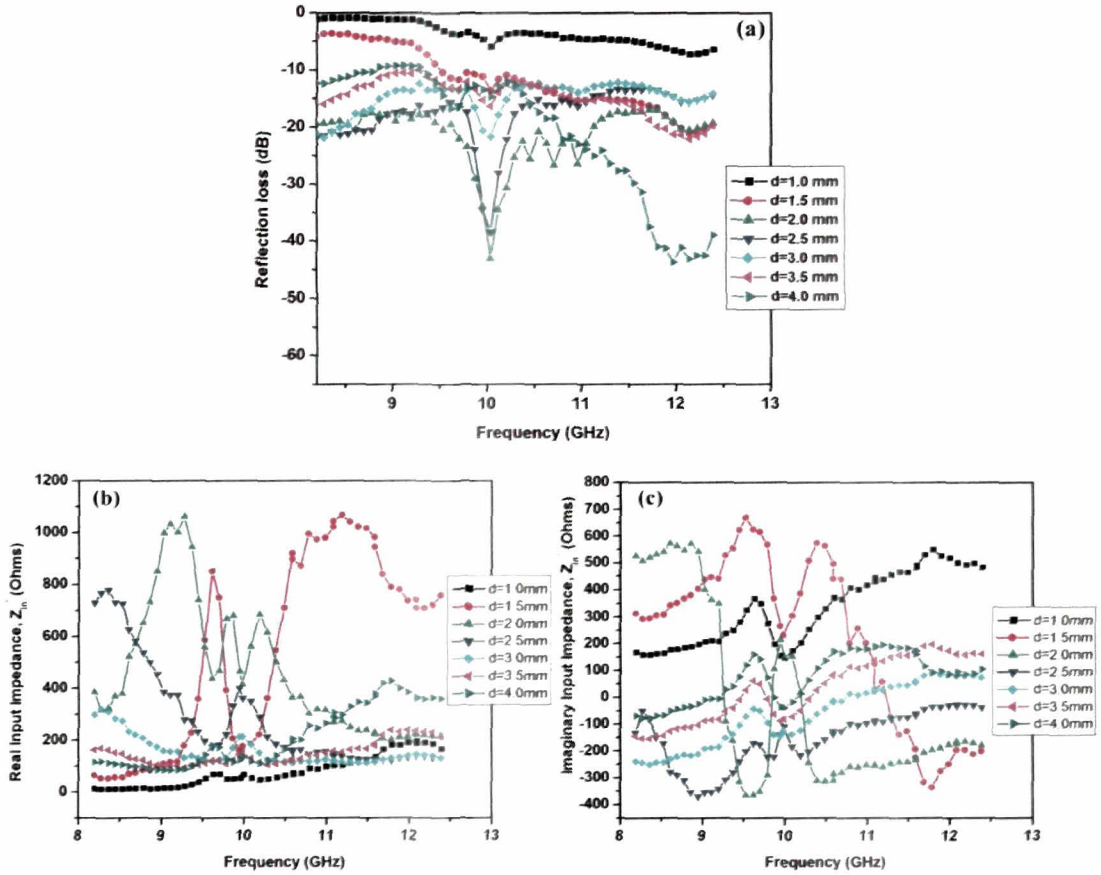

Figure 4.19 Calculated (a) reflection loss, (b) real input impedance, (c) imaginary input impedance of $Ba_{1-x}Sr_xFe_{12-x}O_{19}$ -NPR nanocomposite for x = 0.2 with thickness from 1 mm to 4 mm

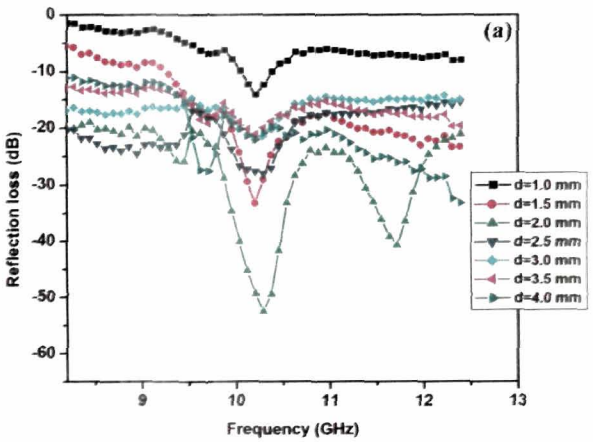

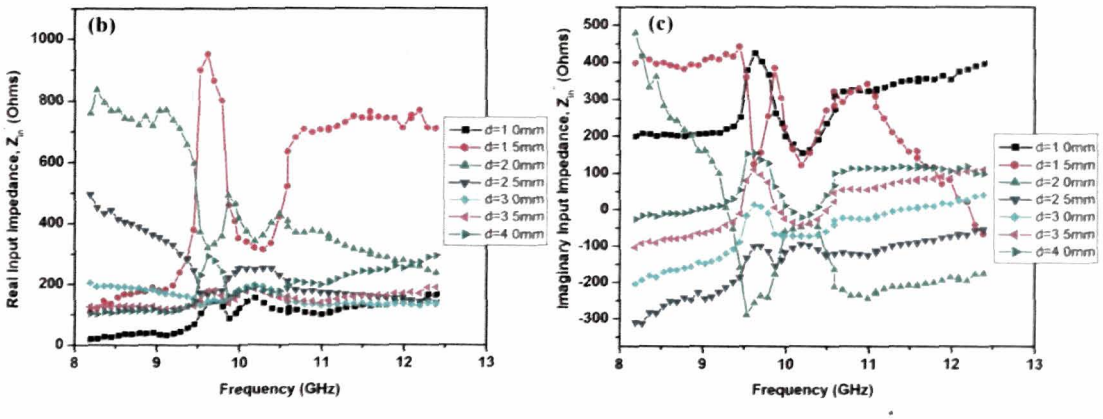

Figure 4.20 Calculated (a) reflection loss, (b) real input impedance, (c) imaginary input impedance of $Ba_{1-x}Sr_xFe_{12-x}O_{19}$-NPR nanocomposite for x = 0.4 with thickness from 1 mm to 4 mm

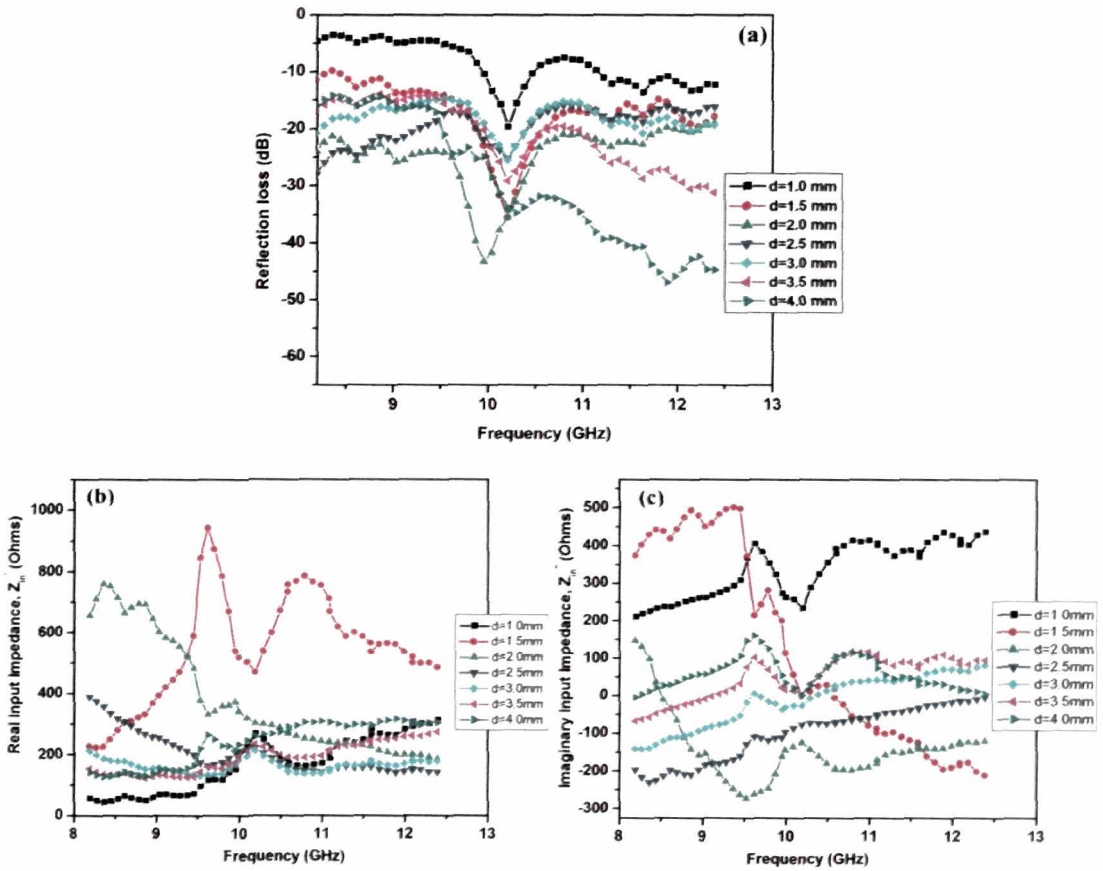

Figure 4.21 Calculated (a) reflection loss, (b) real input impedance, (c) imaginary input impedance of $Ba_{1-x}Sr_xFe_{12-x}O_{19}$-NPR nanocomposite for x = 0.6 with thickness from 1 mm to 4 mm

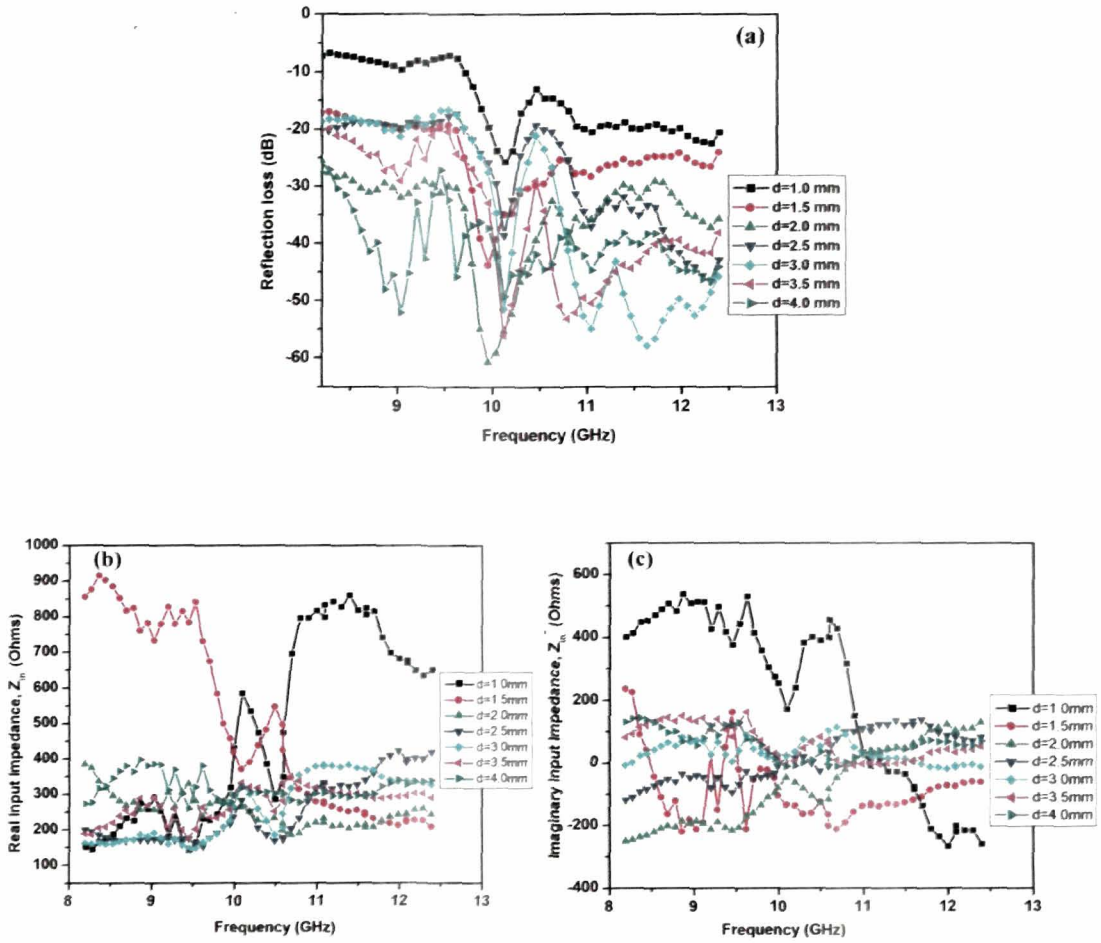

Figure 4.22 Calculated (a) reflection loss, (b) real input impedance, (c) imaginary input impedance of $Ba_{1-x}Sr_xFe_{12-x}O_{19}$-NPR nanocomposite for x = 1.0 with thickness from 1 mm to 4 mm

The details of maximum calculated reflection loss, -20 dB bandwidth and real and imaginary impedance of the $Ba_{1-x}Sr_xFe_{12}O_{19}$-NPR composites with varying thickness are given in table 4.3.

Table 4.3 Reflection loss of $Ba_{1-x}Sr_xFe_{12-x}O_{19}$ -NPR nanocomposite (x=0.2, 0.4, 0.6 and 1.0) with varying thickness

$Ba_{0.8}Sr_{0.2}Fe_{12}O_{19}$-NPR	*d* (mm)	RL_c (dB)	f_r (GHz)	-20dB BW	Z_{in}' (Ω)	Zin'' (Ω)
x=0.2	1.0	-6.13	10.04	-	68.22	160.49
	1.5	-21.32	12.16	0.3	708.10	-192.35
	2.0	-43.05	10.02	1.7	424.12	153.67
	2.5	-38.33	10.04	0.5	355.61	-139.12
	3.0	-21.64	10.05	0.4	198.82	-134.68
	3.5	-16.41	10.04	0.6	138.84	-72.57
	4.0	-44.28	11.98	1.6	381.59	118.18
x=0.4	1.0	-14.83	10.21	-	148.64	156.06
	1.5	-33.20	10.20	1.6	324.32	126.51
	2.0	-52.59	10.30	4.2	363.36	-34.34
	2.5	-27.70	10.22	2.0	254.05	-93.43
	3.0	-22.21	10.21	-	203.30	-70.45
	3.5	-21.37	10.21	-	183.78	-40.90
	4.0	-33.60	12.4	2.9	296.69	100.50
x=0.6	1.0	-19.68	10.21	-	270.87	240.84
	1.5	-35.58	10.21	0.8	473.87	1.28
	2.0	-43.53	9.96	4.2	376.27	-125.12
	2.5	-25.68	10.21	1.7	225.82	-75.56
	3.0	-25.68	10.21	0.45	214.11	-24.26
	3.5	-31.53	12.4	2.29	275.37	98.09
	4.0	-46.96	11.91	3.0	320.72	34.21
x=1.0	1.0	-26.19	10.13	0.3	566.88	198.19
	1.5	-43.91	9.97	2.8	442.39	-54.35
	2.0	-61.22	9.81	4.2	283.67	-124.12
	2.5	-47.31	12.32	2.7	405.05	70.27
	3.0	-57.99	11.64	2.7	371.33	0.65
	3.5	-56.41	10.14	4.2	324.39	27.32
	4.0	-52.55	9.04	4.2	385.08	58.55

RLc=Maximum calculated reflection loss, *d*=thickness of the absorber,
f_r=frequency of maximum absorption, BW=bandwidth,
Z_{in}'=real input impedance and Zin''=imaginary input impedance

From the table 4.3, it is observed that for composite with *d*= 2 mm and 4 mm, both Z_{in}' and Z_{in}'' approaches to the free space impedance, 377 Ω and 0 Ω at the

maximum absorption peak. The sample with d=2 mm shows better -20 dB bandwidth as compared to 4 mm thickness for all the compositions. Fabrication is carried out for all strontium substituted barium ferrite–NPR nanocomposite with thickness of 2 mm.

Measured reflection loss

The RL_m for 2 mm thick 50wt.% $Ba_{1-x}Sr_xFe_{12}O_{19}$-NPR nanocomposites with x= 0.2, 0.4, 0.6 and 1.0 are shown in figure 4.23a. $Ba_{1-x}Sr_xFe_{12}O_{19}$-NPR nanocomposite with x=0.2 shows -34.27 dB at 10.00 GHz. As Sr^{2+} substitutes Ba^{2+} ion in the ferrite nanocomposite, absorption increases and the absorption peak shows a shift towards lower frequency side. $SrFe_{12}O_{19}$-NPR nanocomposite (x=1.0) shows maximum RL_m value of - 43.06 dB at 9.70 GHz with -10 dB bandwidth of 1.8 GHz and -20 dB bandwidth of 0.40 GHz.

Composite system with strontium substitution of x=0.4 shows five absorption peaks > -20dB spread over the X-band at 9.15 GHz, 9.28 GHz, 10.37 GHz,11.46 GHz and 11.7 GHz. . Figure 4.23b shows the RL_c spectra for d=2 mm for the $Ba_{1-x}Sr_xFe_{12}O_{19}$-NPR nanocomposites with x= 0.2, 0.4, 0.6 and 1.0.

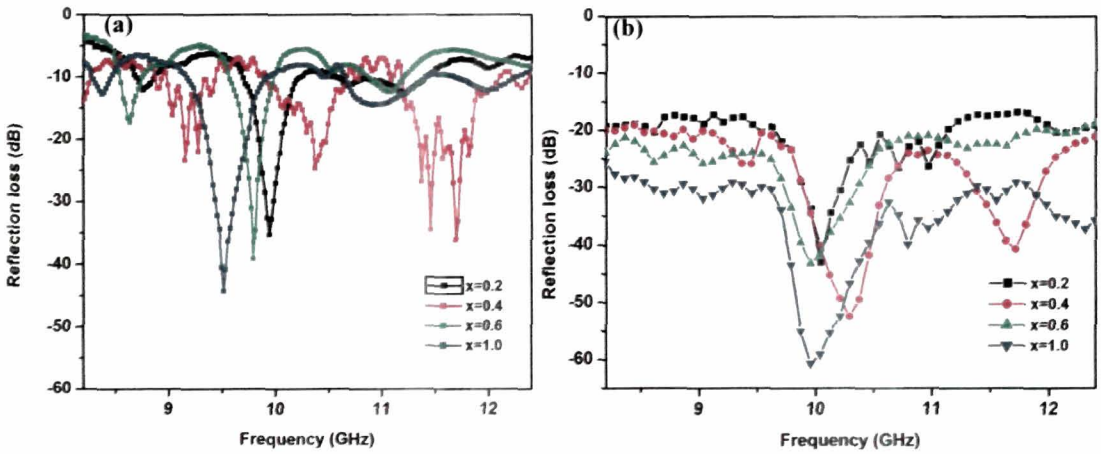

Figure 4.23 Reflection loss parameter of $Ba_{1-x}Sr_xFe_{12}O_{19}$–NPR (x = 0.2, 0.4, 0.6 and 1.0) nanocomposite with 2 mm thickness (a) measured and (b) calculated

Attenuation constant

Using equation 4.8, attenuation constant for strontium substituted barium ferrite-NPR nanocomposite is determined. Figure 4.24 shows the attenuation constant plots with frequency. The attenuation constant increases with x in $Ba_{1-x}Sr_xFe_{12}O_{19}$–NPR nanocomposites. The frequency of attenuation peak corresponds to the complex permeability peak observed in Chapter III, Section 3.4.2. Maximum attenuation of 45.53 dB/cm is observed for x=1.0 at 9.82 GHz.

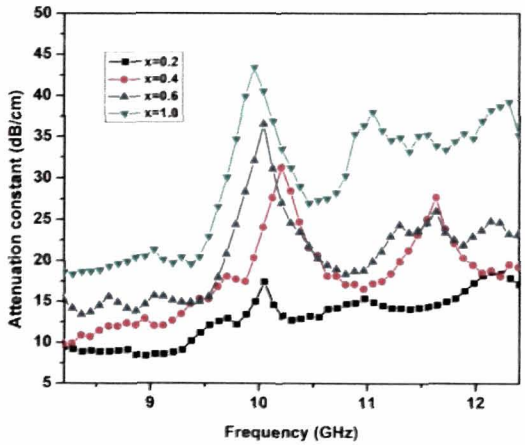

Figure 4.24 Attenuation constant spectra of $Ba_{1-x}Sr_xFe_{12}O_{19}$-NPR (x = 0.2, 0.4, 0.6 and 1.0) composite

Analysis

$Ba_{1-x}Sr_xFe_{12}O_{19}$-NPR nanocomposites show an enhancement in the absorption results with substitution of Ba^{2+} ions by Sr^{2+}. $SrFe_{12}O_{19}$-NPR composite with 2 mm thickness gives a wide -10 dB absorption bandwidth in X-band with maximum absorption. The impedance matching condition and maximum attenuation is achieved for the $SrFe_{12}O_{19}$-NPR composite with 2 mm thickness.

4.5 DISCUSSIONS

The absorber thickness relates to the frequency of operation in a single layer absorber which is basically resonant in nature [18]. Maximal microwave absorption occurs at matching thickness, d_m, when d_m equals to an odd multiple of $\lambda_m / 4$, where, $\lambda_m = \lambda_0 / \left(|\varepsilon_r||\mu_r|\right)^{1/2}$, the condition for phase cancellation [19]. The absorption studies carried out on single layer conductor back ferrite

nanoparticles in NPR matrix, shows that 2 mm layer thickness shows better results as compared to 1 mm, 3 mm and 4 mm for all the compositions. A slight deviation in the calculated and measured reflection loss values for all the ferrite-NPR nanocomposites is observed. TLM models voltage and current distribution within absorber with the shape, dimensions and the properties of the material. Thus the calculated reflection loss from equation 4.7, is determined from overall scattering parameter values. Thus, the approximations in TLM may lead to deviation of maximum absorption frequency and the absorption peak as compared to the measured reflection loss values. Moreover, for fabricated absorber the condition of thickness for destructive interference, $d_m = \frac{\lambda_g}{4}$, is not fulfilled throughout the frequency range and consequently measured bandwidth reduces. Increase in attenuation can be attributed to dielectric relaxation and interfacial polarization [10, 19]. Dielectric relaxation occurs because of the orientation polarization of intrinsic dipoles.

The measured reflection loss using free space technique for 50 wt.%, is tabulated in table 4.4 for all the compositions with 2 mm thickness.

Table 4.4: RLm results for 50 wt % $BaFe_{12}O_{19}$-NPR nanocomposite and Al^{3+} and Sr^{2+} substituted barium ferrite-NPR nanocomposite for d=2 mm

Ferrite	Composition	RLm (dB)	f_r (GHz)	-20 dB BW	-10 dB BW
$BaFe_{12}O_{19}$-NPR	--	-37.06	9.5	0.60	2.05
$BaAl_xFe_{12-x}O_{19}$-NPR	x=1.0	-27.56	9.99	0.29	0.77
	x=1.2	-29.99	11.65	0.36	1.2
	x=1.4	-32.28	9.54	0.37	0.9
	x=1.6	-40. 06	9.46	0.78	4.0
$Ba_{1-x}Sr_xFe_{12}O_{19}$-NPR	x=0.2	-34.27	10.00	0.20	1.0
	x=0.4	-34.58	11.69	0.51	1.3
	x=0.6	-36.91	9.80	0.28	0.5
	x=1.0	-43.06	9.70	0.40	1.8

As aluminium replaces the magnetic ion in $BaAl_xFe_{12-x}O_{19}$ -NPR composite, anisotropy increases which results in increase of absorption. As can be seen for $BaAl_xFe_{12-x}O_{19}$–NPR nanocomposite with x=1.6 showing a maximum absorption of -40.06 dB at 9.56 GHz with -10 dB bandwidth of 4.0 GHz and -20 dB bandwidth of 0.78 GHz. Strontium is also reported to have higher anisotropy than barium, hence increase in Sr^{2+} ion enhances absorption. Maximum absorption of -43.06 dB is obtained at 9.70 GHz with -10dB bandwidth of 1.8 GHz and -20 dB bandwidth of 0.40 GHz for the $Ba_{1-x}Sr_xFe_{12}O_{19}$-NPR composite when x=1.0 i.e. with $SrFe_{12}O_{19}$ inclusions.

The above discussions corroborate the effect of thickness parameters in designing a single layer absorber is very crucial. Barium ferrite-NPR nanocomposites and Al^{3+} and Sr^{2+} substituted barium ferrite nanocomposites show a potential to be developed as thin single layer absorber in X-band. Single layer absorbers are limited in use over a broad frequency range because of the impedance matching taking place at one frequency. Enhancement of bandwidth can be achieved by multilayering and choosing the right combination of single layer ferrite nanocomposites to give a better matching and attenuation condition.

References

1. Saville, P. *Optimisation of Dallenbach Layers using Real Materials,* TECHNICAL MEMORANDUM, DRDC ATLANTIC TM, 2007-012, 2007.
2. Srivastava, R.K., et al. Ni filled flexible multi-walled carbon nanotube–polystyrene composite films as efficient microwave absorbers, *Appl. Phys. Lett.* **99,** 113116-1-3, 2011.
3. Shen, G., et al. Absorbing properties and structural design of microwave absorbers based on W-type La-doped ferrite and carbon fiber composites, *J. Magn. Magn. Mater.* **301**, 325–330, 2006.
4. Park, K. Y., et al. Fabrication and electromagnetic characteristics of electromagnetic wave absorbing sandwich structures, *Compos. Sci. Technol.* **66**, 576-584, 2006.
5. Meshram, M.R., et al. Characterization of M-type barium hexagonal ferrite-based wide band microwave absorber, *J. Magn. Magn. Mater.* **271**, 207-214, 2004.
6. Zhang, B., et al. Microwave-absorbing properties of de-aggregated flake-shaped carbonyl-iron particle composites at 2- 18 GHz, *IEEE Trans. Magn.* **42,** 1178-1781, 2006.
7. Xiao, H. M., et al. Synthesis, magnetic and microwave absorbing properties of core-shell structured $MnFe_2O_4/TiO_2$ nanocomposites, *Compos. Sci. Technol.* **66,** 2003-2008, 2006.
8. Verma, A., et al. Microwave permittivity and permeability of ferrite–polymer thick films, *J. Magn. Magn. Mater.* **263**, 228–234, 2003.
9. Ma, Z., Zhang, et al. Attractive microwave absorption and the impedance match effect in zinc oxide and carbonyl iron composite, *Physica B* **406**, 4620–624, 2011.
10. Fan, Z., et al. Electromagnetic and microwave absorbing properties of multi-walled carbon nanotubes/polymer composites, *Mater. Sci. Eng. B* **132**, 85–89, 2006.

11. He, Y., et al. Optimization of two-layer electromagnetic wave absorbers composed of magnetic and dielectric materials in gigahertz frequency band, *J. Appl. Phys.* **98**, 084903-1-5, 2005.
12. Al-Moayed, N. N., et al. Nano ferrites microwave complex permeability and permittivity measurements by T/R technique in waveguide, *IEEE Trans. Magn.* **44**, 1768-1772, 2008.
13. Kim S. S. and Choi I. K., Design and fabrication of wide band ferrite absorber used in anechoic chamber, *J. Magn.* **2** (1), 25-27, 1977.
14. Ghodgaonkar, D.K., et al. A free-space method for measurement of dielectric constants and loss tangents at microwave frequencies, *IEEE T. Instrum. Meas.* **37**, 789-793, 1989.
15. Varadan, V. V., et al. Free-space, broadband measurements of high-temperature, complex dielectric properties at microwave frequencies, *IEEE T. Instrum. Meas.* **40**, 842-846, 1991.
16. Rozanov, N. K. Ultimate Thickness to Bandwidth Ratio of Radar Absorbers, *IEEE Trans. Antennas Propag.* **48**(8), 1230-1234, 2000.
17. Feng, Y.B., et al. Absorbing properties and structural design of microwave absorbers based on carbonyl iron and barium ferrite, *J. Magn. Magn. Mater.* **318**, 8-13, 2007.
18. Rashid, A. K., et al. *On the optimum design of a single-layer thin wideband radar absorber*, IEEE INTERNATIONAL SYMPOSIUM ON ANTENNAS AND PROPAGATION (AP-S/URSI 2011), Spokane, Washington, 2916–2919, 2011.
19. Zhang, L., et al. The electromagnetic characteristics and absorbing properties of multi-walled carbon nanotubes filled with Er_2O_3 nanoparticles as microwave absorbers, *Mater. Sci. Eng. B.* **153**, 78–82, 2008.

CHAPTER V

THREE-LAYER MICROWAVE ABSORBER: DESIGN OPTIMIZATION, FABRICATION AND REFLECTION LOSS MEASUREMENT OVER THE X-BAND

5.1 INTRODUCTION

Military and civil applications require absorbers which can absorb em wave over large bandwidth. Single layer absorbers, however, are restricted to a narrow frequency of operation. In addition, thickness and light weight are other issues to be considered while designing the absorber [1]. For single layer absorbers, it is usually hard to simultaneously meet the requirement of broad absorption frequency range with reduced thickness [2].

Magnetic single layer absorbers, studied in chapter IV, are of thickness 2 mm and give good absorption peak >-30 dB at single frequencies in X- band, but -20 dB absorption bandwidth is ~ < 1 GHz and -10 dB bandwidth is not spread over the X-band.

Wide absorption band can be obtained by multilayered shields [2-7]. Multilayering reduces the reflection by gradually tapering the impedance from that of free space to a highly lossy state. Controlling the magnetic and dielectric loading of individual layers can lead to enhanced absorption bandwidth. Double layer microwave absorber reported in [8-10] shows enhancement of bandwidth. Three layered absorber gives a larger option to manipulate layer configuration, its thickness and material properties to obtain the matching condition over the band [11-13].

Bandwidth of the microwave absorber can be further enhanced by augmenting number of layers without compromising on the total thickness of the absorbing structure [14]. A three layer structure is designed using transmission line model to achieve absorption over the frequency range 8.2 to 12.4 GHz. [15, 16]. The layers are chosen from the single layer absorption studies conducted on barium ferrite and substituted barium ferrite nanocomposites from chapter IV. Optimization of layer arrangements, thickness of individual layers and overall thickness of multilayer structure is carried out to achieve broadband absorption. The best design results are fabricated as conductor backed Dallenbach three layered structure and tested for free space microwave absorption over the X-band.

5.2 DESIGN AND THICKNESS OPTIMIZATION OF THREE LAYERED ABSORBER

The schematic diagram of a conductor backed three layered absorber is shown in figure 5.1 The input impedance, Z_{in}, and computed reflection loss, RL_c, are determined for the conductor backed multilayer magnetic absorber discussed in chapter I, subsections 1.3.2. For a three layered structure, Z_3, and RL_c, are as below

$$Z_3 = \eta_3 \frac{\eta_2 \frac{\eta_1 \tanh\gamma_1 d_1 + \eta_2 \tanh\gamma_2 d_2}{\eta_2 + \eta_1 \tanh(\gamma_1 d_1)\tanh(\gamma_2 d_2)} + \eta_3 \tanh\gamma_3 d_3}{\eta_3 + \eta_2 \frac{\eta_1 \tanh\gamma_1 d_1 + \eta_2 \tanh\gamma_2 d_2}{\eta_2 + \eta_1 \tanh(\gamma_1 d_1)\tanh(\gamma_2 d_2)} \tanh\gamma_3 d_3} \tag{5.1}$$

$$RL_c = 20\log \left| \frac{\eta_3 \frac{\eta_2 \frac{\eta_1 \tanh\gamma_1 d_1 + \eta_2 \tanh\gamma_2 d_2}{\eta_2 + \eta_1 \tanh(\gamma_1 d_1)\tanh(\gamma_2 d_2)} + \eta_3 \tanh\gamma_3 d_3}{\eta_3 + \eta_2 \frac{\eta_1 \tanh\gamma_1 d_1 + \eta_2 \tanh\gamma_2 d_2}{\eta_2 + \eta_1 \tanh(\gamma_1 d_1)\tanh(\gamma_2 d_2)} \tanh\gamma_3 d_3} - \eta_0}{\eta_3 \frac{\eta_2 \frac{\eta_1 \tanh\gamma_1 d_1 + \eta_2 \tanh\gamma_2 d_2}{\eta_2 + \eta_1 \tanh(\gamma_1 d_1)\tanh(\gamma_2 d_2)} + \eta_3 \tanh\gamma_3 d_3}{\eta_3 + \eta_2 \frac{\eta_1 \tanh\gamma_1 d_1 + \eta_2 \tanh\gamma_2 d_2}{\eta_2 + \eta_1 \tanh(\gamma_1 d_1)\tanh(\gamma_2 d_2)} \tanh\gamma_3 d_3} + \eta_0} \right| \tag{5.2}$$

where, $\eta_1 = \eta_0\sqrt{\mu_{r1} / \varepsilon_{r1}}$ (5.3)

$\eta_2 = \eta_0\sqrt{\mu_{r2} / \varepsilon_{r2}}$ (5.4)

$\eta_3 = \eta_0\sqrt{\mu_{r3} / \varepsilon_{r3}}$ (5.5)

$\gamma_1 = j(2\pi f / c)\sqrt{\mu_{r1}\varepsilon_{r1}}$ (5.6)

$\gamma_2 = j(2\pi f / c)\sqrt{\mu_{r2}\varepsilon_{r2}}$ (5.7)

$\gamma_3 = j(2\pi f / c)\sqrt{\mu_{r3}\varepsilon_{r3}}$ (5.8)

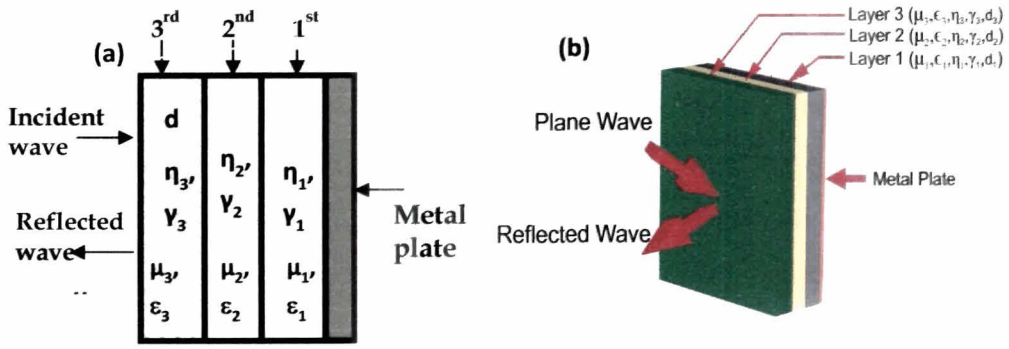

Figure 5.1 A schematic diagram of ferrite NPR graded triple layer absorber

The layer 1 with thickness d_1 and material parameters $\varepsilon_{r1}, \mu_{r1}, \eta_1, \gamma_1$ is in vicinity to the metal plate, layer 2 with thickness d_2 and material parameters $\varepsilon_{r2}, \mu_{r2}, \eta_2, \gamma_2$ is the sandwiched layer and layer 3 with thickness d_3 and material parameters $\varepsilon_{r3}, \mu_{r3}, \eta_3, \gamma_3$ is the interface layer. Thus, the composition (intrinsic properties), and the total layer thickness, d, as well as individual layer thickness is optimized to achieve the best performance i.e. minimum RL_c and broad bandwidth.

The broad bandwidth desired is that -10 dB absorption bandwidth should cover the entire frequency range from 8.2 - 12.4 GHz. Considering this, from the single layer ferrite-NPR nanocomposites studied in the last chapter table 4.4, the following single layers are chosen and tabulated in Table 5.1.

Table 5.1 Selection of ferrite-NPR nanocomposites for three layer design combinations

Ferrite composition	Designation	f_r (GHz)	RL_m (dB)	-10 dB BW (GHz)	-20 dB BW(GHz)
50 wt.%, $BaFe_{12}O_{19}$-NPR	**A**	9.5	-37.06	2.05	0.60
$BaAl_{1.2}Fe_{10.8}O_{19}$-NPR	**B**	11.65	-29.99	1.2	0.36
$Ba_{0.6}Sr_{0.4}Fe_{12}O_{19}$-NPR	**C**	11.70	-34.58	1.3	0.51

$BaFe_{12}O_{19}$-NPR nanocomposite with 50 wt.%, designated as layer **A**, is chosen as it shows maximum absorption of -37.06 dB at 9.65 GHz, as compared to other weight % barium ferrite-NPR series and -10 dB bandwidth of 2.05 GHz. 50 wt.% of $BaAl_xFe_{12-x}O_{19}$-NPR composite with x=1.2 (layer **B**) shows a maximum absorption of -29.99 dB at 11.65 GHz. This composite is chosen as it shows absorption at higher frequency side in X-band. Layer **C** is designated to 50 wt.% $Ba_{1-x}Sr_xFe_{12}O_{19}$-NPR with x=0.4. A reflection loss of >-20dB is observed for this single layer absorber spread over the X band with multiple absorption peaks at 9.15 GHz (-23.54 dB), 9.28 GHz (-22.03 dB), 10.37 GHz (-24.70 dB), 11.46 GHz (-34.46 dB) and 11.70 GHz (-36.08 dB).

Design optimization is carried out for three layered absorber taking following considerations:

- All possible combinations of the three layers are considered as shown in table 5.2. The nomenclature of the layers are carried out according to their compositions e.g. the combination **ABC** corresponds to **A** assigned to layer 1 i.e. the layer adjacent to metal backing, **B** is assigned to the middle layer 2 and **C** is the absorber layer 3 at the interface with air.
- Total thickness, d, where, $d = d_1 + d_2 + d_3$, is combination of d_1 , d_2 and d_3 is the thickness of layers 1, 2, 3, respectively (refer to figure 5.1b).
- A variation in d_1 , d_2 and d_3 are carried out for fixed d value. The thickness combinations are shown in table 5.3.
- The choice of final combinations for fabrication is made considering least thickness, maximum absorption and broad -20 dB bandwidth.

Table 5.2 Design combinations of ferrite-NPR nanocomposites for three layer configuration

Air-absorber interface layer	Sample code I-II-III layer
A-interface	CBA
	BCA
B-interface	ACB
	CAB
C-interface	ABC
	BAC

A MATLAB program is developed for carrying out design optimization, taking into consideration equations 5.1 to 5.8. The total thickness, d, of the absorber is varied from 2 mm to 4 mm in step of 0.5 mm. Minimum thickness of the individual layer is taken as 0.5 mm considering the limitation in fabrication of the absorber.

Table 5.3 Three layer design combination: individual thickness optimization

Total thickness, d (mm)	Thickness of individual layers (mm)			Total thickness, d (mm)	Thickness of individual layers (mm)		
	d_1	d_2	d_3		d_1	d_2	d_3
2	0.5	0.5	1.0	3.0	0.5	0.5	2.0
	0.5	1.0	0.5		0.5	1.0	1.5
	1.0	0.5	0.5		0.5	1.5	1.0
2.5	0.5	0.5	1.5		0.5	2.0	0.5
	0.5	1.0	1.0		2.0	0.5	0.5
	0.5	1.5	0.5		1.5	0.5	1.0
	1.5	0.5	0.5		1.0	0.5	1.5
	1.0	1.0	0.5		1.0	1.5	0.5
	1.0	0.5	1.0		1.5	1.0	0.5
3.5	0.5	0.5	2.5	4.0	0.5	0.5	3.0
	0.5	1.0	2.0		0.5	1.0	2.5
	0.5	1.5	1.5		0.5	1.5	2.0
	0.5	2.0	1.0		0.5	2.0	1.5
	0.5	2.5	0.5		0.5	2.5	1.0
	1.0	2.0	0.5		0.5	3.0	0.5
	1.5	1.5	0.5		1.0	2.5	0.5
	2.0	1.0	0.5		1.5	2.0	0.5
	2.5	0.5	0.5		2.0	1.5	0.5
	2.0	0.5	0.5		2.5	1.0	0.5
	1.5	0.5	1.0		3.0	0.5	0.5
	1.0	0.5	1.5		2.5	0.5	1.0
	-	-	-		2.0	0.5	1.5
	-	-	-		1.5	0.5	2.0
	-	-	-		1.0	0.5	2.5

The algorithm of the program for three layer absorber design is given as below followed by flowchart in figure 5.2.

Step 1: Read data (ε_{r1}, ε_{r2}, ε_{r3}, μ_{r1}, μ_{r2}, μ_{r3}, f) from files.

Step 2: Every combination vary the total thickness from 2 mm to 4 mm in step of 0.5 mm.

Step 3: For every given thickness d, vary the individual thickness of the three layers (>= 0.5 mm) for all possible layer configurations.

Step 4: Determine the RL_c(min), Z_{real}, Z_{imag}, -20 dB bandwidth and -10 dB bandwidth.

Step 5: Store data.

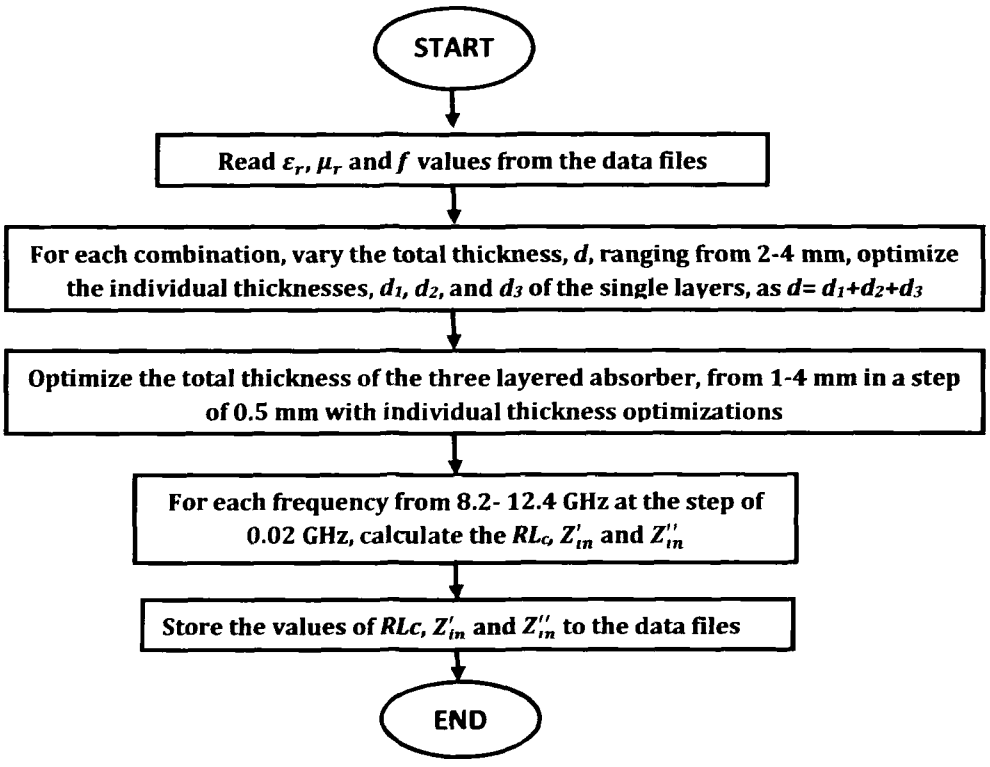

Figure 5.2 Flow chart of three layer absorber design optimization

5.3 CALCULATED REFLECTION LOSS FOR THREE LAYERED MAGNETIC ABSORBER

Three layered design results i.e. calculated RL_c and -20 dB bandwidth, for all the six combinations given in table 5.2 with all possible thickness combinations given in table 5.3, where total thickness, d varies from 2 mm – 4 mm, in step of 0.5 mm are discussed in the sections below.

5.3.1 ABC layer combination

The RL_c plots for **ABC** combinations with varying thicknesses are plotted in figures 5.3(a-e).

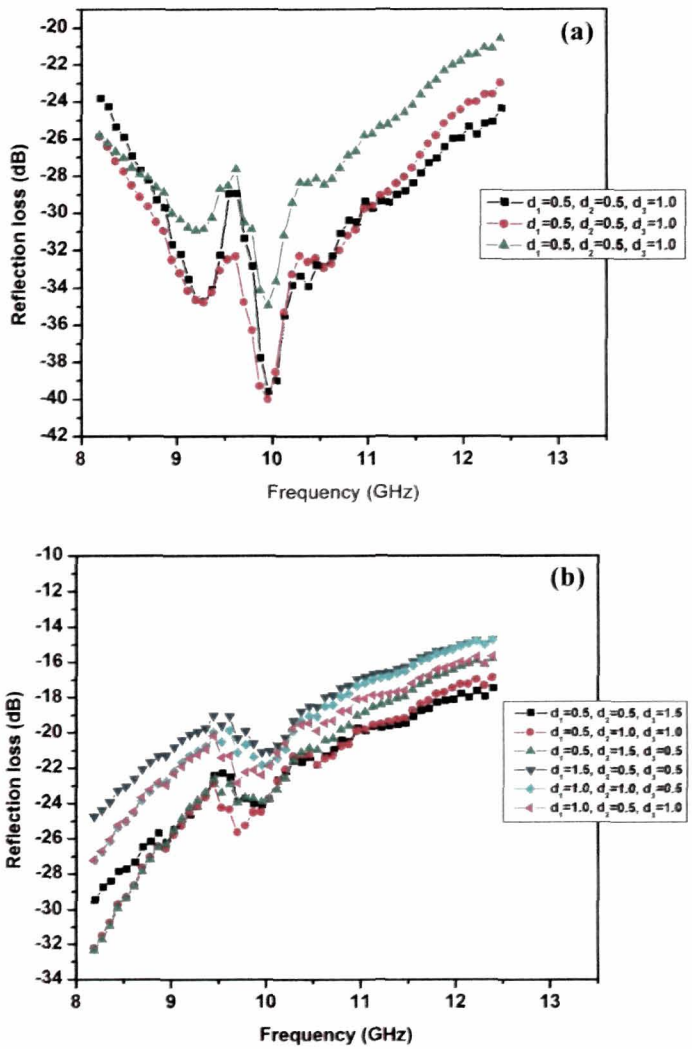

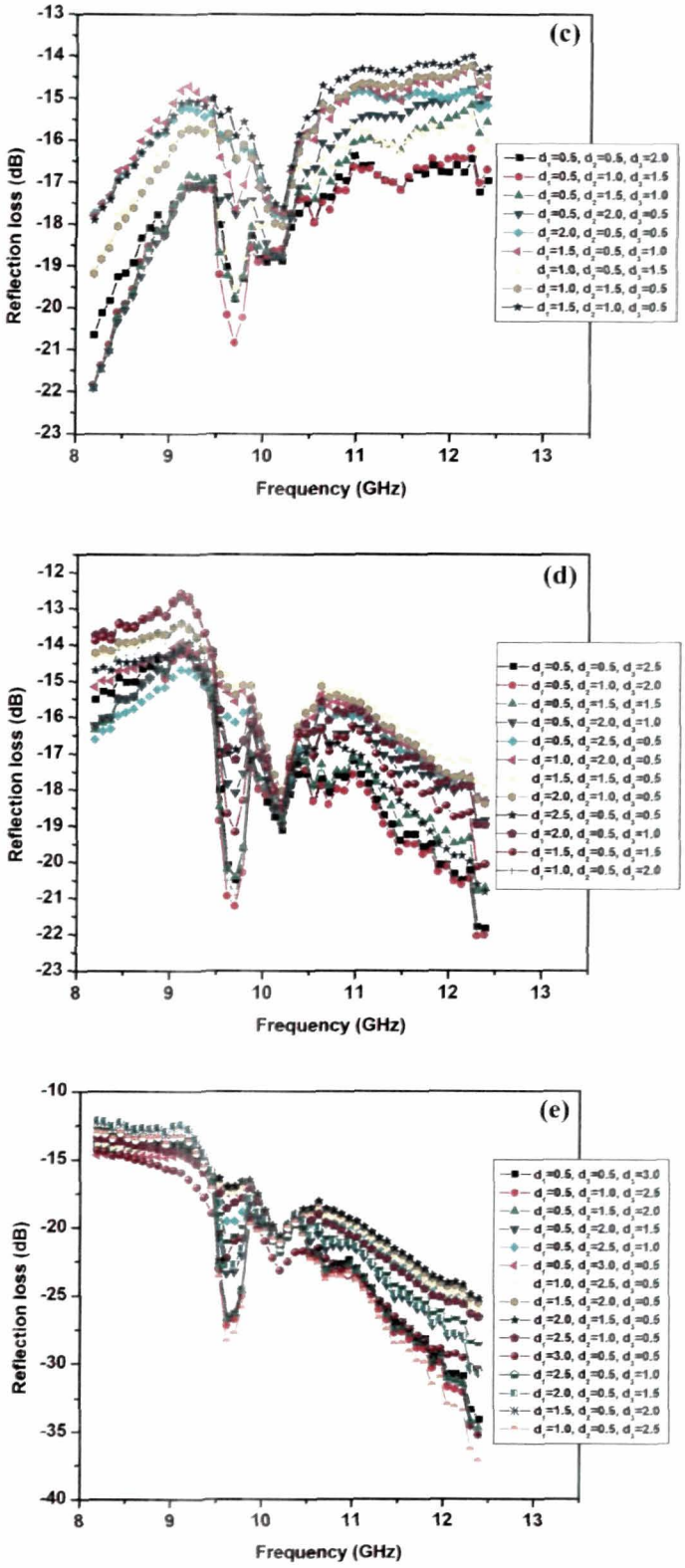

Figure 5.3 Reflection loss of three layered ferrite-NPR nanocomposite for ABC combinations with total thickness (a) 2.0 mm, (b) 2.5 mm, (c) 3.0 mm, (d) 3.5 mm, and (e) 4.0 mm

The maximum absorption peak, -20 dB and -10 dB absorption bandwidth for varying individual layer thickness is tabulated in table 5.4. Maximum absorption row for all thicknesses are shaded. The three layered absorber with d=2 mm with layer thickness, **A**=0.5 mm, **B**=1.0 mm and **C**=0.5 mm, shows a maximum absorption of -40.01 dB at 9.9 GHz with -20 dB bandwidth of 4 GHz.

Table 5.4 Performance parameters of the designed **ABC** triple layer absorber with different thickness of the layers

d (mm)	Thickness of individual layers (mm)			RLc (dB)	f_r (GHz)	-20dB BW (GHz)	d (mm)	Thickness of individual layers (mm)			RLc (dB)	f_r (GHz)	-20dB BW (GHz)
	d_1	d_2	d_3					d_1	d_2	d_3			
2	0.5	0.5	1.0	-39.60	9.9	4.2	3.0	0.5	0.5	2.0	-20.62	8.2	0.2
	0.5	**1.0**	**0.5**	**-40.01**	**9.9**	**4.2**		**0.5**	**1.0**	**1.5**	**-21.90**	**8.2**	**0.5**
	1.0	0.5	0.5	-34.95	9.9	4.2		0.5	1.5	1.0	-21.90	8.2	0.3
2.5	0.5	0.5	1.5	-29.51	8.2	2.7		0.5	2.0	0.5	-21.90	8.2	0.4
	0.5	1.0	1.0	-32.07	8.2	2.7		2.0	0.5	0.5	-17.83	10.2	-
	0.5	**1.5**	**0.5**	**-32.30**	**8.2**	**2.7**		1.5	0.5	1.0	-17.6	9.7	-
	1.5	0.5	0.5	-24.74	8.2	1.6		1.0	0.5	1.5	-19.54	9.7	-
	1.0	1.0	0.5	-27.20	8.2	2.0		1.0	1.5	0.5	-19.10	8.2	-
	1.0	0.5	1.0	-27.21	8.2	2.0		1.5	1.0	0.5	-17.56	10.2	-
3.5	0.5	0.5	1.0	-22.03	12.4	0.7	4.0	0.5	0.5	3.0	-34.10	12.4	2.3
	0.5	**1.0**	**0.5**	**-22.03**	**12.4**	**0.8**		0.5	1.0	2.5	-35.27	12.4	2.4
	1.0	0.5	0.5	-20.80	12.4	0.3		0.5	1.5	2.0	-34.74	12.4	2.3
	0.5	0.5	1.5	-18.94	10.21	-		0.5	2.0	1.5	-30.58	12.4	2.3
	0.5	1.0	1.0	-18.50	10.21	-		0.5	2.5	1.0	-26.75	12.4	1.4
	0.5	1.5	0.5	-18.50	10.21	-		0.5	3.0	0.5	-25.15	12.4	1.3
	1.5	0.5	0.5	-17.98	10.22	-		1.0	2.5	0.5	-26.01	12.4	1.4
	1.0	1.0	0.5	-18.93	12.4	-		1.5	2.0	0.5	-25.47	12.4	1.3
	1.0	0.5	1.0	-20.85	12.4	-		2.0	1.5	0.5	-25.37	12.4	1.3
	0.5	0.5	1.0	-18.93	12.4	-		2.5	1.0	0.5	-26.75	12.4	1.5
	0.5	1.0	0.5	-20.12	12.3	-		3.0	0.5	0.5	-30.58	12.4	2.7
	1.0	0.5	0.5	-22.03	12.4	0.7		2.5	0.5	1.0	-28.56	12.4	2.9
								2.0	0.5	1.5	-30.58	12.4	2.0
								1.5	0.5	2.0	-35.27	12.4	1.9
								1.0	**0.5**	**2.5**	**-37.33**	**12.4**	**2.3**

d = Total thickness, RLc = Reflection loss, f_r = Resonant frequency, BW=Bandwidth

5.3.2 ACB layer combination

The RL_c plots for **ACB** combinations with varying total thickness from 2 – 4 mm, is plotted in figure 5.4(a-e). The maximum absorption peak, -20 dB and -10 dB absorption bandwidth are tabulated in table 5.5.

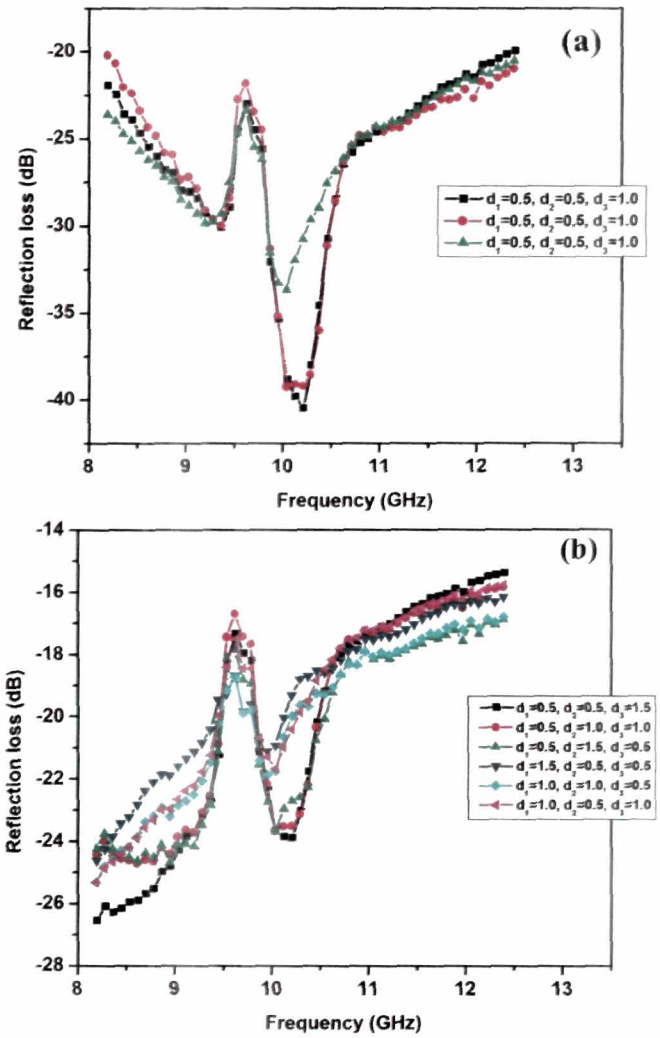

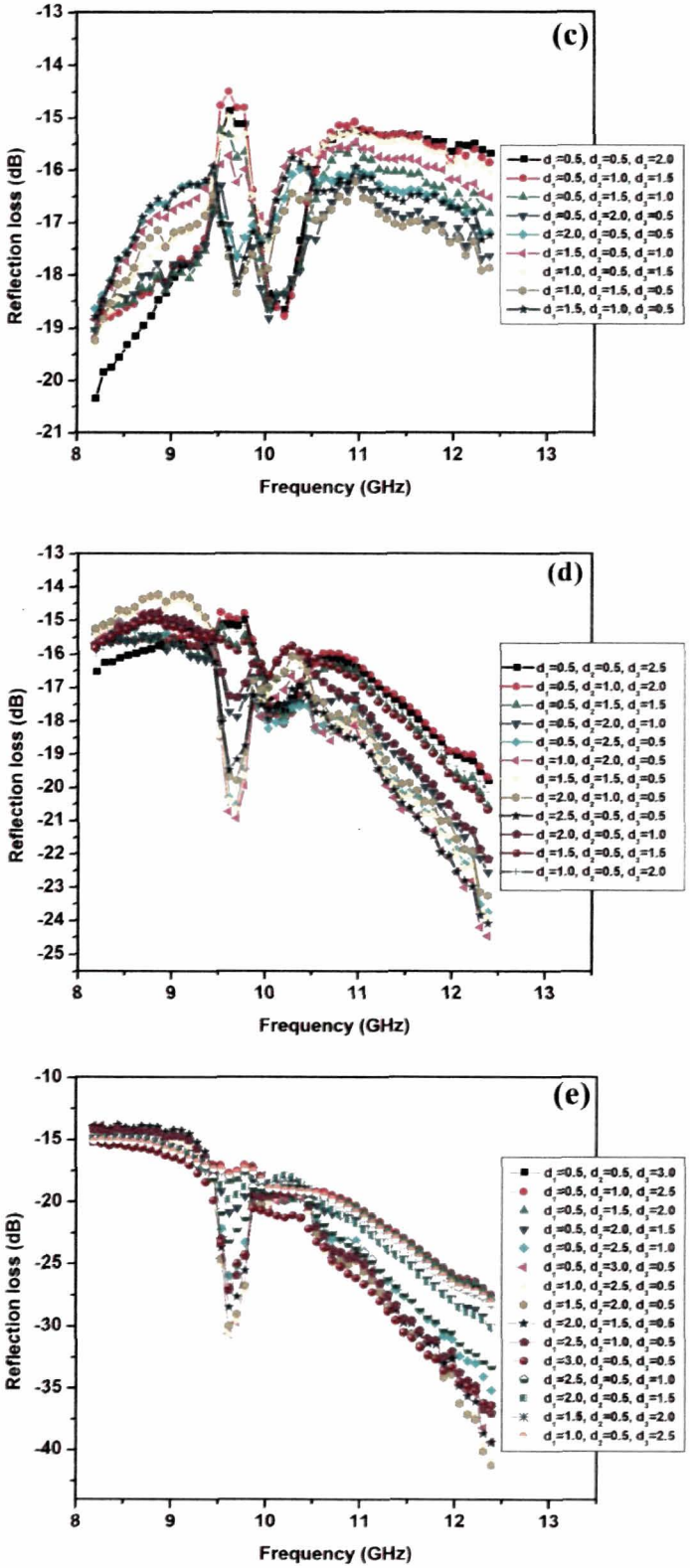

Figure 5.4 Reflection loss of three layered ferrite-NPR nanocomposite for ACB combinations with total thickness (a) 2.0 mm, (b) 2.5 mm, (c) 3.0 mm, (d) 3.5 mm, and (e) 4.0 mm

Table 5.5 Performance parameters of the designed **ACB** triple layer absorber with different thickness of the layers

d (mm)	Thickness of individual layers (mm)			*RLc* (dB)	f_r (GHz)	-20dB BW (GHz)	*d* (mm)	Thickness of individual layers (mm)			*RLc* (dB)	f_r (GHz)	-20dB BW (GHz)
	d_1	d_2	d_3					d_1	d_2	d_3			
2.0	0.5	0.5	1.0	-40.57	10.23	4.2	3.0	0.5	0.5	2.0	-20.34	8.2	0.1
	0.5	1.0	0.5	-39.24	10.20	4.2		0.5	1.0	1.5	-19.18	8.2	-
	1.0	0.5	0.5	-33.74	10.00	4.2		0.5	1.5	1.0	-19.02	8.2	-
2.5	0.5	0.5	1.5	-26.54	8.2	2.0		0.5	2.0	0.5	-19.05	8.2	-
	0.5	1.0	1.0	-24.75	8.64	1.9		2.0	0.5	0.5	-18.64	8.2	-
	0.5	1.5	0.5	-24.66	8.96	2.1		1.5	0.5	1.0	-18.83	8.2	-
	1.5	0.5	0.5	-24.60	8.2	1.5		1.0	0.5	1.5	-18.30	8.2	-
	1.0	1.0	0.5	-25.35	8.2	1.7		1.0	1.5	0.5	-19.23	8.2	-
	1.0	0.5	1.0	-25.39	8.2	1.7		1.5	1.0	0.5	-18.78	8.2	-
3.5	0.5	0.5	1.0	-19.80	12.4	-	4.0	0.5	0.5	3.0	-27.98	12.4	1.6
	0.5	1.0	0.5	-19.69	12.4	-		0.5	1.0	2.5	-27.46	12.4	1.5
	1.0	0.5	0.5	-20.54	12.4	0.2		0.5	1.5	2.0	-27.71	12.4	1.6
	0.5	0.5	1.5	-22.55	12.4	0.7		0.5	2.0	1.5	-30.13	12.4	2.1
	0.5	1.0	1.0	-23.75	12.4	1.2		0.5	2.5	1.0	-35.13	12.4	2.4
	0.5	1.5	0.5	-24.43	12.4	1.3		0.5	3.0	0.5	-39.53	12.4	2.4
	1.5	0.5	0.5	-23.85	10.22	1.2		1.0	2.5	0.5	-40.82	12.4	2.5
	1.0	1.0	0.5	-23.31	12.4	0.8		1.5	2.0	0.5	-41.29	12.4	2.5
	1.0	0.5	1.0	-24.10	12.4	1.1		2.0	1.5	0.5	-39.46	12.4	2.3
	0.5	0.5	1.0	-22.11	12.4	0.6		2.5	1.0	0.5	-37.11	12.4	2.3
	0.5	1.0	0.5	-20.69	12.3	0.3		3.0	0.5	0.5	-36.41	12.4	2.9
	1.0	0.5	0.5	-20.14	12.4	0.1		2.5	0.5	1.0	-33.11	12.4	2.3
								2.0	0.5	1.5	-30.03	12.4	1.8
								1.5	0.5	2.0	-28.36	12.4	1.6
								1.0	0.5	2.5	-28.03	12.4	1.6

d = Total thickness, *RLc* = Reflection loss, f_r = Resonant frequency, BW=Bandwidth

The three layered absorber for **ACB** configuration, *d*=2 mm with interface layer **B**= 0.5 mm, sandwich layer **C**= 0.5 mm and layer near to metal **A** =1.0 mm , shows a maximum absorption of -40.57 dB at 10.23 GHz with -20 dB bandwidth of 4.2 GHz.

5.3.3 BAC layer combination

The RL_c plots for **BAC** combinations with varying total thickness and individual layer thickness is shown in figures 5.5(a-e).

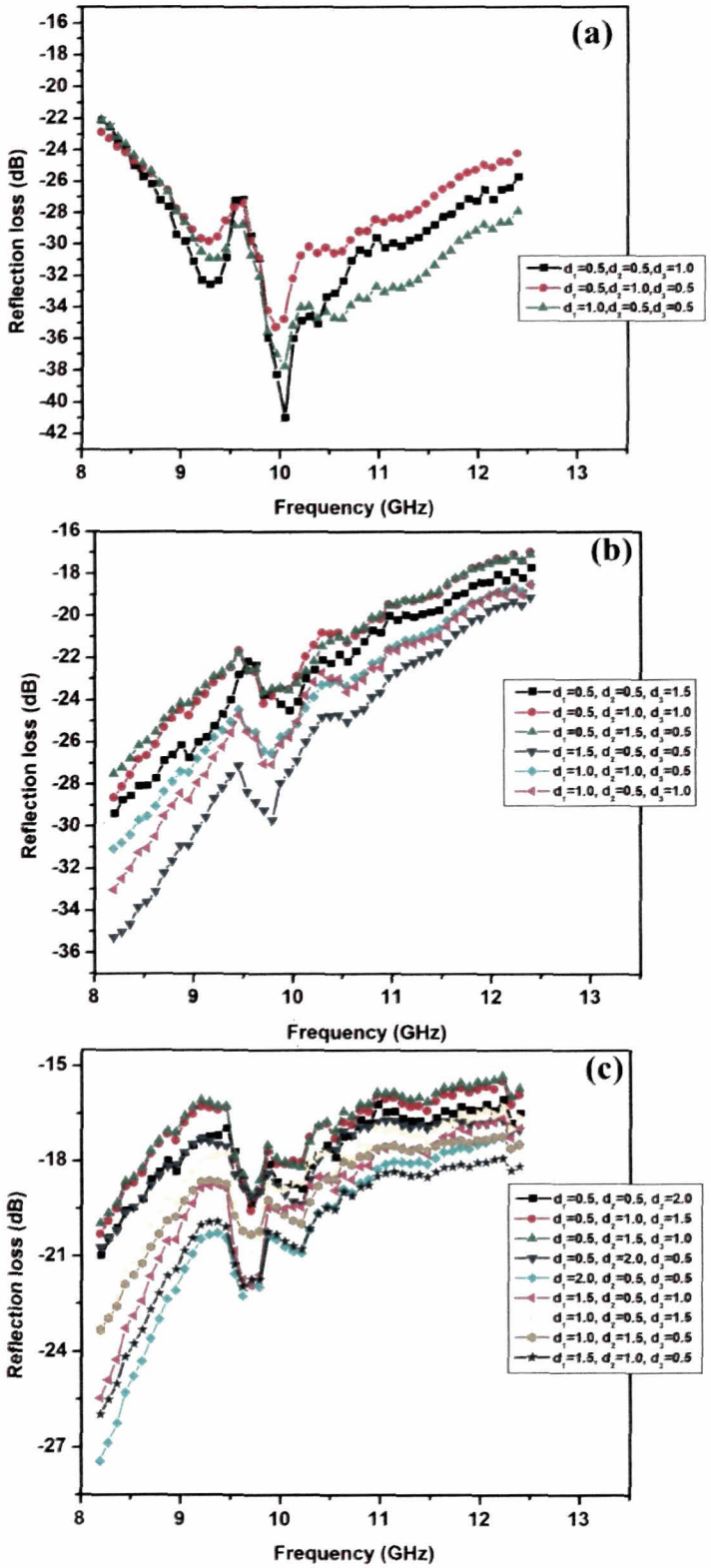
(a)
Reflection loss (dB)
Frequency (GHz)
d1=0.5,d2=0.5,d3=1.0
d1=0.5,d2=1.0,d3=0.5
d1=1.0,d2=0.5,d3=0.5
(b)
Reflection loss (dB)
Frequency (GHz)
d1=0.5, d2=0.5, d3=1.5
d1=0.5, d2=1.0, d3=1.0
d1=0.5, d2=1.5, d3=0.5
d1=1.5, d2=0.5, d3=0.5
d1=1.0, d2=1.0, d3=0.5
d1=1.0, d2=0.5, d3=1.0
(c)
Reflection loss (dB)
Frequency (GHz)
d1=0.5, d2=0.5, d3=2.0
d1=0.5, d2=1.0, d3=1.5
d1=0.5, d2=1.5, d3=1.0
d1=0.5, d2=2.0, d3=0.5
d1=2.0, d2=0.5, d3=0.5
d1=1.5, d2=0.5, d3=1.0
d1=1.0, d2=0.5, d3=1.5
d1=1.0, d2=1.5, d3=0.5
d1=1.5, d2=1.0, d3=0.5

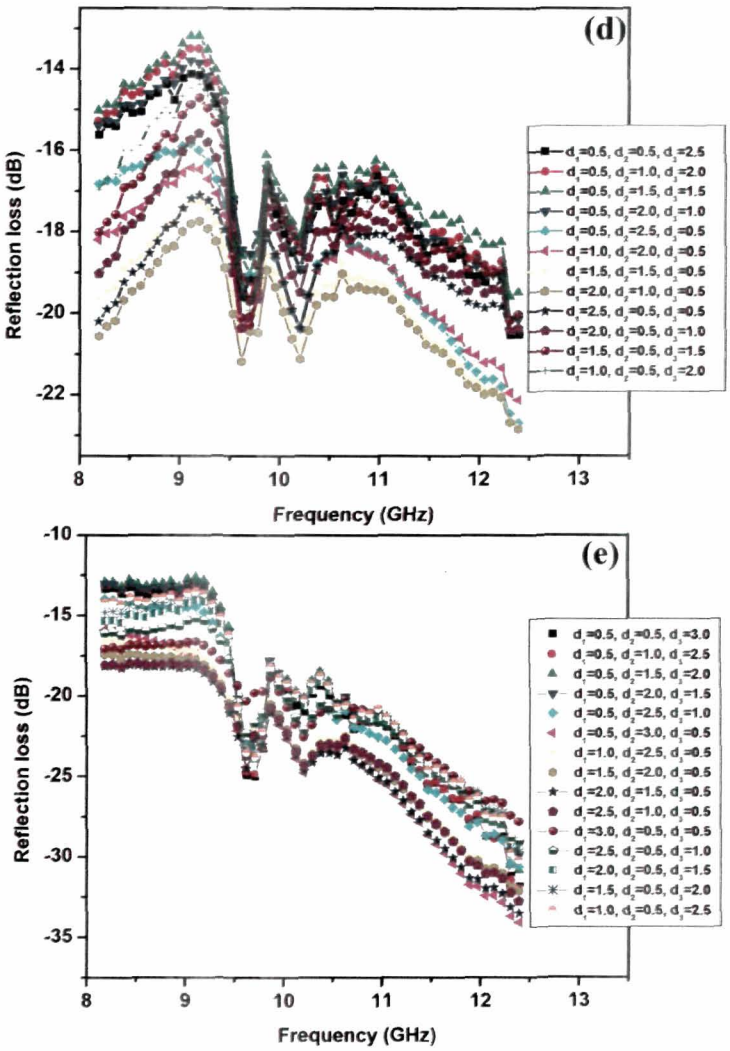

Figure 5.5 Reflection loss of three layered ferrite-NPR nanocomposite for BAC combinations with total thickness (a) 2.0 mm, (b) 2.5 mm, (c) 3.0 mm, (d) 3.5 mm, and (e) 4.0 mm

The maximum absorption peak, -20 dB and -10 dB absorption bandwidth and optimized individual layer thickness is tabulated in table 5.6.

The three layered absorber for **BAC** configurations, *d*=2 mm, with interface layer **C**= 0.5 mm, sandwich layer **A**= 0.5 mm and layer near to metal **B** =1.0 mm shows a maximum absorption of -39.24 dB at 10.05 GHz with -20 dB bandwidth of 4.2 GHz.

Table 5.6 Performance parameters of the designed **BAC** triple layer absorber with different thickness of the layers

d (mm)	Thickness of individual layers (mm)			*RLc* (dB)	f_r (GHz)	-20dB BW (GHz)	*d* (mm)	Thickness of individual layers (mm)			RLc (dB)	f_r (GHz)	-20dB BW (GHz)
	d_1	d_2	d_3					d_1	d_2	d_3			
2.0	0.5	0.5	1.0	-41.02	10.05	4.2	3.0	0.5	0.5	2.0	-20.95	8.2	0.2
	0.5	1.0	0.5	-35.36	9.96	4.2		0.5	1.0	1.5	-20.28	8.2	0.1
	1.0	0.5	0.5	-37.76	10.04	4.2		0.5	1.5	1.0	-19.98	8.2	-
2.5	0.5	0.5	1.5	-29.30	8.2	2.8		0.5	2.0	0.5	-20.72	8.2	0.2
	0.5	1.0	1.0	-28.62	8.2	2.6		2.0	0.5	0.5	-27.31	8.2	2.1
	0.5	1.5	0.5	-27.44	8.2	2.6		1.5	0.5	1.0	-25.35	8.2	1.2
	1.5	0.5	0.5	-35.27	8.2	3.6		1.0	0.5	1.5	-23.39	8.2	0.7
	1.0	1.0	0.5	-30.99	8.2	3.4		1.0	1.5	0.5	-22.29	8.2	0.8
	1.0	0.5	1.0	-33.01	8.2	3.4		1.5	1.0	0.5	-25.94	8.2	1.9
3.5	0.5	0.5	1.0	-20.55	12.4	0.2	4.0	0.5	0.5	3.0	-31.92	12.4	2.4
	0.5	1.0	0.5	-20.16	12.4	0.1		0.5	1.0	2.5	-32.05	12.4	2.2
	1.0	0.5	0.5	-19.59	12.4	-		0.5	1.5	2.0	-30.72	12.4	2.2
	0.5	0.5	1.5	-20.21	12.4	0.1		0.5	2.0	1.5	-29.77	12.4	2.2
	0.5	1.0	1.0	-22.68	12.4	1.0		0.5	2.5	1.0	-30.56	12.4	2.7
	0.5	1.5	0.5	-22.11	12.4	0.9		0.5	3.0	0.5	-30.04	12.4	3.0
	1.5	0.5	0.5	-22.79	12.4	1.4		1.0	2.5	0.5	-32.08	12.4	3.0
	1.0	1.0	0.5	--22.81	12.4	2.0		1.5	2.0	0.5	-32.14	12.4	2.9
	1.0	0.5	1.0	-20.40	10.22	0.4		2.0	1.5	0.5	-33.49	12.4	3.0
	0.5	0.5	1.0	-20.36	9.6	0.3		2.5	1.0	0.5	-32.71	12.4	3.0
	0.5	1.0	0.5	-20.27	9.72	0.2		3.0	0.5	0.5	-27.81	12.4	2.4
	1.0	0.5	0.5	-20.07	12.4	-		2.5	0.5	1.0	-28.99	12.4	2.7
								2.0	0.5	1.5	-29.49	12.4	2.2
								1.5	0.5	2.0	-29.68	12.4	2.2
								1.0	0.5	2.5	-30.32	12.4	2.2

d = Total thickness, *RLc* = Reflection loss, f_r = Resonant frequency, BW=Bandwidth

5.3.4 BCA layer combination

The RL_c plots for **BCA** combinations with varying total thickness from 2 mm – 4 mm, is plotted in figure 5.6 (a-e).

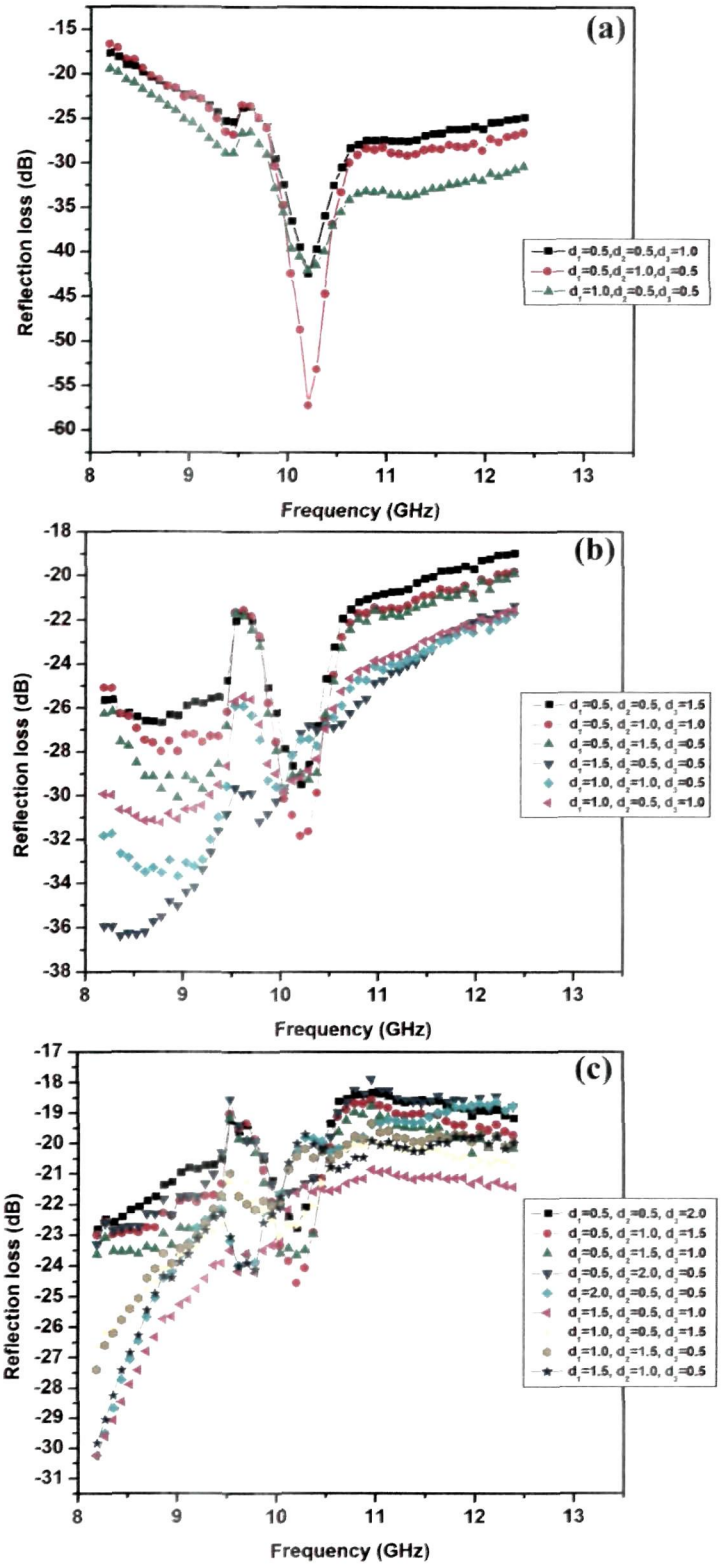
(a)
Reflection loss (dB)
Frequency (GHz)
d1=0.5,d2=0.5,d3=1.0
d1=0.5,d2=1.0,d3=0.5
d1=1.0,d2=0.5,d3=0.5
(b)
Reflection loss (dB)
Frequency (GHz)
d1=0.5, d2=0.5, d3=1.5
d1=0.5, d2=1.0, d3=1.0
d1=0.5, d2=1.5, d3=0.5
d1=1.5, d2=0.5, d3=0.5
d1=1.0, d2=1.0, d3=0.5
d1=1.0, d2=0.5, d3=1.0
(c)
Reflection loss (dB)
Frequency (GHz)
d1=0.5, d2=0.5, d3=2.0
d1=0.5, d2=1.0, d3=1.5
d1=0.5, d2=1.5, d3=1.0
d1=0.5, d2=2.0, d3=0.5
d1=2.0, d2=0.5, d3=0.5
d1=1.5, d2=0.5, d3=1.0
d1=1.0, d2=0.5, d3=1.5
d1=1.0, d2=1.5, d3=0.5
d1=1.5, d2=1.0, d3=0.5

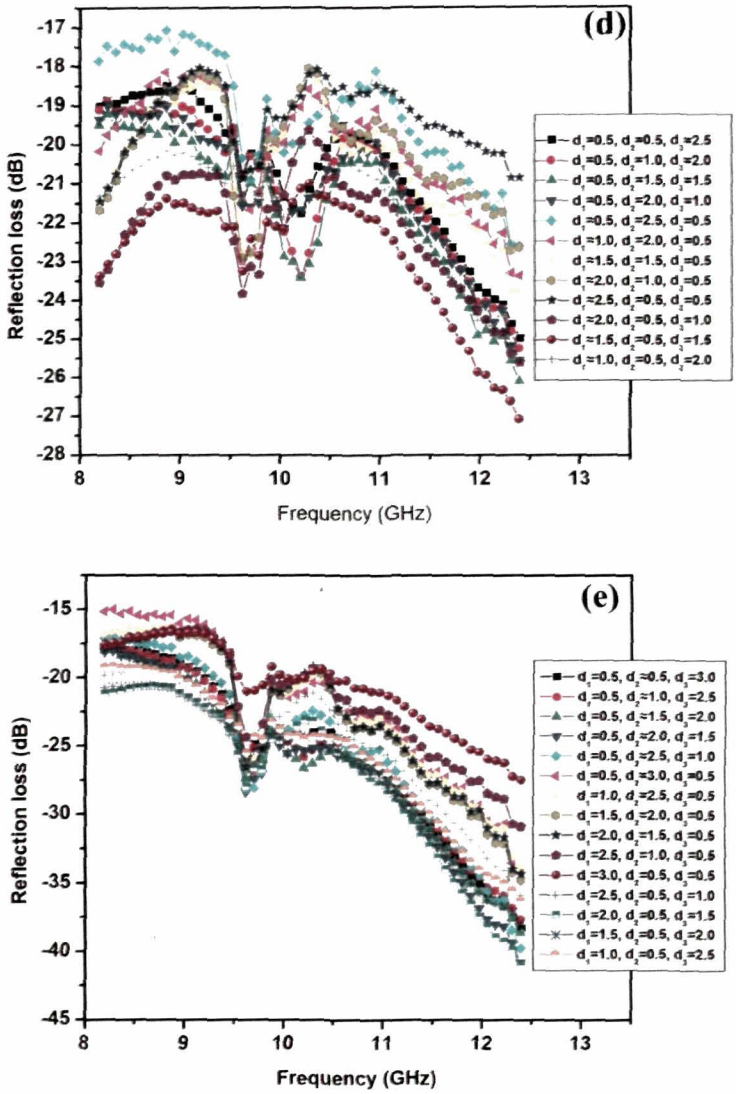

Figure 5.6 Reflection loss of three layered ferrite-NPR nanocomposite for **BCA** combinations with total thickness (a) 2.0 mm, (b) 2.5 mm, (c) 3.0 mm, (d) 3.5 mm, and (e) 4.0 mm

The maximum absorption peak, -20 dB and -10 dB absorption bandwidth and optimized individual layer thickness is tabulated in table 5.7. The three layered absorber for **BCA** configuration, for *d*=2 mm, with interface layer **A**= 0.5 mm, sandwich layer, **C**= 1.0 mm and layer near to metal plate, **B**=0.5 mm, shows a maximum absorption of -57.18 dB at 10.22 GHz with -20 dB bandwidth of 3.8 GHz.

Table 5.7 Performance parameters of the designed **BCA** triple layer absorber with different thickness of the layers

d (mm)	Thickness of individual layers (mm)			RLc (dB)	f_r (GHz)	-20dB BW (GHz)	d (mm)	Thickness of individual layers (mm)			RLc (dB)	f_r (GHz)	-20dB BW (GHz)
	d_1	d_2	d_3					d_1	d_2	d_3			
2.0	0.5	0.5	1.0	-42.80	10.21	3.8	3.0	0.5	0.5	2.0	-22.85	10.21	2.0
	0.5	**1.0**	**0.5**	**-57.18**	**10.22**	**3.8**		**0.5**	**1.0**	**1.5**	**-24.5**	**10.21**	**2.0**
	1.0	0.5	0.5	-42.27	10.21	4.1		0.5	1.5	1.0	-23.69	10.21	2.4
2.5	0.5	0.5	1.5	-27.56	10.21	3.2		0.5	2.0	0.5	-23.31	8.2	2.0
	0.5	1.0	1.0	-31.84	10.21	3.8		2.0	0.5	0.5	-30.28	8.2	2.0
	0.5	**1.5**	**0.5**	**-30.09**	**8.9**	**3.8**		1.5	0.5	1.0	-30.28	8.2	4.2
	1.5	0.5	0.5	-36.64	8.4	4.2		1.0	0.5	1.5	-26.63	8.2	4.2
	1.0	1.0	0.5	-33.47	8.6	4.2		1.0	1.5	0.5	-27.4	8.2	2.5
	1.0	0.5	1.0	-31.26	8.8	4.2		1.5	1.0	0.5	-29.84	8.2	3.3
3.5	0.5	0.5	1.0	-25.07	12.4	2.5	4.0	0.5	0.5	3.0	-38.10	12.4	3.2
	0.5	**1.0**	**0.5**	**-25.27**	**12.4**	**2.5**		0.5	1.0	2.5	-38.12	12.4	3.2
	1.0	0.5	0.5	-26.09	12.4	3.3		0.5	1.5	2.0	-38.58	12.4	3.2
	0.5	0.5	1.5	-25.6	12.4	2.5		0.5	2.0	1.5	-41.00	12.4	3.4
	0.5	1.0	1.0	-22.66	12.4	1.3		0.5	2.5	1.0	-39.73	12.4	3.4
	0.5	1.5	0.5	-23.40	12.4	1.5		0.5	3.0	0.5	-39.20	12.4	2.8
	1.5	0.5	0.5	-23.88	12.4	1.7		1.0	2.5	0.5	-35.8	12.4	2.8
	1.0	1.0	0.5	-22.92	9.6	1.5		1.5	2.0	0.5	-34.89	12.4	2.8
	1.0	0.5	1.0	-20.84	9.6	0.8		2.0	1.5	0.5	-34.20	12.4	2.1
	0.5	0.5	1.0	-25.56	12.4	4.0		2.5	1.0	0.5	-30.85	12.4	2.9
	0.5	1.0	0.5	-27.11	12.4	4.2		3.0	0.5	0.5	-27.39	12.4	1.9
	1.0	0.5	0.5	-25.6	12.4	4.2		2.5	0.5	1.0	-35.7	12.4	3.1
								2.0	**0.5**	**1.5**	**-41.00**	**12.4**	**4.2**
								1.5	0.5	2.0	-38.12	12.4	4.2
								1.0	0.5	2.5	-36.24	12.4	3.4

d = Total thickness, RLc = Reflection loss, f_r = Resonant frequency, BW=Bandwidth

5.3.5 CAB layer combination

The RL_c plots for **CAB** combinations with varying total thickness from 2 mm – 4 mm, is plotted in figures 5.7(a-e).

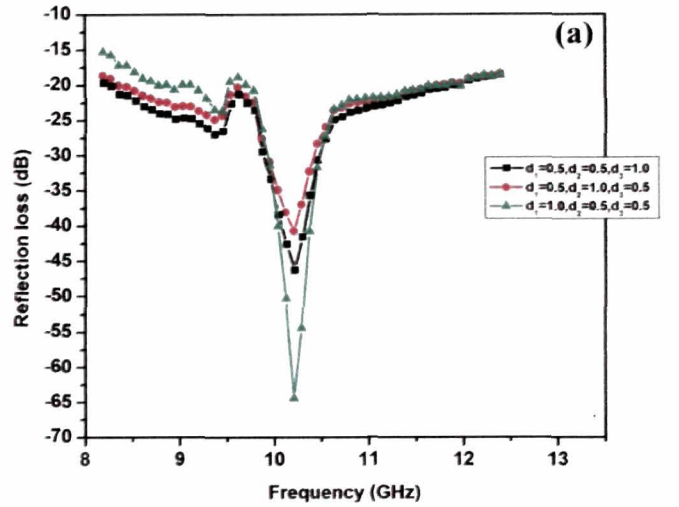
(a)
Reflection loss (dB)
Frequency (GHz)
d1=0.5,d2=0.5,d3=1.0
d1=0.5,d2=1.0,d3=0.5
d1=1.0,d2=0.5,d3=0.5

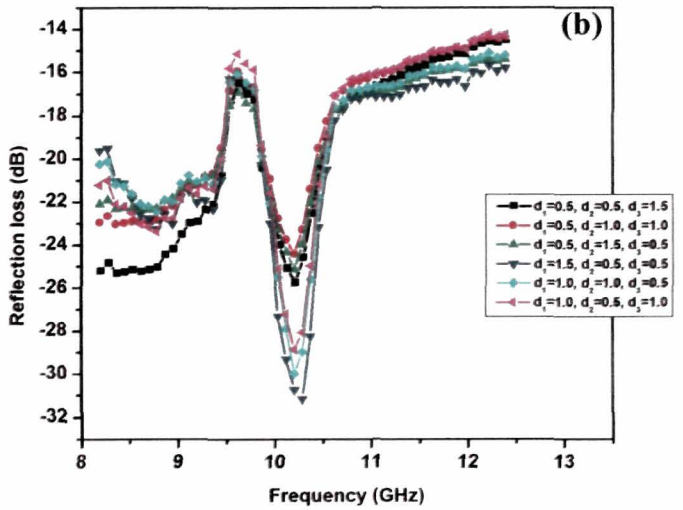
(b)
Reflection loss (dB)
Frequency (GHz)
d1=0.5, d2=0.5, d3=1.5
d1=0.5, d2=1.0, d3=1.0
d1=0.5, d2=1.5, d3=0.5
d1=1.5, d2=0.5, d3=0.5
d1=1.0, d2=1.0, d3=0.5
d1=1.0, d2=0.5, d3=1.0

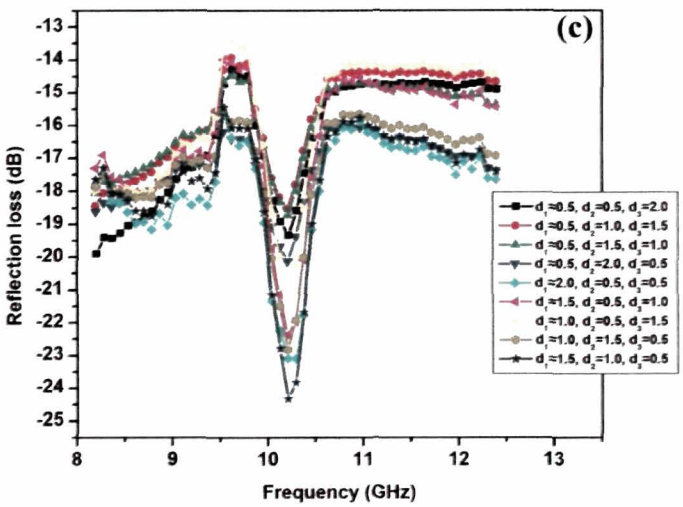
(c)
Reflection loss (dB)
Frequency (GHz)
d1=0.5, d2=0.5, d3=2.0
d1=0.5, d2=1.0, d3=1.5
d1=0.5, d2=1.5, d3=1.0
d1=0.5, d2=2.0, d3=0.5
d1=2.0, d2=0.5, d3=0.5
d1=1.5, d2=0.5, d3=1.0
d1=1.0, d2=0.5, d3=1.5
d1=1.0, d2=1.5, d3=0.5
d1=1.5, d2=1.0, d3=0.5

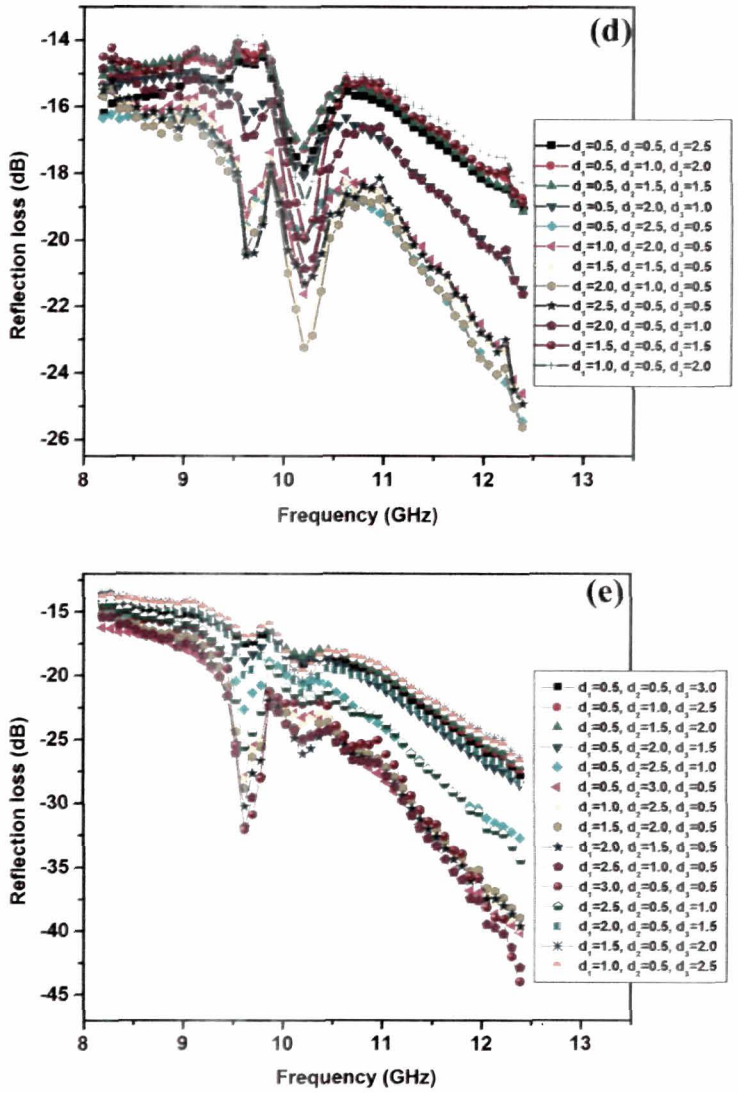

Figure 5.7 Reflection loss of three layered ferrite-NPR nanocomposite for **CAB** combinations with total thickness (a) 2.0 mm, (b) 2.5 mm, (c) 3.0 mm, (d) 3.5 mm, and (e) 4.0 mm

The maximum absorption peak, -20 dB and -10 dB absorption bandwidth and optimized individual layer thickness is tabulated in table 5.8.

The three layered absorber with **CAB** configuration, for *d*=2 mm, with interface layer **B**= 1.0 mm, sandwich layer, **A**= 0.5 mm and layer near to metal plate, **C** =0.5 mm shows a maximum absorption of -64.58 dB at 10.22 GHz with -20 dB bandwidth of 3 GHz.

Table 5.8 Performance parameters of the designed **CAB** triple layer absorber with different thickness of the layers

d (mm)	Thickness of individual layers (mm)			RLc (dB)	f_r (GHz)	-20dB BW (GHz)	d (mm)	Thickness of individual layers (mm)			RLc (dB)	f_r (GHz)	-20dB BW (GHz)
	d_1	d_2	d_3					d_1	d_2	d_3			
2	0.5	0.5	1.0	-46.27	10.21	3.4	3.0	0.5	0.5	2.0	-19.33	10.21	-
	0.5	1.0	0.5	-40.73	10.21	3.3		0.5	1.0	1.5	-18.50	10.21	-
	1.0	0.5	0.5	-64.58	10.22	3.0		0.5	1.5	1.0	-18.71	10.22	-
2.5	0.5	0.5	1.5	-25.75	10.21	1.9		0.5	2.0	0.5	-20.13	10.21	0.2
	0.5	1.0	1.0	-24.37	10.20	1.8		2.0	0.5	0.5	-23.11	10.25	0.4
	0.5	1.5	0.5	-25.18	10.19	1.8		1.5	0.5	1.0	-22.37	10.23	0.3
	1.5	0.5	0.5	-31.58	10.29	1.8		1.0	0.5	1.5	-21.06	10.21	0.2
	1.0	1.0	0.5	-29.89	10.21	1.7		1.0	1.5	0.5	-22.81	10.21	0.4
	1.0	0.5	1.0	-28.83	10.21	1.7		1.5	1.0	0.5	-24.32	10.21	0.4
3.5	0.5	0.5	1.0	-19.10	12.4	-	4.0	0.5	0.5	3.0	-27.85	12.4	1.4
	0.5	1.0	0.5	-18.71	12.4	-		0.5	1.0	2.5	-27.34	12.4	1.4
	1.0	0.5	0.5	-19.13	12.4			0.5	1.5	2.0	-27.05	12.4	1.4
	0.5	0.5	1.5	-21.44	12.4	0.4		0.5	2.0	1.5	-28.53	12.4	1.6
	0.5	1.0	1.0	-25.43	12.4	1.2		0.5	2.5	1.0	-32.67	12.4	2.6
	0.5	1.5	0.5	-24.64	12.4	1.5		0.5	3.0	0.5	-40.04	12.4	3.0
	1.5	0.5	0.5	-24.84	12.4	1.5		1.0	2.5	0.5	-39.76	12.4	3.0
	1.0	1.0	0.5	-25.65	12.4	1.6		1.5	2.0	0.5	-38.89	12.4	3.0
	1.0	0.5	1.0	-24.93	12.4	1.7		2.0	1.5	0.5	-39.61	12.4	3.0
	0.5	0.5	1.0	-21.62	12.4	0.7		2.5	1.0	0.5	-42.93	12.4	3.0
	0.5	1.0	0.5	-19.03	10.22	-		3.0	0.5	0.5	-43.99	12.4	2.9
	1.0	0.5	0.5	-18.89	10.22	-		2.5	0.5	1.0	-34.42	12.4	2.4
								2.0	0.5	1.5	-28.36	12.4	1.5
								1.5	0.5	2.0	-26.41	12.4	1.4
								1.0	0.5	2.5	-26.69	12.4	1.3

d = Total thickness, RLc = Reflection loss, f_r = Resonant frequency, BW=Bandwidth

5.3.6 CBA layer combination

The RL_c plots for **CBA** combinations with varying total thickness and individual layers are plotted in figures 5.8(a-e), respectively.

The maximum absorption peak, -20 dB and -10 dB absorption bandwidth and individual layer thickness is tabulated in table 5.9. The three layered absorber with **CBA** configuration, with d=2 mm, d_1=1.0 mm, d_2=0.5 mm and d_3=0.5 mm,

shows a maximum absorption of -84.14 dB at 10.21 GHz with -20 dB bandwidth of 3.6 GHz.

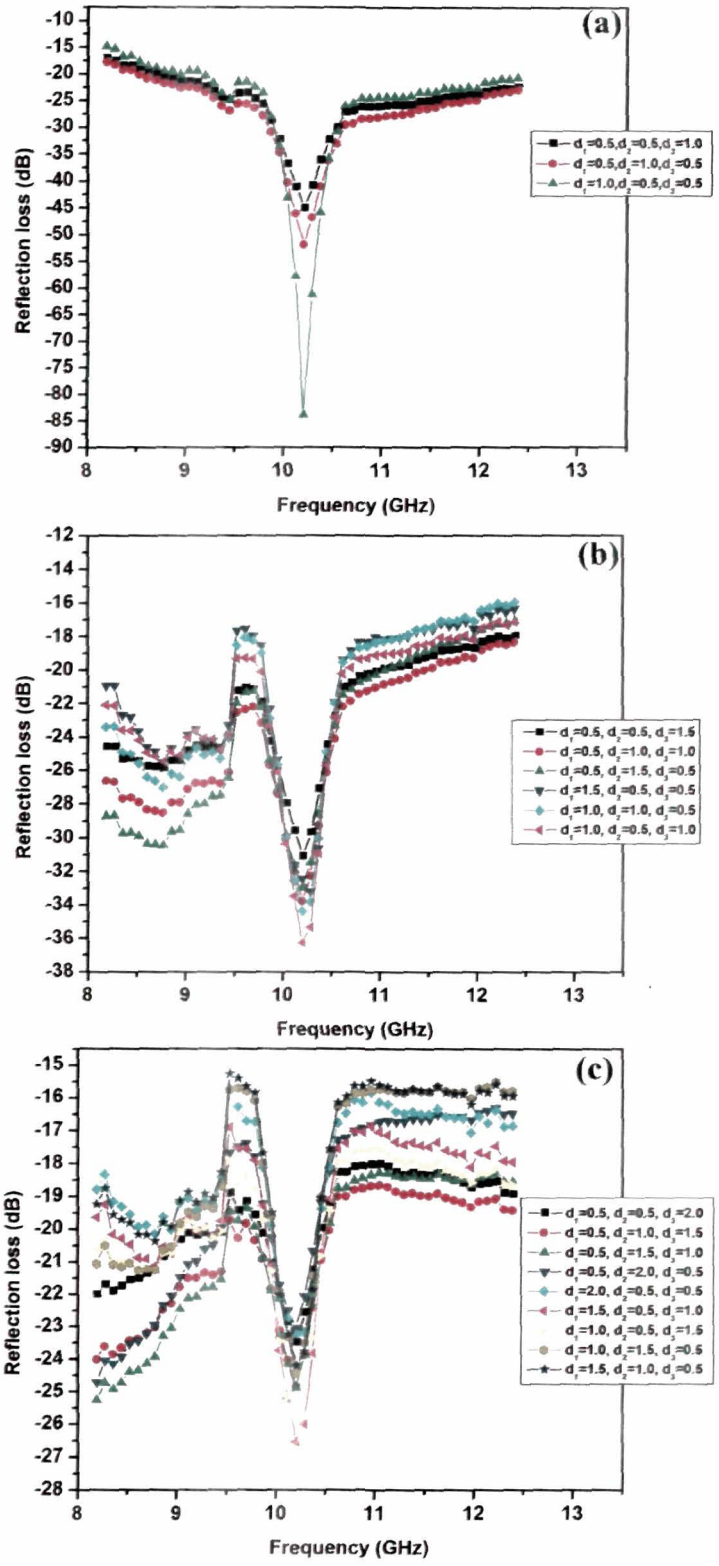

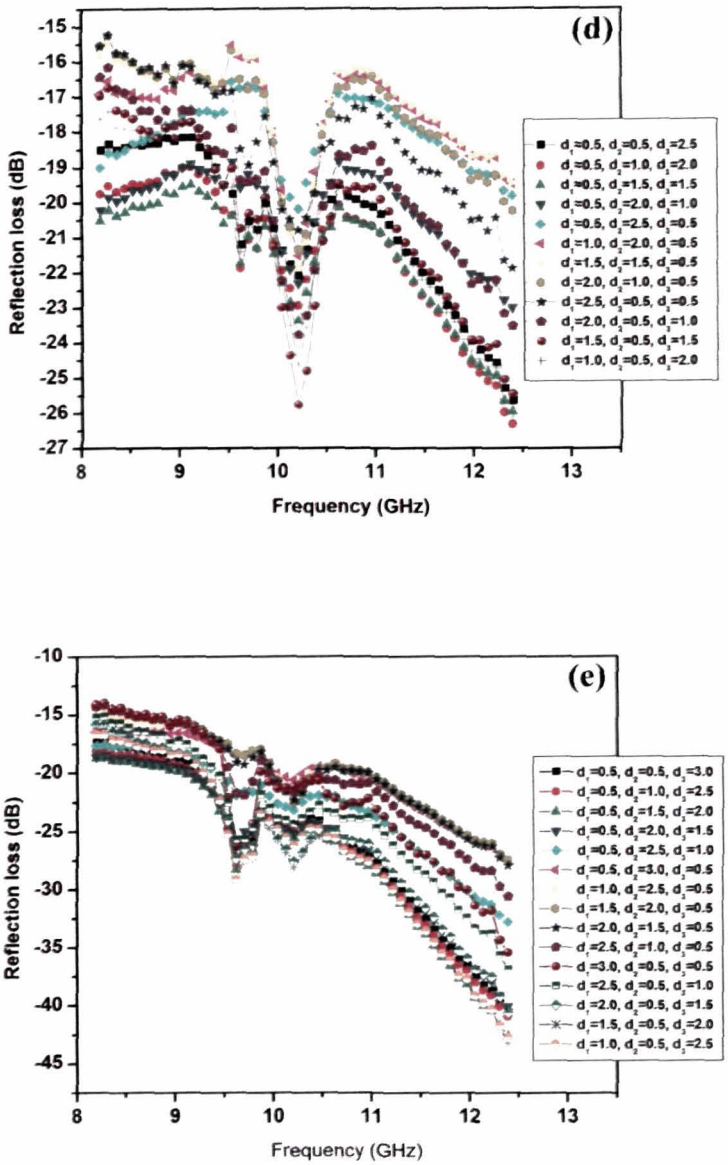

Figure 5.8 Reflection loss of three layered ferrite-NPR nanocomposite for **CBA** combinations with total thickness (a) 2.0 mm, (b) 2.5 mm, (c) 3.0 mm, (d) 3.5 mm, and (e) 4.0 mm

Table 5.9 Performance parameters of the designed **CBA** triple layer absorber with different thickness of the layers

d (mm)	Thickness of individual layers (mm)			RLc (dB)	f_r (GHz)	-20dB BW (GHz)	d (mm)	Thickness of individual layers (mm)			RLc (dB)	f_r (GHz)	-20dB BW (GHz)
	d_1	d_2	d_3					d_1	d_2	d_3			
2.0	0.5	0.5	1.0	-45.20	10.21	3.8	3.0	0.5	0.5	2.0	-23.54	10.21	1.9
	0.5	1.0	0.5	-51.64	10.21	3.9		0.5	1.0	1.5	-24.90	10.21	2.2
	1.0	0.5	0.5	-84.14	10.21	3.6		0.5	1.5	1.0	-25.29	8.2	2.1
2.5	0.5	0.5	1.5	-31.15	10.23	2.8		0.5	2.0	0.5	-24.66	8.2	1.9
	0.5	1.0	1.0	-33.74	10.21	3.2		2.0	0.5	0.5	-23.21	10.21	0.6
	0.5	1.5	0.5	-33.18	10.21	2.8		1.5	0.5	1.0	-26.50	10.21	0.6
	1.5	0.5	0.5	-33.18	10.29	2.1		1.0	0.5	1.5	-26.70	10.21	1.7
	1.0	1.0	0.5	-34.38	10.21	2.1		1.0	1.5	0.5	-24.45	10.21	1.3
	1.0	0.5	1.0	-36.32	10.21	2.1		1.5	1.0	0.5	-24.21	10.21	0.9
3.5	0.5	0.5	1.0	-25.69	12.4	2.6	4.0	0.5	0.5	3.0	-40.20	12.4	3.1
	0.5	1.0	0.5	-26.30	12.4	3.0		0.5	1.0	2.5	-40.90	12.4	3.2
	1.0	0.5	0.5	-26.00	12.4	3.0		0.5	1.5	2.0	-42.90	12.4	3.4
	0.5	0.5	1.5	-22.90	12.4	1.7		0.5	2.0	1.5	-40.10	12.4	3.2
	0.5	1.0	1.0	-20.17	10.21	-		0.5	2.5	1.0	-32.74	12.4	2.9
	0.5	1.5	0.5	-21.50	10.21	0.3		0.5	3.0	0.5	-27.50	12.4	1.6
	1.5	0.5	0.5	-21.95	10.21	0.3		1.0	2.5	0.5	-27.60	12.4	3.1
	1.0	1.0	0.5	-21.40	10.21	0.4		1.5	2.0	0.5	-27.61	12.4	1.6
	1.0	0.5	1.0	-21.88	12.4	0.4		2.0	1.5	0.5	-27.95	12.4	1.6
	0.5	0.5	1.0	-23.79	10.21	1.7		2.5	1.0	0.5	-30.75	12.4	2.5
	0.5	1.0	0.5	-25.74	10.20	2.6		3.0	0.5	0.5	-35.50	12.4	2.6
	1.0	0.5	0.5	-26.09	12.4	2.6		2.5	0.5	1.0	-36.87	12.4	3.0
								2.0	0.5	1.5	-40.70	12.4	3.1
								1.5	0.5	2.0	-43.20	12.4	3.1
								1.0	0.5	2.5	-42.75	12.4	3.1

d = Total thickness, RLc = Reflection loss, f_r = Resonant frequency, BW=Bandwidth

From the above results, it is seen that all the six layer combination with varying thickness, the absorbers with total thickness of 2 mm is giving the maximum absorption with broad bandwidth of absorption.

5.4 DESIGN RESULTS FOR THREE LAYERED FERRITE-NPR COMPOSITE FOR d=2 mm

Table 5.10, tabulates maximum RL_c and -20 dB bandwidth, for d=2 mm with corresponding real impedance, Z_{in}' and imaginary impedance, Z_{in}''. Figures

5.9 (a-c) show the RL_c and real and imaginary input impedance plots for all the combinations, for 2 mm thick three layered absorber.

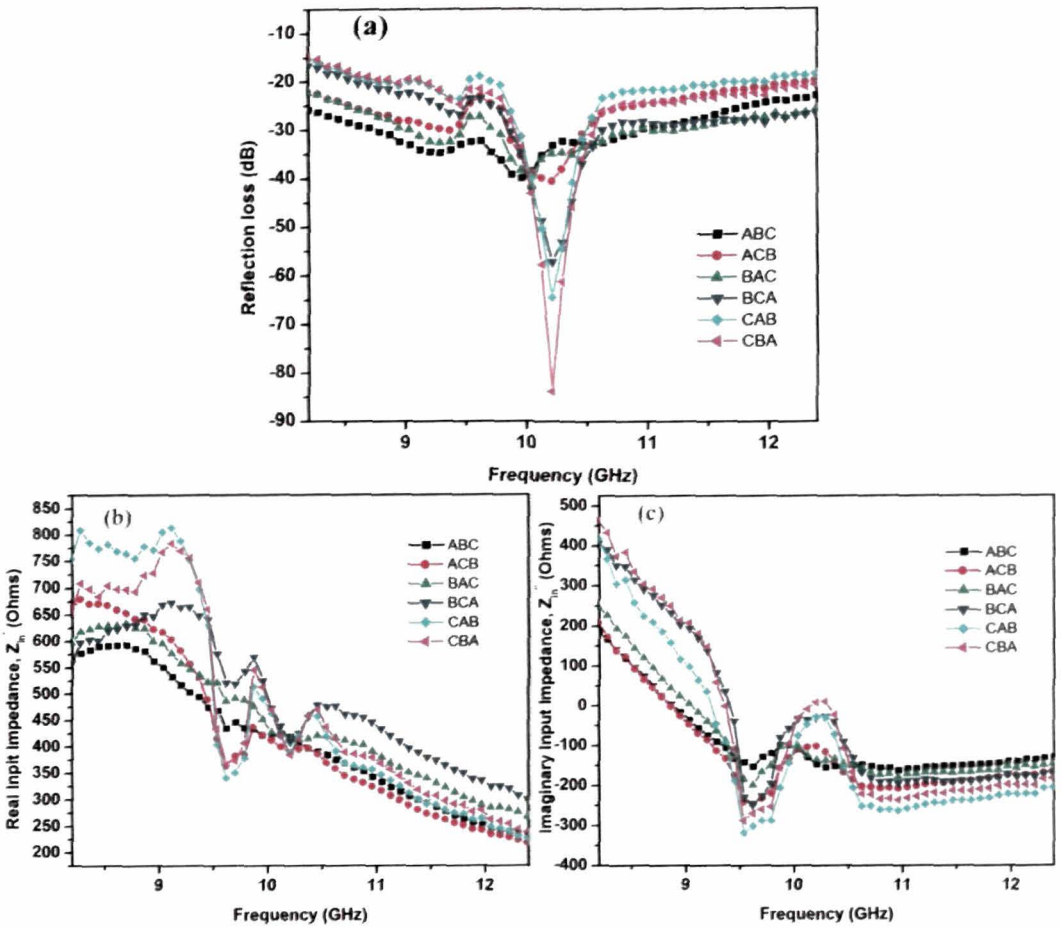

Figure 5.9 Comparative results of three layered ferrite-NPR nanocomposites with different layer combination with total thickness, d=2 mm

Table 5.10 Comparative results of three layered ferrite-NPR nanocomposites with different layer combination with total thickness, d=2 mm

Design combination	d_1	d_2	d_3	Maximum Reflection loss (dB)	Resonant frequency (GHz)	-20dB bandwidth (GHz)	Real impedance, $Z_{in}'(\Omega)$	Imaginary impedance, $Z_{in}''(\Omega)$
ABC	0.5	1.0	0.5	-39.99	9.97	4.2	420.37	-105.55
ACB	0.5	0.5	1.0	-40.57	10.23	4.2	390.56	-104.54
BAC	0.5	0.5	1.0	-41.02	10.05	4.2	427.82	-105.53
BCA	0.5	1.0	0.5	-57.18	10.22	3.8	405.46	-29.04
CAB	1.0	0.5	0.5	-64.58	10.22	3.0	388.07	-31.32
CBA	1.0	0.5	0.5	-84.14	10.21	3.6	380.10	13.12

From table 5.10, it can be seen that both Z_{in}' and Z_{in}'', corresponding to the maximum absorption peak frequency of 10.2 GHz, approaches to impedance matching condition of free space. Layer combination **CBA** i.e. with $Ba_{0.6}Sr_{0.4}Fe_{12}O_{19}$-NPR as the first layer and, $BaFe_{12}O_{19}$-NPR as the interphase layer and thickness ratio, 1.0:0.5:0.5 shows the closest value of 380 Ω and 13.12 Ω approaching to the free space values of 377 Ω and 0 Ω and absorption of -84.14 dB with -20 dB bandwidth of 3.6 GHz. The combination **BCA** ($BaAl_{1.6}Fe_{10.4}O_{19}$-NPR as the first layer and $BaFe_{12}O_{19}$-NPR as the interphase layer) and **BAC** ($Ba_{0.6}Sr_{0.4}Fe_{12}O_{19}$-NPR as the interphase layer and $BaAl_{1.6}Fe_{10.4}O_{19}$-NPR as the first layer), shows sufficiently good absorption peak with a broad -20 dB absorption bandwidth. **BCA** shows maximum absorption of - 57.18 dB with a -20 dB bandwidth of 3.8 GHz. **BAC** show absorption of -41.02 dB with a -20 dB bandwidth of 4.2 GHz. **ACB** is also showing a comparable absorption of -40.75 dB with -20 dB bandwidth of 4.2 GHz. But while comparing the -30 dB bandwidth with the **BAC** design, it is seen that **BAC** is showing a much broader bandwidth than the **ACB** design. The -30 dB bandwidth for **ACB** is 0.6 GHz and that is for **BAC** is 1.7 GHz. **CBA** shows maximum absorption of -84.14 dB at 10.21 GHz with -20 dB bandwidth of 3.6 GHz.

Layer configuration **BCA**, **BAC** and **CBA** are chosen to be fabricated as three layer sheet for measuring reflection loss using free space technique. The choice is done taking maximum absorption peak followed by maximum -20 dB bandwidth.

5.5. RESULTS AND ANALYSIS OF MEASURED REFLECTION LOSS VALUE OF THREE LAYERED MICROWAVE ABSORBER

The three layered absorbers with layer configurations, **BCA**, **BAC** and **CBA** are fabricated with dimensions 152 x 152 mm and thickness 2 mm. The individual layers with thickness, d_1, d_2 and d_3, as mentioned in table 5.10, is made seperately by mechanical mixing and thermal treatment method and then combined using the thermal treatment at 150 °C such that keeping the layer configuration in mind e.g. for **BCA** combination the layers **B** i.e. 50 wt.% $BaAl_{1.6}Fe_{10.4}O_{19}$-NPR

nanocomposite is next to the metal plate and 50 wt.% $BaFe_{12}O_{19}$-NPR nanocomposite as the air-absorber interfacing layer and 50 wt.% $Ba_{0.6}Sr_{0.4}Fe_{12}O_{19}$-NPR nanocomposite as the sandwiched layer. The free space microwave absorption measurement is performed similar to single layer absorption using Agilent E8362C VNA and spot focusing horn lens antenna system described in Chapter IV. The RL_m for **BCA, CBA** and **BAC** three layered absorbers are plotted with frequency in figure 5.10.

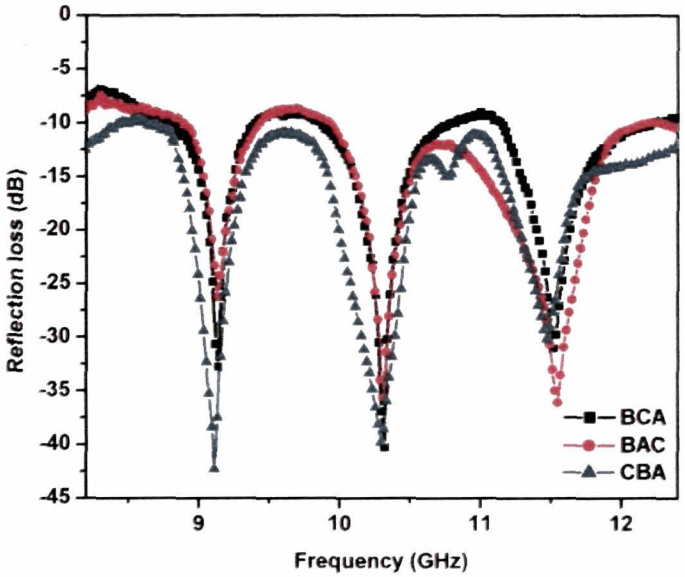

Figure 5.10 Measured reflection loss value of designed triple layer absorbers

Table 5.11 RLm, -20dB and -10dB bandwidth for **BCA**,**BAC** and **CBA** three layered absorber

Performance of absorption	**BCA**	**BAC**	**CBA**
RL_m (dB) at f_r (GHz)	-32.8 dB (9.12 GHz)	-25.9 dB (9.13 GHz)	-42.1 dB (9.12 GHz)
	-40.2 dB (10.31 GHz)	-36.1 dB (10.33 GHz)	-33.4 dB (10.29 GHz)
	-31.1 dB (11.51 GHz)	-35.7 dB (11.55 GHz)	-29.2 dB (11.48 GHz)
-20 dB bandwidth	(9.00-9.3) GHz	(9.00-9.20) GHz	(8.9-9.30) GHz
	(10.10-10.42) GHz	(10.20-10.50) GHz	(9.9-10.5) GHz
	(11.31-11.64) GHz	(11.23-11.76) GHz	(11.2-11.70) GHz
-10 dB bandwidth	(8.5-9.5) GHz	(8.8-9.5) GHz	(8.2-12.4) GHz
	(9.7-10.9) GHz	(9.8-12.4) GHz	
	(11.1-12.4) GHz		

The reflection loss values with corresponding frequencies and -20 dB and -10 dB bandwidth of the three layered absorber with **BCA, BAC** and **CBA** confurations

are given in table 5.11. All the three absorber samples show three maximum absorption peaks. The **BCA, BAC** and **CBA** design absorber show overall -20 dB absorption bandwidth of 0.96 GHz, 1.03 GHz and 1.5 GHz, respectively and overall -10 dB absorption bandwidth for the same layer combinations as 3.5 GHz, 3.3 GHz and 4.2 GHz, respectively. The maximum absorption peak obtained for **CBA** is -42.10 dB at 9.10 GHz, for **BAC** is -36.10 dB at 10.31 GHz and for **BCA** is -40.20 dB at 10.31 GHz. Table 5.12 gives the measured and calculated performance of three layer absorber. Though the maximum absorption values and - 20 dB bandwidth values differes, a close proximity is found for -10 dB bandwidth and the frequency corresponding to the maximum absorption peak.

As mentioned earlier the absorber is modeled as transmission line using some approximations, which may effect the computed values of microwave absorption. The fabrication limitations may reduce the absorption of the layered absorber. The measured reflection loss value of the three layer design structure shows that absorption frequency band can be enhanced and tuned by proper selection of the ferrite-NPR nanocomposition.

Table 5.12 Performance comparison of calculated and measured RLc with -10 dB and -20 dB bandwidth of three layer microwave absorber

Three layer combination	Calculated				Measured			
	RLc_{max} (dB)	f_r (GHz)	-10 dB BW (GHz)	-20 dB BW (GHz)	RLm_{max} (dB)	f_r (GHz)	-10 dB BW (GHz)	-20 dB BW (GHz)
BCA	-57.17	10.22	4.2	3.8	-40.20	10.31	3.5	0.96
CBA	-64.58	10.22	4.2	3.0	-42.10	9.10	4.2	1.50
BAC	-39.24	10.05	4.2	4.2	-36.10	10.31	3.3	1.03

5.6 CONCLUSIONS

The best performance of ferrite-NPR nanocompositions for single and three layered structure in the X-band range is compared, table 5.13. Considering the fact that thickness of both the structure is same, an enhanced -10 dB bandwidth is observed for the layered structures almost covering the entire X-band.

Table 5.13 Performance comparison of conductor backed single, double and triple layer microwave absorber

Performance parameters	Single layer absorber			Three layered(CBA)absorber
	$BaFe_{12}O_{19}$-NPR	$BaAl_{1.6}Fe_{10.4}O_{19}$-NPR	$SrFe_{12}O_{19}$-NPR	
Min*RL*(dB) at GHz	-37.06 dB (9.5 GHz)	-40. 06 dB (9.46 GHz)	-43.06 dB (9.70 GHz)	-42.10 dB (9.10 GHz)
-10dB absorption bandwidth	2.0 GHz	4.0 GHz	1.8 GHz	X-band (8.2-12.4 GHz
-20dB absorption bandwidth	0.60 GHz	0.78 GHz	0.36 GHz	1.5 GHz

The CBA layer combination shows -42.10 dB aborption with -20 dB bandwidth of 1.5 GHz and -10 dB bandwidth i.e. 90% of incident power being absorbed over the whole X-band. The results shows that three layer ferrite-NPR nanocomposite systems can be used as an efficient broad band absorber over the entire X-band.

References

[1] Feng, Y.B., et al. Absorbing properties and structural design of microwave absorbers based on carbonyl iron and barium ferrite, *J. Magn. Magn. Mater.***318,** 8-13, 2007.

[2] Gogoi, J. P. et al. Single layer microwave absorber based on expanded graphite-novolac phenolic resin composite for X-band applications, *Compos. Part, B. Eng.***58,** 518–523, 2014.

[3] Asi, M. J. and Dib, N. I. Design of multilayer microwave broadband absorbers using central force optimization, *Prog. Electromagn. Res. B.* **26,** 101-113, 2010.

[4] Reinert, J. et al. On the potential of graded-chiral dallenbach absorbers, *Microw. Opt. Technol. Lett.***30,** 254–257, 2001.

[5] Kim JW, and Kim SS. Microwave absorbers of two-layer composites laminate for wide oblique incidence angles, *Mater. Design***31,** 1547–1552, 2010.

[6] Zhang, Z. et al. Design principle of single- or double-layer wave-absorbers containing left-handed materials, *Mater. Design***30,** 3908–3912, 2009.

[7] Wei, C. et al. Double-layer microwave absorber based on nanocrystalline $Zn_{0.5}Ni_{0.5}Fe_2O_4$/α-Fe Micıofibers, *Mater. Design***35,** 363–368, 2012.

[8] Feng, YB. et al. Absorbing properties and structural design of microwave absorbers based on carbonyl iron and barium ferrite, *J Magn. Magn. Mater.* **318,** 8–13, 2007.

[9] Liao, ZQ. et al. Effect of FeCoB–SiO2-film-based fractal frequency selective surface on the absorption properties of microwave absorbers, *IEEE Magn. Lett.* **1,** 5000204, 2010.

[10] Chen, MX. et al. Gradient multilayer structural design of CNTs/SiO2 composites for improving microwave absorbing properties, *Mater. Design*32, 3013–6, 2011.

[11] Meshram M. R., *Transmission line modeling (TLM) for evaluation of absorption in ferrite based multi-layer microwave absorber,*CONFERENCE ON CONVERGENT TECHNOLOGIES FOR ASIA-PACIFIC REGION (TENCON 2003), 626-630, 2003.

[12] Liu, H. et al. Three-layer structure microwave absorbers based on nanocrystalline alpha-Fe, Fe0.2(Co0.2Ni0.8)0.8 and Ni0.5Zn0.5Fe2O4 porous microfibers, *J. Nanosci. Nanotechnol.* **14**, 2878-84, 2014.

[13] Zhang, X. and Sun, W. Three-layer microwave absorber using cement-based composites, *Mag. Concrete. Res.* **63**, 157 -162, 2001.

[14] Micheli, D. et al. M. X-Band microwave characterization of carbon-based nanocomposite material, absorption capability comparison and RAS design simulation, *J. Compos. Sc. Tech.* **70**, 400–409, 2010.

[15] Jiang, L. et al. Pareto optimal design of multilayer microwave absorbers for wide-angle incidence using genetic algorithms, *IET Microw. Antennas Propag.* **3**, 572–579, 2009.

[16] Qin, F. and Brosseau, C. A review and analysis of microwave absorption in polymer composites filled with carbonaceous particles, *J. Appl. Phys.* **111**, 061301-1-24, 2012.

CHAPTER VI

FDTD FULL WAVE ANALYSIS FOR MAGNETIC ABSORBER

6.1 INTRODUCTION

Kane Yee in 1966 [1] was first to develop the algorithm for finite-difference time-domain method to determine initial boundary value problems involving Maxwell's equations in the isotropic media. The descriptor "Finite-difference time-domain" and its corresponding "FDTD" acronym originated by Allen Taflove in a 1980 [2]. The FDTD method discretizes the time dependent Maxwell's equation vector components using central difference approximations for space and partial derivatives for time. The EM wave solution in FDTD is found in space grid. The time-stepping algorithm, often called as leap frog arrangement is followed, in which at any point in space - the updated value of the E-field in time is dependent on the stored value of the E-field and the numerical curl of the local distribution of the H-field in space and similarly the updated value of the H-field in time is dependent on the stored value of the H-field and the numerical curl of the local distribution of the E-field in space. The method can solve Maxwell's equations on any scale with almost all kinds of environments [3-6]. FDTD has inherent advantage being simple and versatile [7], and allows the user to specify the material properties at all points within the computational domain. Thus, FDTD scheme has been extensively applied to anisotropic materials and also to dispersive materials [8-10]. However for electromagnetic interference shielding materials, different approaches have been adopted. Jianfeng Xu et. al. reported a study on full wave analysis of magneto dielectric absorbing sheets [11], in this approach a microstrip line is specially designed on the absorbing sheet for the FDTD analysis. Pyramidal absorbers were modelled using FDTD technique by A. Khajehpour and S. A. Mirtaheri employing Debye model [12]. A study on ferrite absorber implementing FDTD technique was carried out by Youji Kotsuka, Mitsuhiro Ammo [13]. Approximations were made to achieve the matching characteristic by punching out small holes in the conventional rubber ferrite.

The 3D FDTD formulation is developed here, for the em wave progressing through a single layer metal backed magnetic absorber using $BaFe_{12}O_{19}$-NPR

nanocomposite. Since there is no external electric or magnetic field perturbation and the magnetic substrate used is homogeneous as depicted from figure 2.13 [section 2.3.3 of chapter II], the permittivity and permeability properties are taken as isotropic.

The chapter initially explains FDTD method to simulate wave propagation in the nanocomposite systems. The implementation of numerical features like the computational domain, stability criteria, boundary conditions, subsequent gridding and time stepping for updating for electric and magnetic fields is discussed consequently. The material properties, ε_r and μ_r, of the $BaFe_{12}O_{19}$-NPR nanonanocomposites with 50 wt.%, measured and analyzed in chapter III, is used for the simulation. The propagation and attenuation of the source pulse within the material is investigated from the scattering parameter study. The FDTD results are compared with experimentally obtained reflection loss results discussed in chapter IV.

6.2 PROBLEM FORMULATION FOR ABSORBER

The FDTD method provides a direct time domain solutions of Maxwell's equations in differential form by discretizing both the physical region and time interval using a uniform grid (figure 6.1a). An electromagnetic wave interaction

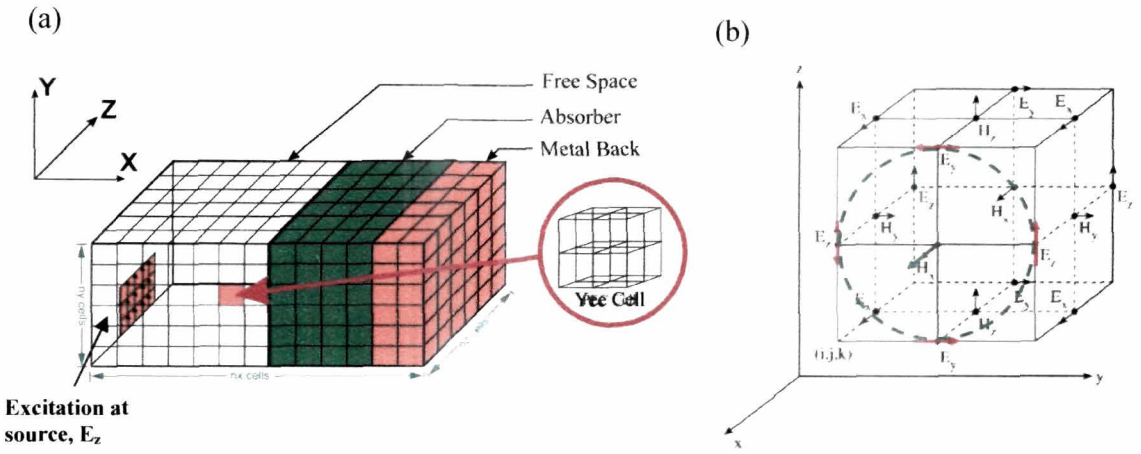

Figure 6.1 (a) Three dimensional gridding in FDTD (b) Basic Yee cell in three dimensions

structure is mapped into the three dimensional space lattice by assigning appropriate values of permittivity to each electric field component, and permeability to each magnetic field component, known as Yee cells and shown in figure 6.1b.

The general form of Maxwell's equation for the magnetic media having isotropic permittivity and permeability [14] is given as,

$$\frac{\partial \underline{D}}{\partial t} = \nabla \times \underline{H} \quad (6.1\ a)$$

$$\underline{D}(\omega) = \varepsilon_0 \varepsilon_r \underline{E}(\omega) \quad (6.1\ b)$$

$$-\mu \frac{\partial \underline{H}}{\partial t} = \nabla \times \underline{E} \quad (6.1\ c)$$

where, $\underline{E}$ is the electric field, $\underline{H}$ is the magnetic field ε_r relative complex permittivity and ε_0 is the free space permittivity. μ is the permeability and is expressed as $\mu = \mu_0 \mu_r$ where μ_0 is the free space permeability and μ_r is the relative complex permeability of the medium.

The computational domain for em wave interaction with absorber is defined in figure 6.1a. In this problem, the magnetic ferrite nanocomposite layer with a metal backing is placed at the +ve X-direction, with a radiating source, shown as shaded region in the Y-Z plane. The numbers of cells in the direction of propagation i.e. along +ve X-direction are kept more than the Y- and Z- direction. Again, the number of cells in free space within the computational domain, is kept larger as compared to the number of cells in the absorber layer and the metal backing. This formulation approximates the far field source and normal incidence of the em wave on the absorber surface.

The 3D FDTD scheme for the magnetic absorber can be realized in two modules:

a) Maxwell's curl equations are expressed in terms of partial differential forms.
b) These scalar equations are expressed in finite differential form in spatial and temporal coordinates

c) The electric field and magnetic field gets updated, both at every space grid coordinates and time stepping.

6.2.1 Expression of E and H curl equations in partial differential form

The Maxwell's curl equations 6.1 (a) and (c) are quite similar. As μ_0 and ε_0 differ by several orders of magnitude, $\underline{E}$ and $\underline{H}$ also differ by several orders of magnitude. This is circumvented by normalizing the Maxwell's curl equations considering the following change of the variables as

$$E = \sqrt{\frac{\varepsilon_0}{\mu_0}}\underline{E} \tag{6.2}$$

$$H = \sqrt{\frac{\varepsilon_0}{\mu_0}}\underline{H} \tag{6.3}$$

All the $\underline{E}$ and $\underline{H}$ components of isotropic magnetic systems from the Maxwell's equations 6.1 (a) and 6.1 (c) can be expressed in scalar form as,

$$\frac{\partial D_x}{\partial t} = \frac{1}{\sqrt{\varepsilon_0\mu_0}}\left(\frac{\partial H_z}{\partial y} - \frac{\partial H_y}{\partial z}\right) \tag{6.4 a}$$

$$\frac{\partial D_y}{\partial t} = \frac{1}{\sqrt{\varepsilon_0\mu_0}}\left(\frac{\partial H_x}{\partial z} - \frac{\partial H_z}{\partial x}\right) \tag{6.4 b}$$

$$\frac{\partial D_z}{\partial t} = \frac{1}{\sqrt{\varepsilon_0\mu_0}}\left(\frac{\partial H_y}{\partial x} - \frac{\partial H_x}{\partial y}\right) \tag{6.4 c}$$

$$\frac{\partial H_x}{\partial t} = \frac{-1}{\mu_r\sqrt{\varepsilon_0\mu_0}}\left(\frac{\partial E_z}{\partial y} - \frac{\partial E_y}{\partial z}\right) \tag{6.5 a}$$

$$\frac{\partial H_y}{\partial t} = \frac{-1}{\mu_r\sqrt{\varepsilon_0\mu_0}}\left(\frac{\partial E_x}{\partial z} - \frac{\partial E_z}{\partial x}\right) \tag{6.5 b}$$

$$\frac{\partial H_z}{\partial t} = \frac{-1}{\mu_r\sqrt{\varepsilon_0\mu_0}}\left(\frac{\partial E_y}{\partial x} - \frac{\partial E_x}{\partial y}\right) \tag{6.5 c}$$

6.2.2 Expression of E and H partial differential equations in finite differential form in spatial and temporal coordinates

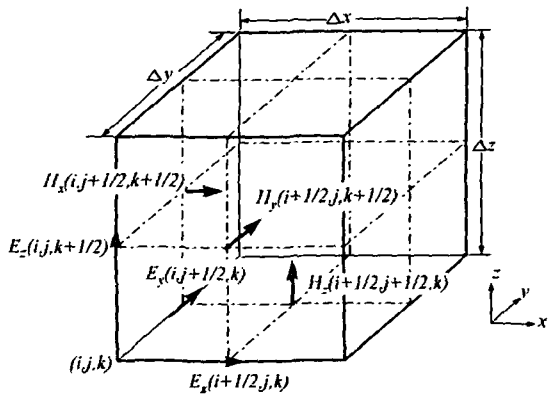

Figure 6.2 Yee's mesh

Finite difference approximation solution of the Maxwell's partial differential equations 6.4 (a-c) and 6.5 (a-c) are found by discretizing the problem space over a finite three dimensional computational domain in spatial and temporal coordinates in accordance to the Yee's mesh as shown in figure 6.2 and is written as

$$D_x^{n+1/2}\left(i+\frac{1}{2},j,k\right)=D_x^{n-1/2}\left(i+\frac{1}{2},j,k\right)+\frac{\Delta t}{\Delta y\cdot\sqrt{\varepsilon_0\mu_0}}\left[H_z^n\left(i+\frac{1}{2},j+\frac{1}{2},k\right)\right.$$
$$\left.-H_z^n\left(i+\frac{1}{2},j-\frac{1}{2},k\right)\right]-\frac{\Delta t}{\Delta z\cdot\sqrt{\varepsilon_0\mu_0}}\left[H_y^n\left(i+\frac{1}{2},j,k+\frac{1}{2}\right)-H_y^n\left(i+\frac{1}{2},j,k-\frac{1}{2}\right)\right] \quad (6.6\text{ a})$$

$$D_y^{n+1/2}\left(i,j+\frac{1}{2},k\right)=D_y^{n-1/2}\left(i,j+\frac{1}{2},k\right)+\frac{\Delta t}{\Delta z\cdot\sqrt{\varepsilon_0\mu_0}}\left[H_x^n\left(i,j+\frac{1}{2},k+\frac{1}{2}\right)-H_x^n\left(i,j+\frac{1}{2},k-\frac{1}{2}\right)\right]$$
$$-\frac{\Delta t}{\Delta x\cdot\sqrt{\varepsilon_0\mu_0}}\left[H_z^n\left(i+\frac{1}{2},j+\frac{1}{2},k\right)-H_z^n\left(i-\frac{1}{2},j+\frac{1}{2},k\right)\right] \quad (6.6\text{ b})$$

$$D_z^{n+1/2}\left(i,j,k+\frac{1}{2}\right)=D_z^{n-1/2}\left(i,j,k+\frac{1}{2}\right)+\frac{\Delta t}{\Delta x\cdot\sqrt{\varepsilon_0\mu_0}}\left[H_y^n\left(i+\frac{1}{2},j,k+\frac{1}{2}\right)\right.$$
$$\left.-H_y^n\left(i-\frac{1}{2},j,k+\frac{1}{2}\right)\right]-\frac{\Delta t}{\Delta y\cdot\sqrt{\varepsilon_0\mu_0}}\left[H_x^n\left(i,j+\frac{1}{2},k+\frac{1}{2}\right)-H_x^n\left(i,j-\frac{1}{2},k+\frac{1}{2}\right)\right] \quad (6.6\text{ c})$$

The modified finite difference equations for the scalar equations 6.5(a) through 6.5(c) are,

$$H_x^{n+1/2}\left(i,j+\frac{1}{2},k+\frac{1}{2}\right)=H_x^{n-1/2}\left(i,j+\frac{1}{2},k+\frac{1}{2}\right)-\frac{\Delta t}{\Delta y\cdot\mu_r\sqrt{\varepsilon_0\mu_0}}\left[E_z^n\left(i,j+1,k+\frac{1}{2}\right)\right.$$
$$\left.-E_z^n\left(i,j,k+\frac{1}{2}\right)\right]+\frac{\Delta t}{\Delta z.\mu_r\sqrt{\varepsilon_0\mu_0}}\left[E_y^n\left(i,j+\frac{1}{2},k+1\right)-E_y^n\left(i,j+\frac{1}{2},k\right)\right] \quad (6.7\text{ a})$$

$$H_y^{n+1/2}\left(i+\frac{1}{2},j,k+\frac{1}{2}\right)=H_y^{n-1/2}\left(i+\frac{1}{2},j,k+\frac{1}{2}\right)-\frac{\Delta t}{\Delta z\cdot\mu_r\sqrt{\varepsilon_0\mu_0}}\left[E_x^n\left(i+\frac{1}{2},j,k+1\right)\right.$$
$$\left.-E_x^n\left(i+\frac{1}{2},j,k\right)\right]+\frac{\Delta t}{\Delta x\cdot\mu_r\sqrt{\varepsilon_0\mu_0}}\left[E_z^n\left(i+1,j,k+\frac{1}{2}\right)-E_z^n\left(i,j,k+\frac{1}{2}\right)\right] \quad (6.7\text{ b})$$

$$H_z^{n+1/2}\left(i+\frac{1}{2},j+\frac{1}{2},k\right)=H_z^{n-1/2}\left(i+\frac{1}{2},j+\frac{1}{2},k\right)-\frac{\Delta t}{\Delta x\cdot\mu_r\sqrt{\varepsilon_0\mu_0}}\left[E_y^n\left(i+1,j+\frac{1}{2},k\right)\right.$$
$$\left.-E_y^n\left(i,j+\frac{1}{2},k\right)\right]+\frac{\Delta t}{\Delta y\cdot\mu_r\sqrt{\varepsilon_0\mu_0}}\left[E_x^n\left(i+\frac{1}{2},j+1,k\right)-E_x^n\left(i+\frac{1}{2},j,k\right)\right] \quad (6.7\text{ c})$$

6.3 CRITERIA FOR FDTD IMPLEMENTATION

At first the computational domain is to be defined, over which the FDTD will be implemented. Figure 6.3 shows the computational domain. The gridding of the 3D structure (figure 6.1 (a)) is carried out considering the stability conditions. The geometry of the concern structure is expressed in terms of material properties. Perfectly matching layer (PML) boundary conditions are initially defined within the actual computational domain. A Gaussian pulse is applied as the input stimulus and at discreet time steps, the *E* and the *H* field components are updated in leap frog manner. The spatial field distribution can be visualized from

the simulated E components in three dimensions. To extract the scattering parameters, Fourier transformation of the transient response is taken.

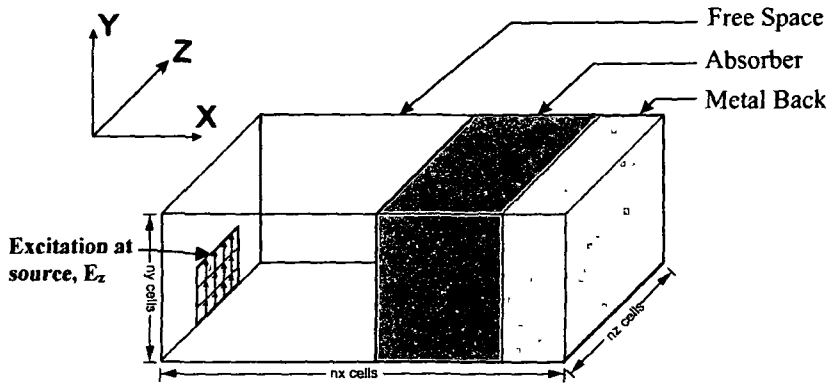

Figure 6.3 Three dimensional problem cell

Important numerical features viz. stability criteria, absorbing boundary condition, source consideration and frequency dependent parameters, required for the 3D FDTD scheme implementation are described in the following sub-sections.

6.3.1 Stability criteria in FDTD

In order to ensure that the central-difference algorithm is numerically stable, there exists a maximum value for the time step and also space discretization which can be used. An electromagnetic wave propagating in free space cannot go faster than the speed of light. To propagate a distance of one cell of dimension Δx, minimum time required is $\Delta t = \Delta x / c_{\max}$. Kunz and Luebbers [15] recommend that to ensure stability, there should be at least four cells per minimum wavelength. For good stability, some particularly sensitive problems [6], up to twenty cells per wavelength are required at the frequency of interest in order to get the required accuracy. Depending on the cell size, the size of the time step, Δt, can be determined from the Courant's stability criterion. For the three dimensional case, the Courant's stability criterion is defined as [7, 15-17]

$$\Delta t \leq \frac{1}{c_{\max}\sqrt{\frac{1}{\Delta x^2}+\frac{1}{\Delta y^2}+\frac{1}{\Delta z^2}}} \tag{6.8}$$

where, c_{max} is the maximum velocity of light within the computational volume. Typically, c_{max} is taken as the velocity of light in free space unless the entire volume is filled with magnetic material. Δx, Δy and Δz are the Cartesian space increments which must be within an order or magnitude of each other. In n dimensional simulation, the maximum time step can be defined in simplified form as

$$\Delta t = \frac{\Delta x}{\sqrt{n}\cdot c_{\max}} \tag{6.9}$$

6.3.2 Absorbing boundary conditions

Effective absorbing boundary conditions (ABC) are required for truncation of an infinite or unbound simulation region. A two dimensional boundary condition, called the perfectly matched layer (PML) was proposed by Berenger in 1994. This condition enables efficient absorption of outgoing radiation [18, 19]. Katz et al. reported that the PML ABC is easily extensible to three dimensions [20]. Implementation of PML ABC was demonstrated by Saario in his Ph. D. thesis, considering the issues such as problem definition, efficient memory utilization and execution speed [17].

The basic scheme of the PML is that if a wave is propagating in medium A and it impinges upon medium B, the amount of reflection is dictated by the intrinsic impedances of the two media, η_A and η_B (figure 6.4)

$$\Gamma = \frac{\eta_A - \eta_B}{\eta_A + \eta_B} \tag{6.10}$$

where,

$$\eta = \sqrt{\frac{\mu}{\varepsilon}} \tag{6.11}$$

and are determined by the permittivity ε and permeability μ of the two media.

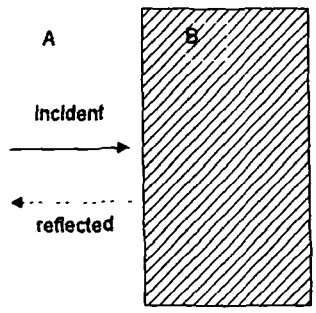

Figure 6.4 The reflection at the interface of two media

The propagating pulse in the absorbing medium covering the computational domain should die out before it reaches the external boundary. For this "fictitious" dielectric constant and permeability of the absorbing media is considered to be lossy and is added to the implementation codes. Thus, the flux density formulations of the Maxwell's curl equations with "fictitious" ε and μ are,

$$\varepsilon_F^* \frac{\partial \underline{E}}{\partial t} = \nabla \times \underline{H} \tag{6.12}$$

$$\underline{D}(\omega) = \varepsilon^*(\omega)\underline{E}(\omega) \tag{6.13}$$

$$\mu_F^* \frac{\partial \underline{H}}{\partial t} = -\nabla \times \underline{E} \tag{6.14}$$

There are two conditions to formulate a PML [21, 22]:

1. The impedance going from the background medium to the PML must be constant,

$$\eta_0 = \eta_m = \sqrt{\frac{\mu_{Fx}^*}{\varepsilon_{Fx}^*}} = 1 \tag{6.15}$$

The impedance is one because of our normalized units (free space).

2. In the direction perpendicular to the boundary (the X direction, for instance), the relative dielectric constant and relative permeability must be the inverse of those in the other directions, i.e.,

$$\varepsilon_{Fx}^* = \frac{1}{\varepsilon_{Fy}^*} \tag{6.16 a}$$

$$\mu_{Fx}^* = \frac{1}{\mu_{Fy}^*} \tag{6.16 b}$$

The 3D PML ABC [16] is included in developing the algorithm for the absorbing boundary treatment and the detail formulation is given as Appendix C.

6.3.3 Source considerations

The excitation can be of any shape, but, normally a Gaussian pulse is considered. This type of pulse has a frequency spectrum that is also Gaussian and thus provides frequency domain information from dc up to a desired cut-off frequency by adjusting the width of the pulse [23, 24]. In order to simulate a voltage source excitation, from a far field source, the pulse is initiated as vertical electric field, E_z, in a rectangular region at a far distance from the problem geometry, as shown in figure 6.3. The form of the input signal in a continuous form is

$$E_z = f(t) = e^{\frac{-(T-T_0)^2}{T_1}} \tag{6.17}$$

where, T is the current time-step, T_0 the pulse delay time-step and T_1 the width of the pulse in time-steps. The width of the Gaussian pulse sets the required cut-off frequency. The pulse width is normally chosen to have at least 20 points per wavelength at the highest frequency, significantly represented in the pulse. The numerical dispersion and truncation error is minimized. Initially, in the simulation, all the electric and magnetic fields are set to zero. The Gaussian pulse applied at the source has only a field component, i.e. E_z. A change in the electric field at the source with respect to time causes a change in the magnetic field in the y-direction.

6.3.4 Frequency dependent parameters

The final transient E field values, obtained after the FDTD simulation, are used to get wide band frequency response. The Fourier transform of the E field $E(t)$ at a frequency f_1 is done by the equation [16]

$$E(f_1) = \int_0^{t_T} E(t) \cdot e^{-j2\pi \cdot f_1 t} dt \tag{6.18}$$

The lower limit of the integral in equation (6.18) is 0, because the FDTD program assumes all casual functions. The upper limit is t_T, the time at which the FDTD iteration is halted. Equation (6.18) can be rewritten in a finite difference form as

$$E(f_1) = \sum_{n=0}^{T} E(n \cdot \Delta t) \cdot e^{-j2\pi \cdot f_1 (n \cdot \Delta t)} \tag{6.19}$$

where T is the number of iterations and Δt is the time step and hence $t_T = T.\ \Delta t$. Equation (6.19) is now divided into its real and imaginary parts as

$$E(f_1) = \sum_{n=0}^{T} E(n \cdot \Delta t) \cdot \cos(2\pi f_1 \cdot \Delta t \cdot n) - j \sum_{n=0}^{T} E(n \cdot \Delta t) \cdot \sin(2\pi f_1 \cdot \Delta t \cdot n) \tag{6.20 a}$$

$$\Rightarrow E(f_1) = \mathrm{Re}(E) - \mathrm{Im}(E) \tag{6.20 b}$$

6.4 IMPLEMENTATION IN COMPUTER PROGRAM

The existing finite difference approximation equations for single layer $BaFe_{12}O_{19}$-NPR nanocomposite is used for developing the code. Performance of absorber is analysed by S_{11} parameter at different time steps. In the formulation, focus is made on the reflection loss in terms of S_{11} parameter and internal field distribution. The single layer absorber is modelled with a metal backing. As S_{11} parameter depends on the geometry and material parameters of the absorber, thus, different cell dimensions in different directions are used.

The materials are defined in the FDTD code with their relative permittivity and permeability. From equation 6.1 (a), the electric field in the media is given by expressions,

$$E_x[i, j.k] = gax[i, j, k] * D_x[i, j, k] \tag{6.21 a}$$

$$E_y[i, j.k] = gay[i, j, k] * D_y[i, j, k] \tag{6.21 b}$$

$$E_z[i, j.k] = gaz[i, j, k] * D_z[i, j, k] \tag{6.21 c}$$

where,

$$gax[i, j, k] = {}^{1}/_{\varepsilon_r} \tag{6.22 a}$$

$$gay[i,j,k] = {}^{1}/_{\varepsilon_r} \quad (6.22\ b)$$

$$gaz[i,j,k] = {}^{1}/_{\varepsilon_r} \quad (6.22\ c)$$

where, ε_r is the relative complex permittivity of the media. The metal backing can be modelled by considering *gax, gay* and *gaz* to be zero at the PEC, in the propagation direction.

The complete flowchart for FDTD algorithm is shown in figure 6.5, highlighting the electric field and magnetic field updating modules. A MATLAB program is developed to implement this algorithm for study of single layer absorber and E and H updating code modules are listed in Appendix D. Other considerations in the algorithm for implementation in the code are summarised in the following sub-sections.

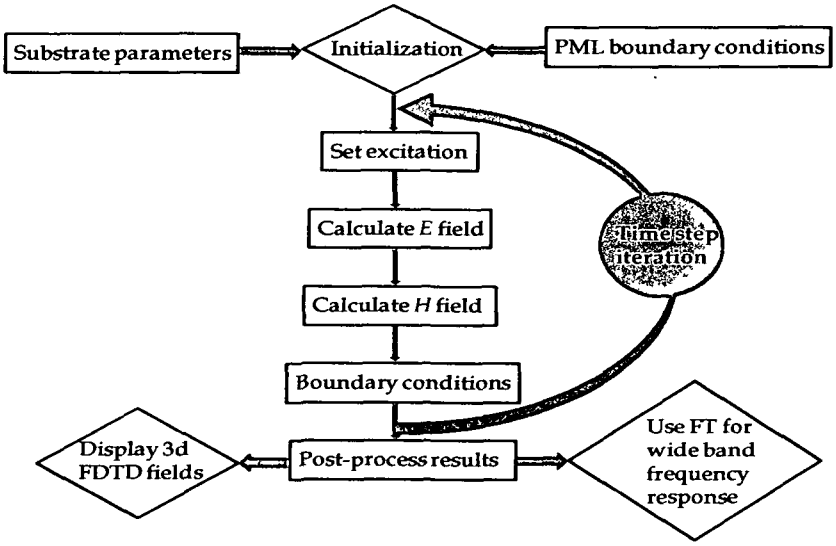

Figure 6.5 Main modules of 3D FDTD simulation algorithm

6.4.1 Stability criteria

The absorber nanocomposite, fabricated using $BaFe_{12}O_{19}$-NPR nanocomposite of dimension, 22.86 mm x 10.16 mm x 2 mm. The Yee's mesh is generated for the geometry by dividing the geometry into grid of different dimensions in different

directions in the computational domain. The computational volume is only partially filled with the nanocomposite material. In choosing the time step, the smallest grid dimension (Δx, Δy or Δz) is used in the Courant stability criterion, given by equation 6.8. Table 6.1 gives the time steps for different element sizes modelled.

6.4.2 Source consideration

The width of the Gaussian pulse for the specified cut-off frequency is determined from the equation 6.17. The pulse delay, T_0, is set at 50 time steps. The width of the pulse, T_1, is set as 20 time-step in order to achieve larger bandwidth. This pulse width of 20 time step and Δt = 0.031 picoseconds, gives a 15 GHz bandwidth.

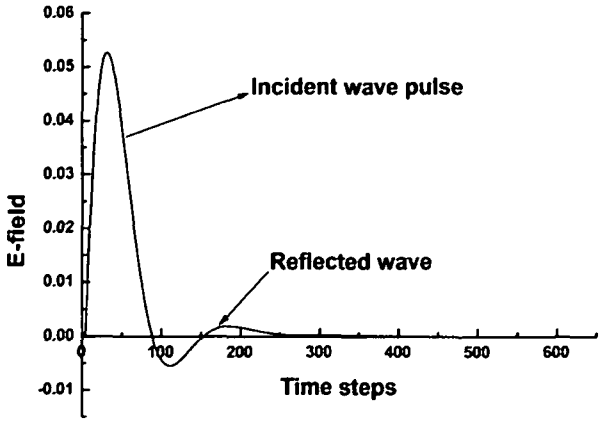

Figure 6.6 Gaussian pulses applied at the input source

The Gaussian pulse has optimum pulse-width and desired cut-off frequency and is used as excitation. The radiating source is excited with an E_z component in the Y-Z plane, as shown in figure 6.3.

6.4.3 PML terminating condition

The PML ABC is employed in the current program. Figure 6.7 illustrates the effectiveness of a 15 point PML with the source offset of one cell from the centre in the x, y and z directions. The RHS PML in the X-direction is replaced by a

perfectly electric conductor (PEC) plate and the propagated em wave is truncated at the termination end, figure 6.3. The outgoing pulse gets partially reflected when the pulse gets within fifteen points of the edge, which is inside the PML, where the distortion starts to occur.

6.4.4 Post processing of the results

After completion of the simulation process, the full wave distribution of the *E* and *H* wave can be viewed in all the planes of interest. To calculate the S_{11}, information at a single point is needed. In this case, the reference point is taken as the point just adjacent to the interface of the material to free space. After the simulation is over, the frequency response is calculated over the entire range of frequencies using Fourier transform. S_{11} parameter is calculated by gathering the voltage information at the point of interest. When the voltage is known, the values of E_z field at the reference point can be found. For first 350 time steps, the field values at the point are considered as input and the rest is considered as the reflected signal. The S_{11} in decibels is then expressed as,

$$S_{11}(f)_{dB} = 10.\log\frac{E_{out}(f)}{E_{in}(f)} \tag{6.23}$$

6.5 FULL-WAVE FDTD ANALYSIS OF $BaFe_{12}O_{19}$-NPR NANONANOCOMPOSITE ABSORBER

The FDTD full wave analysis is applied to single layer absorbing material developed using $BaFe_{12}O_{19}$-NPR nanocomposite with a metal backing. The design parameters used for implementation of FDTD simulation is given in table 6.1. The FDTD simulation implementation realizes as follows:

The FDTD simulation generates data which helps in visualizing the time progression of vector fields throughout the three-dimensional solution space. It gives a physical insight of complex field interactions at different stages of field propagation. In the present analysis, snap shot of E field distribution is taken at different time step.

The interaction of the em field with the single layer $BaFe_{12}O_{19}$-NPR

nanocomposite is analyzed by finding the scattering parameters by taking Fourier transformation of the transient E field component.

Table 6.1 Cell size in different directions for single layer nanocomposite

Substrate	dimension of the nanocomposite (l x b x d) (mm)	Δx (mm)	Δy (mm)	Δz (mm)	Δt (picosec.)
50 wt. % $BaFe_{12}O_{19}$ in NPR	22.86 x 10.16 x 2	0.259	0.285	0.25	0.41

The 3D algorithm applied for the nanocomposite material on substrate is given by the flow chart shown in figure 6.7.

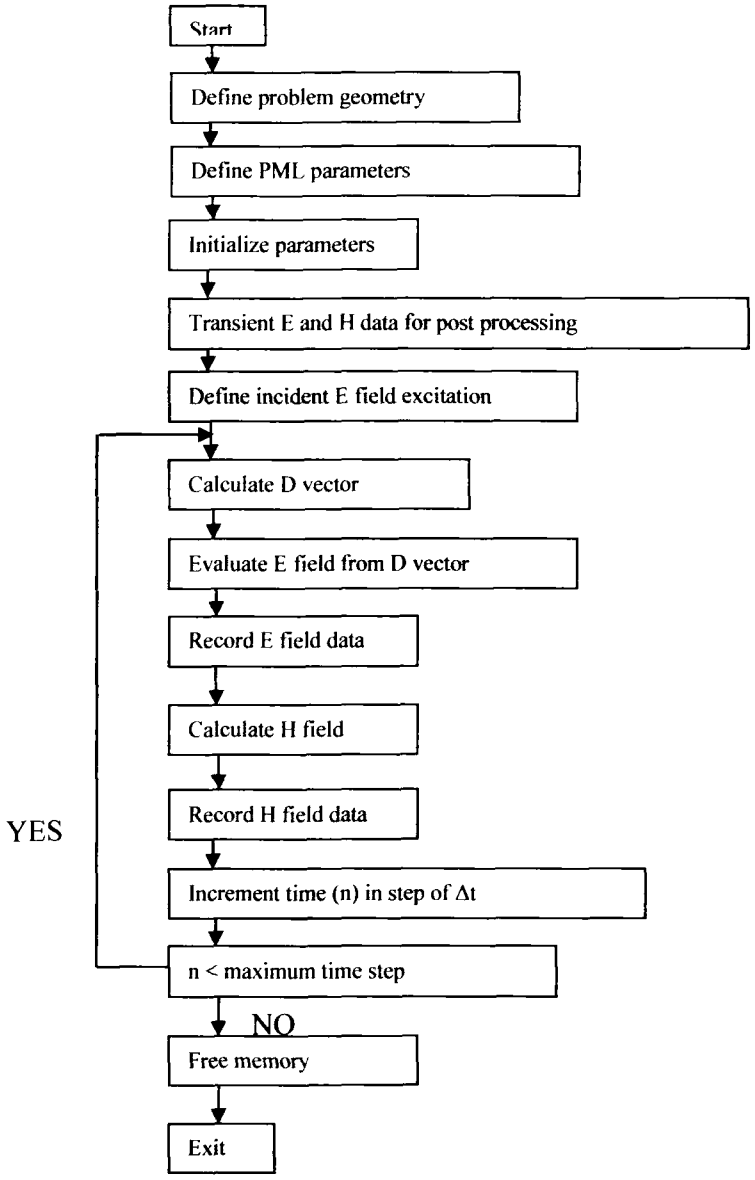

Figure 6.7 Flow chart of FDTD algorithm

6.5.1 E_z field distribution within the absorber

Figures 6.9 to 6.12 give the mode of propagation of E_z component of electric field in the X-Y plane i.e. along the propagation direction within the problem geometry at different time steps.

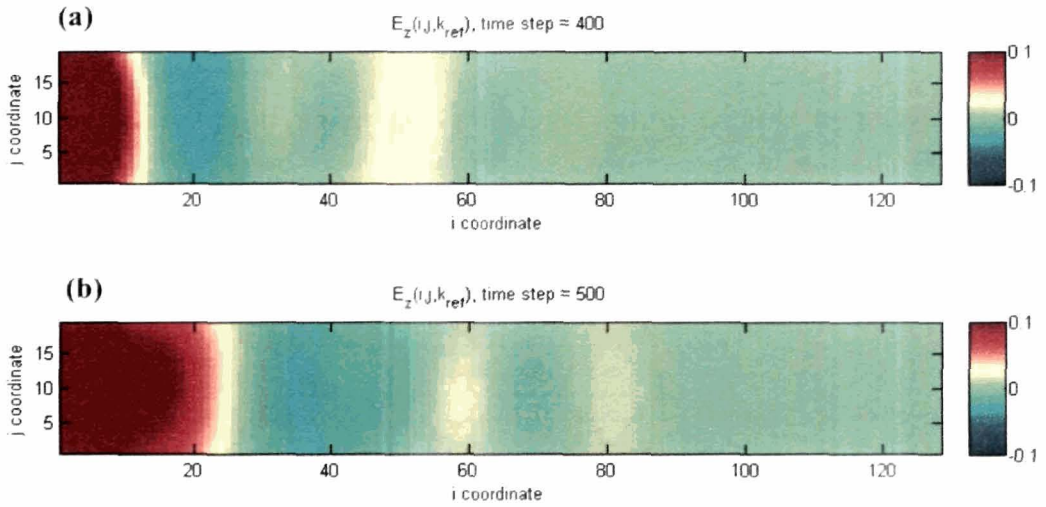

Figure 6.8 The FDTD simulated electric field components within the absorber at (a) 400 time steps and (b) 500 time steps

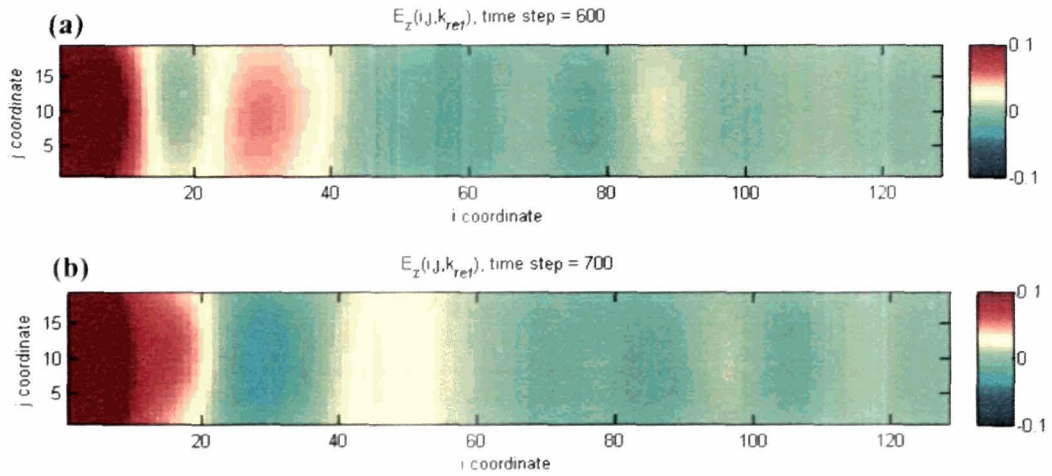

Figure 6.9 The FDTD simulated electric field components within the absorber at (a) 600 time steps and (b) 700 time steps

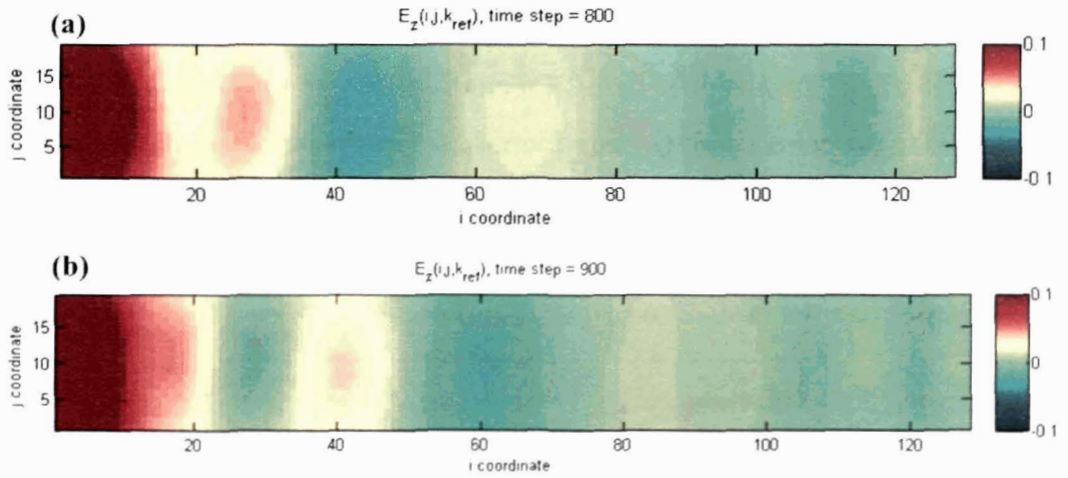

Figure 6.10 The FDTD simulated electric field components within the absorber at (a) 800 time steps and (b) 900 time steps

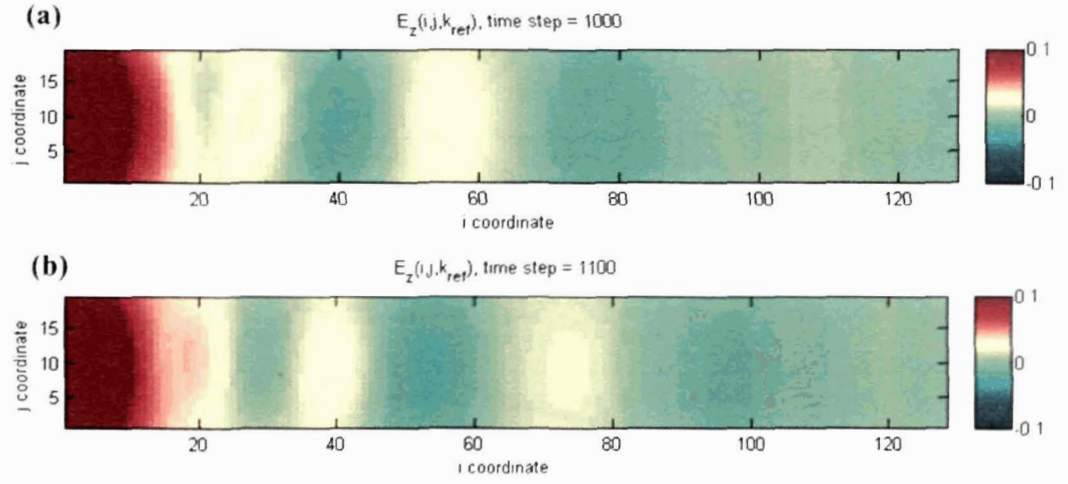

Figure 6.11 The FDTD simulated electric field components within the absorber at (a) 1000 time steps and (b) 1100 time steps

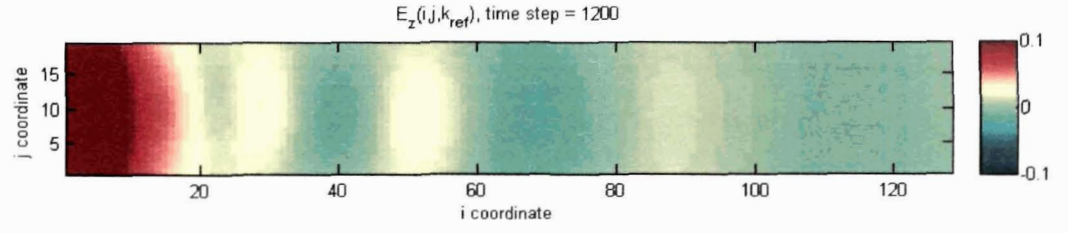

Figure 6.12 The FDTD simulated electric field components within the absorber at 1200 time steps

6.5.2 S_{11} parameter analysis

S_{11} parameters of the absorber using $BaFe_{12}O_{19}$-NPR nanocomposite is calculated in the FDTD program using the equation 6.23. The S_{11} obtained at different time steps are shown in figure 6.13. The S_{11} parameters at times step 1100 and 1200 is -25 dB at 9.5 GHz and -20 dB at 11.9 GHz. The simulated results at time step 1100 is compared with the measured results and shown in figures 6.14a and 6.14b.

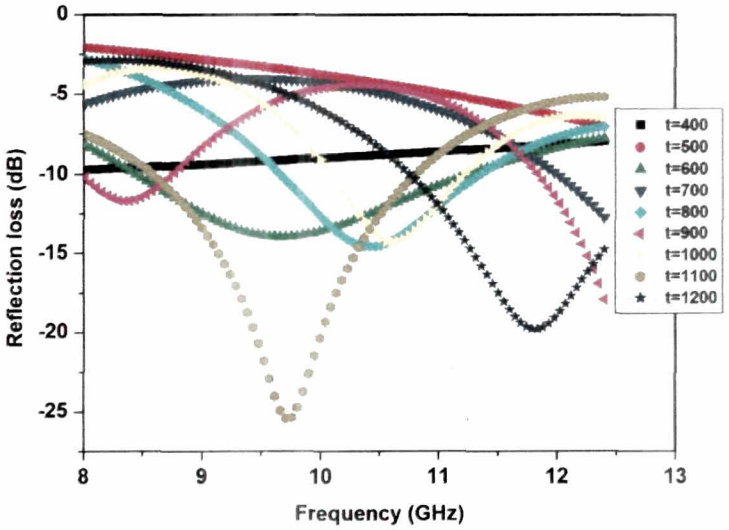

Figure 6.13 Reflection loss (S_{11}) of the 50 wt.% $BaFe_{12}O_{19}$-NPR nanocomposite at different time step

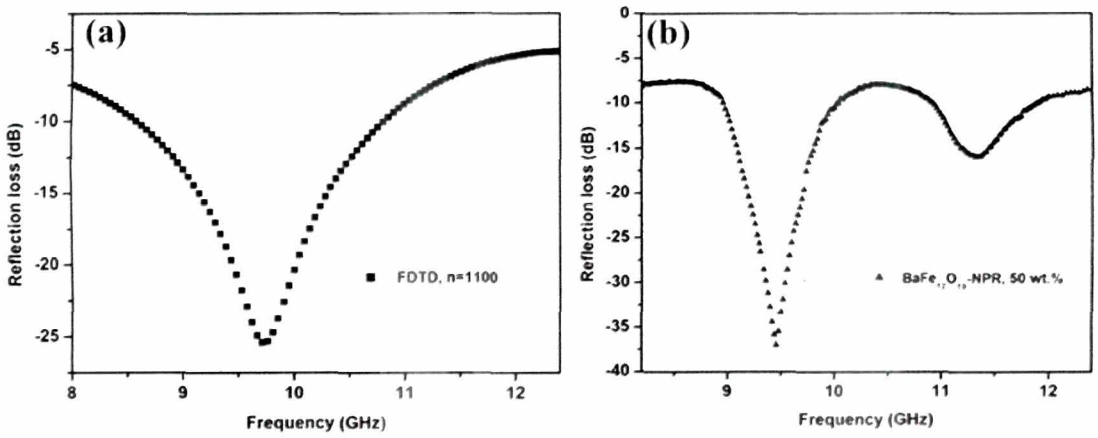

Figure 6.14 Reflection loss (S_{11}) of the 50 wt.% $BaFe_{12}O_{19}$-NPR nanocomposite from (a) FDTD at n=1100 and (b) measured

A comparable reflection loss parameter (S_{11}) of -25 dB is obtained from the FDTD data analysis at time step=1100, whereas for $BaFe_{12}O_{19}$-NPR nanocomposite with 50 wt.%, the measured reflection loss obtained is -37.06 dB at 9.5 GHz.

6.6 CONCLUSIONS

The FDTD technique is implemented for analysis of single layer absorber using $BaFe_{12}O_{19}$-NPR nanonanocomposite, having isotropic permittivity and permeability over the layer. This technique successfully analyses the full-wave electric field distribution and reflection loss of absorber. The electric field pattern shows that due to change in permittivity and permeability values in the magnetic material, the field distribution changes. A comparable reflection loss parameter is obtained for both the measured and FDTD results for the $BaFe_{12}O_{19}$-NPR nanonanocomposite with 50 wt.%. The technique can be implemented for substituted barium ferrite single layer absorber and multilayer absorber with parameter modifications.

References

1. Yee, K. S., Numerical solution of initial boundary value problems involving Maxwell's equations in isotropic media, *IEEE Trans. Antennas Propag.* **14**, 302-307, 1966.
2. Taflove, A. Application of the finite-difference time-domain method to sinusoidal steady state electromagnetic penetration problems, *IEEE Trans. Electromagn. Compat.* **22**(3), 191-202, 1980.
3. Kosmas, P. et al. Three-Dimensional FDTD model for GPR detection of objects buried in realistic dispersive soil, SPIE Aerosense Conference, Orlando, F L, 330-338, April 2002.
4. Taflove A. and Umashankar, K. R. Review of FD-TD numerical modeling of electromagnetic wave scattering and radar cross section, *Proc. IEEE* **77**, 682-699, 1989.
5. Gwarek, W. K. Analysis of arbitrarily shaped two-dimensional microwave circuits by finite-difference time-domain method, *IEEE Trans. Microw. Theory Tech.* **36**, 738- 744, Apr. 1988.
6. Zhang X. and Mei, K. K. Time-domain finite difference approach to the calculation of the frequency-dependent characteristics of microstrip discontinuities, *IEEE Trans. Microw. Theory Techn.* **36**, 1775-1787, 1988.
7. Taflove, A. Computation Electrodynamics: The Finite-Difference Time-Domain Method. (Boston, MA: Artech House, 1995).
8. Kashiwa T. and Fukai, I. A treatment by the FD-TD method of the dispersive characteristics associated with electronic polarization, *Microw. Opt. Technol. Lett.* **3**, 203-205, 1990.
9. Luebbers, R., et al. A frequency-dependent finite-difference time-domain formulation for dispersive materials, *IEEE Trans. Electromagn. Compat.* **32**, 222-227, 1990.
10. Lee, C. F., et al., Finite Difference Method for Electromagnetic Scattering Problems, *Prog. Electromagn. Res.* **4**, 373-442, 1991.

11. Xu J., et al. FDTD Modeling of Absorbing Materials for EMI Applications, 2010 ASIA-PACIFIC INTERNATIONAL SYMPOSIUM ON ELECTROMAGNETIC COMPATIBILITY, April 12-16, 2010, Beijing, China.
12. Khajehpour, A. and Mirtaheri, S. A., Analysis of pyramid em wave absorber by FDTD method and comparing with capacitance and homogenization methods, *Prog. Electromagn. Res. Lett.* **3**, 123-131, 2008.
13. Kotsuka, Y., Ammo, M. A method of effective use of ferrite for microwave absorber, *IEEE MIT-S Digest*, 2001.
14. Taflove, A. and Hagness, S. C. Computation Electrodynamics: The Finite-Difference Time-Domain Method, 2nd Edition. (Boston, MA: Artech House, 2000).
15. Kunz K. S. and Luebbers, R. J., The Finite Difference Time Domain Method for Electromagnetics, (Boca Raton, FL, CRC Press, 1993).
16. Sullivan, D. M., Electromagnetic Simulation Using the FDTD Method. (N.Y.: IEEE Press, 2000).
17. Saario, S. A., FDTD modelling for wireless communications: antennas and materials, Ph. D. Thesis, (Griffith University, September 2002).
18. Berenger, J. P., A perfectly matched layer for the absorbtion of electromagnetic waves, *J. Comput. Phys.* **114**, 185-200, 1994.
19. Berenger, J. P., Perfectly matched layer for the FDTD solution of wave-structure interaction problems, *IEEE Trans. Antennas Propag.* **44**,110-117, 1996.
20. Katz, D. S., et al., Validation and extension to three dimensions of the berenger PML absorbing boundary condition for FD-TD meshes, *IEEE Microw. Guided Wave Lett.* 4, 268-270, 1994.
21. Sullivan, D. M., A simplified PML for use with the FDTD method, *IEEE Microw. Guided Wave Lett.* **6**, 97-99, 1996.
22. Sacks, Z. S., et al., A perfectly matched anisotropic absorber for use as an absorbing boundary condition, *IEEE Trans. Antennas Propag.* **43**, 1460-1463, 1995.
23. Sheen, D., et al., Application of three-dimensional finite- difference method to the analysis of planar microstrip circuits, *IEEE MTT* **38**, 849-857, 1990.

24. Buchanan, W. J., Analysis of electromagnetic wave propagation using the 3D Finite-Difference Time-Domain method with parallel processing, Ph. D. Thesis, Napier University, (March 1996).

CHAPTER VII

ACHIEVEMENTS, LIMITATIONS AND FUTURE DIRECTIONS

Vast use of the gigahertz spectra leads to electromagnetic pollution in the environment which interference with devices causing problems such as jamming of signal, inaccuracy in target detection in warfare, difficulty in communication and also reduced camouflaging. For effective shielding for absorbers, there should be impedance matching (for zero reflection) at the air-absorber interface, amplitude attenuation and phase cancellation (thickness dependence). All the above characteristics are co-related with the material parameter: complex permittivity, ε and permeability, μ, and the frequency of operation.

The present research problem concentrated on development of absorbers with consistent absorption over X-band range, reducing simultaneously both dimension and weight, making it corrosion resistant and lastly cost effective.

M-type barium ferrite nanoparticles are synthesized from nitrate precursor using co-precipitation technique. The size variation is achieved by controlling the annealing conditions. Formation of single phase M-type barium ferrite is confirmed from XRD pattern. The average crystalline size of barium ferrite particles is in nanometre range. TEM analysis of barium ferrite shows the ferrite nanoparticle is hexagonal in shape. Extended rod like shape in one direction is observed for the particles annealed at 900 °C with crystal lattice plane of anisotropy along c-axis with particle size of ~70 nm. Barium ferrite particles with aluminium and strontium substitution also form single phase M-type hexagonal ferrite. Nanosized ferrites are reinforced in novalac phenolic resin (NPR) in different weight ratios. Density measurements showed the compactness of the composite system increases with percentage increase in weight, as quantity of filler increase. The TGA curve shows that the developed composite is thermally stable up to 400 °C. DC conductivity increases with annealing temperature and wt.% of the ferrite nanoparticles. The magnetic measurements confirm the magnetic nature of the composites at room temperature. The comparatively high values of saturation magnetization confirm its applicability as magnetic absorbers at microwave frequencies.

Microwave characterization of ferrite-NPR nanocomposites are performed over the X-band. The complex permittivity and permeability are computed from measured values of S_{21} and S_{11} using Nicolson Ross method. The results obtained from this method are substantiated by cavity resonator method and found to be

in close proximity. $BaFe_{12}O_{19}$ particles annealed at 900 °C and 50 wt.% shows a high permittivity of ~6.55 and permeability of ~3.59 and dielectric and magnetic loss tangent ~0.3 and ~0.26, respectively. Out of the three ferrite compositions in NPR matrix studied, strontium substituted shows maximum loss tangent with $SrFe_{12}O_{19}$-NPR nanocomposite showing the maximum value of ~0.4 and ~0.35.

The absorber thickness relates to the frequency of operation in a single layer absorber which is basically resonant in nature with maximal microwave absorption occurring at matching thickness, d_m, when d_m equals to an odd multiple of $\lambda_m / 4$, where, $\lambda_m = \lambda_0 / (|\varepsilon_r||\mu_r|)^{1/2}$, the condition for phase cancellation. The absorption studies carried out on a conductor backed single layer absorber developed incorporating the ferrite nanoparticles in NPR matrix, shows that 2 mm layer thickness shows better results as compared to 1 mm, 3 mm and 4 mm for all the compositions.

As aluminium replaces the magnetic ion in $BaAl_xFe_{12-x}O_{19}$ -NPR composite, anisotropy increases which results in increase of absorption and x=1.6 shows a maximum absorption of -40.06 dB at 9.56 GHz with -10dB bandwidth of 4.0 GHz and -20 dB bandwidth of 0.78 GHz. Maximum absorption of -43.06 dB is obtained at 9.70 GHz with -10dB bandwidth of 1.8 GHz and -20 dB bandwidth of 0.40 GHz for the $Ba_{1-x}Sr_xFe_{12}O_{19}$-NPR composite when x=1.0 i.e. with $SrFe_{12}O_{19}$ inclusions.

Multilayering shows enhancement of bandwidth with **CBA** design i.e. with $Ba_{0.6}Sr_{0.4}Fe_{12}O_{19}$-NPR as the first layer and, $BaFe_{12}O_{19}$-NPR as the interphase layer, shows -42.10 dB aborption with -20 dB bandwidth of 1.5 GHz and -10 dB bandwidth i.e. 90% of incident power being absorbed over the whole X-band.

The FDTD technique implemented for analysis of single layer absorber using $BaFe_{12}O_{19}$-NPR composite, successfully analyses the full-wave electric field distribution and return loss of absorber. The electric field pattern shows that due to change in permittivity and permeability values in the magnetic material, the field distribution changes.

The studies on ferrite nanocomposites developed for X-band absorption described in references [63, 65, 67, 72, mentioned in chapter I], show that the three layered absorbers developed in the present study (table 5.13) has reflection loss of -42.10 dB with -10 dB bandwidth covering the entire X-band (4.2 GHz) and has a thickness of 2 mm. Ni-Zn ferrite doped with Co, Cu, or Mg in

polyurethane [65] reports an absorption of -43.71 dB but the thickness is ~6 mm with a -10 dB bandwidth of 2.4 GHz. Similar studies, conducted in reference [63] on Zn Co-substituted W-type barium hexagonal ferrite-rubber composite has a thickness of 1 mm with -10 dB absorption bandwidth of 5 GHz, however, the maximum absorption reported is -28.5 dB (at 10.5 GHz). Other absorbers developed in references [67, 72] show maximum absorption of -14 dB and -9 dB, respectively. Co, Cu, Zn substituted barium hexaferrite-polychloroprene nanocomposite reported in [67] has a -10 dB bandwidth of 2.6 GHz with thickness 6 mm. The results shows that M-type barium ferrite-NPR and Al^{3+} and Sr^{2+} substituted M-type barium ferrite-NPR nanocomposite system can effectively be used as an efficient broad band absorber in X-band. The absorbers are light as compared to their bulk counter parts and thickness of 2 mm is sufficient to give good absorption.

Moreover, the composite system is sufficiently resistant to change in environmental conditions like temperature and humidity. The constituents of composite, viz. nanosized barium ferrite and NPR are corrosive resistant and of low cost. The synthesizing technique is simple and can be easily incorporated for mass scale production with some modifications. The cost of development inclusive of the other expenses like electricity etc. for absorber of 15.2 cm x 15.2 cm with thickness of 0.2 cm is about Rs. 1240/-($ 20.42). The cost does not include the measurement equipment and labour cost.

The absorption can further be enhanced and tuned by selecting the various combinations. The right combinations of layers can be made highly selective absorber to be used as band stop filter.

EMI shielding materials developed is confined to X-band only, absorber to cover - C band and Ku band, has to be developed with enhanced bandwidth, for which some structural modifications and change in reinforcers have to done. Reducing the thickness and making the absorber flexible are other issues to be considered. An absorber with more flexibility and higher tensile strength are to be developed for use as absorbing and leakage sealing tapes. This can be carried out by using flexible polymer matrix like e EPDM, LLDPE etc.

Appendix A

A. Theoretical thickness limit for broadband microwave absorption in the frequency range 8.2 GHz to 12.4 GHz

The minimum thickness limit of a dielectric microwave absorber for broadband absorption in a particular frequency ranges, f_1 and f_2, corresponding to wavelength, λ_1 and λ_2 is given as,

$$\left|\int_0^\infty \ln|R(\lambda)|d\lambda\right| \leq 2\pi^2 \sum_i d_i \quad \text{(A.1)}$$

Where, d_i is the thickness of the i^{th} layer of the absorber, $R(\lambda)$ is the frequency dependent reflectance and $d\lambda = \lambda_1 - \lambda_2$.

Introducing decibel scale of the reflectance i.e. RL_c=20log$|R(\lambda)|$ and since $ln|R(\lambda)|$ =2.303log$|R(\lambda)|$, the equation (A.1) is modified to

$$\left|\int_0^\infty 2.303 \frac{RL_c}{40\pi^2} d\lambda\right| \leq \sum_i \mu_{si} d_i \quad \text{(A.2)}$$

For RLc =-30 dB absorption over the wavelength ranges λ_1 = 36.58 mm and λ_2 = 24.19 mm, the minimum total thickness limit of the absorber is derived as

$$2.303 \frac{RL_c}{40\pi^2} (\lambda_1 - \lambda_2) \leq \mu_{si} d \quad \text{(A.3)}$$

For a magnetic absorber, $\mu_{si} > 1$.

Hence, for absorption level of -30 dB in the X-band, the minimum thickness of the absorber can be determined from equation (1.82) and ranges from 0.5 mm for permeability, μ_{si}=4.4 to 1.03 mm for permeability, μ_{si}=2.1.

Appendix B

B. MATLAB program for reflection loss optimization with varying individual layer thickness of multilayer absorber system

The input impedance and reflection loss of a conductor backed multilayer microwave absorber can be calculated using Transmission Line Model. The following program is developed based on the reflection loss expression for three layer microwave absorber.

```
load ('C:\Users\hp\Desktop\tr1.txt');        %loading 'tr1.txt' file containing
                                             frequency, real and imaginary permittivity
                                             and real and imaginary permeability of
                                             ferrite-NPR nanocompositecomposite
f=tr1(:,1);                                  %frequency in X band
c=3*10^8;                                    %free space microwave velocity

e1=tr1(:,2);                                 %Real permittivity of 1st layer ferrite-NPR
                                             composite
e2=tr1(:,3);                                 %Real permittivity of 2nd layer ferrite-
                                             NPR composite
e3=tr1(:,4);                                 %Real permittivity of 1st layer ferrite-NPR
                                             composite
e11=tr1(:,5);                                %Imaginary permittivity of 1st layer
                                             ferrite-NPR nanocomposite
e22=tr1(:,6);                                %Imaginary permittivity of 2nd layer
                                             ferrite-NPR composite
e33=tr1(:,7);                                %Imaginary permittivity of 3rd layer
                                             ferrite-NPR composite
u1=tr1(:,8);                                 %Real permeability of 1st layer ferrite-NPR
                                             composite
u2=tr1(:,9);                                 %Real permeability of 2nd layer ferrite-
                                             NPR composite
u3=tr1(:,10);                                %Real permeability of 3rd layer ferrite-
                                             NPR composite
u11=tr1(:,11);                               %Imaginary permeability of 1st layer
                                             ferrite-NPR nanocomposite
```

```
u22=tr1(:,12);
```
%Imaginary permeability of 2nd layer ferrite-NPR nanocomposite

```
u33=tr1(:,13);
```
%Imaginary permeability of 3rd layer ferrite-NPR nanocomposite

```
d1=1.0*10^-3;
d2=0.5*10^-3;
d3=0.5*10^-3;
```
%thickness of 1st, 2nd and 3rd layer, d_1, d_2 and d_3

```
er1=complex(e1,-e11);
ur1=complex(u1,-u11);
er2=complex(e2,-e22);
ur2=complex(u2,-u22);
er3=complex(e3,-e33);
ur3=complex(u3,-u33);
a1=ur1./er1;
a11=sqrt(a1);
n1=377*a11;
b1=ur1.*er1;
b11=sqrt(b1);
b111=2*pi*f./c;
b1111=b111.*b11;
g1=1i*b1111;
a2=ur2./er2;
a22=sqrt(a2);
n2=377*a22;
b2=ur2.*er2;
b22=sqrt(b2);
b222=2*pi*f./c;
b2222=b222.*b22;
g2=1i*b2222;
a3=ur3./er3;
a33=sqrt(a3);
n3=377*a33;
b3=ur3.*er3;
b33=sqrt(b3);
b333=2*pi*f./c;
b3333=b333.*b33;
g3=1i*b3333;
D1=tanh(g1.*d1);
D2=tanh(g2.*d2);
D3=tanh(g3.*d3);
```

```
B=n3.*D3;
E1=n1.*D1;
E2=n2.*D2;
F=n1.*D1.*D2;
G=E1+E2;
H=G./(n2+F);
A=n2.*H;
C=A.*D3;
K=A+B;
L=n3+C;
M=K./L;
Z3=n3.*M;
Zinr=real(Z3);
Zini=imag(Z3);
R1=Z3-377;
R2=Z3+377;
R3=R1./R2;
R4=abs(R3);
RL=20*log(R4);
plot(f,RL)
```

Appendix C

THREE-DIMENSIONAL PERFECTLY MATCHED LAYER (PML) EQUATIONS

The Maxwell's equations for TM mode

$$\frac{\partial D_z}{\partial t} = \frac{1}{\sqrt{\varepsilon_0 \mu_0}}\left(\frac{\partial H_y}{\partial x} - \frac{\partial H_x}{\partial y}\right) \quad \text{(C.1.a)}$$

$$D_z(\omega) = \varepsilon_r^*(\omega).E_z(\omega) \quad \text{(C.1.b)}$$

$$\frac{\partial H_x}{\partial t} = -\frac{1}{\sqrt{\varepsilon_0 \mu_0}}\frac{\partial E_z}{\partial y} \quad \text{(C.1.c)}$$

$$\frac{\partial H_y}{\partial t} = \frac{1}{\sqrt{\varepsilon_0 \mu_0}}\frac{\partial E_z}{\partial x} \quad \text{(C.1.d)}$$

If a wave is propagating in medium A and it impinges upon medium B, the amount of reflection can be calculated by the intrinsic impedances of the two media as,

$$\Gamma = \frac{\eta_A - \eta_B}{\eta_A + \eta_B} \quad \text{(C.2)}$$

Where,

$$\eta = \sqrt{\frac{\mu}{\varepsilon}} \quad \text{(C.3)}$$

Now the two dimensional Maxwell's curl equations ((1.a) to (1.d), in Fourier domain are,

$$j\omega D_z = c_0\left(\frac{\partial H_y}{\partial x} - \frac{\partial H_x}{\partial y}\right) \quad \text{(C.4.a)}$$

$$D_z(\omega) = \varepsilon_r^*(\omega).E_z(\omega) \quad \text{(C.4.b)}$$

$$j\omega H_x = -c_0\frac{\partial E_z}{\partial y} \quad \text{(C.4.c)}$$

$$j\omega H_y = c_0\frac{\partial E_z}{\partial x} \quad \text{(C.4.d)}$$

The permittivity ε and permeability μ is replaced by fictitious dielectric constant and permeabilities. Thus,

$$j\omega D_z . \varepsilon^*_{Fz}(x) . \varepsilon^*_{Fz}(y) = c_0 \left(\frac{\partial H_y}{\partial x} - \frac{\partial H_x}{\partial y} \right) \tag{C.5.a}$$

$$D_z(\omega) = \varepsilon^*_r(\omega) . E_z(\omega) \tag{C.5.b}$$

$$j\omega H_x . \mu^*_{Fx}(x) . \mu^*_{Fx}(y) = -c_0 \frac{\partial E_z}{\partial y} \tag{C.5.c}$$

$$j\omega H_y . \mu^*_{Fy}(x) . \mu^*_{Fy}(y) = c_0 \frac{\partial E_z}{\partial x} \tag{C.5.d}$$

The two conditions to form PML:

A. The impedance going from the background medium to the PML must be constant,

$$\eta_0 = \eta_m = \sqrt{\frac{\mu^*_{Fx}}{\varepsilon^*_{Fx}}} = 1 \tag{C.6}$$

B. In the direction perpendicular to the boundary the ε^*_{Fx} and μ^*_{Fx} must be inverse of those in the other directions, i.e.

$$\varepsilon^*_{Fx} = \frac{1}{\varepsilon^*_{Fy}} \tag{C.7.a}$$

$$\mu^*_{Fx} = \frac{1}{\mu^*_{Fy}} \tag{C.7.b}$$

Now,

$$\varepsilon^*_{Fm} = \varepsilon_{Fm} + \frac{\sigma_{Dm}}{j\omega\varepsilon_0} \qquad for \qquad m = x \ \ or \ y \tag{C.8.a}$$

$$\mu^*_{Fm} = \mu_{Fm} + \frac{\sigma_{Hm}}{j\omega\mu_0} \qquad for \qquad m = x \ \ or \ y \tag{C.8.b}$$

The following selection of parameters satisfies equations (A.7.a) and (A.7.b)

$$\varepsilon_{Fm} = \mu_{Fm} = 1 \tag{C.9.a}$$

$$\frac{\sigma_{Dm}}{\varepsilon_0} = \frac{\sigma_{Hm}}{\mu_0} = \frac{\sigma_D}{\varepsilon_0} \tag{C.9.b}$$

So, equation (A.6) becomes,

$$\eta_0 = \eta_m = \sqrt{\frac{\mu^*_{Fx}}{\varepsilon^*_{Fx}}} = \sqrt{\frac{1 + \sigma(x)/j\omega\varepsilon_0}{1 + \sigma(x)/j\omega\varepsilon_0}} = 1$$

Implementing a PML only in the X direction, equations ((C.5.a)-(C.5.d))

$$j\omega D_z.\varepsilon^*_{Fz}(x) = c_0\left(\frac{\partial H_y}{\partial x} - \frac{\partial H_x}{\partial y}\right)$$

$$j\omega H_x.\mu^*_{Fx}(x) = -c_0\frac{\partial E_z}{\partial y}$$

$$j\omega H_y.\mu^*_{Fy}(x) = c_0\frac{\partial E_z}{\partial x}$$

And use the values of equations (A.9.a) and (A.9.b),

$$j\omega\left(1+\frac{\sigma_D(x)}{j\omega\varepsilon_0}\right)D_z = c_0\left(\frac{\partial H_y}{\partial x} - \frac{\partial H_x}{\partial y}\right) \quad \text{(C.10.a)}$$

$$j\omega\left(1+\frac{\sigma_D(x)}{j\omega\varepsilon_0}\right)^{-1}H_x = -c_0\frac{\partial E_z}{\partial y} \quad \text{(C.10.b)}$$

$$j\omega\left(1+\frac{\sigma_D(x)}{j\omega\varepsilon_0}\right)H_y = c_0\frac{\partial E_z}{\partial x} \quad \text{(C.10.c)}$$

Again to put into the FDTD formulation, following modifications are performed,

$$j\omega\left(1+\frac{\sigma_D(x)}{j\omega\varepsilon_0}\right)D_z = j\omega D_z + \frac{\sigma_D(x)}{\varepsilon_0}D_z$$

$$\frac{\partial D_z}{\partial t} + \frac{\sigma_D(i)}{\varepsilon_0}D_z \cong \frac{D_z^{n+1/2}(i,j) - D_z^{n-1/2}(i,j)}{\Delta t} + \frac{\sigma_D(i)}{\varepsilon_0}\frac{D_z^{n+1/2}(i,j) + D_z^{n-1/2}(i,j)}{2}$$

$$= D_z^{n+1/2}(i,j)\frac{1}{\Delta t}\left[1+\frac{\sigma_D(i).\Delta t}{2.\varepsilon_0}\right] - D_z^{n-1/2}(i,j)\frac{1}{\Delta t}\left[1-\frac{\sigma_D(i).\Delta t}{2.\varepsilon_0}\right]$$

$$D_z^{n+1/2}(i,j) = gi3(i).D_z^{n-1/2}(i,j) +$$
$$gi2(i).0.5.\left[H_y^n(i+1/2,j) - H_y^n(i-1/2,j) - H_x^n(i,j+1/2) + H_x^n(i,j-1/2)\right] \quad \text{(C.11)}$$

Using the Courant stability,

$$\frac{\Delta t}{\Delta x}c_0 = \frac{\Delta x/(2.c_0)}{\Delta x}c_0 = \frac{1}{2}$$

The parameters are defined as,

$$gi2(i) = \frac{1}{1+\sigma_D(i).\Delta t/(2.\varepsilon_0)} \tag{C.12.a}$$

$$gi3(i) = \frac{1-\sigma_D(i).\Delta t/(2.\varepsilon_0)}{1+\sigma_D(i).\Delta t/(2.\varepsilon_0)} \tag{C.12.b}$$

An identical treatment to equation no (A.10.c) gives,

$$H_y^{n+1}(i+1/2,j) = fi3(i+1/2).H_y^n(i+1/2,j) + fi2(i+1/2).0.5\left[E_z^{n+1/2}(i+1,j) - E_z^{n+1/2}(i,j)\right] \tag{C.13}$$

where,

$$fi2(i+1/2) = \frac{1}{1+\sigma_D(i+1/2).\Delta t/(2.\varepsilon_0)} \tag{C.14.a}$$

$$fi3(i+1/2) = \frac{1-\sigma_D(i+1/2).\Delta t/(2.\varepsilon_0)}{1+\sigma_D(i+1/2).\Delta t/(2.\varepsilon_0)} \tag{C.14.b}$$

Equation (A.10.b) require a somewhat different treatment as,

$$j\omega H_x = -c_0\left[\frac{\partial E_z}{\partial y} + \frac{\sigma_D(x)}{\varepsilon_0}\frac{1}{j\omega}\frac{\partial E_z}{\partial y}\right]$$

$$\frac{\partial E_z}{\partial y} \cong \frac{E_z^{n+1/2}(i,j+1) - E_z^{n+1/2}(i,j)}{\Delta x} = -\frac{curl\_e}{\Delta x}$$

$$\frac{H_x^{n+1}(i,j+1/2) - H_x^n(i,j+1/2)}{\Delta t} = -c_0\left[\frac{curl\_e}{\Delta x} - \frac{\sigma_D(x)}{\varepsilon_0}\Delta t\sum_{n=0}^{T}\frac{curl\_e}{\Delta x}\right]$$

$$H_x^{n+1}(i,j+1/2) = H_x^n(i,j+1/2) + \frac{c_0.\Delta t}{\Delta x}curl\_e + \frac{c_0.\Delta t}{\Delta x}\frac{\sigma_D(x).\Delta t}{\varepsilon_0}I_{Hx}^{n+1/2}(i,j+1/2)$$

$$= H_x^n(i,j+1/2) + \frac{c_0.\Delta t}{\Delta x}curl\_e + \frac{\sigma_D(x).\Delta t}{2\varepsilon_0}I_{Hx}^{n+1/2}(i,j+1/2)$$

Equation (A.10.b) is implemented as the following series,

$$curl\_e = \left[E_z^{n+1/2}(i,j) - E_z^{n+1/2}(i,j+1)\right] \tag{C.15.a}$$

$$I_{Hx}^{n+1/2}(i,j+1/2) = I_{Hx}^{n-1/2}(i,j+1/2) + curl\_e \tag{C.15.b}$$

$$H_x^{n+1}(i,j+1/2) = H_x^n(i,j+1/2) + 0.5.curl\_e + fi1(i).I_{Hx}^{n+1/2}(i,j+1/2) \tag{C.15.c}$$

with

$$fil(i) = \frac{\sigma(i).\Delta t}{2\varepsilon_0} \tag{C.16}$$

Instead of varying conductivities, we calculate an auxiliary parameter,

$$xn = \frac{\sigma.\Delta t}{2.\varepsilon_0}$$

Then,

$$xn(i) = .333 * \left(\frac{i}{length\_pml}\right)^3 \qquad i = 1,2,.....,length\_pml \tag{C.17}$$

$$fil(i) = xn(i) \tag{C.18.a}$$

$$gi2(i) = \left(\frac{1}{1+xn(i)}\right) \tag{C.18.b}$$

$$gi3(i) = \left(\frac{1-xn(i)}{1+xn(i)}\right) \tag{C.18.c}$$

Similarly considering y- direction,

$$j\omega\left(1+\frac{\sigma_D(x)}{j\omega\varepsilon_0}\right)\left(1+\frac{\sigma_D(y)}{j\omega\varepsilon_0}\right)D_z = c_0\left(\frac{\partial H_y}{\partial x} - \frac{\partial H_x}{\partial y}\right) \tag{C.19.a}$$

$$j\omega\left(1+\frac{\sigma_D(x)}{j\omega\varepsilon_0}\right)^{-1}\left(1+\frac{\sigma_D(y)}{j\omega\varepsilon_0}\right)H_x = c_0\left(-\frac{\partial E_z}{\partial y}\right) \tag{C.19.a}$$

$$j\omega\left(1+\frac{\sigma_D(x)}{j\omega\varepsilon_0}\right)\left(1+\frac{\sigma_D(y)}{j\omega\varepsilon_0}\right)^{-1}H_y = c_0\left(\frac{\partial E_z}{\partial x}\right) \tag{C.19.c}$$

Equation (A.11) is replaced by the following,

$$D_z^{n+1/2}(i,j) = gi3(i).gj3(j).D_z^{n-1/2}(i,j) + gi2(i).gj2(j).(0.5).\left[H_y^n(i+1/2,j) - H_y^n(i-1/2,j) - H_x^n(i,j+1/2) + H_x^n(i,j-1/2)\right]$$

H_y will be implemented as,

$$curl\_e = \left[E_z^{n+1/2}(i+1,j) - E_z^{n+1/2}(i,j)\right] \tag{C.20.a}$$

$$I_{Hy}^{n+1/2}(i+1/2,j) = I_{Hy}^{n-1/2}(i+1/2,j) + curl\_e \tag{C.20.b}$$

$$H_y^{n+1}(i+1/2,j) = fi3(i+1/2).H_y^n(i+1/2,j) - fi2(i+1/2).(0.5).curl\_e + fj1(j).I_{Hy}^{n+1/2}(i+1/2,j) \quad \text{(C.20.c)}$$

Finally, H_x in the X direction becomes,

$$curl\_e = \left[E_z^{n+1/2}(i,j) - E_z^{n+1/2}(i,j+1)\right] \quad \text{(C.21.a)}$$

$$I_{Hx}^{n+1/2}(i,j+1/2) = I_{Hx}^{n-1/2}(i,j+1/2) + curl\_e \quad \text{(C.21.b)}$$

$$H_x^{n+1}(i,j+1/2) = fj3(j+1/2).H_x^n(i,j+1/2) + fj2(j+1/2).(0.5).curl\_e + fi1(i).I_{Hx}^{n+1/2}(i,j+1/2) \quad \text{(C.21.c)}$$

In three dimensional problem,

$$j\omega.\left(1+\frac{\sigma_x(x)}{j\omega\varepsilon_0}\right)\left(1+\frac{\sigma_y(y)}{j\omega\varepsilon_0}\right)\left(1+\frac{\sigma_z(z)}{j\omega\varepsilon_0}\right)^{-1} D_z = c_0.\left(\frac{\partial H_y}{\partial x} - \frac{\partial H_x}{\partial y}\right) \quad \text{(C.22)}$$

Rewriting equation (A.22),

$$j\omega.\left(1+\frac{\sigma_x(x)}{j\omega\varepsilon_0}\right)\left(1+\frac{\sigma_y(y)}{j\omega\varepsilon_0}\right)D_z = c_0\left(1+\frac{\sigma_z(z)}{j\omega\varepsilon_0}\right).\left(\frac{\partial H_y}{\partial x} - \frac{\partial H_x}{\partial y}\right)$$
$$= c_0.curl\_h + c_0.\frac{\sigma_z(z)}{\varepsilon_0}\frac{1}{j\omega}curl\_h \quad \text{(C.23)}$$

where,

$$I_{Dz} = \frac{1}{j\omega}curl\_h$$

Equation (A.23) becomes,

$$j\omega.\left(1+\frac{\sigma_x(x)}{j\omega\varepsilon_0}\right)\left(1+\frac{\sigma_y(y)}{j\omega\varepsilon_0}\right)D_z = c_0.\left(curl\_h + \frac{\sigma_z(z)}{\varepsilon_0}I_{Dz}\right) \quad \text{(C.24)}$$

Equation (A.24) is implemented into FDTD as,

$$curl\_h = \begin{bmatrix} H_y^n(i+1/2,j,k+1/2) - H_y^n(i-1/2,j,k+1/2) \\ -H_x^n(i,j+1/2,k+1/2) + H_x^n(i,j-1/2,k+1/2) \end{bmatrix} \quad \text{(C.25.a)}$$

$$I_{Dz}^n(i,j,k+1/2) = I_{Dz}^{n-1}(i,j,k+1/2) + curl\_h \quad \text{(C.25.b)}$$

$$D_z^{n+1/2}(i,j,k+1/2) = gi3(i).gj3(j).D_z^{n-1/2}(i,j,k+1/2) + gi2(i).gj2(j).0.5.\left(curl\_h + gk1(k).I_{Dz}^n(i,j,k+1/2)\right) \quad \text{(C.25.c)}$$

Appendix D

3D FDTD CODE MODULES FOR D_z, E_z AND H_z UPDATE FOR SINGLE LAYER MAGNETIC ABSORBERS

The variables used in the code are defined in chapter VI. After initialization of variables and specifying the calculation domain, the D_z, E_z and H_z fields are updated using FDTD update equations. Here the codes for updating D_z, E_z and H_z fields are illustrated in the following sections,

D1. Code for updating D_z and $E_z$field

```
curl_h=(ra_x*(hy(i,j,k)-hy(i-1,j,k))-ra_y*(hx(i,j,k)-hx(i,j-1,k)));
dz(i,j,k)=gi3(i)*gj3(j)*dz(i,j,k)+gi2(i)*gj2(j)*.5*(curl_h);
 kzh=k-kb;
curl_h=ra_x*(hy(i,j,k)-hy(i-1,j,k))-ra_y*(hx(i,j,k)-hx(i,j-1,k));
idzh(i,j,kzh)=idzh(i,j,kzh)+curl_h;
dz(i,j,k)=gi3(i)*gj3(j)*dz(i,j,k)+gi2(i)*gj2(j)*.5*(curl_h+gk1(k)*idzh(i,j,kzh));
ez(i,j,k)=gaz(i,j,k)*dz(i,j,k);
```

D2. Code for updating H_z fields

```
curl_e=(ra_y*(ex(i,j+1,k)-ex(i,j,k))-ra_x*(ey(i+1,j,k)-ey(i,j,k)));
hz(i,j,k)=fi3(i)*fj3(j)*hz(i,j,k)+fi2(i)*fj2(j)*.5*(curl_e);
 kzh=k-kb;
curl_e=(ra_y*(ex(i,j+1,k)-ex(i,j,k))-ra_x*(ey(i+1,j,k)-ey(i,j,k)));
ihzh(i,j,kzh)=ihzh(i,j,kzh)+curl_e;
hz(i,j,k)=fi3(i)*fj3(j)*hz(i,j,k)+fi2(i)*fj2(j)*.5*(curl_e+fk1(k)*ihzh(i,j,kzh));
```

Publications

Published in referred journals

1. S. Özah and N. S. Bhattacharyya "Nanosized barium hexaferrite in Novolac Phenolic Resin as microwave absorber for X-band application", Journal of Magnetism and Magnetic Materials 342, pp. 92-99, 2013
2. **S. Ozah** and N.S. Bhattacharyya, "Development of $BaAl_xFe_{12-x}O_{19}$-NPR nanocomposite as an efficient absorbing material in the X- band", Journal of Magnetism and magnetic materials 374, pp.516-524, 2015.

Published in international conference proceedings

3. S. **Ozah,** J. P. Gogoi and N. S. Bhattacharyya "Microwave absorbing properties of $CoFe_2O_4$/ bamboo charcoal/titania -LDPE polymer composite", *IEEE proc. AEMC 2009, Kolkata* doi: 10.1109/AEMC.2009.5430636
4. **S. Ozah** and N.S. Bhattacharyya, "Effect of annealing temperature of nano-sized $BaFe_{12}O_{19}$ in Novolac Phenolic Resin on microwave properties for use as EMI shielding material in X-band", *Proc. of SPIE Vol. 8760 87600Q-1*
5. **S. Ozah** and N. S. Bhattacharyya, "Microwave Absorption Measurement of Nanocomposite Using Free Space Technique", (Extended abstract) , National workshop on nuclear and atomic techniques based pure and applied sciences (NATPAS-11), organized by UGCDAE and Tezpur university, Tezpur University , India, February, 2011.

Papers communicated/under preparation

1. **S. Ozah** and N. S. Bhattacharyya, "Enhancement of absorbtion in X-band as strontium substitutes barium in M-type nanoferrite in Novolac Phenolic Resin", *communicated to Journal of Electronic Materials.*
2. **S. Ozah** and N. S. Bhattacharyya, "Broadband absorber over the X-band using M-type hexagonal nanoferrite composites in multilayer structure- Design, optimization and synthesis", *Under preparation, to be sent to IEEE trans. on Electromagnetic Compatibility.*